Aus dem Institut für Veterinär-Pathologie der Justus-Liebig-Universität Gießen

Betreuer: Prof. Dr. Jens P. Teifke

und

dem Friedrich-Loeffler-Institut, Bundesforschungsinstitut für Tiergesundheit, Greifswald – Insel Riems

Betreuerin: Prof. Dr. Anca Dorhoi

Comparative analysis of Cedar virus entry and antiviral innate immune responses in human, porcine, and fruit bat cell culture systems

INAUGURAL-DISSERTATION
zur Erlangung des Grades eines
Dr. med. vet.
beim Fachbereich Veterinärmedizin
der Justus-Liebig-Universität Gießen

eingereicht von

Lea Lenhard

Tierärztin aus Schweinfurt

Gießen 2026

Mit Genehmigung des Fachbereichs Veterinärmedizin

der Justus-Liebig-Universität Gießen

Dekan: Prof. Dr. Dr. Stefan Arnhold

1. Gutachter: Prof. Dr. Jens P. Teifke
2. Gutachter: Prof. Dr. Anca Dorhoi
3. Gutachter: Prof. Dr. Friedemann Weber

Tag der Disputation: 01.04.2026

Teile dieser Arbeit wurden bereits in wissenschaftlichen Fachjournalen publiziert:

Lenhard L, Müller M, Diederich S, Loerzer L, Friedrichs V, Köllner B, Finke S, Dorhoi A, Pei G. Ephrin B1 and B2 Mediate Cedar Virus Entry into Egyptian Fruit Bat Cells. *Viruses*. 2025; 17(4):573. https://doi.org/10.3390/v17040573

Daten aus dieser Arbeit wurden auf internationalen Fachtagungen präsentiert und in Tagungsbänden veröffentlicht:

VIA 2024 : Annual Meeting „Veterinärmedizinischer Arbeitskreis“; Jena, July, 3-5, 2024: Program, 2024., VIA Meeting. Presented at the VIA; (Hannover) : 2022.09.06-07.

International Symposium “Proteases in Inflammation and Infection”, 2024., RTG 2719 Conferences and Workshops. Presented at the RTG2719_PRO Conference; (Rostock-Warnemünde) : 204.09.25-27.

“I can live with doubt and uncertainty and not knowing. I think it’s much more interesting to live not knowing than to have answers, which might be wrong. I have approximate answers and possible beliefs and different degrees of certainty about different things, but I’m not absolutely sure of anything.”

- *Richard P. Feynman*

Table of Contents

1. Introduction and objective

Henipaviruses, such as Hendra virus (HeV) and Nipah virus (NiV), are emerging threats to global public health and are currently listed on the WHO Blueprint list of epidemic threats, which require immediate research and development efforts [1,2]. Their high pathogenicity and ability to inhibit the host's innate immune response complicate research into antiviral drugs and vaccines [3–5]. The discovery and isolation of the first non-pathogenic henipavirus, Cedar virus (CedV), from black flying foxes in Australia has created new possibilities for henipavirus research under low biosafety conditions [6]. Although CedV's low virulence has been demonstrated in animal trials and some cell culture experiments [6–8], the mechanisms by which CedV enters the cells of its natural host, fruit bats, and whether such infection activates innate immune responses and cellular stress remain poorly understood.

CedV enters human cells via the cell surface proteins, ephrin B1 and B2, and with lower efficiency, A2 and A5 [9–11]. The first objective of this project was to determine which fruit bat ephrins mediate CedV entry, using Egyptian rousette bats (ERB, *Rousettus aegyptiacus*) as a model species. Receptor usage can influence viral spread and disease progression [12]. Therefore, investigating the contribution of specific ephrins to viral entry is a first step in assessing virulence in that species. To this end, entry of a recombinant fluorescent CedV (rCedV-nTurbo635) was evaluated in different assays, including cells that stably express single ERB ephrins and specific ERB ephrin knockdown cells.

Secondly, the innate immune responses of ERB, porcine, and human epithelial cells to rCedV-nTurbo635 infection were evaluated at both the transcriptional and translational level. Replication competence was assessed under various conditions, including the inhibition of interferon signaling. As HeV and NiV proteins are known to suppress type I interferon (IFN) induction and signaling [13–18], when individually expressed in cell culture systems, similar experiments were carried out with CedV proteins F, G, M, N, P, and C to evaluate their effects on IFN induction.

The third objective focused on whether rCedV-nTurbo635 could trigger ER stress and cell death in epithelial cell lines and primary ERB lung endothelia-like cells. Apoptosis was assessed using Western blot and high-content microscopy to determine the activation and activity of caspase-3 and -7, the key apoptotic caspases.

In all, this project sheds light on the receptors used by CedV to enter fruit bat cells, as well as the innate immune processes and cytopathic effects that follow the infection of different epithelial cell lines.

2. Literature review

2.1. Henipaviruses – an emerging global threat

2.1.1. Henipaviruses – a reason for concern?

In 1994, in Queensland, Australia, a horse trainer and 14 of his horses died from a febrile illness. The causative agent was later isolated and named Hendra virus (HeV), representing a novel genus, *Henipavirus*, within the family *Paramyxoviridae*[19–21]. Within the same decade (1998/99), Nipah virus (NiV), which is closely related to HeV, emerged among pig farmers and their livestock in Malaysia [22]. Both viruses cause respiratory and neurological symptoms, with high case fatality rates of 40-75% [23,24]. Pathology is dominated by thrombosis and severe vasculitis in small blood vessels, most prominently in the brain and lungs, characterized by destruction of the endothelial lining and necrosis of the vessel walls [4]. The reservoir hosts for both viruses are fruit bats of the genus *Pteropus*, which transmit the virus to terrestrial mammals indirectly via contamination of fruit and date palm sap, or likely also directly through bites and scratches [1,25–28]. Initially, most human HeV and NiV infections occurred through contact with intermediate hosts, such as horses or pigs [19,22] (**Figure 2.1**). However, more recent NiV outbreaks in Bangladesh and India have raised concern, as human-to-human transmission has been reported [29,30].

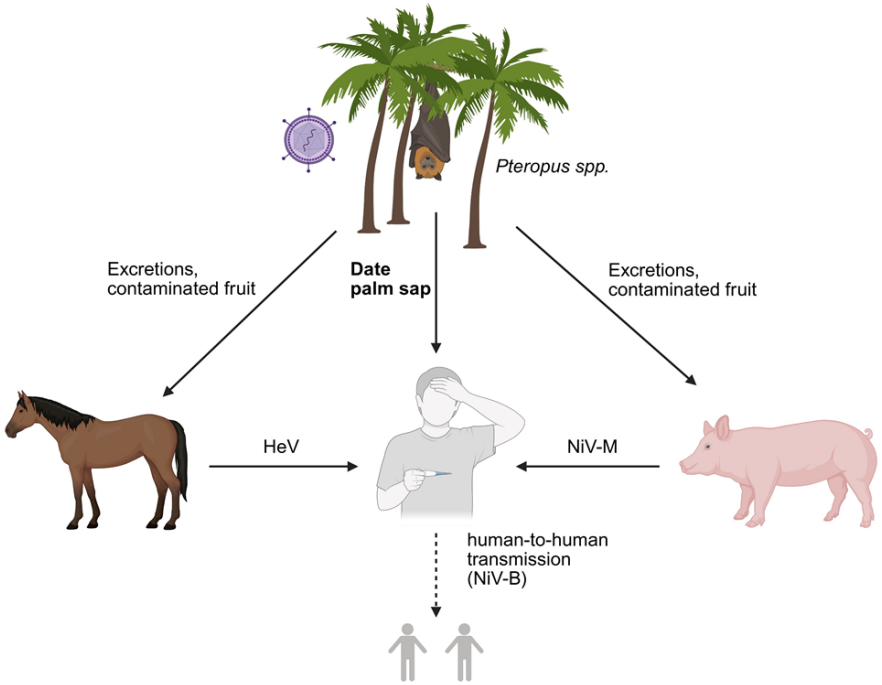

Figure 2.1. Henipavirus transmission.

Illustration of henipavirus transmission from reservoir hosts (*Pteropus spp.*) to intermediate hosts (horses, pigs) and humans. NiV-M: Nipah virus Malaysia, NiV-B: Nipah virus Bangladesh, HeV: Hendra virus. Image was modified from Quarleri *et al.* [1] and created with Biorender.com.

As their distinctive genome, high virulence, and broad host range distinguish HeV and NiV from other paramyxoviruses, a new genus, *Henipavirus,* has been created. Due to the current lack of specific treatments or vaccines, they are classified as biosafety level 4 (BSL-4) pathogens [31,32].

2.1.2. Novel henipaviruses and bats

In recent years, an increasing number of novel henipavirus(-like) sequences have been identified all across the globe, with some successfully isolated from patients or reservoir hosts (**Table 2.1**). Different fruit bat species play a significant role in harboring henipaviruses, but shrews and rodents have also been implicated as reservoirs [33,34].

Table 2.1. Novel henipavirus-like viruses.

Viruses marked with a star (*) are not formally classified as henipaviruses by ICTV as of March 2025. *Crocidura sp.*= shrew species; *Marmosa demerarae* = woolly mouse opossum; *Rattus flavipectus* = Asian house rat; *Eidolon dupreanum/ Eidolon helvum/ Pteropus alecto* = fruit bat species.

Virus	Host species	Country of origin	Live virus isolation	Human infections reported
***Angavokely virus[35]**	*Eidolon dupreanum*	Republic of Madagascar	no	no
Cedar virus[6]	*Pteropus alecto*	Australia	yes	no
***Daeryong virus[34]**	*Crocidura sp.*	Republic of Korea	no	no
***Denwin virus[36]**	*Crocidura russula*	Belgium	no	no
***Gamak virus[34]**	*Crocidura sp.*	Republic of Korea	yes	no
Ghanian bat virus[33]	*Eidolon helvum*	Ghana	no	no

***Langya virus**[37]	*Crocidura sp.*	China	yes	yes
***Melian virus**[36]	*Crocidura grandiceps*	Guinea	no	no
***Mòjiāng virus**[38]	*Rattus flavipectus*	China	no	yes
***Peixe-Boi virus**[39]	*Marmosa demerarae*	Brazil	no	no

On the ever-growing list of novel henipaviruses, Cedar virus (CedV) stands out as the only non-pathogenic virus that has been successfully isolated and can now be used to study the genus under low biosafety conditions [6,10]. The low virulence and pathogenicity becomes apparent *in vivo,* as challenged hamsters, ferrets, and guinea pigs display no clinical signs, even though CedV can replicate in both the upper and lower respiratory tract [6,8]. Genetically, CedV is very similar to HeV and NiV; it does not, however, possess the important virulence factors V and W that inhibit the host's innate immune response and thereby enhance viral replication (discussed in chapter 2.2.4) [6,8,10,40].

Henipavirus-like sequences have been identified during screenings of bat species across Africa, including various non-*Pteropus* bat families, such as *Pteronotus parnellii*, *Carollia perspicillata*, ERB, and *Eidolon helvum* [33,41–43]. The sequences detected in ERB are most similar to the Australian CedV isolate [42]. Despite this, the experimental intranasal challenge of ERB was unsuccessful, as none of the animals seroconverted or became PCR-positive during the trial [44]. These results either indicate resistance to CedV or a suboptimal route of infection. Along those lines, ERB are also refractory to intraperitoneal NiV infection, and even though ERB-derived cells express the necessary receptors for viral entry, productive replication cannot be observed [45]. As experimental data contradict evidence in free-ranging bats, more research is required to elucidate the role of ERB as a potential henipavirus reservoir. In contrast, *Pteropus poliocephalus*, challenged with HeV, present a clear picture of subclinical disease, characterized by the absence of apparent clinical signs, by seroconversion, and minor endothelial damage [46,47]. HeV is even transmitted transplacentally without disruption of the pregnancy [46,47]. NiV infected *Pteropus vampyrus* and *Pteropus alecto*, the confirmed reservoir hosts, seroconvert, but only a few individuals shed infectious virus, while all remain clinically healthy [28,48].

2.1.3. Genome organization and role of viral proteins

Henipaviruses belong to the family *Paramyxoviridae* [49]. Paramyxoviruses are enveloped viruses with a single-stranded, negative-sense, non-segmented RNA genome and share a similar basic organizational structure [49,50]. The HeV and NiV genomes encode for 9 proteins, N, P, C, V, W, M, F, G and L, whereas the CedV genome only encodes for 7, omitting V and W [49,51]. The genome is transcribed from 3' to 5' end in a decreasing mRNA gradient, starting with the most abundant nucleocapsid protein (N) that binds and encapsidates the viral genomic RNA (**Figure 2.2**) [51]. Next in line for transcription is the phosphoprotein (P), which, together with the large protein (L), forms the RNA-dependent RNA polymerase (RdRp) [52]. The RdRp generates 5' capped and methylated, 3' polyadenylated mRNAs for viral protein synthesis [53]. When sufficient nucleocapsid protein is synthesized, the RdRp starts replicating the viral genome by first generating a full-length antigenomic strand, which serves as a template for subsequent genome replication [51,52,54–56]. During this process, the L protein is responsible for enzymatic activity, while the P protein links the polymerase to its RNA template [52,54]. In case of HeV and NiV, the P gene also encodes for the accessory V and W proteins by "RNA editing" (insertion of guanine residues, which change the open reading frame) and for the C protein by alternative translation initiation at the ribosomal site [50]. The editing of the P mRNA is linked to the "rule of six"; however, the reason for this connection has not been elucidated, thus far [57]. This concept, inherent to *Paramyxovirinae*, states that for the virus to replicate efficiently, the genome length in nucleotides must be divisible by six [57]. The matrix protein (M) regulates virion assembly and budding at the plasma membrane by connecting the ribonucleoprotein complex (genomic RNA encapsidated by N) with the glycoprotein G and the fusion protein F [58,59]. The glycoprotein G, also known as the receptor binding protein (RBP), is expressed as tetramers on the envelope surface and attaches to its cell surface receptor, such as ephrins, in the case of most thoroughly investigated henipaviruses [60,61]. This attachment triggers structural alterations in the G monomer head domain, as well as conformational changes in F_1 protein trimers, which form membrane fusion pores to mediate complete membrane fusion and the release of the viral genome into the host cell [60,62]. The F_0 protein, translated initially from the viral mRNA, is processed through the ER, expressed on the cell surface, and then internalized into endosomes to be cleaved by the host protease cathepsin L, resulting in the two fragments F_1 and F_2 [63–65]. The now biologically active F_1 fragment reassembles into homotrimers, which are still linked to F_2 homotrimers through disulfide bonds, before being transported back to the cell surface [62].

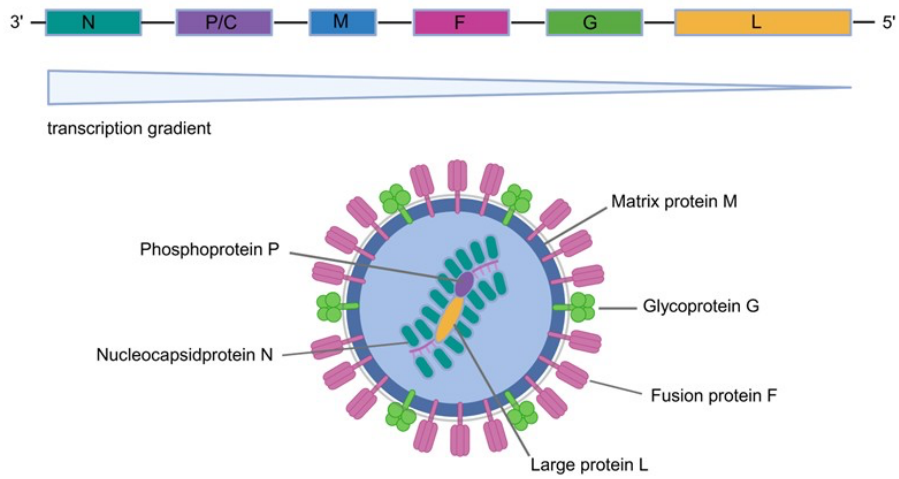

Figure 2.2. CedV genome and viral particle constituents.

The henipavirus genome is transcribed from 3' to 5' end in a decreasing gradient. The glycoprotein G and fusion protein F are expressed on the surface of virions and mediate entry and fusion. The matrix protein M is responsible for virion assembly and budding. The viral RNA genome is encapsidated by the nucleocapsid protein N and the phosphoprotein P mediates binding of the RNA-dependent RNA polymerase (large protein) to the viral RNA. Sizes are not up to scale. Image was modified from Rima *et al*. [49] and Marsh *et al.* [6] and created with Biorender.com.

2.1.4. Influence of entry receptors on tissue tropism and pathology

HeV and NiV enter host cells by attaching to the receptor-binding domain of the cell-surface-associated proteins ephrin B2 and B3 [66–68]. Ephrins are divided into two groups: the ephrin A class, containing ephrin A1 to A5, and the ephrin B class, including ephrin B1 to B3. B ephrins comprise an Eph-receptor binding domain (G-H-loop), a transmembrane segment, and a cytoplasmic region [69,70]. A ephrins, as the smaller family members, only consist of the Eph-receptor binding region in combination with a Glycosylphosphatidylinositol (GPI) anchor [69,70]. Physiologically, ephrin-Eph-receptor signaling plays a crucial role in communication between neighboring cells, particularly during the embryonic development of the central nervous system, as well as in various cellular processes in the adult organism [71–73]. Therefore, ephrins are expressed in almost all tissues [69]. In case of henipavirus infections, ephrin tissue distribution partially explains the neurotropism of HeV and NiV, as ephrin B3 is predominantly expressed in the neural tube midline during embryogenesis and is generally significant for synapse formation in the hippocampus and forebrain [73,74]. One characteristic feature of HeV/NiV infections is the involvement of capillaries and small blood vessels leading to vasculitis, necrosis, and hemorrhages in multiple organs, which has been connected to ephrin B2 expression on endothelial cells [4,67,75–77]. Since ephrins and their receptors are widely

conserved among vertebrates, HeV and NiV have an unusually broad host spectrum when compared to other paramyxoviruses. It includes, in addition to the hosts mentioned above, cats, dogs, guinea pigs, hamsters, and various fruit bat species [48,75,78–81]. Susceptibility to infection is, however, not only determined by expression of the appropriate receptors, but also dependent on other cellular factors. For instance, a mouse and a rat cell line that express ephrin B2 have been shown to be refractory to NiV infection, suggesting a mechanism that limits viral replication at the post-entry step [82].

CedV utilizes ephrins B1 and B2 to enter human cells and additionally shows moderate binding affinity to ephrins A2 and A5 [9]. CedV G protein only shares 30% homology with its NiV counterpart, which explains the difference in receptor usage [6,11]. While HeV and NiV G proteins interact with the tyrosine residue in the G-H loop of human ephrin B3, CedV G protein has an asparagine residue at the equivalent position, rendering receptor binding unstable [9]. CedV, on the other hand, can utilize human ephrin B1, because in contrast to HeV/NiV G proteins, CedV G protein can accommodate the Tyr-Met motif, present within the ephrin B1 G-H-loop [11]. As ephrin B1 is widely distributed across multiple organs and is usually expressed at high levels, its usage could be advantageous regarding systemic infections [11] .

2.2. Henipavirus pathogenicity and host defense

2.2.1. Bats harbor many zoonotic viruses without developing disease

Bats (Order: Chiroptera) consist of more than 1,400 different species making them the second most species-rich mammalian order after rodents [83]. Fruit bats belong to the suborder Yinpterochiroptera and differ, e.g., in physiology, habitat, and feeding from their generally smaller relatives, the Yangochiroptera (Vespertilioniformes) [84]. Egyptian Rousette bats (ERB) are widely, but patchily, distributed across Africa, the Arabian Peninsula, and the eastern Mediterranean region [84,85]. Unlike most fruit bats, ERB roost in large numbers in caves instead of trees and use tongue clicking for echolocation [84]. They are, next to *Pteropus* bats, one of the more thoroughly researched bat species. As cave-roosting species, they can be sampled more easily, they are not in danger of extinction and the establishment of breeding colonies has been successful in various institutions [44,86,87]. They are the natural reservoir for the highly pathogenic Marburg virus (MARV) and Sosuga virus, and a plethora of other paramyxo- and coronaviruses have been shown to be associated with ERB as well [41,42,87–92].

In recent years, accumulating evidence has placed bats at the center of attention as reservoir hosts for many zoonotic viruses [93]. Even though they are susceptible to infection with highly

pathogenic viruses, such as MARV [88,89], NiV [94], severe acute respiratory syndrome virus (SARS)-like coronaviruses [95], etc., they exhibit no overt symptoms or succumb to disease [48,87,96]. Unraveling why bats are so impervious to viral diseases is an important task, as it could have far-reaching implications for antiviral treatments in humans. Currently, various theories exist regarding how the bat immune system effectively combats viral infections. During flight, their body temperature increases up to 42°C, which could limit pathogen replication ("Flight as fever" hypothesis) [97,98]. Additionally, some bat species, such as *Pteropus,* constitutively express type I Interferon (IFN I) [99] and show reduced inflammasome activation upon stimulation of Toll-like receptors (TLRs) [100,101]. During the evolution of powered flight, genes associated with DNA repair pathways, such as those encoding for DNA-PKc (DNA-dependent protein kinase catalytic subunit) or KU80, were positively selected in bats to counteract heat-related DNA release into the cytosol and increased reactive oxygen species (ROS) formation [102]. This improvement in DNA repair is accompanied by attenuated DNA sensing [102–106]. Many bat genomes currently available lack the Pyrin and HIN domain (PYHIN) gene family, e.g., *AIM2* [107], *IFI16* [108], *Pyhin 1* [109], which are responsible for cytosolic DNA sensing and inflammasome activation [102–106]. This can explain dampened reactivity to DNA viruses and cellular damage [102–106]. The dampened NLRP3 inflammasome activation also results in less IL1β secretion, a pro-inflammatory cytokine, which causes tissue damage and inflammation [101,105]. Along those lines, ERB react to MARV infection with the upregulation of antiviral pathways, but in contrast to human patients, the bat immune system is able to control (hyper-) inflammation [110,111]. Supporting viral replication while controlling adverse immune reactions is referred to as "disease tolerance" [96,112]. Another theory for why bats harbor as many highly pathogenic viruses is an improved ability to control viral replication, termed "host resistance/host defense" [112,113]. Overall, bats have been shown to balance restricting viral loads and preventing pathological inflammation [96,112]. However, bats can develop diseases and succumb to some infections. For example *Eidolon helvum* bats succumb to Lagos bat virus[114,115] , rabies virus can cause disease symptoms and death in *Eptesicus fuscus* [116] and *Myotis* spp. in the US have nearly been eradicated by the fungus *Pseudogymnoascus destructans* ("white nose syndrome") [117,118]. A challenge in bat immunology is the often fragmented data, which is limited to a few individual species, making it difficult to draw conclusions about bats as a whole order.

2.2.2. Type I interferon induction and signaling

Interferons (IFNs) were first discovered in 1957 as a novel substance interfering with influenza virus replication [119–124]. We now differentiate between three subclasses: type I IFN, consisting of IFNα, β, δ, ε, κ, τ, ω; type II IFN (IFNγ); and type III IFN, also called IFNλ [122]. IFNs are an

essential part of the innate immune response and undisputed in their role as antiviral effectors. Cells recognize pathogen- and damage-associated molecular patterns (PAMPs, DAMPs), such as double- or single-stranded RNA, extranuclear DNA, bacterial membrane components like lipopolysaccharide (LPS) or peptidoglycans, via pattern recognition receptors (PRRs) [125]. In case of RNA-virus infections, the responsible PRRs include the endosomal Toll-like receptors (TLRs 3, 7, 8), the cytosolic family of RIG-I-like receptors (RLR): retinoic acid inducible gene 1 (RIG-I), melanoma differentiation-associated gene 5 (MDA5), and Laboratory of Genetics and Physiology 2 (LGP2) [126–128]. Upon ligand recognition, TLRs can recruit Toll/IL-1R domain-containing adaptor-inducing IFNB (TRIF) or myeloid differentiation primary response-88 (MYD88), which leads to IFN induction via Interferon regulatory factors 3 and 7 (IRF3, IRF7) translocation to the nucleus [129]. RIG-I and MDA5 activation results in the recruitment of kinases TBK1 and IKKε via the mitochondrial antiviral signaling protein (MAVS), ultimately leading to IRF3/7-dependent type I IFN transcription [122,126] (**Figure 2.3**). IFNs are secreted and can affect both the activated cells themselves (autocrine) and neighboring cells (paracrine) [122].

The type I IFNs all activate the same receptor pair, IFNAR1 and 2, which leads to Janus kinase (JAK1) and tyrosine kinase 2 (TYK2) mediated phosphorylation of signal transducer and activator of transcription 1 (STAT1) and STAT2. STAT1 heterodimerizes with STAT2, associates with IFN regulatory factor 9 (IRF9), and, after nuclear translocation, activates IFN-stimulated response element (ISRE)-dependent transcription of IFN-stimulated genes (ISGs) [122]. STAT1 can also form homodimers, which translocate to the nucleus and initiate gamma interferon activation site (GAS) dependent gene transcription [122]. As the name suggests, GAS elements are inducible by IFNγ receptor (IFNGR1 and 2) activation, in addition to IFNAR1/2, since IFNGR-dependent JAKs also phosphorylate STAT1. IFNγ is primarily secreted by natural killer cells and activated T cells, thereby bridging the gap to the adaptive branch of the immune system [130–132]. Type III IFNs, IFNλ1, λ2, and λ3, bind to their own receptor, consisting of the two subunits IFNLR1 and IL10R2, which leads to the initiation of JAK-STAT signaling, similar to type I IFN signaling [133–136]. One difference in cellular response between type I and type III IFNs is due to the tissue distribution of the respective receptors [137]. IFNAR1, IFNAR2, and IL10R are expressed on almost all cells, whereas IFNLR1 expression is more limited to specific organs (e.g., lungs, stomach, intestine) or cell types (e.g., dendritic or epithelial cells) [137,138]. IFNLR1/IL10R2 is particularly abundant at mucosal barrier sites, where it confers increased protection against pathogen entry [133,136,138]. Additionally, the expression levels of the respective IFN receptors, the timing of IFN secretion and receptor binding, inhibitory mechanisms, as well as unknown factors, all play a role in nuanced responses to different IFNs [137].

2.2.3. Antiviral innate immune responses in fruit bats: similar, but different?

With an increase in bat immunology research in recent years, the black box of the bat immune system is slowly being decoded. Since in ERB only 2.75% of genes are associated with the immune system, in comparison to ~ 7% in humans, differences in signaling and functionality between these two species are inevitable [139,140]. In general, foreign RNA sensing, IFN induction, and signaling seem to be conserved among bats; however, in such a diverse order, some distinctions must be made, and knowledge about one species might not apply to another. For the TLRs 1-9, homologs have been found in the ERB genome, whereas *P. alecto* also encode a functional *TLR10* and a *TLR13* pseudogene [139,141,142]. Additionally, all three RLRs (RIG-I, MDA5, LGP2) have been sequenced and functionally characterized in *P. alecto,* revealing a high level of similarity to their human counterparts, which suggests a conserved mode of foreign RNA sensing in bats [142,143]. MAVS, as an essential adaptor molecule downstream of RLRs, is present in the ERB genome, and its expression has been demonstrated in other bat species as well [139,144]. However, in contrast to the RLRs and some ISGs, e.g., Myxoma resistance 1 (*MX1)* or 2',5'-oligoadenylate synthetase (*OAS1)*, the degree of amino acid similarity to MAVS of other species is low, which could indicate functional deviation [141,143,145,146]. In *P. alecto,* IRF7 is constitutively expressed in most tissues, which could enable a stronger and more rapid IFN response in the event of viral infections [147]. Additionally, Banerjee *et al*. demonstrated that an alternative IRF3 phosphorylation site, found in multiple bat species, already confers enhanced antiviral protection against vesicular stomatitis virus (VSV) [148].

The *P. alecto* genome reveals a contracted type I IFN locus and, surprisingly, constitutive expression of IFNα [99]. On the contrary, ERB underwent expansion of the *IFNB* locus, and there is no evidence of elevated baseline levels of IFNα [149,150]. IFNα signaling via IFNAR1 and IFNAR2 has pronounced antiviral effects, resulting in the transcription of a plethora of ISGs, some of which have no homolog in humans [151]. IFNλ1 and IFNλ2 from *P. alecto* have been sequenced and functionally characterized, revealing antiviral properties and distinct expression patterns compared to type I IFNs [152]. While *P. alecto* cells induce IFNβ in response to polyI:C (dsRNA) transfection, which stimulates cytosolic RLRs, and treatment, activating endosomal TLR3, IFNλ2 is only upregulated in response to cytosolic RLR stimulation [152]. IFNλ1 expression, on the other hand, is stimulated by infection with ssRNA viruses, such as Tioman Paramyxovirus, suggesting distinct roles for the two type III IFNs [152]. Expression of the corresponding receptors, IFNLR1 and IL10R2, on epithelial and immune cells is also in alignment with human data [153]. IFN signaling is also conserved, as key players have been

identified in all thoroughly sequenced species [139,154–156]. ERB STAT1 is capable of translocating to the nucleus to initiate transcription of ISGs [154].

Most ISGs, induced in fruit bat cells, are conserved in their expression and function when compared to human data [139,142,146,157,158]. Interestingly, the time course and intensity of gene induction differ distinctly, with shorter ISG induction and lower fold changes measured in bat cells [157]. Ribonuclease L (RNase L), which is activated by OAS and degrades viral and cellular RNA, has been discovered as a novel ISG in *P. alecto*, but not ERB [151,157,159,160]. Enhanced RNA degradation, in addition to its obvious benefits during viral infections, can also potentiate IFN responses and lead to apoptosis, ultimately providing increased antiviral defense [161,162]. Recently, structural changes in the *ISG15* of certain bat species have been demonstrated to lead to more efficient restriction of viral replication, while simultaneously reducing the pro-inflammatory secretion of *ISG15* dimers [163]. In contrast, *TRIM40* is a fruit bat-specific ISG, which promotes NiV replication by inhibiting RLR-mediated IFN induction [164].

One key difference in bat antiviral responses, first suggested by Banerjee *et al*. [113], might be the reduced induction of pro-inflammatory cytokines, as demonstrated for c-Rel-mediated suppression of tumor necrosis factor α (*TNFA*) signaling in the big brown bat and evidence of nuclear factor κ-light-chain-enhancer of activated B cells (NF-κB) related gene losses in recently annotated bat genomes [156,165]. Similarly, the low induction of pro-inflammatory cytokines *TNFA* and interleukin 6 (*IL6*) has also been observed in cells of the Mexican free-tailed bat in response to RNA virus infections [145]. In terms of improved viral control, bat protein kinase R (*PKR*) was positively selected for and underwent a duplication event during evolution, suggesting diversification in function or specificity [166]. PKR is activated by dsRNA, phosphorylates the translation initiation factor eIF2α, and thereby inhibits translation, which slows down viral replication, while also enhancing IFN production [167–169].

Large-scale bat genome analyses reveal an evolution toward reduced inflammation, while maintaining adequate antiviral mechanisms [103,156,163,170]. Each new bat genome annotation also provides some unannotated contigs with ORFs, suggesting expression of order-, and even species-specific genes that could be relevant in immunity [139,142,151].

2.2.4. Inhibition of innate immunity by paramyxoviral proteins

Many paramyxovirus P gene products influence the host's innate immune system to enhance viral replication, e.g., Sendai virus (SeV) C proteins [171], Mumps V protein [172], and human parainfluenza virus 2 (HPIV-2) V protein [173] all antagonize IFN induction and signaling. The IFN antagonistic abilities of HeV and NiV P gene products were discovered early on in cell

culture experiments [174]; however, the extent and exact mechanism are still subject to much debate (**Figure 2.3**) [175]. Since V and W stem from RNA editing of the P mRNA, all three proteins share the same N-terminal domain, which binds to STAT1 and 2, but not STAT3 [3,5]. This prevents the phosphorylation of the tyrosine residue by Janus kinase (JAK) and thereby inhibits STAT activation [13,14,16,176]. While P and V are expressed in the cytoplasm, W is more prominent in the nucleus, where it prevents ISRE-dependent transcription of ISGs by sequestering unphosphorylated STAT1 [15,177]. In cells that express NiV W, STAT1 is already located in the nucleus in its inactive form, and its localization does not change after IFNβ stimulation [16]. NiV nucleocapsid protein N interferes with STAT import into the nucleus, thereby reducing ISG induction, yet without altering phosphorylation of STAT [18]. In contrast to some other paramyxoviruses (e.g., Simian virus 5, HPIV-2) [178], henipavirus infection does not cause increased STAT degradation, but rather sequestration [177]. Similar observations have also been made using recombinant NiV infection [177]. Conversely, Virtue *et al*. report no influence on IFN signaling in response to henipavirus infections in human cells and hypothesize that the observed STAT inhibitions are merely an artifact of overexpression models [179].

CedV P gene does not encode a V or W protein and exhibits very low sequence homology to HeV/NiV P genes [6,7]. Overexpression of CedV P is not able to prevent STAT 1/2 translocation to the nucleus, whereas CedV infection merely has a limited effect on IFN-induced STAT signaling, all in all suggesting a negligible influence on this pathway [7].

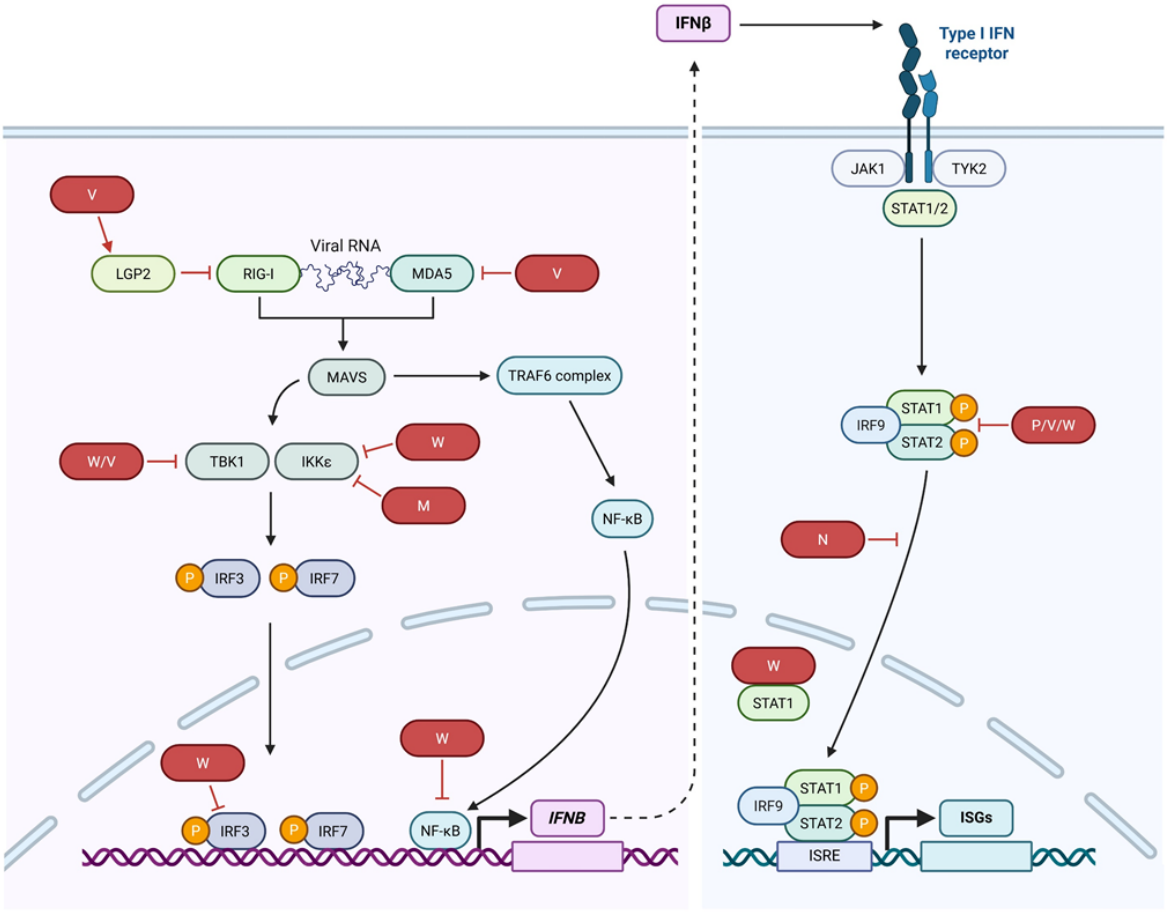

Figure 2.3. Henipaviruses inhibit interferon induction and signaling.

HeV/NiV V protein inhibits *IFNB* induction by preventing dephosphorylation of MDA5, stabilizing the LGP2-dependent inhibition of RIG-I, and through interaction with TBK1. The W protein inhibits IKKε and TBK1, reduces the amount of phosphorylated IRF3 in the nucleus and suppresses NF-κB-mediated transcription. Thereby, V and W expression decrease IFN production. HeV/NiV/CedV M proteins reduce IKKε-mediated IRF3/7 activation.

P, V, and W share the same N-terminus, which binds to STAT1/2 to prevent activating phosphorylation. Additionally, the W protein sequesters unphosphorylated STAT1 in the nucleus, preventing transcription of ISGs. The N protein interferes with the nuclear translocation of STAT.

LGP2, Laboratory of genetics and physiology 2; RIG-I, Retinoic acid inducible gene I; MDA5, Melanoma differentiation-associated gene 5; MAVS, Mitochondrial antiviral signaling protein; TBK1, TANK-binding kinase 1; IKKε, I-kappa-B kinase ε; IRF, Interferon regulatory factor; NF-κB, Nuclear factor κ-light-chain-enhancer of activated B cells; TRAF6, Tumor necrosis factor receptor-associated factor 6; JAK, Janus kinase; STAT, Signal transducer and activator of transcription 1; ISRE, Interferon-stimulated response elements; ISG, Interferon stimulated gene;

The illustration was created in Biorender.com, using a template generated by J. Tucker [175].

Additionally, HeV and NiV V proteins inhibit MDA5-mediated IFN induction by interacting with phosphatases PP1α and PP1γ to prevent dephosphorylation of MDA5 [180–182]. In viral infections, the cytosolic PRR MDA5 binds to dsRNA, is then dephosphorylated by PP1α and PP1γ, which enables its interaction with MAVS [183,184]. Interestingly, the V protein-mediated inhibition of PP1 does not extend to interactions with RIG-I, as RIG-I phosphorylation levels remain unaltered

by V protein expression. This demonstrates a specific mechanism that only obstructs MDA5 dephosphorylation [182]. Nevertheless, paramyxoviruses have also evolved mechanisms to prevent RIG-I-mediated signaling. LGP2 is part of the RIG-I-like receptors (RLR), but its role in IFN induction is controversial. Since it lacks a CARD domain, which is required for the downstream activation of MAVS, LGP2 has to interact with either RIG-I or MDA5 to influence IFN induction [185,186]. There is agreement that LGP2 enhances MDA5 signaling; however, whether it has a positive or negative regulatory effect on RIG-I remains under debate and may be virus-specific [187–189]. Paramyxoviral V proteins of parainfluenza virus-5 (PIV-5), HeV, and NiV interact with LGP2, which enhances the RIG-I/LGP2/V complex formation and stabilizes the RIG-I inhibition that is already visible in mere LGP2 overexpression [189,190].

Moreover, NiV and HeV W proteins increase the accumulation of the regulatory protein 14-3-3 in the nucleus and enhance its inherent ability to suppress NF-κB-mediated transcription of various cytokines [191,192]. In the presence of W, 14-3-3 causes p65, an NF-κB family member, to dissociate from the DNA and translocate back to the cytoplasm [191]. Furthermore, Shaw *et al.* have demonstrated that NiV W protein influences intracellular dsRNA sensing by interfering with TBK1 and IKKε, and additionally decreases the amount of phosphorylated IRF3 in the nucleus, thereby inhibiting transcriptional activation of the *IFNB* promoter downstream of TLR3 and RLRs [15]. NiV V protein, in turn, has a much weaker influence on *IFNB* induction, as it only inhibits TBK1-mediated phosphorylation of IRF3 [15]. Interestingly, NiV, HeV, and CedV M proteins all decrease IKKε activation by degrading the Ubiquitin ligase TRIM6, a mechanism that has not been described for other paramyxoviruses [17].

When focusing solely on *in vitro* data, it appears that W protein is the primary IFN antagonist. Surprisingly, *in vivo* experiments with recombinant NiV deficient of either V or W protein paint a very different picture [40,193]. Ferrets challenged with a V-deficient NiV suffer a febrile illness, but do not succumb to the disease. At the same time, animals challenged with a W-knockout (NiV-Wko) strain present with severe neurological signs and attenuated respiratory disease, but unaltered lethality [40]. Those observations suggest that the V protein is the essential pathogenicity factor, and the presence of the W protein influences tissue tropism towards lung pathology, thereby altering the disease course [40].

Of the three non-structural proteins, the C protein and its influence on replication, as well as immune responses, is the most ambiguous. NiV C deletion mutants (NiV-Cko) consistently grow to lower titers in cell culture [193–196]; however, C protein expression can impede minigenome replication [197]. Some studies have shown a weak ability to inhibit IFN [174,193], whereas others report more potent effects on IFN and proinflammatory cytokine levels [195,196].

While NiV-Cko virulence is drastically decreased in the golden hamster model [193,195], ferrets succumb to the infection within a similar time frame as WT-infected animals [194]. Similar to Measles virus C protein [198], NiV C protein reduces the amount of cytoplasmic dsRNA that could activate PRRs and thereby indirectly reduces IFN induction [196]. Additionally, a direct mechanism takes effect on *IFNB* induction, as well as cytokine expression, which has not been elucidated thus far [195,196]. The NiV C protein's influence on TLR7/9 dependent *IFNA* induction has, however, been demonstrated as being mediated by reduced IRF7 phosphorylation [199].

Some of the aforementioned mechanisms of IFN inhibition have also been demonstrated in fruit bat cells from different species. The NiV V and W proteins exhibit comparable IFN-antagonistic properties in both bat and human cells [155,200]. In *P. alecto* and *P. vampyrus* cells, both IFN induction and signaling are inhibited in response to HeV/NiV infection, suggesting *Pteropodidae* could have developed an IFN-independent mechanism of coping with henipaviruses [155,201]. Transcriptomic and proteomic analyses of HeV-infected *P. alecto* kidney cells (PaKi) indicate that death receptor-mediated apoptosis plays a role in limiting the infection. [202,203]. PaKi cells respond more vigorously to CedV infection than to HeV, exhibiting an upregulation of type I and III IFNs, cytokines, apoptosis-related genes, and regulators of enriched pathways [203]. In general, apoptosis, alongside controlled innate immune responses, likely contributes to the effective limitation of henipavirus infections.

2.2.5. Cellular stress and the unfolded protein response during viral infection

The endoplasmic reticulum (ER) is responsible for protein, lipid, and steroid synthesis and maturation, as well as Ca2+ homeostasis, and it provides a large surface area for important cellular reactions [204]. In case of adverse stimuli, such as hypoxia, viral infections, or Ca2+ imbalance, misfolded or unfolded proteins can accumulate, which eventually leads to the unfolded protein response (UPR) to relieve ER stress. The UPR decreases the load of un- or misfolded proteins through ER-associated protein degradation (ERAD), slows down *de novo* protein synthesis, and increases the expression of ER chaperones, such as heat shock proteins 60, 70 and 90, as well as calreticulin or BiP (GRP78, *HSP5A*) [205]. This can result in either the recovery of cellular steady-state or autophagy, or cell death by apoptosis [204]. The ER transmembrane proteins PKR-like ER kinase (PERK), activating transcription factor 6 (ATF6), and inositol-requiring enzyme 1 (IRE1) initiate the UPR as soon as BiP binds to unfolded proteins in the cytosol and thereby detaches from its receptors [206]. PERK homodimerizes and autophosphorylates before phosphorylating the eukaryotic translation initiation factor 2 (eIF2α), consequently reducing protein synthesis in order to relieve ER stress (**Figure 2.4**) [207,208]. Phosphorylated eIF2α increases translation of ATF4, which in turn leads to

the transcription of cytoprotective genes [209]. In case of prolonged or severe ER stress, activated ATF4 induces transcription of C/EBP homologous protein (CHOP, *DDIT3*) and other apoptosis-related genes, as well as growth arrest and DNA damage-inducible phosphatase GADD34, which, as part of the protein phosphatase 1 (PP1), dephosphorylates eIF2α (negative feedback) [210–212]. CHOP, on the other hand, initiates the expression of additional pro-apoptotic genes, such as death receptor 5 (DR5) [213] , decreases the expression of the apoptosis regulator Bcl2, and activates ER-resident thiol oxidoreductase (ERO1α), which increases reactive oxygen species (ROS) production [214,215] . UPR-associated apoptosis is initiated by Ca2+ efflux from the ER mediated by Bax and Bak [216]. The alteration in intracellular Ca2+ homeostasis eventually leads to caspase-12 and subsequently caspase-9 activation, and it also depolarizes the mitochondrial membrane, causing cytochrome c release [217]. In addition to Calpain-induced activation of caspase-12, caspase-7 can also activate caspase-12 at the outer ER membrane [218–220]. Both pathways lead to apoptosome formation, composed of caspase-9, cytochrome c, and apoptotic protease-activating factor 1 (Apaf1), which ultimately results in caspase-3 activation [221,222]. Activation of the effector caspases, caspase-3 and -7, by initiator caspases, caspase-9 and -12, leads to the well-known hallmarks of apoptosis: cell condensation, DNA fragmentation, formation of apoptotic bodies and membrane blebs [222,223]. The extrinsic apoptosis pathway is induced by members of the TNF superfamily, such as TNFα, TRAIL, or CD95L, which bind to their respective death receptors on the cell surface [224,225]. This binding leads to caspase-8 activation, followed by the recruitment of caspase-3 and programmed cell death [224,225].

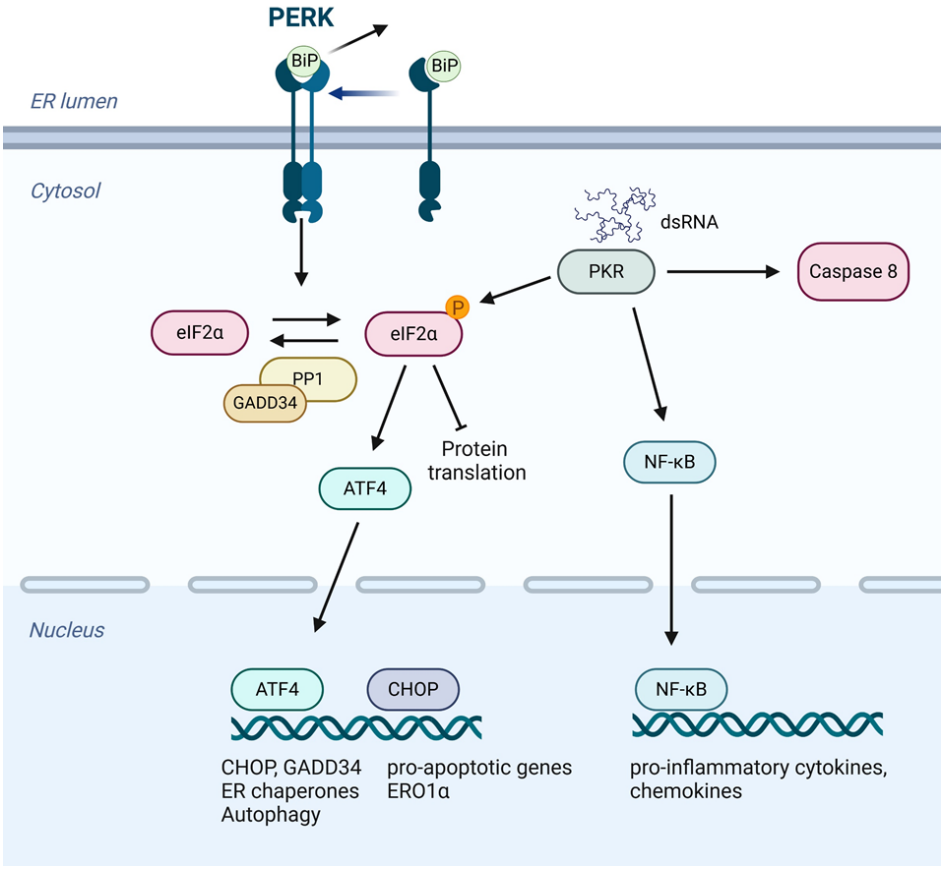

Figure 2.4. PERK-eIF2α-ATF4 signaling and the involvement of PKR.

BiP dissociates from PERK when un-/misfolded proteins accumulate in the ER, thereby triggering this branch of the UPR. EIF2α phosphorylation at Ser51 inhibits further protein translation, but leads to increased translation of transcription factor ATF4, which induces the transcription of pro- and anti-apoptotic genes, as well as those relevant to autophagy. GADD34, as a subunit of phosphatase 1 (PP1), promotes the dephosphorylation of eIF2α, thereby relieving translational shutdown. CHOP induces transcription of pro-apoptotic genes. Activation of PKR by viral dsRNA can also induce eIF2α phosphorylation alongside NF-κB signaling and caspase-8 activation, which triggers apoptosis.

BiP, Binding immunoglobulin protein; PERK, PKR-like ER kinase; eIF2α, eukaryotic translation initiation factor 2 α; PP1, Phosphatase 1; PKR, Protein kinase R; ATF4, activating transcription factor 4; NF-κB, nuclear factor κ-light-chain-enhancer of activated B cells; CHOP, C/EBP homologous protein; GADD34, growth arrest and DNA damage-inducible protein. The illustration was created using Biorender.com, modified from a template generated by Emma Madden (BioRender Science Design Team) and a schematic of the signaling pathway published by Li *et al.* [207].

Many RNA viruses are known to take advantage of the ER membrane for viral replication and vesicle, as well as membrane formation [204]. Some even manipulate specific branches of the UPR to promote their replication, while inhibiting host protein synthesis. A common target, used, for example, by Chikungunya virus and Japanese encephalitis virus, is the inhibition of eIF2α phosphorylation to prevent apoptosis [226,227]. On the other hand, for viruses like the

coronavirus infectious bronchitis virus, it appears to be beneficial to induce the eIF2α-ATF4-CHOP axis and apoptosis, leading to virion release from the cell [228]. The paramyxoviruses Simian virus 5 and SeV induce BiP (*HSP5A*) transcription in human and monkey cells, as existing BiP is sequestered by the accumulation of viral glycoproteins in the ER [229,230]. Bovine parainfluenza virus 3 activates PERK and ATF6, which, through involvement of autophagy, promotes viral replication [231].

Protein kinase R (PKR) is an ISG, and its activation through dsRNA binding leads to IFN induction via NF-κB signaling. Additionally, PKR inhibits protein translation through eIF2α phosphorylation, making it an important connecting link between cellular stress responses and innate immunity [232,233]. In case of some paramyxovirus infections (Respiratory Syncytial virus (RSV), SeV), PKR is activated by copy-back viral genomes and subsequently inhibits protein translation, thereby impeding viral replication, entirely independently of innate immune responses [234]. RSV and SeV also affect the ATF6-IRE1α-XBP1 branch of the cellular stress response, which plays a role in chronic airway disease following acute infection [235,236].

Those examples of how paramyxoviruses influence the host's cellular stress response emphasize the complex machinery of the UPR and the many possibilities of viral interference associated with it. Whether the induction of ER stress is beneficial for viral replication or serves as an antiviral mechanism may be virus and host cell-specific. Whether and how CedV influences the UPR has not been investigated in depth to date.

3. Material

3.1. Laboratory devices

Table 3.1. Laboratory devices used.

Denomination	Origin/Vendor
Biometra Trio PCR thermal cycler	Analytik Jena
BD FACSymphony™ A3 Cell Analyzer	BD Biosciences
CellInsight CX7 Pro HCS-Plattform	ThermoFisher Scientific
Centrifuge 5427R	Eppendorf
Centrifuge 5810R	Eppendorf
ChemiDoc™Imaging Systems	Bio Rad
CO2 Incubator	Sanyo
Cryo-freezing unit	VWR
Finnpipette® F2 multichannel pipettes	ThermoFisher Scientific
Finnpipette® F2 pipettes	ThermoFisher Scientific
Freezer, -20°C/-80°C	Liebherr
C1000™ Thermal Cycler **CFX96 Deep Well™** **Real-Time System**	BioRad
Liquid Nitrogen Preservation System, -190°C	Messer
Magnetic stirrer, RCT basic	IKA
Magnetic stirrer, MR standard	Heidolph

NanoDrop™One	ThermoFisher Scientific
neoFuge® 8-6K micro centrifuge	neoLab
Nikon Eclipse TS2 microscope	Nikon
Nikon Eclipse Ti microscope	Nikon
Optima™ L-100 XP Ultracentrifuge	Beckman Coulter
Bench meter pH50	VioLab
PowerPac™ Basic Power Supply	Bio Rad
Precision scale	Sartorius handy
QuantStudio 6 Flex **qRT-PCR thermal cycler**	Applied Biosystems, ThermoFisher Scientific
REAX 2000 vortex	Heidolph
Refrigerator, 4°C	Liebherr
Scale (EMB 100-3)	KERN
Spark® multimode microplate reader	Tecan.
Sub-Cell® GT, large horizontal gel chamber	Bio Rad
Sub-Gel Mini, small horizontal gel chamber	ThermoFisher Scientific
TapeStation	Agilent Technologies
Ultraflex TOF/TOF Massenspektrometer	Bruker

3.2. Glassware and Tools

Table 3.2. Glassware and tools used.

Denomination	Origin/Vendor
Glass bottles	Schott-DURAN
Glass pipettes	Scherf-Präzision
Glass tumblers	Schott-DURAN
Neubauer counting chamber	Carl Roth
Slides for microscopy	R. Langenbrinck

3.3. Plastics and Consumables

Table 3.3. Plastics and consumables used.

Denomination	Origin/Vendor
6-,12-, 24-, 48-, 96-well plate, flat bottom	Corning
Cell culture flask: T25, T75, T175	Corning
Centrifuge tubes: 15ml, 50ml	Greiner Bio-One
Cryo.s freezing tubes	Greiner Bio-One
EASY strainer ^{TM} cell sieve	Greiner Bio-One
Eppendorf tubes Safe Lock (0.5 ml, 1.5 ml, 2 ml)	Eppendorf AG
FACS tubes	Sarstedt
MicroAmp® Optical 96-well reaction plate	Applied Biosystems, ThermoFisher Scientific

MicroAmp® Optical adhesive film	Applied Biosystems, ThermoFisher Scientific
Nunc™ FluoroNunc™/LumiNunc™ 96-Well Plates	Thermo Scientific
Nylon filter sheet	VWR
Nitrocellulose membrane	Cytiva
Reaction tubes (1.5 ml, 2 ml)	Sarstedt

3.4. Antibodies, dyes and fluorophores

Table 3.4. Antibodies, dyes and fluorophores used for immunofluorescence, flow cytometry, Western blot and high-content microscopy.

Denomination	Conjugate	Host/isotype	clone	Cat. No.	Origin/Vendor
α-β-Actin	-	Mouse/IgM	7D2C10	60008-1-Ig	Proteintech
α-BiP	-	Rabbit/IgG	C50B12	3177S	Cell Signaling Technology
α-caspase-3	-	Rabbit/IgG	D3R6Y	14220S	Cell Signaling Technology
α-cleaved caspase-3	-	Rabbit/IgG	5A1E	9664S	Cell Signaling Technology
α-human-CD31	FITC	Mouse/IgG1, κ	WM59	303103	BioLegend
α-human-CD34	APC	Mouse/IgG1, κ	581	343513	BioLegend
α-DYKDDDDK-tag	-	Mouse/IgG2b	8H6A10	66008-4-Ig	Proteintech
α-DYKDDDDK-tag	-	Rabbit/IgG	polyclonal	20543-1-AP	Proteintech

α- eIF2α	-	Rabbit/IgG	polyclonal	11170-1-AP	Proteintech
α-Phospho-eIF2α (Ser51)	-	Rabbit/IgG	119A11	3597S	Cell Signaling Technology
α-GAPDH	-	Mouse	6C5	AM4300	invitrogen
α-GFP-tag	-	Mouse/IgG2a	1E10H7	66002-1-lg	Proteintech
α-Histone H4		Mouse/IgG1	ab31830		abcam
α-IRF3	-	Rabbit	D6I4C	11904S	Cell Signaling Technology
α-2P-IRF3	-	Rabbit	D6O1M	29047S	Cell Signaling Technology
α-mouse-IgG	Alexa Fluor 488	Goat/IgG (H+L)	Goat, Polyclonal	A-11001	Invitrogen
α-mouse-IgG	BV-421	Goat/polyclonal IgG	Poly4053	405317	BioLegend
α-mouse-IgG	HRP	Goat	Polyclonal	A9044-2ML	Invitrogen
A-pan cytokeratin	FITC	Mouse/IgG1	PCK-26	GTX26401	GeneTex
α-PARP	-	Rabbit	46D11	9532S	Cell Signaling Technology
α-rabbit-IgG	HRP	Goat	polyclonal	A16096	Invitrogen
α-rabbit-IgG	Alexa Fluor 488	Goat/IgG (H+L)	polyclonal	A-11008	Invitrogen
α-Von-Willebrand-factor VII	-	Rabbit	polyclonal	A0082	Dako
CellEvent™ Caspase-3/7 Detection Reagents	FITC	-	-	C10423	ThermoFisher Scientific

4',6-Diamidino-2-phenylindol (DAPI)	-	-	-	D9542	Sigma Aldrich
Zombie UV™ Fixable Viability Kit	-	-	-	423107	BioLegend
Zombie NIR™ Fixable Viability Kit	-	-	-	423105	BioLegend

3.5. Chemicals and reagents

Table 3.5. Chemicals and reagents used.

Denomination	Application	Cat. No.	Origin/Vendor
Ambion™ nuclease-free water	Dilution, reconstitution	AM9930	Invitrogen
Bovine serum albumin (BSA)	IF, WB	A9418	Sigma Aldrich
Chloroform	mRNA extraction	C2432-25ML	Sigma Aldrich
Cycloheximide	Apoptosis induction	C1988-1G	Sigma Life Science
DTT solution 1 mol/l	Laemmli buffer	A3668, 0100	PanReac, AppliChem
Ethylenediamine tetraacetic acid (EDTA)	Buffer preparations	8043.2	Carl Roth
Ethanol	Wash steps	9065.3	Carl Roth
Glycerol	Glycerol stock	SHBJ0588	Sigma Aldrich
IFNα B/D hybrid (1.65 x 10^3 U/ml)	Cell culture IFN stimulation	CGP-35269	Novartis
Isopropanol	mRNA extraction	6752.3	Carl Roth

LE Agarose	DNA gels	840004	Biozym
Lipofectamine 3000™ Transfection reagent	Transfection of HEK-*MX1*-FLuci cells	L300008fire	ThermoFisher Scientific
Methanol	Blotting buffer	4627.4	Carl Roth
Nail polish, gloss 'n roll	IF	-	essence
PageRuler™ Prestained Protein	Protein ladder for Western blot	26616	ThermoFisher Scientific
Phenol-Chloroform-Isoamyl-alcohol	Genomic DNA extraction	A156.2	Carl Roth
Pierce™ Phosphatase Inhibitor Mini Tablets	In 1x RIPA buffer for generation of protein samples	A32957	ThermoFisher Scientific
Pierce™ Protease Inhibitor Mini Tablets, EDTA-Free	In 1x RIPA buffer for generation of protein samples	A32955	ThermoFisher Scientific
Polyethylenimine (PEI)	Transfection	24314-2	Polysciences
Poly(I:C)-LMW/LyoVec™	polyI:C transfection	tlrl-picwlv	InvivoGen
ProLong™ Diamond Antifade Mountant with DAPI	IF	P36962	ThermoFisher Scientific
Proteinase K (>600 U/ml)	Genomic DNA extraction	EO0491	ThermoFisher Scientific
RNAse A (Monarch)	Genomic DNA extraction	T3018-2	New England Biolabs
Saponin	IF	S4521	Sigma Aldrich
Skim Milk Powder	WB	/	Hobbybäcker-Versand
Sodium chloride (NaCl)	Buffer preparations	3957.1	Carl Roth

Sodium Dodecyl Sulfate (SDS) PlusOne	SDS-PAGE	GE17-1313-01	Amersham Biosciences
Staurosporine	Apoptosis induction	569397	Sigma Aldrich
SuperSignal™ West Femto Stable Peroxide	WB	34096	ThermoFisher Scientific
SuperSignal™ West Femto Luminol/Enhancer	WB	34096	ThermoFisher Scientific
TE-buffered phenol (ROTI®Phenol)	Genomic DNA extraction	0038.2	Carl Roth
N,N,N′,N′-Tetramethyl ethylenediamine (TEMED)	SDS-PAGE	236/1	Carl Roth
Tween® 20	WB	P1379	Sigma Aldrich
Tunicamycin	Cell culture treatment (ER stress)	T7765	Sigma Aldrich
TurboFect	Transfection of RaNep cells	R0531	ThermoFisher Scientific
TRIzol™	BSL-4 mRNA samples	15596018	Ambion
UltraPure™ Tris	Buffer preparation	15504-020	Invitrogen

3.6. Reagents for cloning/plasmids/vectors

Table 3.6. Reagents and commercially available plasmids used for cloning.

Denomination	Application	Cat. No.	Origin/Vendor
Gel Loading Dye Purple (6X)	Agarose gel	B7024A	New England Biolabs

HindIII-HF®	Restriction enzyme cloning	R3104S	New England Biolabs
KAPA HiFi HotStart ReadyMix	PCR	7958935001	Roche
KpnI-HF®	Restriction enzyme cloning	R3142S	New England Biolabs
NEBuilder® HiFi DNA Assembly Master Mix	DNA assembly	E2621S	New England Biolabs
pcDNA-FLAG	Cloning	20011	Addgene
p3xFLAG-ATF6	Cloning	11975	Addgene
pNiFty3-IAN-Lucia	Lucia luciferase assay	pnf3-lc7	invivoGen
pEGFP-C1	Cloning	discontinued	Clontech Laboratories
pLKO.1	Cloning for shRNA knockdown	10878	Addgene
pRL Renilla Luciferase Control Reporter Vector (TK promoter)	Renilla luciferase assay	E2241	Promega
Quick-Load® DNA Ladder	DNA Ladder, agarose gel	N0469S	New England Biolabs
Q5® High-Fidelity DNA Polymerase	Mutagenesis PCR	M0491S	New England Biolabs
rCutSmart™Buffer	Restriction enzyme cloning	B6004S	New England Biolabs
STBL3™chemically competent *E. coli*	Transformation	C737303	ThermoFisher Scientific
XhoI	Restriction enzyme cloning	R0146S	New England Biolabs

Table 3.7. Cloned plasmids.

Insert	Characteristics	Backbone	Tag	Origin
CedV N	Human optimized codon sequence	pEGFP-C1	GFP (C-terminus)	author
CedV P	Human optimized codon sequence	pEGFP-C1	GFP (C-terminus)	author
CedV C	Human optimized codon sequence	pEGFP-C1	GFP (C-terminus)	author
CedV M	Human optimized codon sequence	pEGFP-C1	GFP (C-terminus)	author
CedV G	Amplified from cDNA of infected cells	pEGFP-C1	GFP (C-terminus)	author
CedV F	Synthesized by GeneArt	pCAGGS	HA (C-terminus)	Dr. Sandra Diederich (FLI)
ERB ephrin A1	Amplified from PELEPI cDNA	pcDNA-FLAG	FLAG (C-terminus)	author
ERB ephrin A2	Human optimized codon sequence	pcDNA-FLAG	FLAG (C-terminus)	author
ERB ephrin A3	Human optimized codon sequence	pcDNA-FLAG	FLAG (C-terminus)	author
ERB ephrin A4	Human optimized codon sequence	pcDNA-FLAG	FLAG (C-terminus)	author
ERB ephrin A5	Amplified from PELEPI cDNA	pcDNA-FLAG	FLAG (C-terminus)	author
ERB ephrin B1	Human optimized codon sequence	pcDNA-FLAG	FLAG (C-terminus)	author
ERB ephrin B2	Amplified from PELEPI cDNA	pcDNA-FLAG	FLAG (C-terminus)	author

ERB ephrin B3	Human optimized codon sequence	pcDNA-FLAG	FLAG (C-terminus)	author
ERB ephrin A3	Human optimized codon sequence	p3xFLAG	3x FLAG (N-terminus)	author
ERB ephrin A5	Human optimized codon sequence	p3xFLAG	3x FLAG (N-terminus)	author
RIG-I-CA	-	pcDNA-FLAG	FLAG (C-terminus)	Dr. Gang Pei
TBK1	-	pcDNA-FLAG	FLAG (C-terminus)	Dr. Gang Pei
ERB *IFNB* promoter	-	pNiFty3-IAN-Lucia	Lucia luciferase	Dr. Gang Pei
IRF3-5D	-	pcDNA3	FLAG (N-terminus)	Dr. Christine Luttermann
IKKε	-	pcDNA3	FLAG (N-terminus)	Dr. Christine Luttermann
MDA5	-	pCAGGS-FLAG	FLAG (N-terminus)	Dr. Christine Luttermann

3.7. Media, cell lines and supplements

Table 3.8. Media, cell lines, and supplements used for cell culture.

Denomination	Application	Cat. No.	Origin/Vendor
ATV (trypsin 1:250, pH 7.2)	Trypsinization	-	FLI Riems, Biobank
Carbenicillin Dinatriumsalz	Bacterial selection	6344.2	Roth

Cultrex®Rat Collagen I, Lower Viscosity	Coating of cell culture dishes/flasks for PELENDO	3443-100-01	R&D Systems
DMEM (E, high glucose, 4.5 g/l)	HEK-293T, A549 cultivation	-	FLI Riems, Biobank
ECGS	PELENDO	E0760	Sigma Aldrich
Epidermal growth factor (recombinant human), EGF	PELEPI	585508	BioLegend
Fetal Calf Serum (FCS)	Cell culture medium	P30-3302	Pan biotech
Geneticin G418 - Sulfat 50 mg/ml	Selection of ephrin expressing CHO-K1 cells	A6798	AppliChem
Ham's F12 / IMDM (1:1)	PELEPI, RaNep	-	FLI Riems, Biobank
Heparin-Natrium/5 ml (25.000 I.E.)	Basal medium	10067	Rotexmedica
HEPES Buffer 1 M	Basal medium	MS01IF200H	biowest
Insulin-Transferrin-Selenium-X (100x)	PELENDO	51500-056	Gibco® by Life Technologies
Kanamycin	Bacterial selection	T832.5	Roth
L-Glutamine solution, 200mM (100X)	Cell culture medium	MDTC25-005-CV	VWR
MEM (H) + MEM (E) + NEAA	BHK-21, SK-6 cultivation	-	FLI Riems, Biobank
Opti-MEM	Transfections	-	FLI Riems, Biobank
Penicillin-Streptomycin (100X) (P/S)	Cell culture medium	392-0406	VWR

Puromycin dihydrochloride	Selection of ephrin KD cells	ACRO227420100	VWR
Sodium Pyruvate	HEK-293T	12539059	Gibco® by Life Technologies
Vascular endothelial growth factor 165 (recombinant human)	PELENDO	583704	BioLegend

3.8. Composition of media and buffers

Table 3.9. Composition of media and buffers.

Denomination	Contents	Application
Basal medium	IMDM/Ham's F12 (1:1), 2% FCS, Ascorbic Acid (1 µg/ml), Hydrocortisone (1 µg/ml), Heparin (1 Units/mL, 1:5,000), HEPES (1:100), Penicillin/Streptomycin (1:100), Amphotericin B (2.50 µg/mL).	Basal medium for preparation of endothelial cell medium
Coelenterazine stock solution	Solution of 5 mg/mL in acidified methanol	Diluted 1:2,000 with PBS/5 mM NaCl, pH 7.2 for *IFNB* promoter luciferase assay = coelenterazine working solution
Endothelial cell medium	Basal medium, ECGS (15 µg/ml), Insulin-transferrin-Selenium (1:1,000), recombinant human vascular endothelial growth factor (10 ng/ml)	Cultivation of PELENDO
Epithelial cell medium	DMEM/F12 (Gibco), 5% FCS, Glutamine (1:100), HEPES (1:100), Penicillin/Streptomycin (1:100), Amphotericin B (2.50 µg/mL), Cholera toxin (50ng/ml), Insulin-	Cultivation of primary lung or trachea derived bat epithelial cells

	Transferrin-Selenium (1:1,000), EGF (50 ng/ml)	
Firefly luciferase lysis buffer	40 mM Tri-Cl (pH 7.5), 50 mM NaCl, 2 mM EDTA, 1 mM $MgSO_4$/$MgCl_2$, 5 mM DTT, 1% Triton X-100	Cell lysis for Renilla luciferase assay
G lysis buffer	50 mM Tris, 50 mM EDTA, 1% SDS, pH 8.8	Cell lysis for genomic DNA extraction
Infection medium	DMEM (E, high glucose, 4.5 g/l) + 10% FCS	Used for most infections with rCedV
Laemmli	250mM Tris HCl pH 6,8, 40% Glycerol, 8% SDS, bromophenol blue	Preparation of protein samples for SDS-PAGE
LB agar	LB medium, 1.5% agar	Agar for bacterial cultivation
Luria-Bertani (LB) liquid medium	5 g tryptone, 5 g NaCl, 2.5 g yeast extract in 500 ml; adjusted to pH 7.0	Medium for bacterial cultivation
Luciferin assay solution	Coenzyme A: 1.55 mg, Luciferin: 1.07 mg, ATP: 2.21 mg and add them into 7.5 ml reaction buffer (20mM Tri-Cl (pH7.5), 1 mM $MgSO_4$/$MgCl_2$, 5 mM DTT)	Measurement of firefly luciferase in cell lysate
10X RIPA buffer	0.5 M TrisHCl (pH 7,4), 1.5 M NaCl, 2,5% Deoxycholic Acid, 10% NP-40, 10 mM EDTA	Preparation of protein samples for SDS-PAGE
SOB medium	2.5 g yeast extract, 10 g tryptone, 0.292 g NaCl, 0.093 g KCl, 1.0 g $MgCl_2 6H_2O$	Bacterial transformation
20% Sucrose Buffer	SM Buffer: 100 mM NaCl, 8 mM $MgSO_4$, 50 mM Tris-HCl, pH 7.5 + 20% sucrose	Ultracentrifugation

Trizol	Phenol (38%), guanidine thiocyanate (0.8 M), ammonium thiocyanate (0.4 M), sodium acetate (0.1M), glycerol (5%)	Used to lyse cells for mRNA extraction

3.9. Viruses

Table 3.10. Viruses used.

Denomination	Fluorescent protein	Accession no.	Origin
rCedV-nTurbo635 KD13 1.P.1.E. / BSRT7	Turbo FP635 (Katushka) Excitation: 588 nm Emission: 635 nm		FLI Riems, Lab Finke [237]
Nipah virus (NiV) Malaysia	-	AF212302	FLI Riems, Lab Diederich
Wild type Cedar virus (CedV WT)	-	JQ001776	FLI Riems, Lab Diederich

3.10. Primers

Table 3.11. qPCR primers (innate immunity and cellular stress).

Gene symbol	Gene name	Species	Primer sequence: 5' to 3'
ATF4	Activating transcription factor 4	*Homo sapiens*	F: GTTCTCCAGCGACAAGGCTA R: ATCCTGCTTGCTGTTGTTGG
BiP*/HSPA5*	heat shock protein family A (Hsp70) member 5	*Homo sapiens*	F: TGTTCAACCAATTATTATCAGCAAAC R: TTCTGCTGTATCCTCTTCACCAG

CHOP/*DDIT3*	DNA damage inducible transcript 3	*Homo sapiens*	F: AGAACCAGGAAACGGAAACAGA R: TCTCCTTCATGCGCTGCTTT
CXCL10	C-X-C motif chemokine ligand 10	*Homo sapiens*	F: GTGGCATTCAAGGAGTACCTC R: TGATGGCCTTCGATTCTGGATT
GAPDH	Glyceraldehyde-3-phosphate dehydrogenase	*Homo sapiens*	F: GGAGCGAGATCCCTCCAAAAT R: GGCTGTTGTCATACTTCTCATGG
IFNB1	Interferon beta 1	*Homo sapiens*	F: ATGACCAACAAGTGTCTCCTCC R: GGAATCCAAGCAAGTTGTAGCTC
IL1B	Interleukin 1b	*Homo sapiens*	F: CTCTCACCTCTCCTACTCAC R: GACACTGCTACTTCTTGCC
IL6	Interleukin 6	*Homo sapiens*	F: ACTCACCTCTTCAGAACGAATTG R: CCATCTTTGGAAGGTTCAGGTTG
TNFA	Tumor necrosis factor alpha	*Homo sapiens*	F: ACTACAGACCCCCCCTGAAAAC R: GAAGAGGCTGAGGAACAAGCAC
ATF4	Activating transcription factor 4	*Sus scrofa*	F: GAAGCCAGACTCCACTACTTAC R: TAGGAGTCAGGGCTCATACA
BiP/*HSPA5*	heat shock protein family A (Hsp70) member 5	*Sus scrofa*	F: GTTCTTGTTGGTGGCTCTACT R: ACAGCCTCATCTGGGTTTATG
CHOP/*DDIT3*	DNA damage inducible transcript 3	*Sus scrofa*	F: GAGGAGGAAGACCAAAGAAGA R: CTGTGCCACTTTCCTTTCATTC
CXCL10	C-X-C motif chemokine ligand 10	*Sus scrofa*	F: CCTGTTAATCCGAGGTCCTTAG R: CGACTCTGGATTCAGACATCTT
GAPDH	Glyceraldehyde-3-phosphate dehydrogenase	*Sus scrofa*	F: GAACATCATCCCTGCTTCTACC R: GTCAGATCCACAACCGACAC

IFNB1	Interferon beta 1	*Sus scrofa*	F: TTCTCCACCACAGCTCTTTC R: GGACCTCGAAGTTCATCCTATC
IL6	Interleukin 6	*Sus scrofa*	F: GGAGACCTGCTTGATGAGAATC R: CAGCCTCGACATTTCCCTTAT
TNFA	Tumor necrosis factor alpha	*Sus scrofa*	F: CACGTTGTAGCCAATGTCAAAG R: GAAGAGGACCTGGGAGTAGAT
ATF4	Activating transcription factor 4	*Rousettus aegyptiacus*	F: ACTCCAGATCATTCCTTTAGCTTAG R: GGCTCATACAGATGCCACTATC
BiP*/HSPA5*	heat shock protein family A (Hsp70) member 5	*Rousettus aegyptiacus*	F: CCAAGAACCAGCTCACCTCC R: ACTTGATGTCCTGCTGCACA
CDH5/VE-cadherin	Vascular endothelial cadherin	*Rousettus aegyptiacus*	F: CATGGCTACAGTGATCGAAGTG R: CCAGTCGTTGAGGAAGTCATAATC
CHOP*/DDIT3*	DNA damage inducible transcript 3	*Rousettus aegyptiacus*	F: CTTCACCACTCTTGACCCCG R: CCGTTTCCGTTTCCTGGGTA
CXCL10	C-X-C motif chemokine ligand 10	*Rousettus aegyptiacus*	F: CTTTAGAAGTACACGCTGTGTCTGC R: ACCTTTCCTTGCTAATTGCTTTCAGT
EEF1A1	Eukaryotic translation elongation factor 1 alpha 1	*Rousettus aegyptiacus*	F: GTATGCCTGGGTCTTGGATAAA R: GCCTGTGATGTGCCTGTAA
HSP60	Heat shock protein 60	*Rousettus aegyptiacus*	F: GATGCTGTAGCCGTTACTATGG R: CCCAGCCTCTTCATTTGTATTATTG
IFNB1	Interferon beta 1	*Rousettus aegyptiacus*	F: CAGAAGGAGGACGCAGTATT R: GGCTGTATCCAGAAGGTCTATC
IFNL1	Interferon lambda 1	*Rousettus aegyptiacus*	F: GGCTTTGGAGGCTGAACT R: AGGCGGAAGAGGTTGAATG

IL6	Interleukin 6	*Rousettus aegyptiacus*	F: GGTCCTCCTTTGACATCCTATC R: CATCGTTGCCACACATCTTATT
IL1B	Interleukin 1 beta	*Rousettus aegyptiacus*	F: AGACGGTGTACCTCGAAGAT R: CAGGAAGACGGGCATCTG
TNFA	Tumor necrosis factor alpha	*Rousettus aegyptiacus*	F: CAGGTCCTCTTCAAAGGTCAAG R: AGTCAAGATAGTCAGGCAGGT
VEGFR2	Vascular endothelial growth factor receptor 2	*Rousettus aegyptiacus*	F: GGCAAAGACTACATCGTTCTTCC R: CTGACTGATTCCTGCTGTGTTG

Table 3.12. ERB *ephrin* qPCR primers.

Target	Primer sequence	Amplicon size
ERB *ephrin A1*	F: TGGGCAAGGAGTTCAAAGAG R: AACCTCAAGCACCTGTCTTC	97bp
ERB *ephrin A2*	F: GCTCTTCACGCCCTTCTC R: GCCGCACGTAGACCTTC	122bp
ERB *ephrin A3*	F: CATGCGGTGTACTGGAACAG R: TTGTAGTGCGGGCAGTAAATATC	104bp
ERB *ephrin A4*	F: AAGGAGAGCAAGTCGGAGTC R: TCAGAGAACTCGCAGGAGTC	147bp
ERB *ephrin A5*	F: TCTACTGGAACAGCAGCAAC R: GGACATAACGCTCGGTCTTATC	135bp
ERB *ephrin B1*	F: GACTGTGAACCAGGAAGAGAAG R: CCGTCAGGAAGATGATGATGAG	152bp

ERB *ephrin B2*	F: TGGTACTATACCCACAGATAGGAG R: TTTGGCACAGTTGAGGAGAG	167bp
ERB *ephrin B3*	F: GAGAAGGTGAGTGGTGACTATG R: GTAGATGTTTGGAGGACTCTGG	90bp

3.11. Kits

Table 3.13. Commercial kits used.

Denomination	Application	Cat. No.	Origin/Vendor
BigDye® Terminator v1.1 cycle sequencing kit	Sequencing	15771836	Applied Biosystems
High Sensitivity RNA Screen Tape kit	RNA quality control	5067-5579	Agilent
High Sensitivity RNA ScreenTape Ladder	RNA quality control	5067-5581	Agilent
High Sensitivity RNA ScreenTape Sample Buffer	RNA quality control	5067-5580	Agilent
LDH-Cytox™ Assay Kit	Cytotoxicity Measurement	426401	BioLegend
LunaScript® RT SuperMix Kit	Reverse transcription of mRNA	E3010	New England BioLabs
Luna Universal qPCR Master Mix	qPCR	M3003	New England BioLabs
Macherey-Nagel™ NucleoBond™ Xtra Midi	Plasmid extraction from bacterial cultures	REF 740410.50	ThermoFisher Scientific
QIAamp® Viral RNA Mini Kit (50)	Viral RNA extraction from cell culture supernatant	52904	Qiagen

QIAquick Gel Extraction Kit (50)	DNA extraction from agarose gels	28704	Qiagen
True-Nuclear™ Transcription Factor Buffer Set	Fixation of cells for flow cytometry analysis	424401	BioLegend
ZymoPURE Plasmid Miniprep Kit	Plasmid extraction from bacterial cultures	D4210	Zymo Research

3.12. Databases, Services and Software

Table 3.14. Databases, services and software used.

Denomination	Application	Origin/Vendor
BD FACSDiva™ software	Flow cytometry data acquisition	BD Biosciences
Cedar virus genome	Primer design, consensus analysis	NCBI; ViralProj264921; Australian Animal Health Laboratory, CSIRO (2014). Isolate: CG1a. RefSeq: GCF000924595.1
Citavi 6.19	Citation program	Swiss Academic Software
ESPript 3.0	Visualization of protein consensus analysis	https://espript.ibcp.fr/ESPript/ESPript/[238]
FlowJo™ (v_10.9.0)	Analysis of flow cytometry data	BD Life Sciences
Geneious Prime 2021.0.1	Primer design, consensus analysis	Biomatters
GraphPad Prism10 Version 10.1.2(324)	Statistical analysis and data visualization	GraphPad Software
***Homo sapiens* genome**	Primer design, consensus analysis	NCBI; GRCh38.p14

ImageJ/Fiji 1.48v; Java 1.6.0_20[64-bit]	Image editing and analysis	National Institute of Health (NIH)
Image Lab 6.0.1	Western blot analysis	BioRad
OligoAnalyzer™ Tool	Quality control of qPCR primers	Integrated DNA Technologies (IDT)
Microsoft Office Professional Plus 2019 (Word, Power Point, Excel)	Manuscript writing, collection of figures, data analysis	Microsoft
PrimerQuest™ Tool	qPCR primer design	Integrated DNA Technologies (IDT)
***Rousettus aegyptiacus* genome**	Primer design, consensus analysis	NCBI; mRouAeg1.p
***Sus scrofa* genome**	Primer design, consensus analysis	NCBI; Sscrofa11.1
Thermo Scientific HCS Studio 5.0 Cell Analysis Software	Establishment of CX7 protocol, image and data acquisition	ThermoFisher Scientific
TubeSeq Service	Amplicon and plasmid sequencing	Eurofins Genomics
In house sequencing service	Amplicon and plasmid sequencing	FLI Riems, Lab Luttermann

4. Methods

4.1. Basic molecular biology methods

4.1.1. Cloning

Gene sequences used for consensus analysis and gene synthesis were taken from NCBI (CedV RefSeq: GCF000924595.1; ERB: mRouAeg1.p). Cedar virus genes N, P, and C were synthesized with codons optimized to human usage at Twist Bioscience and expressed in the pEGFP-C1 vector (Clontech Laboratories) by performing HIFI DNA assembly (**Supplementary Figure 10.6**). Subcloning of the other viral genes (F, G, and M) was described previously [237,239]. ERB ephrins A1, A5, and B2 were amplified from cDNA obtained from ERB lung epithelial cells. The remaining ephrins (A2, A3, A4, B1, and B3) were synthesized at Eurofins Genomics with nucleotide sequences optimized to human codon usage. All ERB ephrins were first cloned into a pcDNA-FLAG vector by restriction enzyme cloning. Due to low expression levels in HEK-293T cells, A3 and A5 were additionally subcloned into a p3xFLAG-ATF6 vector, thereby tagging them with three consecutive FLAG-tags. Chemically stable *E. coli* (STBL3) were transformed with ~100 ng DNA and subsequently selected for the desired expression by antibiotic selection on agar plates. Plasmids were purified using a commercial kit (ZymoPURE Plasmid Miniprep Kit or Macherey-Nagel™ NucleoBond™ Xtra Midi). Cloning success was determined by visualizing insert sizes on agarose gels after test digestion with the enzymes used for restriction enzyme cloning. Those clones were then sequenced with a forward and complementary reverse primer at Eurofins Genomics, respectively, the in-house sequencing service (FLI), to uncover nucleotide mutations. Sequence alignments were done using Geneious Prime. If amino acid-altering mutations occurred, the sequences were reverted to the original sequence using mutagenesis polymerase chain reaction (PCR).

IRF3-5D and human IKKε were subcloned into a pcDNA3 vector with the FLAG tag at the N-terminus and the human MDA5 was expressed in a pCAGGS-FLAG vector. All three plasmid constructs were kindly shared by Dr. Christine Luttermann (IFI, FLI) and sequenced before usage. Human constitutively active RIG-I (RIG-I-CA) and human TBK1 were already present in the lab, expressed in a pcDNA-FLAG vector with the tag at the C-terminal end. Dr. Gang Pei generated the ERB-*IFNB*-promoter-Lucia plasmid by substituting the murine *IFNB* promoter with the ERB *IFNB* promoter in the commercial plasmid (pNiFty3-IAN-Lucia, InvivoGen).

4.1.2. Transfections

HEK-293T cells were transfected using Polyethylenimine (PEI) [240] at a DNA to PEI ratio of 1:2. For transfection of RaNep cells TurboFect was used according to the manufacturer's instructions at a DNA to TurboFect ratio of 1:4. Due to poor transfection efficiency using PEI, for HEK-*MX1*-FLuci, Lipofectamine 3000™ was used at a DNA to transfection reagent ratio of 1:2 with addition of P3000™ enhancer reagent to the DNA tubes.

4.1.3. PolyI:C stimulation

A stock solution of the poly(I:C)-LMW/LyoVecTM was prepared (50 µg/ml) in endotoxin-free water and incubated at room temperature (RT) for 15 min before first use. A549, RaNep, and SK-6 were stimulated in 12-well plates with 40 µl of the polyI:C solution diluted in 200 µl opti-MEM that was incubated for 15 min at RT before gently dripping it onto the cells. Samples were collected in 1 ml of Trizol 24 h later.

4.1.4. SDS-PAGE and Western blotting

A549, RaNep, and SK-6 were seeded in 6-well plates (4.5 x 10^5 cells per well) and on the next day, after starvation in serum-reduced medium (0-2% FCS) for 1 h, infected with rCedV-nTurbo635 at MOI 0.1, respectively MOCK-infected with PBS. As a positive control for apoptosis, cells were stimulated with Cycloheximide at 50 µg/ml (100 µg/ml for RaNep) or Staurosporine at 1 µM (2 µM for RaNep) for 16 h to 24 h. As a positive control for ER stress, cells were treated with Tunicamycin (5 µg/ml) for different periods ranging from 30 min to 8 h. In subsequent experiments, stimulation times of 2 h and 8 h were used. For each time point post-infection/stimulation, after washing the monolayer twice with ice-cold PBS, cells were resuspended in 300 µl RIPA buffer containing protease and phosphatase inhibitors, incubated on ice for 10 min, and then centrifuged for 10 min at 4°C at 14,000 rpm. Resulting supernatants were mixed 3:1 with Laemmli buffer and boiled for 5 min at 95°C. Subsequently, protein samples were run on a 12.5% SDS gel at 65 V for 30 min and 120 V for 60 min. Proteins were blotted onto nitrocellulose membranes, which were then blocked in 5% skim milk in PBST (PBS + 0.05% Tween) for 2-3 h. Primary antibody incubation took place overnight at 4°C, while the secondary antibody was used at RT for 1 h.

To investigate the influence of viral proteins on IRF3 translocation, HEK-293T cells were seeded in 6-well plates (0.5 x 10^6 cells per well) and transfected on the next day with 1 µg of either human RIG-I-CA or IRF3-5D in addition to 1 µg (G and F 2 µg, due to low expression levels) of the viral genes. Separation of the cytosolic and the nuclear fraction was performed 24 h after transfection. The protocol was modified from the paper published by Senichkin *et al*.

[241], with the addition of one wash step using the hypotonic buffer without NP-40 before incubating the cells in hypotonic buffer containing 0.1% NP-40. The isotonic buffer, used for the final wash step of the nuclear fraction, was supplemented with 0.2% NP-40, and the DNAse buffer step was omitted. Protein samples were prepared as described before.

4.1.5. Polymerase chain reaction (PCR)

4.1.5.1. Genomic DNA extraction

2 x 10^5 cells were seeded in a 12-well plate and cultivated overnight. Cells were lysed in 200 µl G lysis buffer (50 mM Tris, 50 mM EDTA, 1% SDS, pH 8.8), and lysates were transferred into 1.5 ml Eppendorf tubes. After adding 10 µl of protease K (20 mg/ml), the tubes were incubated at 55 °C overnight. To inactivate protease K, samples were heated at 98°C for 5 min. When samples were cooled down to RT, 5 µl of RNase A (20 mg/ml) per tube was used to remove the RNA. After 2 h at 37°C, 200 µl of TE-buffered phenol was added, samples were vortexed for 30 s, and centrifuged at 14,000 rpm for 5 min. Subsequently, the aqueous phase was transferred to a new tube and mixed with an equal volume of phenol-chloroform-isoamyl alcohol (~ 200 µl) to be then centrifuged again at 14,000 rpm for 5 min. The protocol was continued using the aqueous phase from this step, which was mixed with 1 ml ethanol in a new tube. After centrifugation at 14,000 rpm for 5 min, ethanol was discarded and DNA was left to dry at RT. The genomic DNA was dissolved in 50 µl of nuclease-free water, and the DNA concentration was measured using the NanoDrop.

4.1.5.2. Species identification – *CO1* barcoding

To exclude cross-contamination with other cell lines cultivated in the lab, cytochrome c oxidase subunit 1 (*CO1*) barcoding was performed to confirm the ERB origin of the primary lung endothelia-like cells and the ephrin knockdown RaNep. The species identification PCR was performed with genomic DNA according to the protocol established by Cooper *et al*. [242] and additional primers, as previously published [237], were used (**Table 4.1.**).

Table 4.1. Primer sequences used for barcoding in addition to the ones published by Cooper *et al* [242].

Species	Primer sequence	Amplicon size
Egyptian Rousette bat *CO1*	F: TTC TAC CCC CAT CTT TTC TTC TTC TAT TAG R: GGA TAG GGC TGG TGG TTT TAT ATT AAT AAT	250 bp
Tamarin monkey *CO1*	F: TCA ACT TCA TCA CCA CAA TCA TTA ACA TAA R: CTC ATA CGA TAA ACC CTA AAA ATC CGA TAG	400 bp

4.1.5.3. Agarose gel electrophoresis

1% agarose gels were prepared in 1 x TAE buffer, boiled for 3 min, and supplemented with GelRed at a 1:20,000 dilution. DNA samples were mixed with loading dye (1:6) and loaded on the gel next to a marker (range 100 bp – 10 kb). Gels were run in a gel electrophoresis chamber in 1 x TAE buffer for 45 min at 100 V. Amplicon sizes were visualized using a ChemiDoc. For primer specificity validation, amplicons were cut, purified, and either sent for sequencing at Eurofins Genomics or sequenced in-house (FLI sequencing service).

4.1.5.4. Quantitative PCR (RT-qPCR)

mRNA was extracted according to the protocol established by Chomczynski *et al.* [243], and qPCR was performed as previously published [237,244,245]. Three randomly chosen mRNA samples from the BSL-4 animal trial were quality-checked (RNA Analyzer Kit, Tape Station, Agilent) with the assistance of Jennifer Lorke (FLI, Lab Pfaff) to determine the degree of RNA degradation, which is likely caused by the handling of the organ samples in the high-containment area. Most primers for the investigation of immunological parameters in human, porcine, and ERB cells were already validated in the lab [244,245]. The remaining ones were designed using Geneious Prime and the PrimerQuest Tool (Integrated DNA Technologies) according to the following standards: 17-30 bp in length, GC content of 45%-55%, amplicon sizes between 100 bp and 250 bp, and melting temperature of 60-62°C (the complete cycler protocol can be found in **Table 4.2.**). Resulting primer candidates were checked for the

formation of homo- and heterodimers using the OligoAnalyzer Tool (Integrated DNA Technologies). Primer specificity was evaluated by amplicon sizes on agarose gels and by sequencing purified amplicons (Eurofins Genomics/in-house sequencing service). The efficiency of primer sets was determined by calculating the slope and efficiency using Ct values of serially diluted cDNA, with values between 85% and 115% being accepted.

Table 4.2. qPCR cycler protocol.
Temperature changed at a rate of 1.6°C/s, except for the last temperature change at 0.05°C/s. Measurements were taken during steps marked with a star (*).

	Step	Temperature	Time
		95°C	1 min
PCR: 40x	**Denaturation**	95°C	15 s
	Annealing	60-62°C	20 s
	Extension*	72°C	20 s
Melt curve		95 °C	15 s
		60 °C	1 min
	Dissociation*	95 °C	15 s

4.1.5.5. Viral titer determination by RT-qPCR

Cell culture supernatant of CedV WT and NiV-infected cells was inactivated in AVL buffer (QIAamp Viral RNA Kit)/Ethanol and transferred from the S4 facility to the S2 area. RNA extraction was done using the RNA extraction kit and RT-qPCR was performed according to the protocols published by Mohl *et al*. [44] and Feldman *et al.* [246] using the BioRad C1000™ Thermal Cycler.

4.2. Cell culture

4.2.1. Immortalized cell lines

All cell lines were kindly provided by the FLI Biobank, except for the *Rousettus aegyptiacus* nose epithelial cells (RaNep) that were generated at the Institute of Immunology, as described [237]. Human embryonic kidney (HEK-293T) cells and human lung carcinoma cells (A549) were cultured in Dulbecco's modified Eagle's medium (DMEM) (high glucose, 4.5 g/l), supplemented with 10% fetal calf serum (FCS), 1% Penicillin-Streptomycin, 2 mM L-Glutamine, 1% non-essential amino acids (NEAA) and 1 mM sodium pyruvate. Baby hamster kidney (BHK-21) and swine kidney (SK-6) cells were maintained in Minimum Essential Medium (MEM) with Earle's and Hanks' balanced salts and NEAA with the addition of 10% FCS, 1% Penicillin-Streptomycin, and 2 mM L-Glutamine. For Chinese hamster ovary (CHO-K1) cells and RaNep, Ham's F12 / Iscove's Modified Dulbecco's Medium IMDM (1:1) containing 10% FCS, 1% Penicillin-Streptomycin, and 2 mM L-Glutamine was used. Flasks and cell culture plates were kept in a humidified incubator at 37 °C and 5% CO2. Generation, characterization, and maintenance of primary ERB lung endothelia-like cells is described below (chapter 4.3).

4.2.2. Generation of ERB ephrin expressing CHO-K1 (CHO-EFN)

Generation of the CHO-EFN cells was described before [237]. Briefly, CHO-K1 cells were seeded in 12-well plates at 2 x 10^5 cells/well and transfected with 2 µg of the ERB ephrins (A1-A5, B1-B3) or the empty pcDNA-FLAG vector, using PEI. Since expression levels of ERB ephrins A2 and A4 were lower than for the other ephrins, 4 µg of plasmids were used for transfection. To select cells that express the exogenous ephrins, Geneticin (G418) was employed at a concentration of 300 µg/ml and maintained at this level during subsequent cultivation. CHO-EFN cells were expanded to cell culture flasks as soon as the cell monolayer reached confluency, and the empty vector-transfected control had died due to the antibiotic treatment.

4.3. Generation, cultivation, and characterization of primary cells

4.3.1. Generation of primary ERB lung endothelia-like and epithelial cells

Three healthy adult Egyptian Rousette bats (1 male, 2 female) were anesthetized with isoflurane and euthanized by cardiac bleeding (PD Dr. Balkema-Buschmann, INNT). After necropsy, the trachea, gut, and lung were suspended in basal medium, transferred to the lab, and washed multiple times with sterile PBS in glass petri dishes to remove blood and other contaminants. Next, the organs were cut into small pieces (~1 mm) and incubated in 5 ml of

trypsin for 4-6 h, shaking at 37°C. Afterwards, cells were centrifuged (350 xg, 10 min) and plated on sterile, collagen-coated petri dishes in endothelial (lung endothelial cells) or epithelial (gut, lung, trachea epithelial cells) cell culture medium. As soon as larger cell monolayers with the desired morphology formed, those cells were detached and transferred to collagen-coated cell culture flasks.

4.3.2. Characterization of primary ERB lung endothelia-like cells (PELENDO)

PELENDO were characterized by morphology and expression of endothelial cell-specific markers in conventional microscopy, (q)PCR, immunofluorescence staining, transmission electron microscopy (TEM), and flow cytometry.

Electron microscopy

Sample preparation for the electron microscopy and imaging was done by Dr. Kati Franzke (IMED, FLI). To that end, low passage PELENDO were washed in 0,1 M Na-cacodylate buffer, pre-fixed in 2,5 % glutaraldehyde in 0,1 M Na-cacodylate buffer for 15 min at RT and then for 2 h at 4°C, and washed twice using the same buffer as before. Samples were then embedded in 1,8% low-melting agarose in 0,1 M Na-cacodylate buffer and fixed in 1% Osmium acid (OsO_4) for 2 h at 4°C. After two additional washes, contrasting was performed using 1% uranyl acetate overnight. The next day, samples were dehydrated in a rotator utilizing a series of graded alcohols (30%-100% ethanol), followed by two changes using propylene oxide as an intermediate solvent. Samples were then placed in a propylene oxide/resin (glycid ether) (1:1) solution for 1 h 15 min and were subsequently embedded in 100% resin, which was replaced after one day. After polymerization (3 days at 60°C), samples were sharpened (Leica, TRIM2) and semi-thin sections were cut with an ultramicrotome (UC7, Leica; diamond knife: Diatome) to determine the area of interest. Ultra-thin sections were cut using the same machine and placed on mesh grids (Nickel, 300 mesh, Plano GmbH). They were re-contrasted with uranyl acetate or lead citrate, and after drying, analyzed in a transmission electron microscope (Talos F200i, Thermo Fisher Scientific) using an acceleration voltage of 80 kV. Images were taken with a digital camera (Ceta, 16 MP, Software Velox).

Immunohistochemistry

Immunohistochemistry was performed on lung tissue of uninfected ERB by Silvia Schuparis (ATB, FLI) to validate the cross-reactivity of the anti-Von-Willebrand-factor antibody against ERB endothelial cells. Paraffin-embedded tissue was incubated overnight with the anti-Von Willebrand-factor antibody (1:200) and then counterstained with a secondary α-rabbit antibody.

4.4. Virology methods – rCedV-nTurbo635

4.4.1. rCedV-nTurbo635 propagation

The generation of the recombinant Cedar virus, used in subsequent experiments, was previously published by Schrell and Fuchs *et al.* [237,247]. To generate the rCedV-nTurbo635 the coding sequence for the Turbo635 fluorescent protein was attached to triple the sequence for the nuclear localization signal of SV40 and inserted into the CedV cDNA after the P and before the M gene [237]. The Turbo635, also called Katushka, emits a very bright red fluorescent signal with the excitation/emission maxima at 588/635 nm [248]. The resulting recombinant virus is classified as a BSL-2 pathogen. For viral propagation, BHK-21 cells (3 x10^6 in a T175 flask) were infected at a multiplicity of infection (MOI) of 0.1, and the medium was changed 6 h p.i. Supernatant was collected after 72 h, centrifuged at 1,000 xg, 15 min, 4°C, and the resulting supernatant was concentrated by ultracentrifugation with a 20% sucrose gradient for 1 h, 24,100 rpm (100,000 xg, SW32Ti) at 4°C. The virus pellet was resuspended in 1 ml of sterile PBS and frozen in 100-200 µl aliquots at -80°C until further use.

4.4.2. rCedV-nTurbo635 titration

Viral titers were always determined on BHK-21 and, additionally, on A549, RaNep, and SK-6, if the batch was to be used for infection of these cells. Dilution rows (10^{-1} - 10^{-12}) were performed in MEM + NEAA in duplicate, and each dilution row was used for infection twice. At 48 h p.i., plates were fixed in 4% PFA, washed with PBS, and analyzed using the Nikon Eclipse Ti microscope. Titers were calculated using the Spearman-Kärber formula.

$$TCID50 = D^{\left(\frac{n}{p} + 0.5\right)} * \frac{1}{V}$$

TCID50 = tissue culture infection dose 50
D = dilution factor (10)
n = number of positive wells
p = number of parallel wells/number of titration rows
V = sample volume in ml (0.01)

To determine the titer of each batch, titrations were performed at least twice in two independent experiments (**Table 4.3.**).

Table 4.3. TCID50 calculations of virus propagation 11/23.

Cell line	A549	RaNep	SK-6	BHK-21
TCID50	8.2 x 10^5	8.9 x 10^6	3.7 x 10^6	7.2 x 10^7

4.4.3. rCedV-nTurbo635 infection *in vitro*

In vitro infections were performed in infection medium (DMEM + 10 % FCS) for 90 min before changing the medium back to regular cell culture medium. MOIs were calculated using the titers determined for each cell type and the cell count seeded 24 h prior to infection.

4.4.4. rCedV-nTurbo635 replication kinetics

A549, RaNep, SK-6, and BHK-21 were seeded in 24-well plates (1.2 x 10^5 cells per well) and 24 h later infected at MOI 0.1 in infection medium. After 90 min, cells were washed carefully with PBS, and the medium was changed back to the individual cell culture growth media containing 2 % FCS. For each time point (0, 24 h, 48 h, 72 h), microscopy images were taken, and both the supernatant and cells were saved. The cell monolayer was washed carefully with PBS twice before freezing the plates in 300 µl PBS/well at -80°C for at least 2 h. After thawing, the cell suspensions were mixed thoroughly and centrifuged at 14,000 rpm for 10 min at 4°C. The resulting supernatant was used for titrations directly or frozen at -80°C for later use.

4.4.5. rCedV-nTurbo635 replication on AZD4604-treated epithelial cell lines

AZD4604 effect was tested on A549, RaNep, and SK-6 by treating 12-well plates (2 x 10^5 cells/well) with 0.17 µM AZD4604 (1 µg/ml) for 1 h before stimulating the cells with 1,600 U/ml universal IFNα for 4 h ("AZD + IFN"). Positive controls for ISG induction were MOCK-treated with DMSO and then stimulated with IFNα ("IFN"). The "AZD" group was only treated with AZD4604, and MOCK-stimulated, and the negative control consists of completely untreated cells. Subsequently, samples were frozen in Trizol at -20°C until mRNA extraction was performed. Meanwhile, AZD4604 toxicity was tested in LDH assays (see Chapter 4.10.1).

To test how rCedV-nTurbo635 replicates on JAK-STAT inhibited cells, A549, RaNep, and SK-6 were pre-treated with AZD4604 (0.085 µM = 0.5 µg/ml) for 1 h, before cells were infected at MOI 0.1, as described above. After infecting the cells for 90 min, the medium was changed back to 2% FCS regular cell culture medium supplemented with 0.5 µg/ml AZD4604. At zero, 24 h, 48 h, and 72 h p.i. the supernatant was collected and stored at -80 °C until titration on BHK-21 96-well plates.

4.5. Luciferase assays

4.5.1. Lucia luciferase assay

5 x 10^4 HEK-293T/RaNep cells were seeded in a 48-well plate, incubated overnight, and transfected with 100 ng of the Lucia luciferase plasmid (either murine or ERB *IFNB* promoter-dependent luciferase expression), 100 ng RIG-I-CA/TBK1/IKKε/IRF3-5D in addition to 150 ng

of plasmids encoding for the viral proteins (F, G, M, N, P, C), or the empty vector. The negative control was only transfected with 100 ng of the Lucia luciferase, plus 250 ng of the empty vector to ensure that equal amounts of DNA were used in the assay. Measurements were performed using a microplate reader (Spark® Tecan.) 24 h post-transfection, immediately after adding 50 µl of the coelenterazine working solution to 25 µl of the cell culture supernatants in white LumiNunc microplates.

To investigate the potential of the viral proteins for STAT inhibition, HEK-293T cells were seeded in a 48-well plate, incubated overnight, and transfected with 100 ng of the Lucia luciferase plasmid, plus 150 ng of the viral genes. 24 h post-transfection, cells were either stimulated with 800 U/ml IFNα or MOCK-stimulated with PBS in 250 µl cell culture medium per well. After an additional 24 h, luciferase induction was measured as described above. Transfection and stimulation were done in duplicate, and measurements were conducted in two technical replicates in each of the 3 independent experiments.

4.5.2. Renilla luciferase assay

HEK-293T cells were seeded as described above and transfected with 250 ng of a Renilla plasmid with a constitutively active promoter, plus 100 ng of the viral genes, or the empty vector. 24 h post-transfection, the supernatant was discarded, and the cells were incubated in 100 µl of firefly luciferase lysis buffer for 10 min on ice. Then, the cell lysates were resuspended, and 25 µl thereof were mixed with 50 µl of the coelenterazine working solution. Renilla luciferase was immediately measured in the microplate reader (Spark® Tecan.).

4.5.3. Firefly luciferase assay of HEK-*MX1*-promoter-Fluci

HEK-293T expressing a firefly luciferase under the human *MX1* promoter (HEK-*MX1*-promoter-FLuci) were previously generated in the Lab Pei. Cells were seeded in a 48-well plate (3.5×10^4 cells/well), and transfected with plasmids expressing CedV genes (F, G, M, N, P, C), or the empty vector. 24 h after transfection, half of the wells were stimulated with IFNα (final concentration 800 U/ml); the negative control was MOCK-stimulated using PBS instead of active IFNα. Another 24 h later, cells were incubated on ice with 50 µl of the firefly luciferase lysis buffer for 10 min. Then, 20 µl of the cell lysate was transferred to a white microplate and 50 µl of the luciferin assay solution was added. Firefly luciferase luminescence was immediately measured using the same microplate reader as in chapter 4.5.1.

4.6. Immunofluorescence

CHO-EFN cells were seeded on glass coverslips in 12-well plates (1×10^5 cells/well) and after re-transfection of the A ephrins with 1 µg of plasmid, infected at MOI 2. 24 h p.i. cells were

fixed in 4% PFA for 20 min and washed in wash buffer (0.01% saponin in PBS) for 10 min. Subsequently, samples were incubated in 500 µl blocking buffer (3% BSA, 0.01% saponin in PBS) for 1 h at RT. The saponin in both the wash and blocking buffer was used to permeabilize the cells for intracellular staining. Primary antibody (mouse anti-DYKDDDDK-tag antibody (1:1,250)) incubation was done for 1 h, shaking at room temperature (RT), and afterwards samples were washed three times. Samples were stained with the Alexa Fluor 488-conjugated anti-mouse IgG antibody as a secondary antibody at a 1:400 dilution for 30 min and washed three more times. The coverslips were fixed to slides, and simultaneously stained with DAPI using the ProLong™Diamond Antifade Mountant with DAPI. Slides were kept at 4 °C overnight in the dark at high humidity, and on the next day, dried before the coverslips were permanently fixed to the slides using clear nail polish. Images were captured on a Nikon Eclipse Ti microscope, and brightness and contrast adjustments were done in ImageJ/Fiji (1.48v; Java 1.6.0_20[64-bit]).

VWF and pan-cytokeratin staining of PELENDO and PELEPI was done similarly, except that cells were cultivated on collagen-coated 12-well plates instead of glass coverslips, and primary antibodies were incubated overnight. As a secondary antibody to the VWF staining, the AlexaFluor488-conjugated α-rabbit-IgG antibody was used. The nuclei were stained with DAPI (1:1,000 in 0.1% saponin in PBS) at RT for 20 min before images were acquired using the “acquire only” mode (wide field) of the CellInsight CX7.

4.7. High-content microscopy of rCedV-nTurbo635 entry

CHO-EFN cells were seeded at 1 x 10^4 in 96-well plates, and A ephrins were re-transfected (0.3 µg) before rCedV-nTurbo635 infection at MOI 1, 2, and 5 on the next day. Each plate also contained two wells of BHK-21 infected at MOI 1 as a positive control and virus-inoculated CHO-pcDNA-FLAG as a negative control. 24 h p.i., plates were fixed in 4% PFA and nuclei were stained with DAPI (1:1,000 in 0.1% saponin in PBS) at RT for 20 min. After two wash steps in PBS, infection rates were quantified using high-content microscopy on the CellInsight™ CX7 platform. The valid cell count was achieved by selecting nuclei with the appropriate size, shape, and brightness in the DAPI channel, and infection was determined by the parameter “Average intensity of channel 2” (ex. 561 nm), when red fluorescence was directly adjacent to a nucleus. Thresholds for infection were set using the positive and negative controls. More information on the CX7 protocol and automated image analysis can be found in the supplements (**Supplementary Figure 10.3**).

4.8. Flow cytometry analysis of rCedV-nTurbo635 entry

To quantify the infection rates in CHO-EFN, and RaNep *EFN* knockdown cells, flow cytometry was employed, measuring the fluorescence intensity of the Turbo635 protein in the PE-CF-594 channel. CHO-EFN were incubated in 6-well plates (3 x 10^5 cells per well) overnight, and on the following day, re-transfected with 5 µg of their respective ephrin plasmids. 3 h post-transfection, the medium was changed to 2% FCS cell culture medium. CHO-EFN were infected at MOI 5, as determined by titration on BHK-21, whereas RaNep were infected at MOI 1. BHK-21 infected at MOI 0.1 served as a positive control for infection to optimize gate placement. Cells were carefully washed with PBS and detached using 0.5 ml of 0.5% trypsin per well 48 h p.i. Trypsinization was stopped by adding 1 ml of cell culture medium, and the cells were pelleted by centrifugation (350 xg, 5 min, 4°C). The FACS buffer used in subsequent steps for washing and resuspending the cells was produced by adding 0.1% BSA and 0.1% sodium azide to Ca2+/Mg2+-free PBS. Samples were washed once before staining them with the Zombie UV™ Fixable Viability Kit at a 1:500 dilution in 100 µl FACS buffer for 20 min at 4°C. Cells were washed again and fixed using the True-Nuclear™ Transcription Factor Buffer Set for 30 min at RT in the dark. Careful cell permeabilization for ephrin staining was achieved with the permeabilization buffer included in the kit. Consequently, the mouse anti-DYKDDDDK tag antibody was diluted 1:1,000 in permeabilization buffer, and cells were stained for 20 min at 4°C. After another wash step, samples were incubated with the BV-421-conjugated α-mouse IgG antibody (1:50 in permeabilization buffer) for 20 min at 4°C. Lastly, samples were washed two more times, resuspended in 500 µl (RaNep 800 µl) of FACS buffer, and filtered using a 150 µm nylon filter sheet. Samples were acquired on the BD FACSymphony A3™ and data were analyzed in FlowJo™ (v_10.9.0). More information on the gating strategy can be found in the supplements (**Supplementary Figure 10.4**).

4.9. shRNA knockdown of ERB ephrins

The shRNA oligos, used for lentivirus generation, were designed on the Broad Institute's Genetic Perturbation Platform (https://portals.broadinstitute.org/gpp/public/seq/search) and ordered from metabion GmbH. For each ephrin, three targeting sequences were chosen (**Table 4.4.**), and shRNA oligos were cloned into a pLKO.1-GFP vector, an altered version of the AddGene pLKO.1 plasmid containing a GFP-tag, as described before [237]. Correct plasmid sequences were validated by Sanger sequencing (Eurofins Genomics).

Table 4.4. Targeting sequences used for shRNA knockdown.

shRNA	Target	Targeting sequence
shRNA1	ERB ephrin B2	AGGAGACAAATTGGATATTAT
shRNA2	ERB ephrin B2	GCCGGACATTCTGGGAATAAT
shRNA3	ERB ephrin B2	TGTTGGCCAGTATGAATATTA
shRNA4	ERB ephrin B1	TGGTCATCTACCCAAAGATTG
shRNA5	ERB ephrin B1	AGCACCATGATTACTACATTA
shRNA6	ERB ephrin B1	TGTGCTGGTCACCTGCAATAA

For lentivirus generation, HEK-293T cells were cultivated in 12-well plates (2 x 10^5 cells/well), and transfected with 1.0 µg of the packaging plasmid (psPAX2), 1.0 µg of the envelope plasmid (pMD2.G), and 2.0 µg of the shRNA constructs, or a scrambled RNA control. To improve lentivirus yield in the supernatant, the medium was changed 6 h post-transfection to 20% FCS in DMEM. At 48 h post-transfection supernatants were collected, centrifuged at 350 xg for 10 min, and immediately used to transduce RaNep cells. RaNep were seeded in 12-well plates at low confluency (8.0 x 10^4 cells per well) the day before. 1 ml of lentivirus-containing supernatant was mixed with 1 ml cell culture medium supplemented with 2 µg/ml polybrene and 5 µg/ml cyclosporin A to inhibit innate immunity and thereby enhance transduction efficiency. Starting 72 h later, RaNep, which had successfully incorporated the shRNAs, were selected using Puromycin at 1 µg/ml. When the non-transduced control well had completely died off due to Puromycin treatment, positive colonies were expanded into cell culture flasks, and knockdown efficiency was evaluated by qPCR.

4.10. Cell death assays

4.10.1. Lactate dehydrogenase assay (LDH)

A549, RaNep, and SK-6 were seeded in 96-well plates with for each cell line individually titrated cell amounts per well (A549: 1.7 x 10^4, RaNep: 5 x 10^4 (8 h), 3.5 x 10^4 (24 h, 48 h), SK-6: 1.7 x 10^4(8 h), 1.4 x 10^4 (24 h, 48 h)), incubated overnight, and either infected with rCedV-

nTurbo635 in infection medium at MOI 1, or MOCK-treated with PBS. The medium was changed back to cell culture medium containing 5% FCS (to reduce background) 90 min p.i. For each cell line, measurements were performed in triplicate at 8 h, 24 h, and 48 h p.i. in at least 3 independent experiments. Plates also contained “high control” (cell lysis), “low control” (untreated), and medium controls to calculate cytotoxicity according to the manufacturer’s instructions (BioLegend® LDH-Cytox™ Assay Kit). AZD4604 toxicity was measured in a similar manner; however, with 2 x 10^4 cells/well irrespective of the cell line and at 6 h post-treatment (0.17 µM).

4.10.2. Detection of CellEvent™ Caspase-3/7 activation

rCedV-nTurbo635-induced cell death was further investigated using a dye-based cell death assay kit (CellEvent™, Thermo Fisher). A549, RaNep, and SK-6 were seeded in 96-well plates (8 x 10^3 cells per well), and on the following day, infected with rCedV-nTurbo635 at MOI 0.1 or MOCK-infected with PBS. At 24 h, respectively 48 h, p.i., the detection reagent, diluted 1:500 in cell culture medium, was added to the cells. After 45 min incubation, the wells were washed with PBS, and A549 and RaNep were additionally stained with the Zombie NIR™ viability dye (1:500 in PBS) for 20 min. Subsequently, the cells were re-washed with PBS, fixed in 4% PFA, washed, and stained with DAPI (1:1,000) in 0.01% saponin in PBS, before acquiring the plates in the CellInsight CX7 high-content microscope. Early apoptosis was defined as caspase-3/7-positive, whereas late-stage apoptotic cells were defined as double-positive for caspase-3/7 and Zombie NIR. Sole Zombie NIR staining indicated necrosis. The Turbo635 signal of rCedV-nTurbo635 was measured at 561 nm, the green caspase-3/7 dye emitted in the FITC channel (excitation: 485 nm), and Zombie NIR was measured at 650 nm. Thresholds for truly positive signals were determined by including single fluorescent controls as well as fluorescence-minus-one controls (FMO), if possible.

4.11. BSL-4 experiments

4.11.1. *In vitro*: CedV WT and NiV infection of A549 and RaNep

12-well plates of A549 and RaNep (2 x 10^5 cells/well) were prepared in the BSL-2 lab and transferred to the high containment area (BSL-4), where the CedV WT (GenBank accession no. JQ001776) and NiV Malaysia WT (GenBank accession no. AF212302) infections were performed by Dr. Sandra Diederich (INNT, FLI). The cells were infected at MOI 0.1 in triplicate and cells, as well as supernatant, were harvested at 6 h, 12 h, 24 h, and 48 h p.i. Additionally, pictures were taken using a Nikon Eclipse TS100 microscope (Software: Axiovision). Cells were resuspended in Trizol and transferred to the BSL-3 (later BSL-2) facility in accordance

with biosafety regulations. 140 µl of the cell culture supernatants were resuspended in 560 µl AVL buffer offset with carrier RNA and MS2, incubated for 10 min, and then transferred to a fresh tube containing 100% ethanol. After vortexing, samples were incubated again for 10 min at RT before transfer to the BSL-3 (later BSL-2) facility in accordance with biosafety regulations.

4.11.2. *In vivo*: CedV WT infection of ERB

For the *in vivo* qPCR data, organ samples were received resuspended in Trizol from the animal trial published by Mohl *et al.* [44]. The competent authority of the Federal State of Mecklenburg-Western Pomerania, Germany, approved the execution of this animal trial (file number: 7221.3-1.1-054/20) on the grounds of the EU council directive 2010/63/EU and national laws. All animal trials at the FLI are authorized by the Animal Care and Use Committee and audited by the Animal Welfare Officer. This study was conducted under BSL-4 conditions at the FLI in accordance with legal requirements.

4.12. Mass Spectrometry/Proteomics

4.12.1. Sample preparation

Samples for mass spectrometry were generated as six biological replicates by seeding A549, RaNep, and SK-6 in 6-well plates at 4.5 x 10^5 cells per well in cell culture medium containing 2% FCS overnight. On the next day, cells were infected with rCedV-nTurbo635 at MOI 0.2. At 24 h p.i., the plates were placed on ice, and the cells were washed three times with 2 ml of ice-cold PBS. After removing the PBS, cells were lysed in 500 µl of 1% SDC buffer (sodium deoxycholate in 100 mM Tris-HCl, pH 8.5), and the lysates were boiled at 95°C for 10 min. The resulting protein samples were then sonicated for 2 min at 80% power to improve cell lysis and protein yield, while reducing possible contaminations. Lastly, samples were centrifuged at 14,000 rpm for 10 min at 4°C. Supernatants were stored at -80°C until further use. Dr. Axel Karger and his lab performed the subsequent steps. Protein samples were digested with trypsin, and peptides were measured by mass spectrometry (Ultraflex TOF/TOF Massenspektrometer, Bruker) to reconstruct the proteome.

4.12.2. Mass spectrometry: data analysis

The software DIA-NN 1.8.1 was used to assess and quantify unmodified spectra, which were then imported into Perseus (version 2.0.11) for further analysis. The three final annotated matrices for A549, RaNep, and SK-6, including t-tests, were imported into RStudio and analyzed using the following packages: clusterProfiler [249], enrichplot [250], ggstar [251], ggnewscale

[252], DOSE [253], and org.hs.eg.db [254]. Differentially expressed proteins with statistical significance, as determined by t-test results, served as the basis for Gene Ontology enrichment analysis (package: clusterProfiler) and resulting illustrations.

The heat maps generated from proteomics data, were created by me using RStudio 4.4.2. with the packages “tidyverse” [255], “dplyr” [256], and “RColorBrewer” [257].

4.13. Software and Programs

4.13.1. Statistical analyses and graph design

Statistical analyses were performed in GraphPad Prism 10 (Version 10.1.2(324)). Non-parametrically distributed data were analyzed using a Kruskal-Wallis test without Dunn’s correction. Differences were considered statistically significant, if $p < 0.05$ (*), $p < 0.01$(**), $p < 0.001$(***), and $p < 0.0001$ (****).

4.13.2. Other programs

4.13.2.1. Ephrin protein alignments

Protein sequences were downloaded from NCBI Gene bank, aligned in Geneious Prime, and consensus was visualized using ESPript 3.0 [238].

4.13.2.2. Manuscript writing

While drafting the manuscript, DeepL, GrammarlyPro and Thesaurus.com were used as aids.

5. Results

5.1. rCedV-nTurbo635 enters ERB cells using ephrins B1 and B2

CedV enters human host cells via ephrins B1, B2, and, with lower affinity, A2 and A5 [9–11]. The first aim of the project was to elucidate the receptors used by CedV to enter fruit bat cells, exemplified by *Rousettus aegyptiacus* (ERB). *In silico* protein alignments between human, *Pteropus alecto* (black flying fox), and ERB revealed little difference in sequences or sizes (**Supplementary Figure 10.1**). However, even single mutations or different glycosylation profiles could alter binding affinities and receptor usage [9,11,81]. Whether the same ERB ephrins mediate the entry of CedV needs to be validated experimentally.

5.1.1. rCedV-nTurbo635 entry into CHO-K1 is mediated by ERB ephrins B1, B2 and A5

Chinese hamster ovary cells (CHO-K1) express negligibly low levels of endogenous ephrins and are therefore a suitable model to investigate the role of single exogenous ephrins as entry receptors [82,258]. To generate CHO-K1 cells stably expressing ERB ephrins (CHO-EFN), those ephrins were subcloned into a pcDNA-FLAG vector by restriction enzyme cloning. The resulting constructs were first sequenced and then transfected into HEK-293T cells to evaluate protein expression in Western blot. Due to insufficient expression levels in HEK-293T cells, ephrins A3 and A5 were further cloned into a p3xFLAG-ATF6 vector and these constructs were used in subsequent experiments in CHO-K1 (**Figure 5.1)**. Ephrin A4 is, with 201 amino acids, the smallest of the A ephrins, and ephrin A3 is the largest (230 aa). The B ephrins comprise an extracellular receptor binding domain, a transmembrane domain, and a cytoplasmic tail [69]. They are therefore substantially larger (333 aa – 346 aa) than the A ephrins, which are bound to the cell surface by a GPI anchor [69] (**Figure 5.1**, **Supplementary Figure 10.1)**.

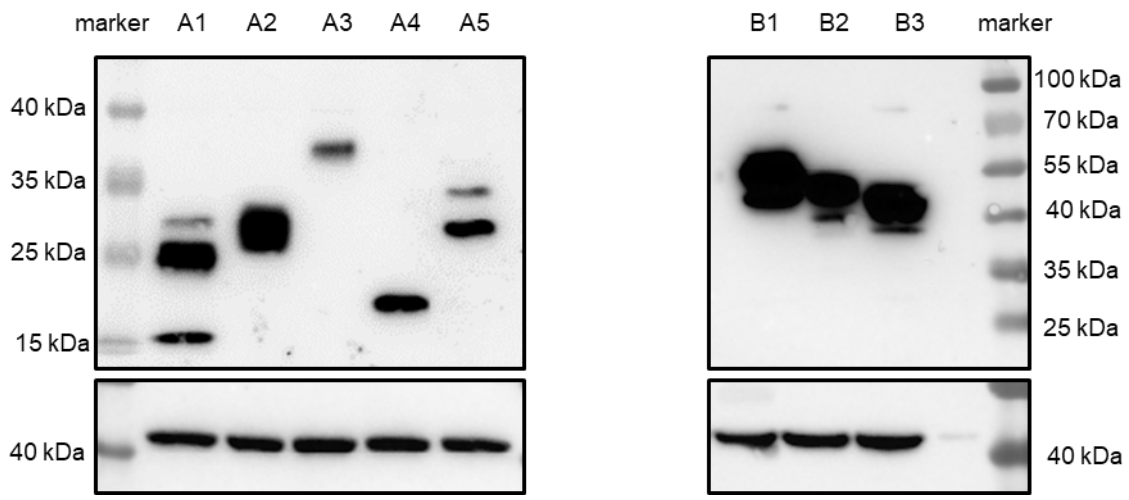

Figure 5.1. Cloning of ERB ephrins and expression in HEK-293T.

Western blot analysis of HEK-293T expressing ERB ephrins. HEK-293T cells were seeded in a 12-well plate and transfected with plasmids encoding for the ERB ephrins. A1, A2, A4, and B ephrins were expressed in a pcDNA-FLAG vector, A3 and A5 were expressed in p3xFLAG-ATF6. FLAG-tag was visualized using the proteintech mouse anti-DYKDDDDK-tag antibody and an HRP-conjugated α-mouse-IgG secondary antibody. Loading control: β-Actin.

Since the original wildtype (WT) isolate of CedV (CedV WT) was first isolated in a BSL-4 laboratory, its use is now restricted to high-biosecurity facilities. Therefore, in almost all subsequent experiments, we decided to use a recombinant CedV, which expresses a Turbo635 fluorescent reporter protein that localizes to the nucleus of infected cells (rCedV-nTurbo635) [237,247]. Thus, infected cells can be easily distinguished by examining red fluorescence in the nucleus. This reporter virus contains the Turbo635 reporter gene between the P and the M gene within the CedV cDNA, as well as the nuclear localization signal of SV40 [237,247]. Expression of the ERB ephrins on CHO-EFN was evaluated by staining the FLAG-tagged ephrins using the Proteintech mouse anti-DYKDDDDK-tag antibody and subsequently an Alexa488-conjugated secondary antibody. Immunofluorescence assays revealed markedly higher expression levels of ephrin B1 and B2 in comparison to other ephrins (**Figure 5.2**, **Supplementary Figure 10.2**). Only CHO cells, expressing ERB ephrins B1 and B2, show fluorescence in the Cy3 channel (red), indicating rCedV-nTurbo635 entry.

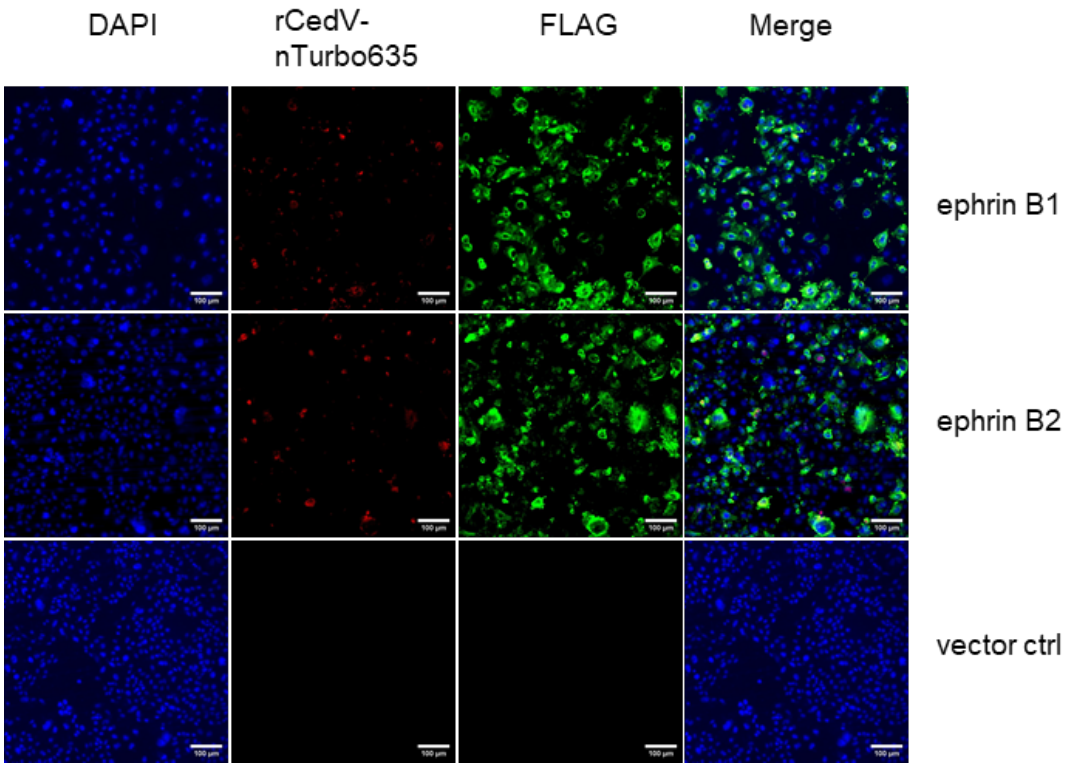

Figure 5.2. rCedV-nTurbo635 enters CHO-K1 via ERB ephrins B1 and B2.

Immunofluorescence images of CHO-K1 stably expressing ERB ephrins B1/B2, or the empty vector infected with rCedV-nTurbo635 at MOI 2. Cells were fixed 24 h p.i. and visualized using a Nikon Eclipse Ti microscope. FLAG-tagged ephrins were stained with an Alexa488 fluorophore and Turbo635 was visualized in the Cy3 channel. Images are representative of 3 independent experiments. Scale bar: 100 µm. Figure was modified from Lenhard *et al.* [237].

To compensate for unequal expression levels of the ephrins, larger cell quantities were analyzed in high-content microscopy using the CellInsight™ CX7 platform. CHO-EFN were seeded in 96-well plates, A ephrins were re-transfected to increase their expression, and cells were infected with rCedV-nTurbo635 at MOI 1, 2, and 5. Matching the IFA data, significant rCedV-nTurbo635 entry could only be detected in CHO-B1 and -B2 (**Figure 5.3**, **Supplementary Figure 10.3**). Infection rates were dose-dependent and reached a maximum in ephrin B2-expressing cells. Even at the highest MOI (MOI 5), A ephrins were not capable of mediating significant rCedV-nTurbo635 entry (**Supplementary Figure 10.3 B**).

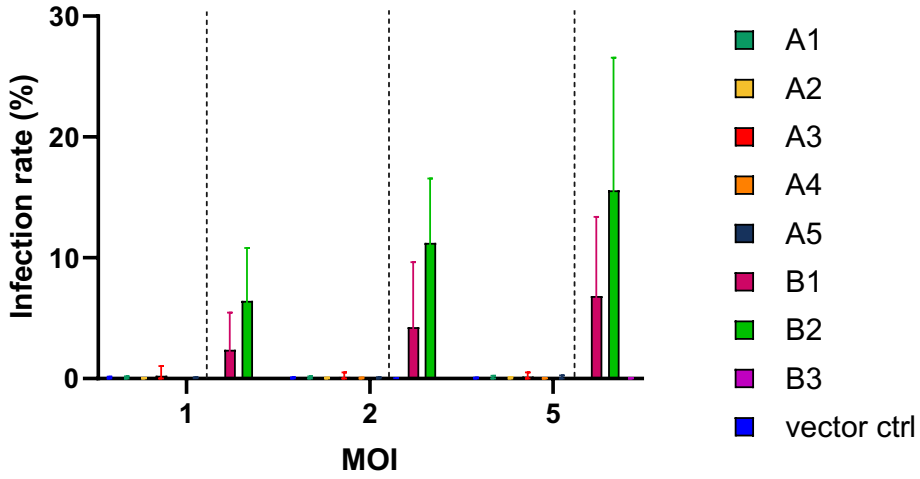

Figure 5.3. High content imaging reveals that ERB ephrins B1 and B2 mediate rCedV-nTurbo635 entry. Percentage of rCedV-nTurbo635 infected CHO-EFN cells broken down by MOI. CHO-EFN were grown in 96-well plates, A ephrins were re-transfected, and cells were infected with rCedV-nTurbo635 at MOI 1, 2, and 5. Infection rate was analyzed using the CellInsight CX7 high-content analysis platform. Three independent experiments were performed in duplicate. Graph shows median and range. Figure was modified from Lenhard *et al.* [237].

Infection rates of CHO-EFN were additionally analyzed in flow cytometry, since gating on merely the ephrin-positive population enables more accurate quantification. This experiment was conducted at 48 h p.i., as CedV entry via human ephrins A2 and A5 has only been demonstrated for the later infection time point [9]. In addition to the previously reported ephrin B1 and B2 usage, rCedV-nTurbo635 entered A5 expressing cells at low, but significant levels (**Figure 5.4 A**). In line with the immunofluorescence data, ephrin expression levels differed markedly, with the highest percentages of ephrin B1-positive cells (**Figure 5.4 B**). However, in all quantitative assays, rCedV-nTurbo635 favored ephrin B2 usage over ephrin B1 (**Figure 5.3, Figure 5.4**).

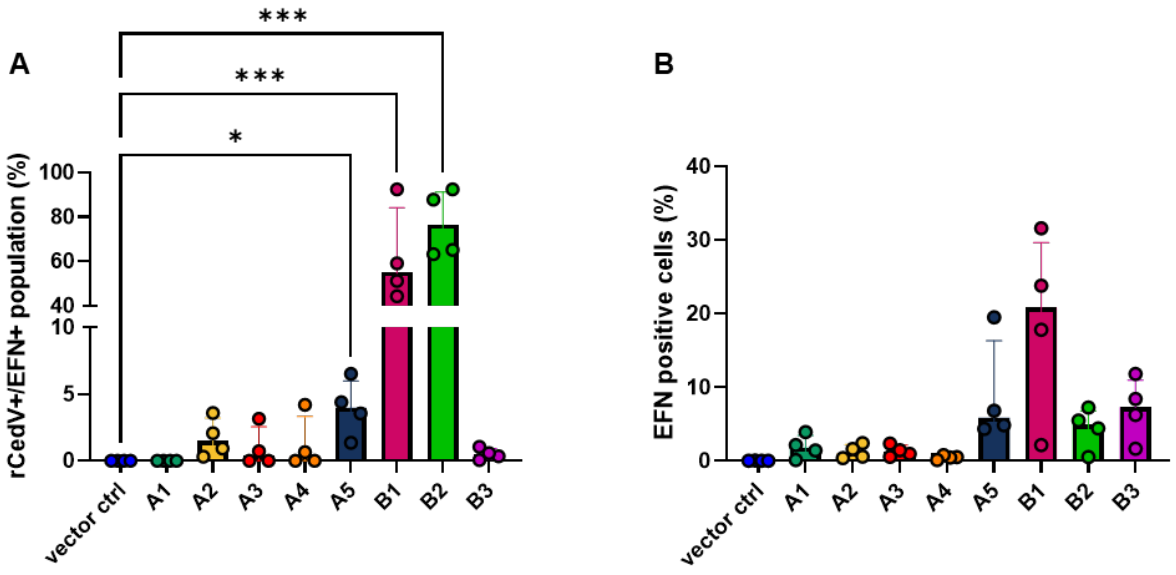

Figure 5.4. Flow cytometry demonstrates rCedV-nTurbo635 entry is mediated by ERB ephrins B1 and B2. Flow cytometry analysis of rCedV-nTurbo635 infection rate in CHO-EFN (**A**) and ephrin expression levels in percent of all measured cells (**B**). CHO-EFN were re-transfected to increase expression rate of the ephrins and infected at MOI 5. Infection rate was quantified 48 h p.i. Graphs show median ± *IQR* calculated from 4 independent experiments, each capturing at least 30,000 events. Statistical test: Kruskal-Wallis without Dunn's correction. $p < 0.05$ (*), $p < 0.01$(**), $p < 0.001$(***). Figure was modified from Lenhard *et al.* [237].

5.1.2. Ephrin B2 knockdown significantly impairs rCedV-nTurbo635 entry into ERB cells

To further substantiate those findings, immortalized ERB nose epithelial cells (RaNep) were used to generate endogenous ephrin B1/B2 knockdown cells. Since both ephrin B1 and B2 were expressed at sufficient levels on RaNep (**Figure 5.5**), those cells were chosen to continue with the lentivirus-based shRNA knockdown.

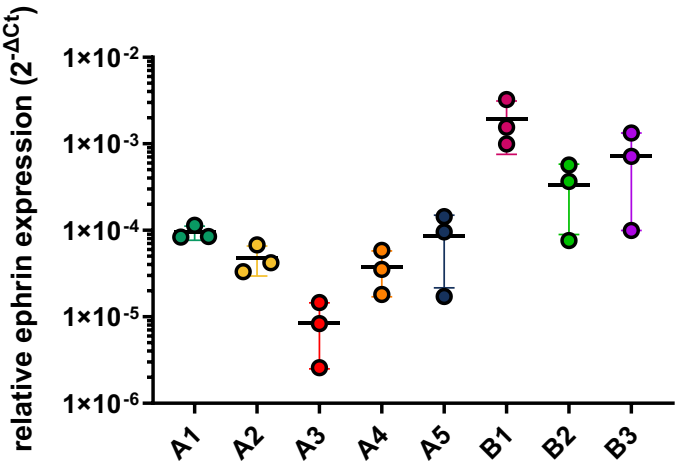

Figure 5.5. RaNep express ephrins relevant for CedV entry.

RT-qPCR data of RaNep ephrin expression relative to housekeeping gene *EEF1A1*. Graph shows mean ± *SD* of 3 independent experiments in technical duplicate. Figure was modified from Lenhard *et al.* [237].

Ephrin B2 single knockdown (KD) and ephrin B1/B2 double KD RaNep were generated and KD efficiency was evaluated by RT-qPCR. *CO1* barcoding was performed to identify potential carry over contamination from lentivirus containing HEK-293T supernatant (**Supplementary Figure 10.5**). Generating a single ephrin B1 KD clone was not successful, as sufficient knockdown efficiency was defined as a residual activity of less than 30%, compared to the scrambled shRNA control and none of the generated clones complied with this standard. In ephrin B2 KD clone 1 (*EFNB2* KD#1) the ephrin B2 expression was reduced by 65% and in clone 2 (*EFNB2* KD#2) by 80% (**Figure 5.6 A**). The *EFNB1/B2* double KD showed a residual activity of only 6% and additionally a reduction in ephrin B1 expression of 63%, whereas the ephrin B1 expression in the single ephrin B2 KD clones remained unaltered (**Figure 5.6 B**).

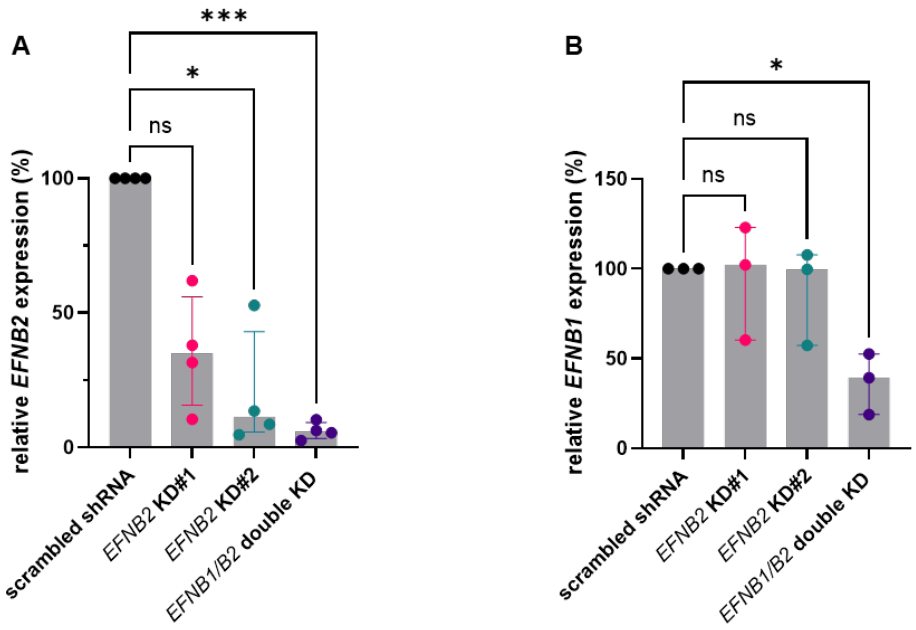

Figure 5.6. ERB ephrin B2 knockdown in RaNep.

qPCR data of ephrin B2 (A) and ephrin B1 (B) expression in ephrin knockdown cells relative to the scrambled shRNA control. *EFNB2* KD#1 and *EFNB2* KD#2 were transduced with a shRNA targeting endogenous ERB ephrin B2, whereas *EFNB1/B2* double KD cells were generated using two different shRNAs, one targeting *EFNB1* and the other *EFNB2*. Graphs show median ± *IQR* of at least 3 independent experiments in technical duplicate. Statistical test: Kruskal-Wallis without Dunn's correction; $p < 0.05$ (*), $p < 0.01$(**), $p < 0.001$(***). Figure was modified from Lenhard *et al.* [237].

To assess the effect of reduced receptor expression on virus entry, RaNep ephrin KD clones were infected with rCedV-nTurbo635 at MOI 1, and the infection rate was quantified in flow cytometry 48 h p.i. in relation to the scrambled shRNA control. The single ephrin B2 KD of *EFNB2* KD#2 significantly reduced the infection rate by half (**Figure 5.7**). The additional ephrin B1 KD did not have a major effect on virus entry, underlining the importance of ERB ephrin B2 as a CedV receptor.

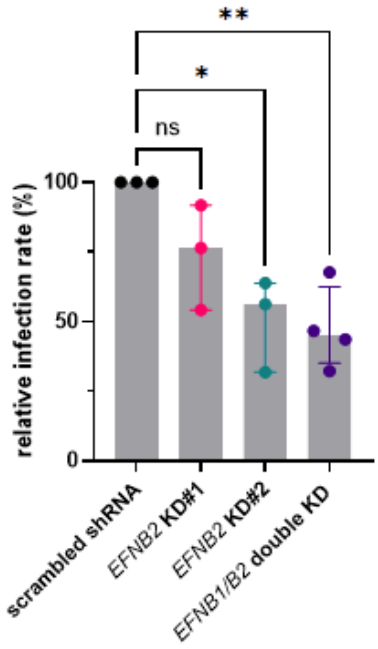

Figure 5.7. Ephrin B2 knockdown significantly decreases rCedV-nTurbo635 infection rate in RaNep. Flow cytometry results of RaNep ephrin knockdown cells infected with rCedV-nTurbo635 at MOI 1 48 h p.i. Depicted is the infection rate in percent, normalized to the scrambled shRNA control. Graph shows median ± *IQR* of 3 independent experiments. Statistical test: Kruskal-Wallis without Dunn's correction; $p < 0.05$ (*), $p < 0.01$(**), $p < 0.001$(***). Figure was modified from Lenhard *et al.* [237].

In all conducted experiments, rCedV-nTurbo635 entry was mediated by ERB ephrins B1 and B2, while entry through ERB ephrin A5 was only a minor contributor.

5.2. CedV nucleocapsid protein impairs *IFNB* induction in HEK-293T

To elucidate whether the CedV P protein has retained any IFN inhibiting qualities or if other viral proteins perform similar tasks, as reported for NiV M and N [17,18], first, CedV N, P, and C were cloned into a pEGFP-C1 vector (**Supplementary Figure 10.6**) and a set of luciferase assays was conducted. This experimental set-up was limited by the lack of a positive control for IFN inhibition, such as the afore mentioned NiV proteins. Human embryonic kidney cells (HEK-293T) were transfected with a Lucia luciferase, expressed under the murine *IFNB* promoter, one key component in the *IFN* induction pathway (RIG-I-CA, TBK1, IKKε, IRF3-5D) and one of the CedV genes (F, G, M, N, P or C), or the empty pEGFP-C1 vector as a control. The measured luciferase activity in the supernatant reflects the extent of *IFN* induction. In this

set-up, both RIG-I-CA and IRF3-5D were constitutively active mutants of their wildtype counterparts that induce a drastic activation of the IFN pathway. RIG-I-CA only contained the caspase activation and recruitment domains (CARDs) of RIG-I, which are essential for downstream signaling [259]. To generate IRF3-5D, five Ser-Thr motifs were mutated to Asp, which resulted in altered phosphorylation and constitutive activation [260]. Establishing a luciferase assay in RaNep was not successful, as in contrast to comparable experiments in HEK-293T, the luminance induction in the RIG-I-CA expressing positive control did not differ significantly from the negative control (**Supplementary Figure 10.7**). In HEK-293T, however, in addition to a slight reduction in luminance after transfection of CedV matrix protein (M), a significant reduction could only be observed in cells expressing the nucleocapsid protein (N) (**Figure 5.8**). Moreover, the luciferase induction was even marginally higher than the positive control (empty pEGFP-C1 vector) when cells co-expressed CedV fusion protein (F). Here, the different vector backbone, F being expressed in a pCAGGS instead of pEGFP-C1, could have played a role.

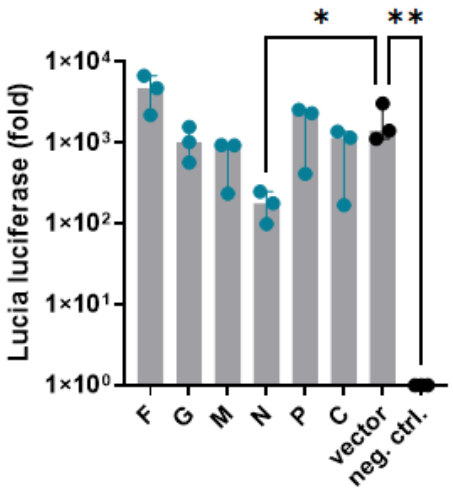

Figure 5.8 CedV N protein inhibits *IFNB* induction in RIG-I-CA expressing HEK-293T.
HEK-293T cells were transfected with constitutively active RIG-I (RIG-I-CA), a plasmid expressing Lucia luciferase under the murine *IFNB* promoter, and the different CedV genes, or the empty vector. The negative control consisted of just the luciferase plasmid and the empty vector, adjusted to the same total amount of transfected DNA. The data show median ± *IQR* of 3 independent experiments in duplicate normalized to the negative control. Statistical test: Kruskal-Wallis without Dunn's correction. $p < 0.05$ (*), $p < 0.01$(**).

The same assay with transient expression of human MDA5 instead of RIG-I-CA did not induce sufficient luciferase expression in the positive control to be able to deliver meaningful results (**Supplementary Figure 10.8**). The correct sequence and open reading frame of the MDA5

construct was determined by Dr. Christine Luttermann via forward and reverse sequencing, its functional activity was, however, not assessed further.

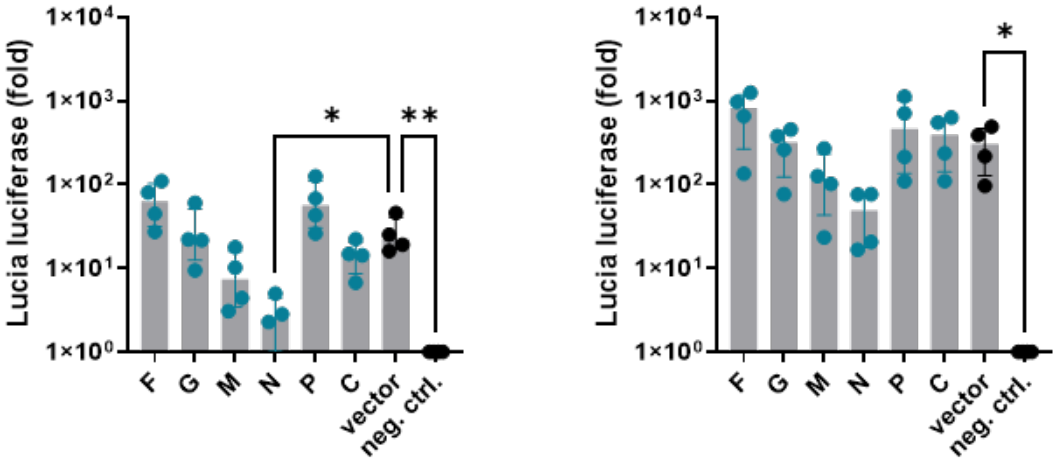

Figure 5.9. CedV N protein inhibits *IFNB* induction in TBK1 (left) and IKKε (right) expressing HEK-293T. HEK-293T cells were transfected with TBK1/IKKε, a plasmid expressing Lucia luciferase under the murine *IFNB* promoter, and the different CedV genes, or the empty vector. The negative control consisted of just the luciferase plasmid and the empty vector, adjusted to the same total amount of transfected DNA. The data show median ± *IQR* of 4 independent experiments in duplicate normalized to the negative control. Statistical test: Kruskal-Wallis without Dunn's correction. $p < 0.05$ (*), $p < 0.01$(**).

Co-transfection of the kinases TBK1 or IKKε had similar effects to RIG-I-CA expression. A substantial reduction in luciferase activity occurred only in cells expressing CedV N protein (**Figure 5.9**). When HEK-293T cells expressed constitutively phosphorylated IRF3 (IRF3-5D), luciferase induction in N-expressing cells was still reduced by two-thirds (**Figure 5.10**).

Since inhibition of luminance induction could be observed for N protein throughout the *IFNB* induction pathway, including IRF3-5D expression, the interference either occurred at a late-stage, i.e., IRF3 translocation, or the expression of N protein altered transcription, respectively translation in general. CedV N binds to viral and cellular RNA and can thereby influence its accessibility, both in the cytoplasm and the nucleus [18,51,261].

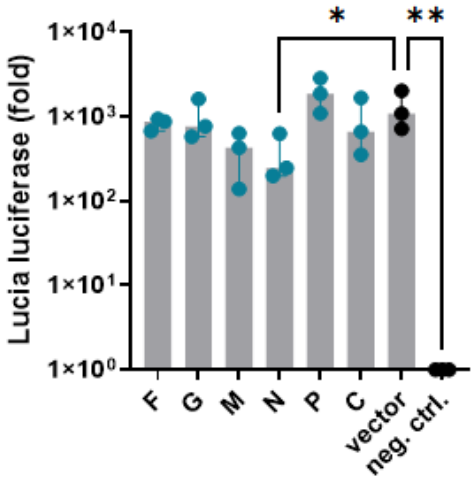

Figure 5.10. CedV N protein inhibits *IFNB* induction in IRF3-5D expressing HEK-293T.

HEK-293T cells were transfected with IRF3-5D, which is constitutively phosphorylated, a plasmid expressing Lucia luciferase under the murine *IFNB* promoter, and the different CedV genes, or the empty vector. The negative control consisted of just the luciferase plasmid and the empty vector, adjusted to the same total amount of transfected DNA. The data show median ± *IQR* of 3 independent experiments in duplicate normalized to the negative control. Statistical test: Kruskal-Wallis without Dunn's correction. $p < 0.05$ (*), $p < 0.01$(**).

To exclude a non-specific influence on transcription or translation, a reporter assay using a Renilla luciferase, expressed under a constitutive HSV-thymidine kinase promoter, was performed. HEK-293T cells were transfected with the Renilla luciferase plasmid and the plasmids encoding for one of the six different CedV proteins, or the empty pEGFP vector. The Renilla luciferase expression was measured after 24 h. If the N protein were able to alter nuclear import, transcription or translation, the Renilla luciferase expression would differ substantially from the expression in the control samples. Since no significant difference between N protein-expressing cells and the control was observed (**Figure 5.11**), a non-specific influence on transcription or translation was excluded as an explanation for previous results. Instead, the potential interaction of N protein with IRF3 was investigated more closely.

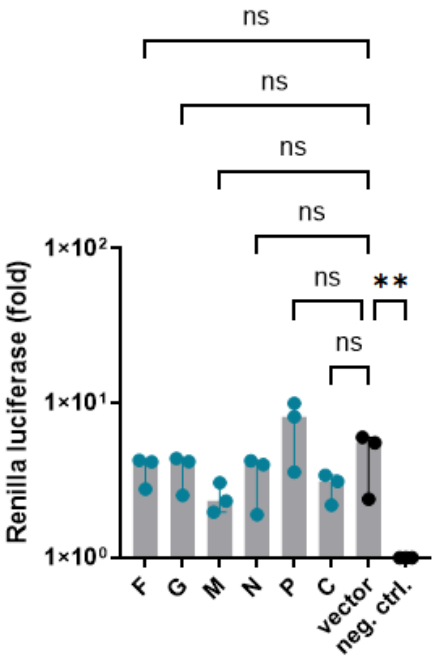

Figure 5.11. Expression of CedV proteins does not cause translational shut-down.
HEK-293T cells were transfected with a plasmid expressing Renilla luciferase and plasmids encoding for the different CedV proteins, or the empty vector. For the negative control, only the empty vector was transfected adjusted to an equal total amount of DNA. The data show median ± *IQR* of 3 independent experiments in duplicate normalized to the negative control. Statistical test: Kruskal-Wallis without Dunn's correction. $p < 0.05$ (*), $p < 0.01$(**).

HEK-293T cells were transfected with 1 µg of plasmids encoding for the different viral proteins, or the empty vector, and either 1 µg RIG-I-CA or IRF3-5D. After 24 h, subcellular fractionation was performed to analyze cytosolic and nuclear fractions separately in SDS-PAGE and Western blot. Preliminary results comparing RIG-I-CA/IRF3-5D transfected and non-transfected cells confirmed an effect of the RIG-I-CA/IRF3-5D expression on IRF3 translocation. Histone H4 detection served as a positive control for clean separation of the nuclear fraction, whereas GAPDH was employed as a control for the cytosolic fraction, since it is mainly present in the cytosol. Additionally, for each experiment, viral protein expression was confirmed for all proteins except CedV F, which is not GFP-tagged, and G protein, for which expression levels were low. In HEK-293T cells expressing CedV N, there was neither a significant difference in the total amount of IRF3 translocation to the nucleus, nor in the amount of phosphorylated IRF3 (**Figure 5.12**). CedV F showed a slight positive, however not statistically significant, trend on IRF3 translocation to the nucleus, when co-expressed with RIG-I-CA. Since an empty pCAGGS control was not included, an influence of the different vector backbone could not be excluded.

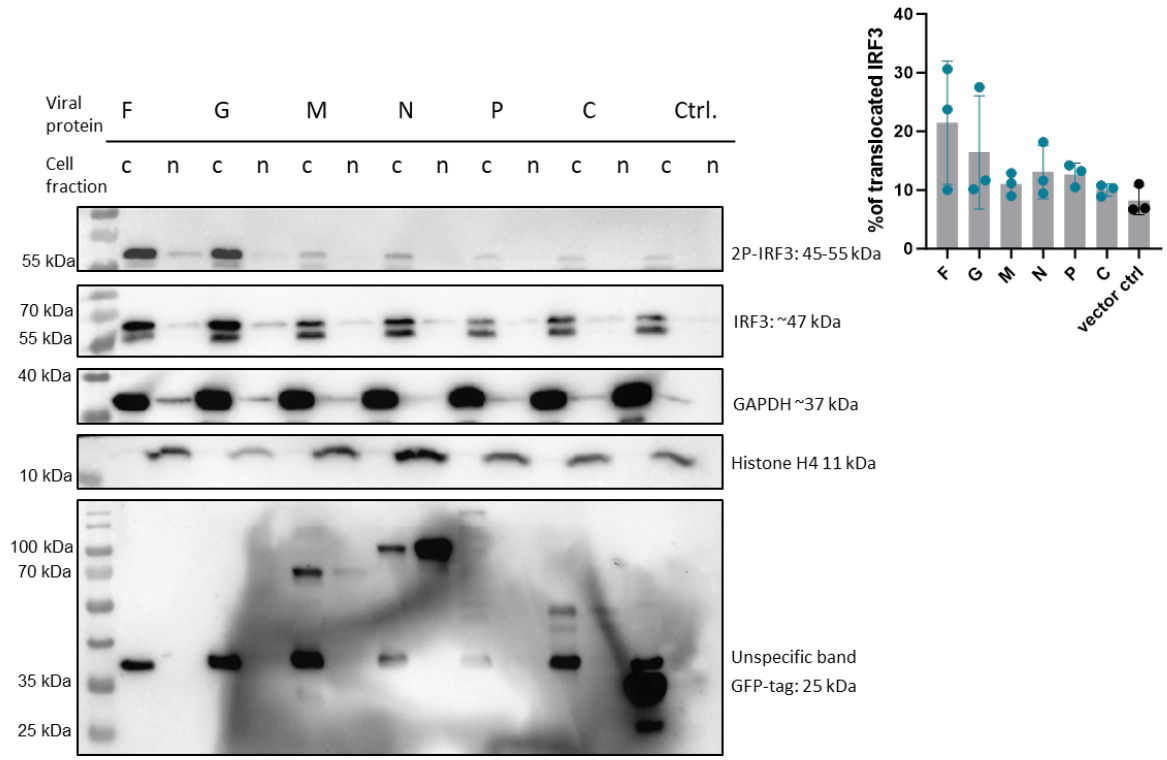

Figure 5.12. Nuclear IRF3 remains unaltered by CedV proteins in HEK-293T expressing RIG-I-CA.
Western blot analysis of HEK-293T transfected with RIG-I-CA and plasmids encoding for the different CedV proteins. Subcellular fractionation was performed to analyze cytosolic (c) and nuclear (n) fraction separately. Successful separation was determined by GAPDH detection in the cytosolic fraction and Histone H4 detection in the nuclear fraction. The expression of GFP-tagged CedV proteins (G, M, N, P, C) was evaluated with an anti-GFP antibody. Total IRF3, and Ser396-phosphorylated IRF3 amounts were determined using the respective antibodies. Densitometry analysis was performed in Image Lab and nuclear translocation was quantified as percentage of total measured IRF3 (c + n). Images are representative of 3 independent experiments.

HEK-293T cells that expressed IRF3-5D exhibited a similar pattern, with no significant differences observed in the nuclear translocation of IRF3 (**Figure 5.13**).

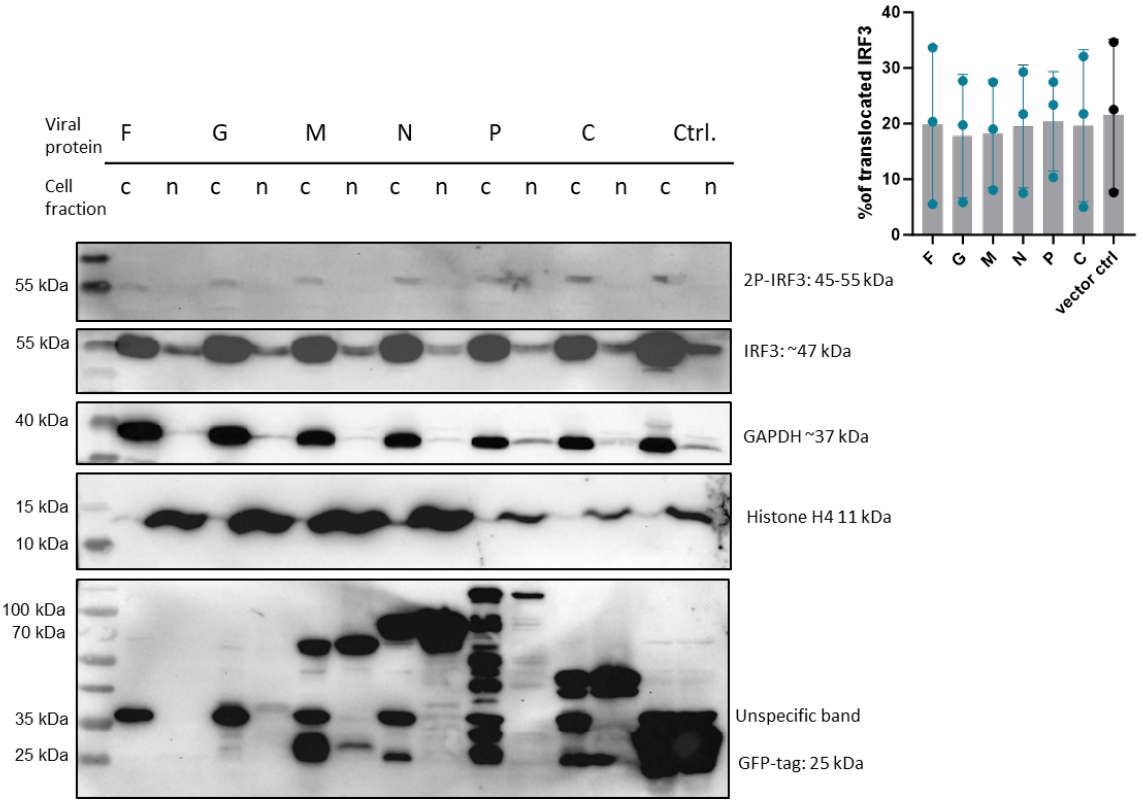

Figure 5.13. Nuclear IRF3 remains unaltered by CedV proteins in HEK-293T expressing IRF3-5D.
Western blot analysis of HEK-293T transfected with IRF3-5D and plasmids encoding for the different CedV proteins. Subcellular fractionation was performed to analyze cytosolic (c) and nuclear (n) fraction separately. Successful separation was determined by GAPDH detection in the cytosolic fraction and Histone H4 detection in the nuclear fraction. The expression of GFP-tagged CedV proteins (G, M, N, P, C) was evaluated with an anti-GFP antibody, total IRF3 and at Ser396 phosphorylated IRF3 amounts were determined using the respective antibodies. Densitometry analysis was performed in Image Lab and nuclear translocation was quantified as percentage of total measured IRF3 (c + n). Images are representative of 3 independent experiments.

Contrary to the initial hypothesis, CedV N protein did not significantly alter IRF3 translocation or phosphorylation in this experimental set-up. It must be noted, however, that no construct, which verifiably alters IRF3 translocation, was included as a positive control to determine the sensitivity of the assay. Furthermore, carry-over between the cytosolic and nuclear fraction cannot be excluded completely, as light Histone H4 bands appear in some of the cytosolic lanes. On the other hand, GAPDH in the nuclear fraction is not necessarily a sign of cross-contamination, as GAPDH can translocate to the nucleus in response to oxidative stressors [262,263]. Since other henipavirus proteins have been reported to inhibit IFNβ signaling through STAT sequestration [13,177,264], the influence of CedV proteins on IFNβ signaling and the IFNβ positive feedback loop was also investigated. HEK-293T cells were transfected with the plasmid encoding for a Lucia luciferase, the different viral genes, or the empty vector control, and 24 h later, stimulated with IFNα or MOCK-stimulated with PBS. The pNiFty3-IAN-Lucia

plasmid also contains, in addition to the sequence coding for the Lucia luciferase and the murine *IFNB* promoter, transcription factor binding sites (e.g. ISRE), which can be activated by STAT dimers [122]. Luciferase induction was measured 24 h after IFNα treatment. If CedV N were capable of inhibiting STAT-dependent type I IFN signaling, significantly lower luminance would be induced when cells express N protein compared to the empty vector control. Unexpectedly, CedV F and M repressed luciferase induction to a small, non-significant, extent, whereas CedV P induced positive feedback exceeding the positive control (**Figure 5.14**). G, N, and C expression did not influence luciferase induction in comparison to the vector control.

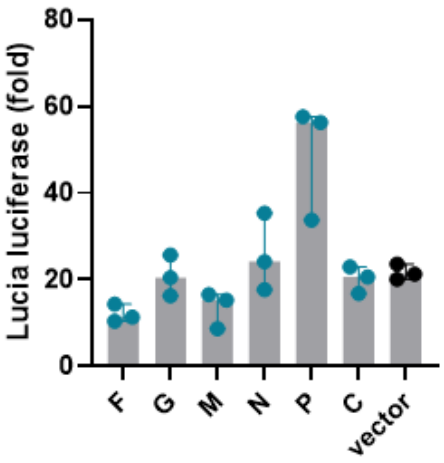

Figure 5.14. Negligible influence of CedV proteins on type I IFN signaling.
Luciferase assay of HEK-293T cells transfected with a plasmid expressing a Lucia luciferase under the murine *IFNB* promoter and transcription factor binding sites (ISRE, AP-1 binding site, NF-κB binding site), the different CedV genes and 24 h post-transfection stimulated with 800 U/ml IFNα. Fold change was calculated between non-stimulated groups and IFN-stimulated samples. The data show median ± *IQR* of 3 independent experiments in duplicate. Statistical test: Kruskal-Wallis without Dunn's correction. $p < 0.05$ (*), $p < 0.01$(**).

IFNB is induced via multiple pathways (TLRs, RIG-I/MDA5, cGas/STING) that all result in translocation of transcription factors (AP-1, NF-κB, IRFs) into the nucleus [265]. Initiation of *IFNB* transcription is regulated by two negative and four positive regulatory domains, which can result in very nuanced activation of transcription [265]. To get a clearer picture of the effect of CedV protein expression and stimulation with IFNα on type I IFN signaling, HEK-293T cells, which stably expressed a firefly luciferase downstream of the *MX1* promoter (HEK-MX1-FLuci), were employed. *MX1* is an interferon-stimulated gene [266], so transcription depends solely on IFN levels. Those HEK-*MX1*-FLuci cells were transfected with 250 ng of plasmids encoding for the CedV proteins and stimulated with IFNα or PBS (MOCK control) for 24 h. Luciferase

induction in response to IFNα stimulation was measured in the cell lysate and normalized to the non-stimulated control. Luminance was directly proportional to the *MX1* promoter activation, thereby enabling quantification of functional JAK-STAT signaling.

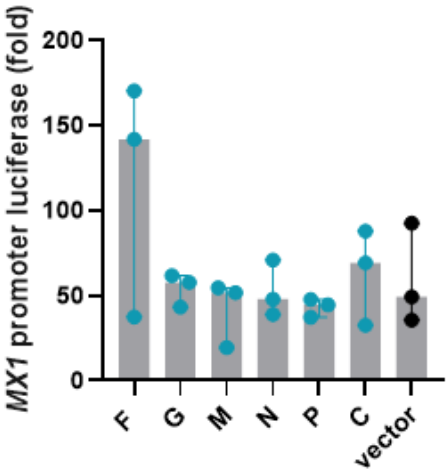

Figure 5.15. Influence of CedV proteins on IFN signaling in HEK-*MX1*-FLuci cells.
Luciferase assay of HEK-*MX1*-FLuci cells (expressing a firefly luciferase downstream of the *MX1* promoter), transfected with plasmids encoding for CedV proteins, and 24 h post-transfection stimulated with 800 U/ml IFNα. Fold change was calculated between the non-stimulated control and the IFNα-stimulated samples each. The data show median ± *IQR* of 3 independent experiments in duplicate. Statistical test: Kruskal-Wallis without Dunn's correction. $p < 0.05$ (*), $p < 0.01$(**).

Unexpectedly, HEK-*MX1*-FLuci cells reacted unreliably to transfections and stimulation with IFNα. Luciferase induction fluctuated substantially between experiments and cells downregulated the luciferase expression within few passages. When focusing on the three experiments with sufficient transfection efficiency and acceptable luciferase induction relative to the unstimulated control, N protein did not inhibit the induction of *MX1* promoter activity (**Figure 5.15**).

In all, the luciferase experiments demonstrated that CedV N protein inhibits the induction of *IFNB*. Although the exact mechanism is still unclear, translational shut-down, an alteration of IRF3 translocation, and inhibition of JAK-STAT signaling could be excluded.

5.3. Cell line specific replication kinetics of rCedV-nTurbo635

A human (A549), a porcine (SK-6), and an ERB epithelial cell line (RaNep) were chosen to compare replication kinetics and innate immune responses at different time points after infection. Admittedly, the three cell lines stem from different tissues (lung, kidney, nose); however, they are all of epithelial cell origin and are capable of mounting innate immune responses. ERB cells were chosen, as *Rousettus spp.* have been shown to harbor many different paramyxoviruses, including henipavirus-related viruses [41,42], and could therefore be a natural host of CedV. Pigs are an important intermediate, respectively, amplifying host for NiV-M infections [22]. So far, no human CedV infections have been reported, and CedV is very likely non-pathogenic, but humans are highly susceptible to HeV and NiV, with often lethal outcome [7,19–22]. Those three species were chosen to give a comprehensive overview of the spectrum of host immune responses to CedV infection, using the rCedV-nTurbo635. In the interest of comparability between immune reactions of different cell lines, every newly propagated rCedV-nTurbo635 batch was titrated on each cell line to achieve approximately the same MOI for each cell type and infection.

5.3.1. rCedV-nTurbo635 replication varies among cell lines and is affected by IFN competence

5.3.1.1. rCedV-nTurbo635 differentially replicates in epithelial cell lines

BHK-21 cells were used for rCedV-nTurbo635 propagation, due to their deficiency in type I IFN induction [267,268], which allows for efficient viral replication. Whether rCedV-nTurbo635 is able to replicate in the above-mentioned, IFN-competent, cell lines, was another subject of investigation. The BHK-21 replication curve served as a positive control for maximum replication of rCedV-nTurbo635. The highest titer, with approximately 10^8 TCID50, was measured in the supernatant of infected BHK-21 at 48 h p.i. Viral titers increased within the first 24 h in A549 and RaNep to then decrease at later time points (**Figure 5.16 A, B**). In contrast, titers in SK-6 peaked at 48 h p.i. (10^6 TCID50) with a maximum titer increase of 10^3 in the supernatant (**Figure 5.16 A**).

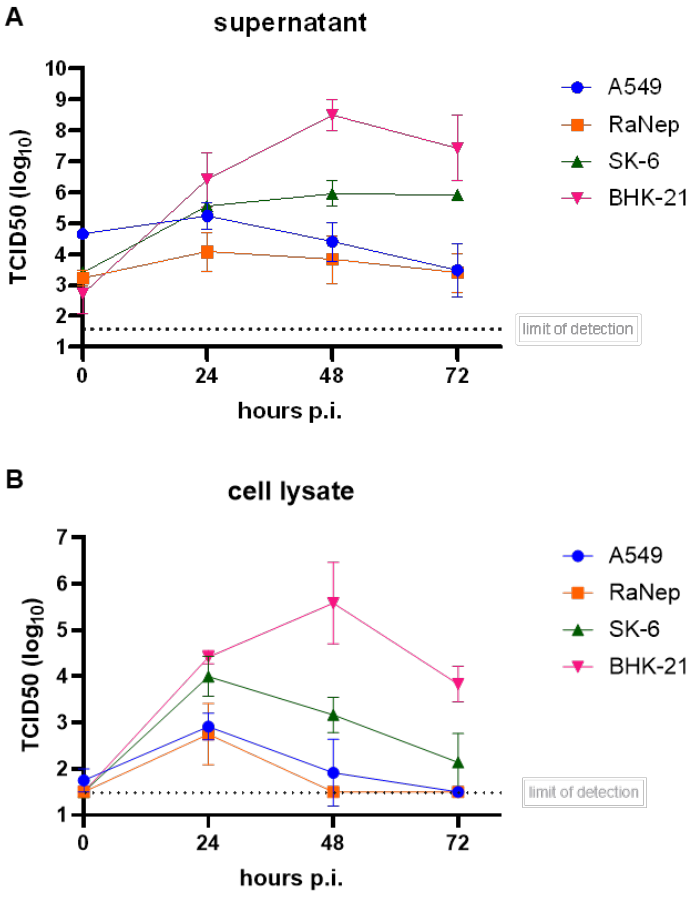

Figure 5.16. rCedV-nTurbo635 differentially replicates in epithelial cells lines of various origins.
Titers were determined on BHK-21 from supernatants (A) and cell lysates (B) of cells infected with rCedV-nTurbo635 at MOI 0.1 at zero, 24 h, 48 h, and 72 h. TCID50 was calculated using the Spearman-Kärber formula. The data show geometric mean ± *SD* of 2 independent experiments. Each dilution row and titration were performed in duplicate.

For each cell line, fluorescence images were taken at the above-mentioned time points (**Figure 5.17**). Interestingly, fluorescent intensity of the Turbo635 protein appeared dimmer in RaNep and brighter in BHK-21, compared to the other two cell lines.

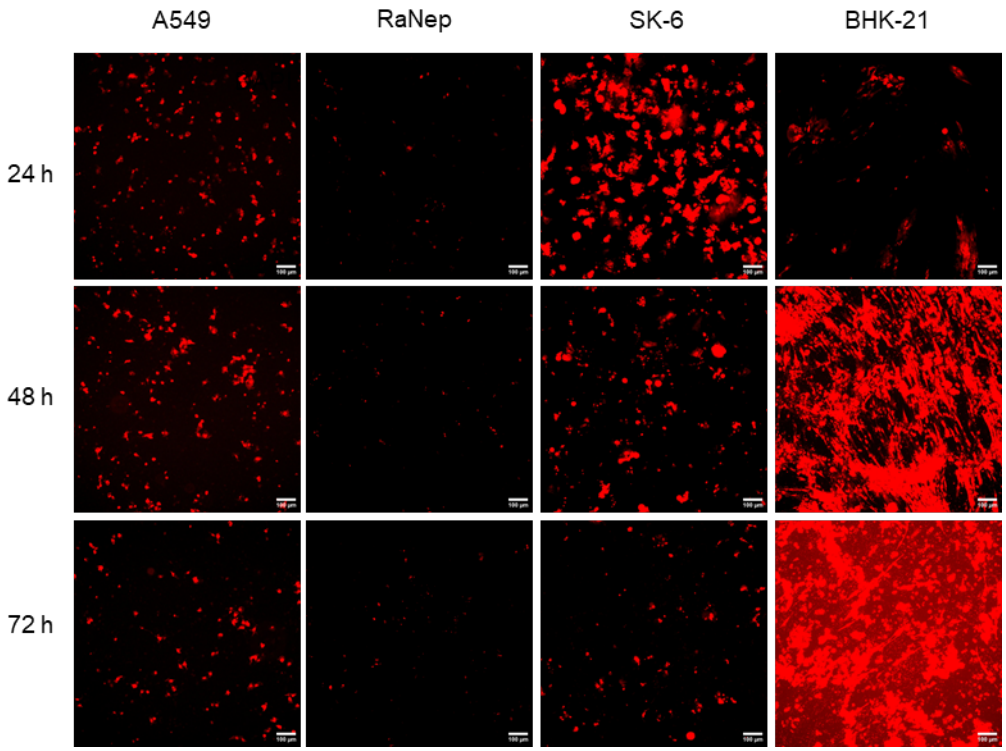

Figure 5.17. Intensity of Turbo635 fluorescence is dependent on cell line.
Fluorescent images of rCedV-nTurbo635 infected (MOI 0.1) A549, RaNep, SK-6, and BHK-21 at 24 h, 48 h, and 72 h. Images were taken with a Nikon Eclipse Ti microscope and brightness adjustments were done in Image J. Pictures are representative of 2 independent experiments. Scale bar: 100 µm.

These observations led to the hypothesis that A549 and RaNep are capable of eliminating rCedV-nTurbo635 in the medium term. To investigate this further, cells were infected at MOI 0.1 and split in low dilutions every two to three days. Supernatants were collected each time before passaging the cells and titrated again on BHK-21. Over the course of two weeks, all cell lines could maintain low to medium levels of viral replication (**Figure 5.18**).

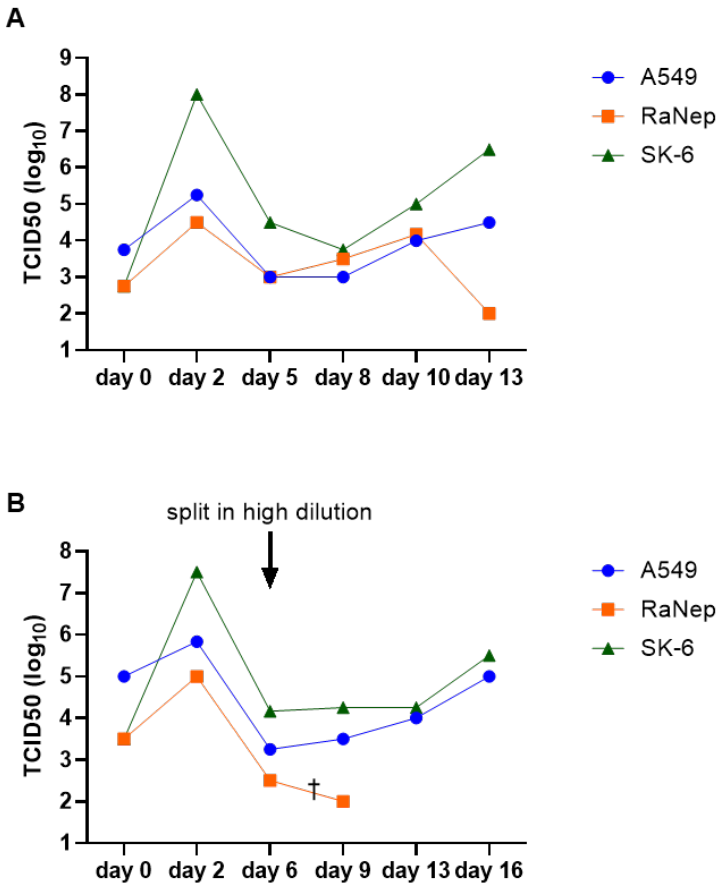

Figure 5.18. rCedV-nTurbo635 infection is maintained over the course of 2 weeks.
Viral titers were determined in BHK-21 from supernatants of cells infected with rCedV-nTurbo635 at MOI 0.1. Samples of the supernatant were taken before cells were split (every 2 to 3 days). TCID50 was calculated using the Spearman-Kärber formula. Each graph shows one independent experiment. Each dilution row and titration was performed in duplicate.

In this cell culture splitting set-up, rCedV-nTurbo635 titers on SK-6 reached up to 10^8 TCID50 at 48 h p.i.; however, SK-6 coped with intense viral replication unexpectedly well and survived until the end of the experiment. RaNep died in one experiment on day 7 and in the second one on day 13, which was not necessarily a direct response to the viral infection, but could also be caused by frequent splitting of already sparsely populated flasks. A549 continuously produced moderate titers (~ 10^4 TCID50) over the course of two weeks without displaying changes in morphology or cytopathic effects (**Figure 5.18**, **Figure 5.19**, bright field (BF)). The still rCedV-nTurbo635-infected SK-6 did not grow to a confluent monolayer and appeared more rounded than usual.

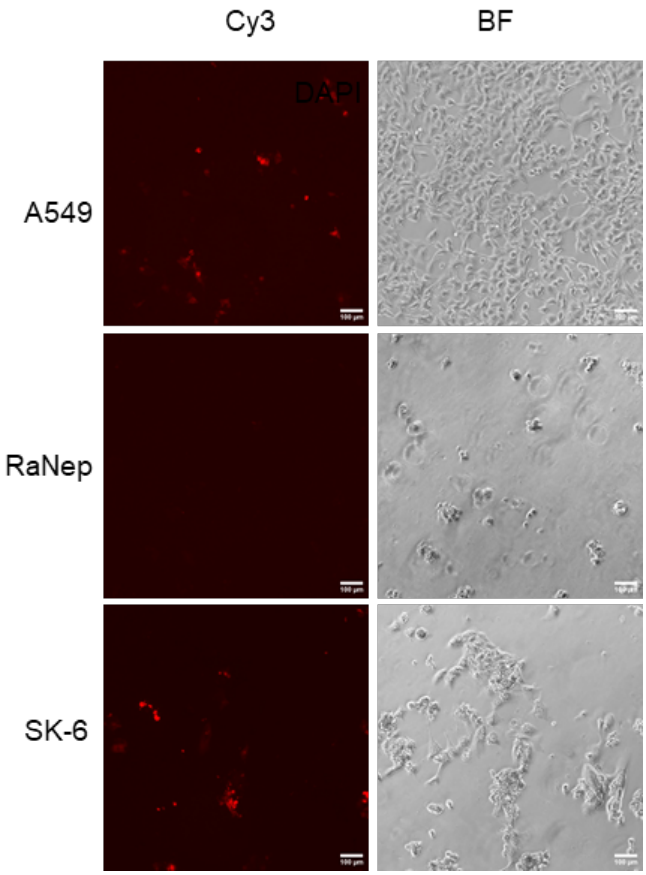

Figure 5.19. rCedV-nTurbo635 infection can be stably maintained throughout 2 weeks of cell passaging. Fluorescent images of rCedV-nTurbo635 infected A549, RaNep, and SK-6 cells on day 13 p.i. Images were taken with a Nikon Eclipse Ti microscope and brightness adjustments were done in Image J. Pictures are representative of 2 independent experiments. Scale bar: 100 µm.

5.3.1.2. rCedV-nTurbo635 replication is enhanced in cell lines with impaired IFN signaling

A plausible reason why rCedV-nTurbo635 replicates to exceptionally high titers in BHK-21 is the impaired IFN induction in these cells [267,268] .Whether titers of similar magnitude can be achieved on A549, RaNep, or SK-6 when JAK-STAT signaling is abrogated remains elusive. In this study, we used the JAK1 inhibitor AZD4604 to suppress IFN signaling in epithelial cells before infection. As AZD4604 has, to our knowledge, only been used on rodent and human cells/specimens, its efficacy and toxicity were first examined in our cell culture systems. Cells were either treated with 0.17 µM AZD4604 or MOCK-treated with DMSO for 1 h. Subsequently, half of the samples were stimulated with a high dose of IFNα for 4 h. To determine whether IFN signaling was sufficiently blocked at the applied concentration of AZD4604, induction of

the ISG *CXCL10* was measured by qPCR. AZD4604 completely blocked IFN signaling in A549, RaNep, and SK-6, as demonstrated by a lack of *CXCL10* induction in the "AZD+IFN" group (**Figure 5.20**).

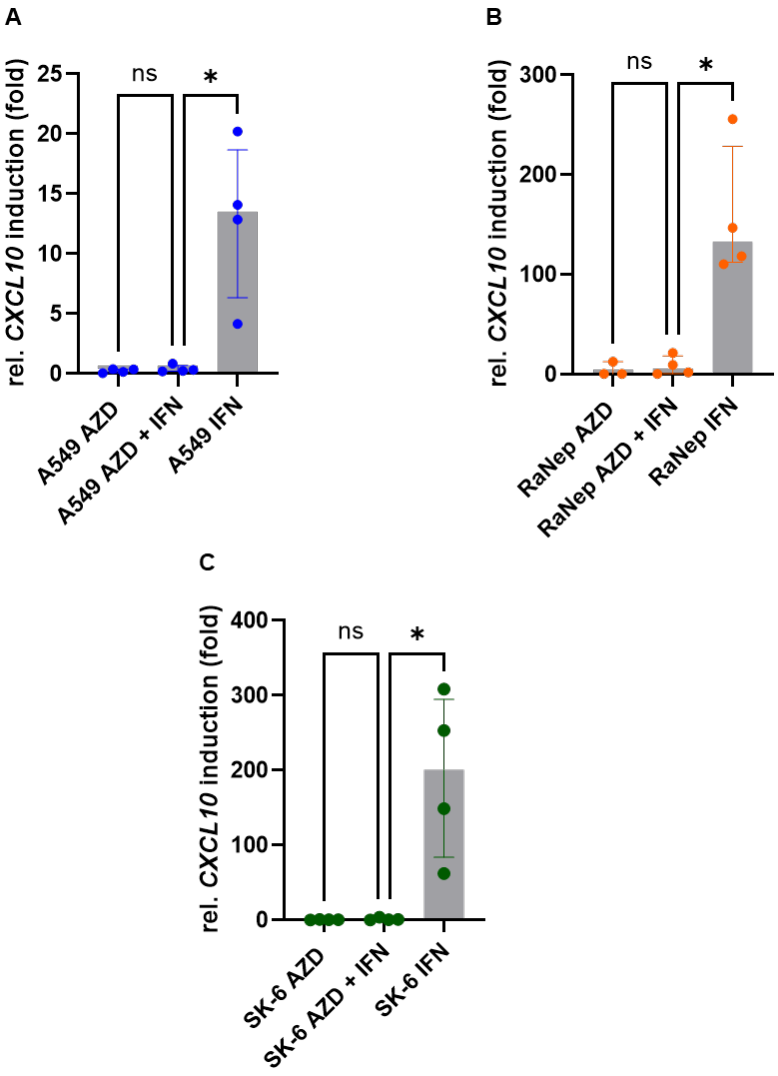

Figure 5.20. AZD4604 efficiently inhibits JAK-STAT signaling following IFNα stimulation.
qPCR results of *CXCL10* induction in A549 (A), RaNep (B), and SK-6 (C), treated with AZD4604 (0.17 µM) or MOCK-treated with DMSO, and 1 h later stimulated with IFNα or MOCK-treated for 4 h. Ct values were normalized to the respective housekeeping genes and induction is depicted as fold change relative to mean of the untreated control. The data show median ± *IQR* of at least 3 independent experiments in technical duplicate. Statistical test: Kruskal-Wallis without Dunn's correction. $p < 0.05$ (*).

To exclude lower ISG induction due to an increased number of dying cells after AZD4604 treatment, the cytotoxic effect of AZD4604 at a concentration of 0.17 µM was evaluated using an LDH release assay as a readout for cell death. AZD4604 did not cause significant LDH

release in any of the cell lines compared to the MOCK-treated control at 6 h post-treatment (**Figure 5.21**).

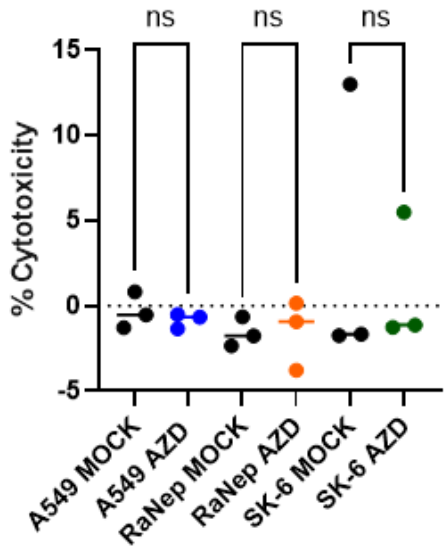

Figure 5.21. AZD4604 is not cytotoxic to A549, RaNep and SK-6.
LDH release assay of A549, RaNep, and SK-6 treated with 0.17 µM AZD4604 or MOCK-treated with DMSO for 6 h. Background was subtracted from each measurement and cytotoxicity was calculated in relation to completely lysed wells (high control). The data show median of 3 independent experiments in triplicate. Statistical test: Kruskal-Wallis without Dunn's correction. $p < 0.05$ (*).

Preliminary experiments showed an increase in cell death after combining AZD4604 treatment and rCedV-nTurbo635 infection. Therefore, a lower AZD4604 concentration of 0.085 µM (= 0.5 µg/ml) was used to investigate the influence of an IFN signaling block on viral replication. SK-6 had to be excluded from this experiment, since cell death in the AZD4604-treated and infected wells prevailed, despite the lower AZD4604 concentration. A549 replication curves deviated from the DMSO control at 24 h p.i., when titers in the DMSO control started to decrease, whereas titers on JAK-STAT inhibited A549 increased to a maximum of 10^6 TCID50 after 72 h (**Figure 5.22**). Differences between DMSO and AZD4604-treated RaNep started occurring at 48 h p.i. and were more pronounced. Here, titers reached a maximum of 10^8 TCID50 at 72 h p.i.

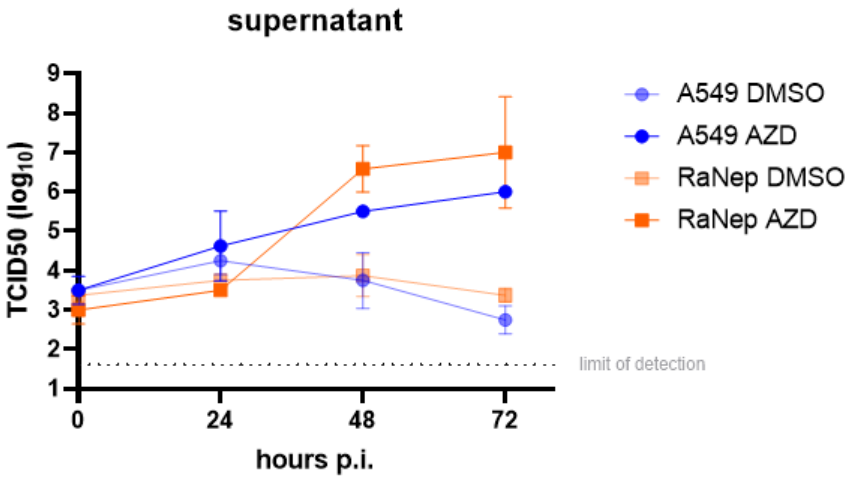

Figure 5.22. rCedV-nTurbo635 titers increase drastically in JAK-STAT inhibited cells.
A549 and RaNep were seeded in 24-well plates at 1 x 10^5 cells/well, and on the next day, either treated with AZD4604 (0.5 µg/ml) or DMSO for 1 h, before rCedV-nTurbo635 infection at MOI 0.1 for 90 min. Subsequently, medium was changed back to normal cell culture medium, supplemented with AZD4604, or DMSO as a control. Supernatants were collected at zero, 24 h, 48 h, and 72 h p.i. and titrated in duplicate on BHK-21. Semi-transparent lines show replication curve for DMSO-treated cells, whereas saturated colors depict replication on JAK1-inhibited cells. The data show geometric mean ± *SD* of two independent experiments in duplicate.

This strikingly demonstrates the importance of IFN signaling for controlling rCedV-nTurbo635 replication in both A549 and RaNep starting 48h p.i. However, the impact of other JAK1-mediated signaling pathways, such as those triggered by γ-chain cytokines (IL-2, IL-4, IL-13, etc.), or for example IL-6, could not be excluded [269].

5.4. Innate immune responses to rCedV-nTurbo635 infection *in vitro*

5.4.1. Similar transcriptional induction of innate immune genes in human, porcine, and ERB-derived epithelial cell lines

Innate immune responses to rCedV-nTurbo635 infection were evaluated by qPCR at four different time points (4 h, 8 h, 24 h, 48 h) p.i. at MOI 0.1 and 24 h after transfection of synthetic dsRNA (polyI:C). *IFNB* induction was of particular interest, as HeV and NiV inhibit type I IFN induction in susceptible hosts and thereby weaken the innate immune defense [174]. All three investigated cell lines induced *IFNB*; however, A549 responded earlier (24 h) than the other

two and already decreased *IFNB* levels at 48 h p.i. (**Figure 5.23**). *IFNB* transcripts increased in RaNep and SK-6 at 48 h p.i., with the highest fold changes measured in SK-6.

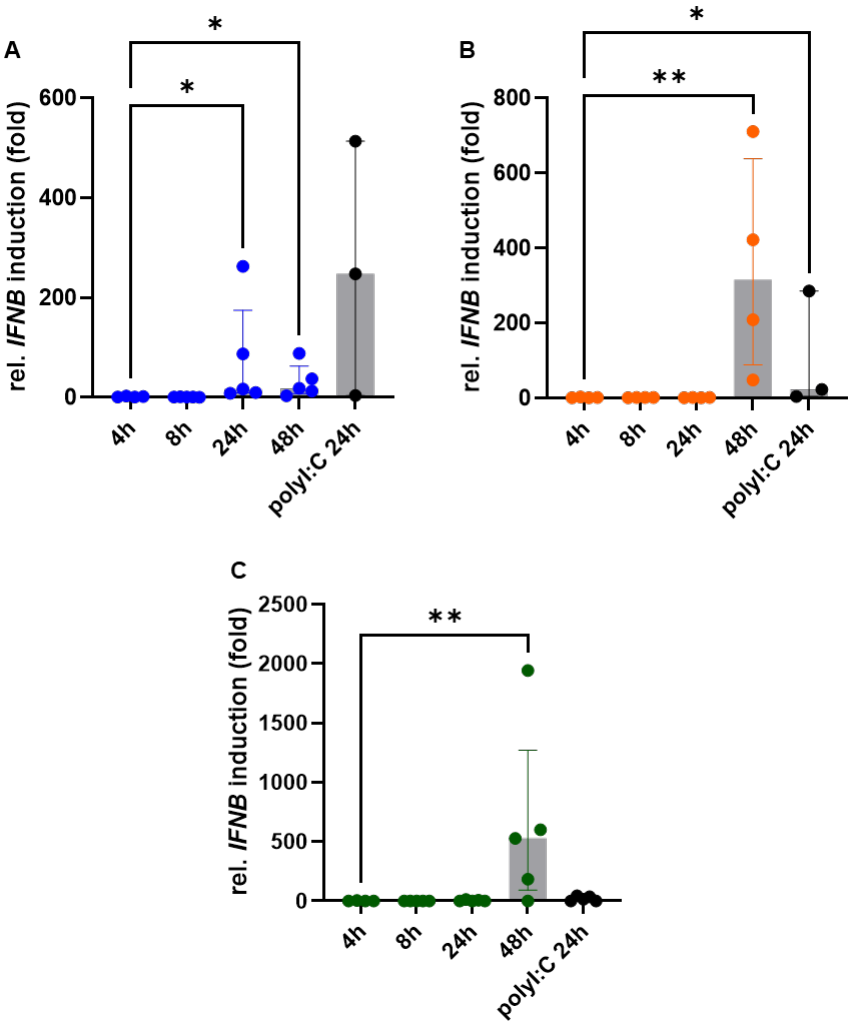

Figure 5.23. *INFB* is induced earlier in A549 than in RaNep or SK-6.
qPCR data of *IFNB* expression in A549 (A), RaNep (B), and SK-6 (C) 4 h, 8 h, 24 h, and 48 h p.i. with rCedV-nTurbo635 at MOI 0.1 and after polyI:C treatment for 24 h normalized to a MOCK-infected control. The data show median ± *IQR* of 3 independent experiments in duplicate. Statistical test: Kruskal-Wallis without Dunn's correction. $p < 0.05$ (*), $p < 0.01$(**).

A similar pattern could be observed for the ISG *CXCL10* and the pro-inflammatory cytokines *IL6* and *TNFA* (**Figure 5.24, Figure 5.25**). *CXCL10* increased about 40-fold in A549, in comparison to almost 1,800-fold in RaNep and 30,000-fold in SK-6.

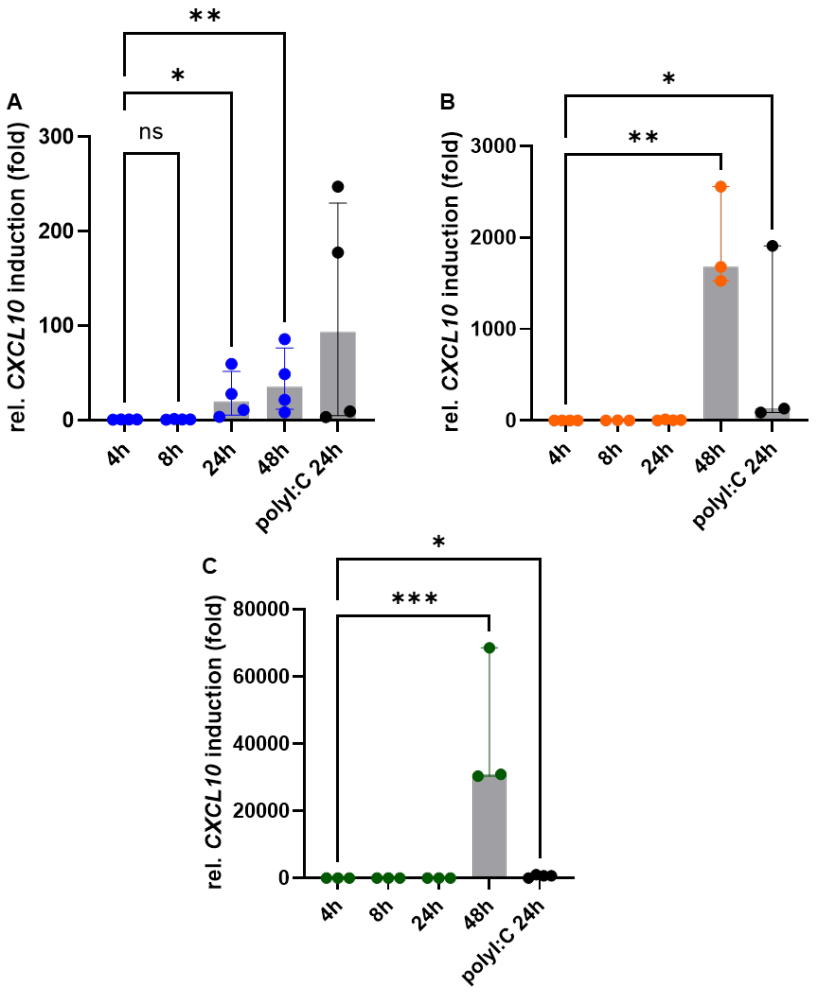

Figure 5.24. *CXCL10* is induced earlier in A549 than in RaNep or SK-6.

qPCR data of *CXCL10* expression in A549 (A), RaNep (B), and SK-6 (C) 4 h, 8 h, 24 h, and 48 h p.i. with rCedV-nTurbo635 at MOI 0.1 and after polyI:C treatment for 24 h, normalized to a MOCK-infected control. The data show median ± *IQR* of at least 3 independent experiments in duplicate. Statistical test: Kruskal-Wallis without Dunn's correction. $p < 0.05$ (*), $p < 0.01$(**), $p < 0.001$(***).

Regarding the pro-inflammatory cytokines *IL6* and *TNFA*, fold changes were substantially lower in RaNep compared to SK-6. A549 induced higher levels of *IL6* than RaNep, but responded with similarly low levels of *TNFA* to the rCedV-nTurbo635 infection. The induction of *IL6* transcripts in RaNep did not reach significance when compared to the uninfected control.

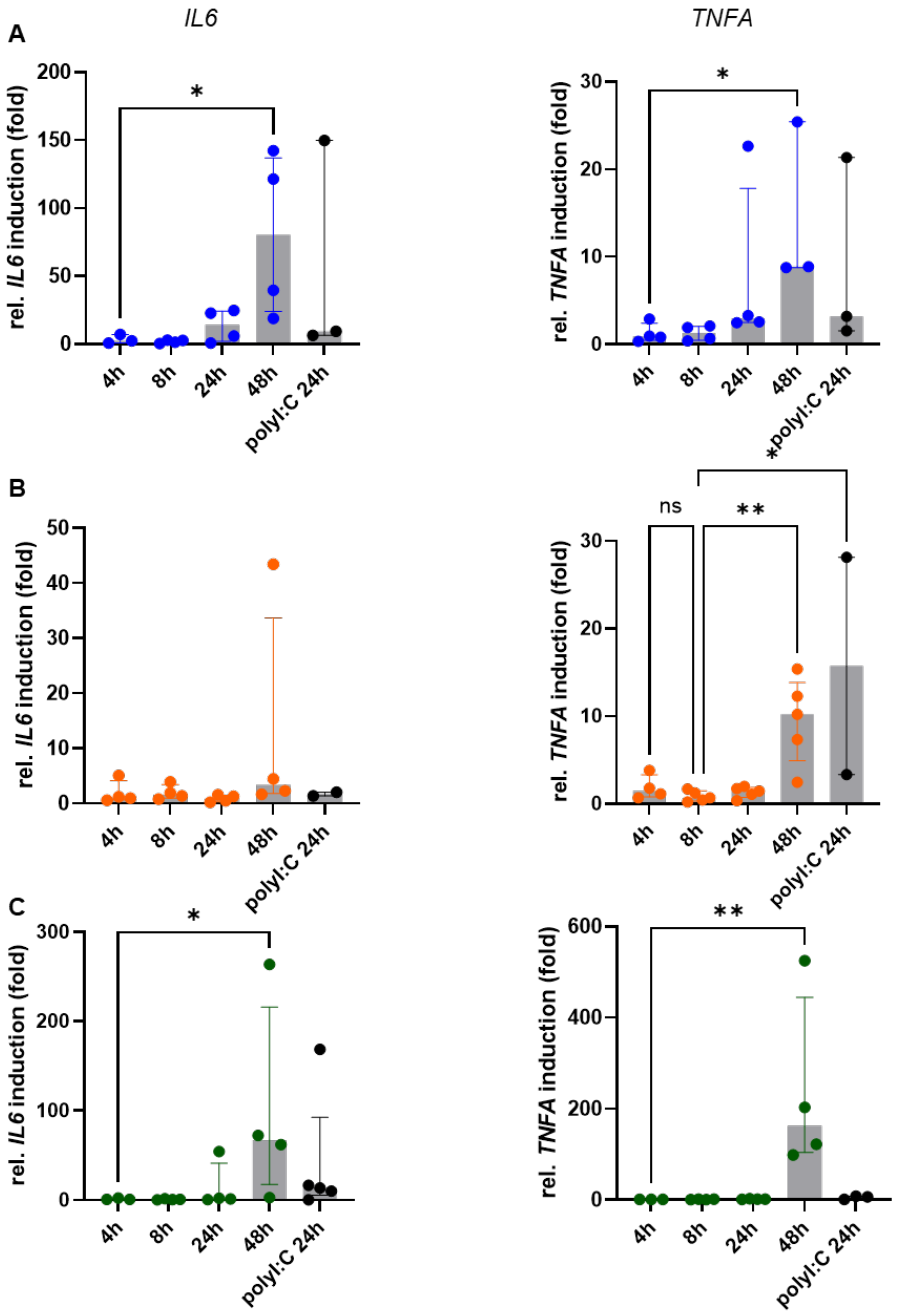

Figure 5.25. Genes encoding for the pro-inflammatory cytokines *IL6* and *TNFA* are induced 24 h earlier in A549 than in RaNep or SK-6.

qPCR data of *IL6* (left) and *TNFA* (right) expression in A549 (A), RaNep (B), and SK-6 (C) 4 h, 8 h, 24 h, and 48 h p.i. with rCedV-nTurbo635 at MOI 0.1 and after polyI:C treatment for 24 h normalized to a MOCK-infected control. The data show median ± *IQR* of at least 3 independent experiments in duplicate. Statistical test: Kruskal-Wallis without Dunn's correction. $p < 0.05$ (*), $p < 0.01$(**).

IFNL and *IL1B* expression were only evaluated in RaNep (**Figure 5.26**). In RaNep, *IFNL* induction was measured additionally, as it is an important antiviral defense mechanism of mucosal surfaces, such as the upper respiratory tract, from which RaNep are derived [270,271]. *IFNL* was induced at 48 h p.i., similar to *IFNB*, but at a lower magnitude. Expression of the pro-

inflammatory cytokine associated with inflammasome activation, *IL1B*, was moderately increased at 48 h p.i. (**Figure 5.26 B**).

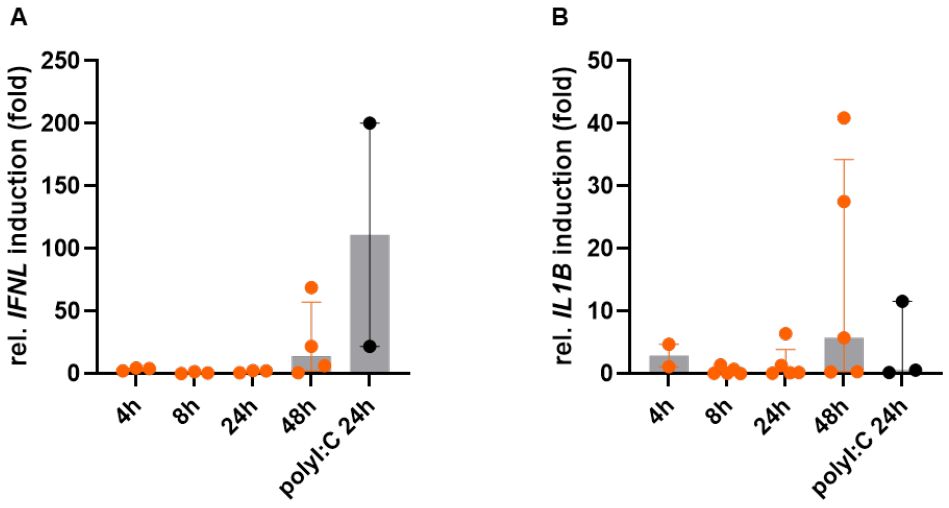

Figure 5.26. Expression of *IFNL* and *IL1B* is upregulated at 48 h p.i. in RaNep.
qPCR data of *IFNL* (A) and *IL1B* (B) expression in RaNep at 4 h, 8 h, 24 h, and 48 h p.i. with rCedV-nTurbo635 at MOI 0.1 and after polyI:C treatment for 24 h, normalized to a MOCK-infected control. The data show median ± *IQR* of at least 3 independent experiments in duplicate.

Overall, all cell lines demonstrated similar induction of genes related to innate immune responses following rCedV-nTurbo635 infection, although there were distinct timing differences observed in A549.

5.4.2. Comparable proteomic profile in response to rCedV-nTurbo635 infection in three epithelial cell lines

To obtain an overview of global proteome changes in response to rCedV-nTurbo635 infection, A549, RaNep, and SK-6 were infected at MOI 0.2, and samples were prepared for mass spectrometry at 24 h p.i. Volcano plots comparing MOCK and infected cells showed an upregulation of IFN-induced proteins, such as MX1, ISG15, and members of the IFIT family, in all three cell lines (**Figure 5.27**, **Figure 5.28**, **Figure 5.29**). Oligoadenylate synthase (-like) proteins (OAS, OASL), as part of the antiviral defense, were among the most abundant proteins in all infected samples. CedV-nTurbo635 proteins were readily detected in all infected

samples with nucleocapsid, respectively, matrix protein, among the most abundant and large protein (L) expressed at the lowest level.

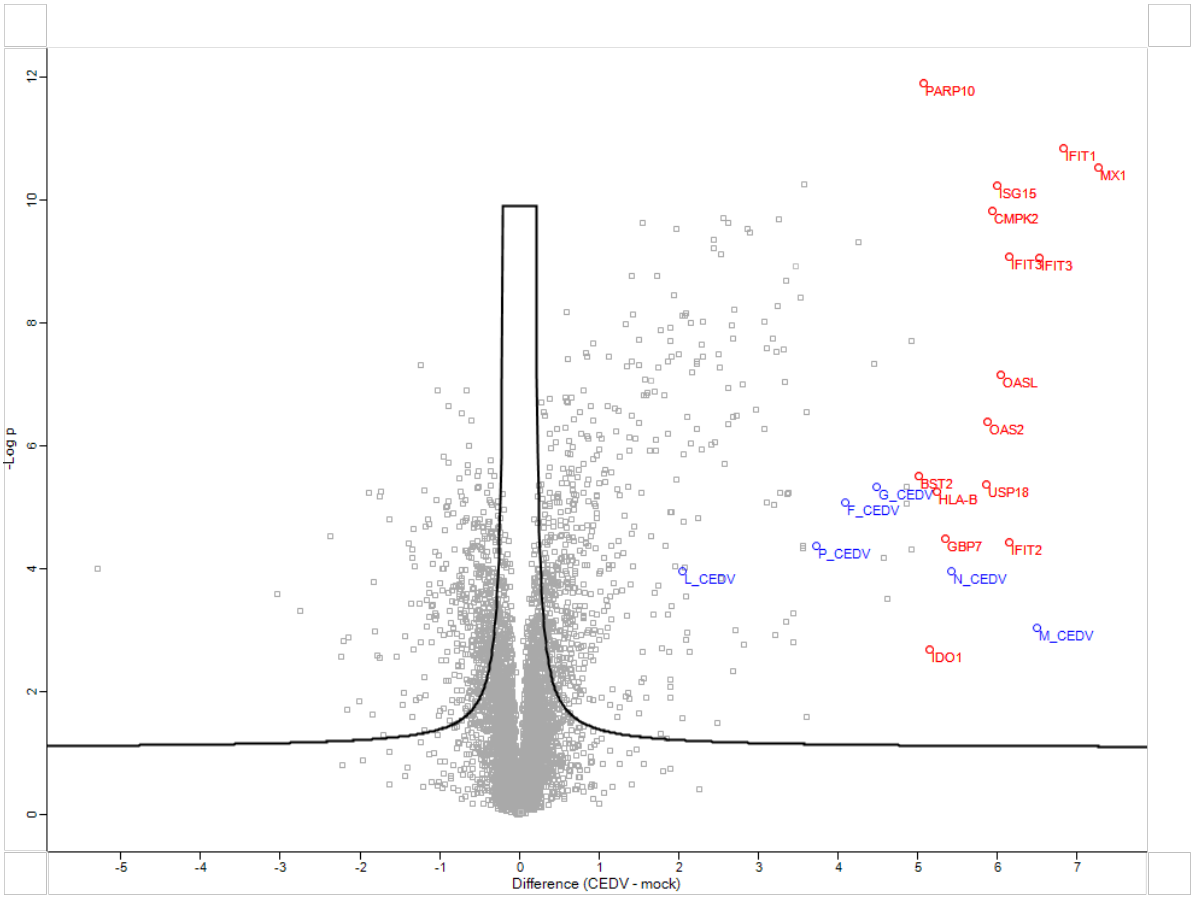

Figure 5.27. Increased expression of typical ISGs and antiviral proteins in A549.

Volcano plot of proteomics data. A549 were infected with rCedV-nTurbo635 at MOI 0.2 and samples were prepared for mass spectrometry 24 h p.i X-axis shows the differences in protein expression levels (log_2 fold changes) between MOCK and rCedV-nTurbo635 infected samples. The negative logarithmic P values (log_{10}) for each protein are depicted as their y-values. rCedV-nTurbo635 proteins are illustrated in blue. Proteome was annotated and t-tests were performed in Perseus by Dr. Axel Karger. Volcano plots were generated in R Studio (packages: clusterProfiler, enrichplot, ggstar, ggnewscale, DOSE and org.hs.eg.db).

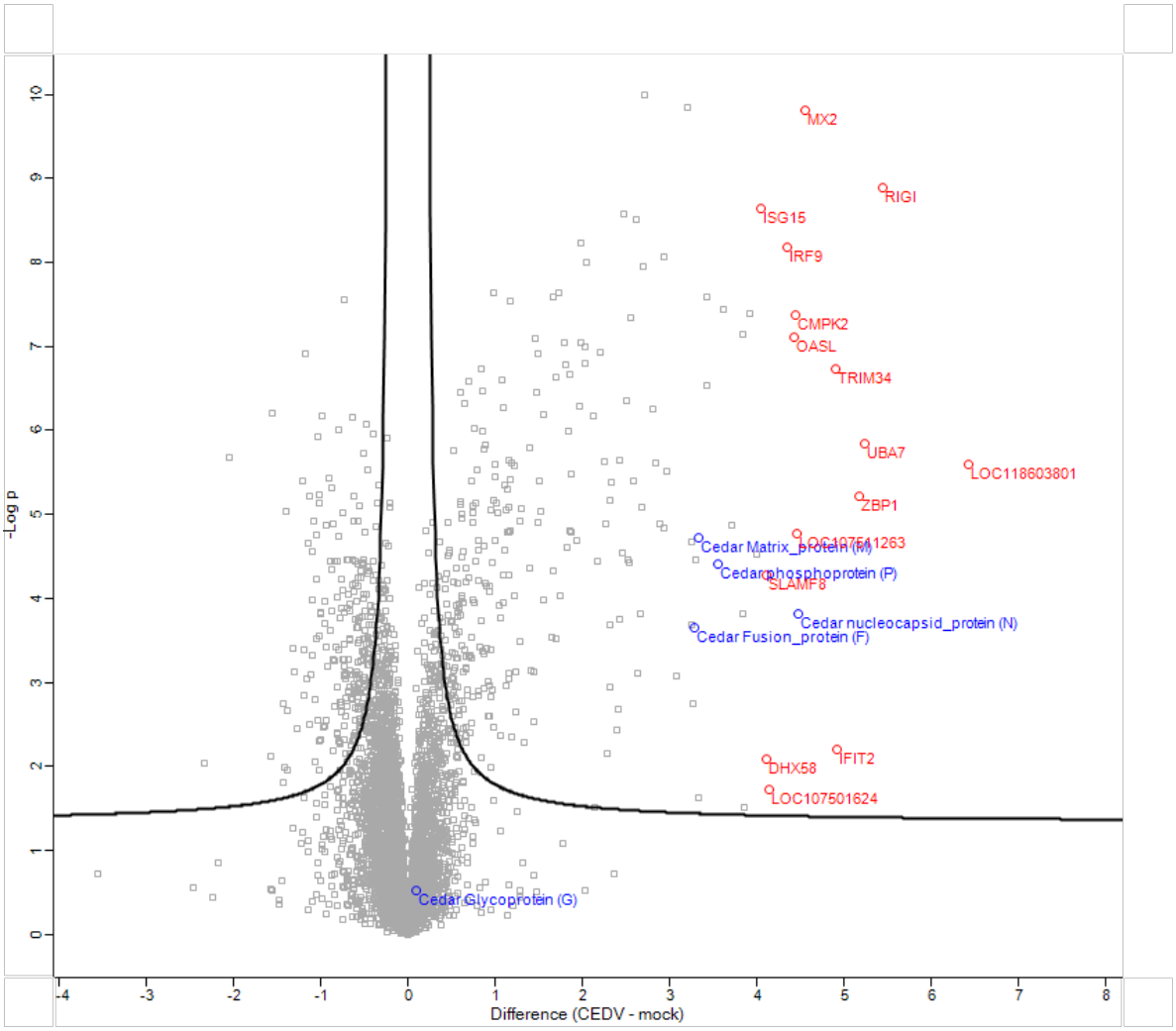

Figure 5.28. Increased expression of typical ISGs, antiviral and ERB specific proteins in RaNep.

Volcano plot of proteomics data. RaNep were infected with rCedV-nTurbo635 at MOI 0.2 and samples were prepared for mass spectrometry 24 h p.i. X-axis shows the differences in protein expression levels (log_2 fold changes) between MOCK and rCedV-nTurbo635 infected samples. The negative logarithmic P values (log_{10}) for each protein are depicted as their y-values. rCedV-nTurbo635 proteins are illustrated in blue. Proteome was annotated and t-tests were performed in Perseus Dr. Axel Karger. Volcano plots were generated in R Studio (packages: clusterProfiler, enrichplot, ggstar, ggnewscale, DOSE and org.hs.eg.db).

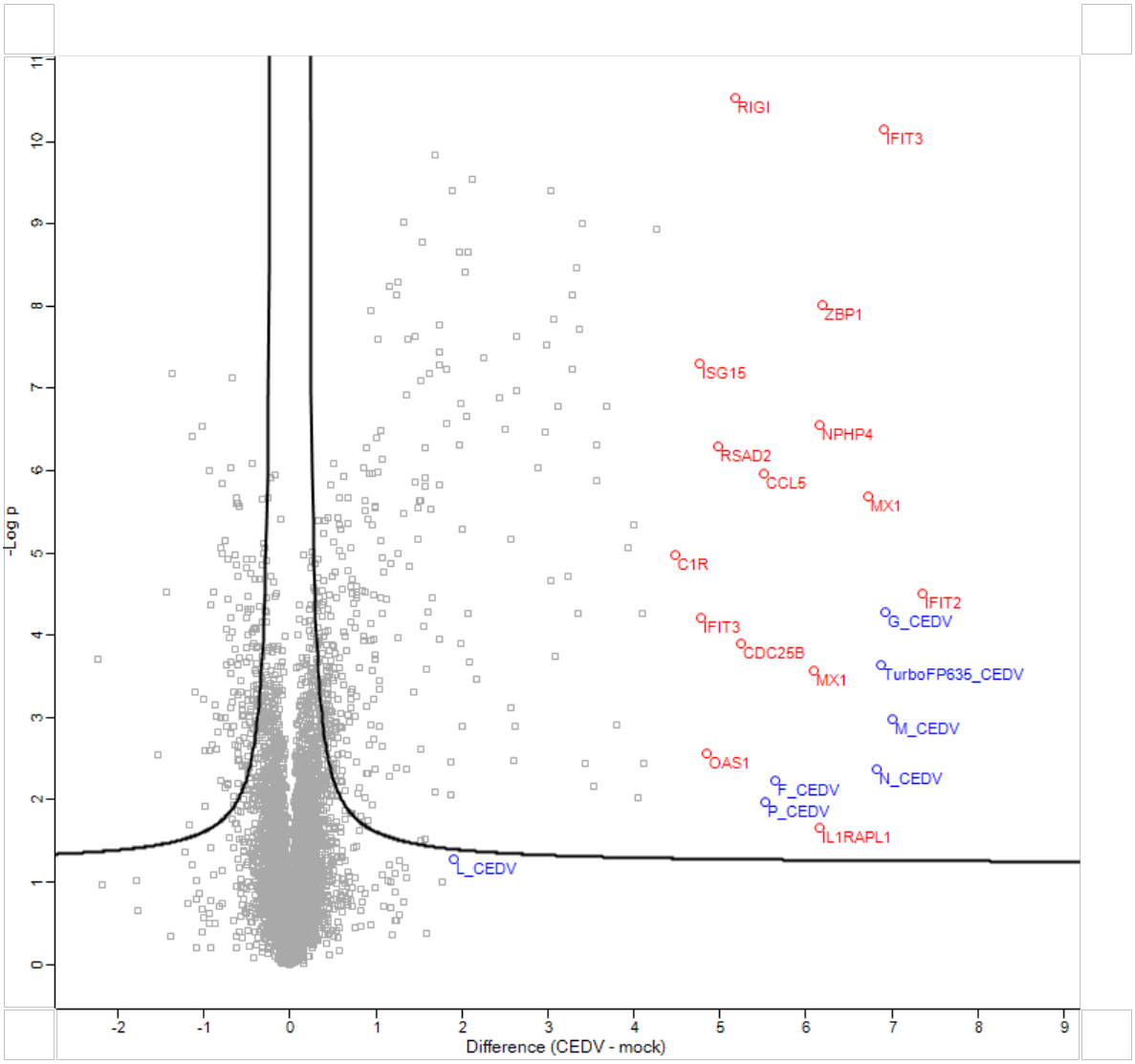

Figure 5.29. Increased expression of typical ISGs and antiviral proteins in SK-6.

Volcano plot of proteomics data. SK-6 were infected with rCedV-nTurbo635 at MOI 0.2 and samples were prepared for mass spectrometry 24 h p.i. X-axis shows the differences in protein expression levels (log_2 fold changes) between MOCK and rCedV-nTurbo635 infected samples. The negative logarithmic P values (log_{10}) for each protein are depicted as their y-values. rCedV-nTurbo635 proteins are illustrated in blue. Proteome was annotated and t-tests were performed in Perseus Dr. Axel Karger. Volcano plots were generated in R Studio (packages: clusterProfiler, enrichplot, ggstar, ggnewscale, DOSE and org.hs.eg.db).

The cell lines also resembled each other in pathway enrichment analysis, highlighting pathways associated with antiviral defense, viral life cycle, IFN production, and NF-κB signaling (**Figure 5.30, Supplementary Figure 10.10**). Differences emerged in ribosomal/mitochondrial processes, as well as energy metabolism (**Supplementary Figure 10.11**), which were significantly upregulated only in SK-6, suggesting a demand for increased protein translation capacities in response to viral infection.

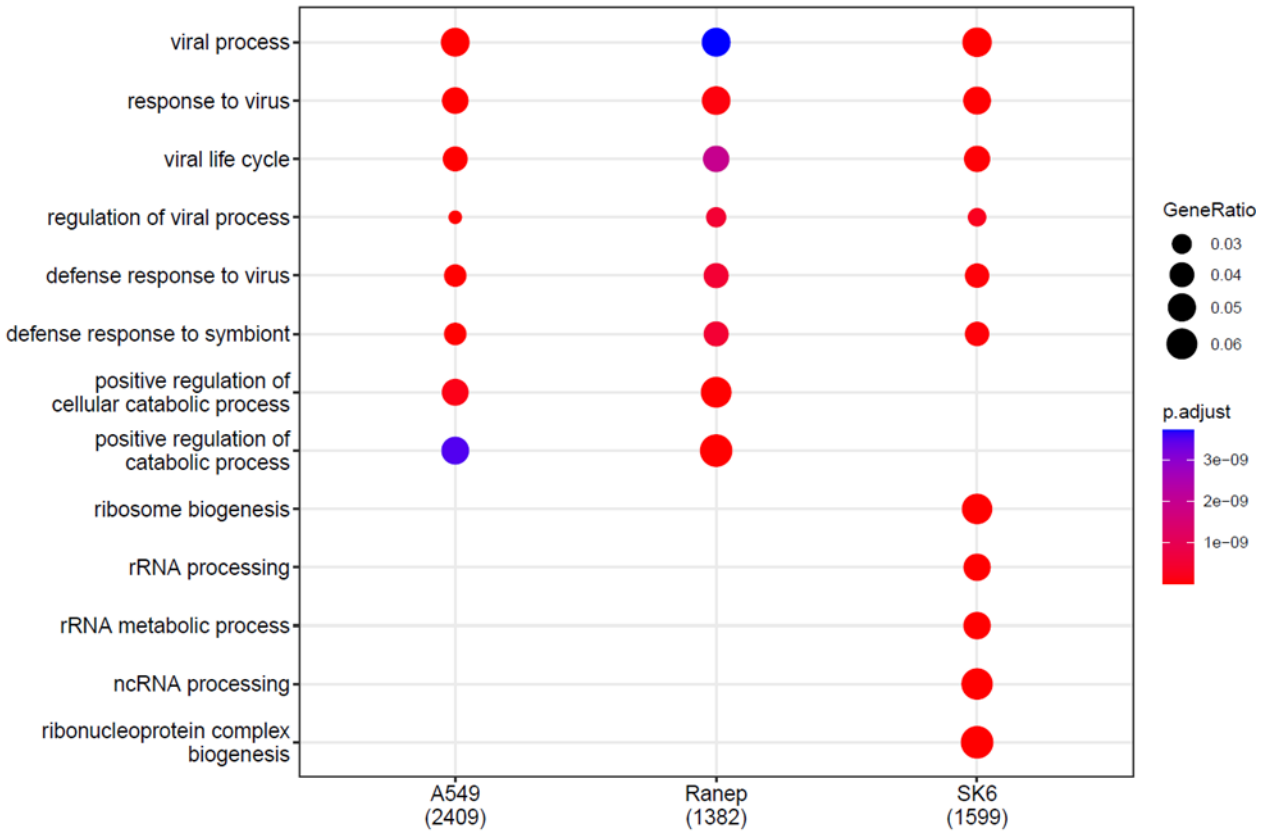

Figure 5.30. Biological process (BP) pathway enrichment analysis reveals differences in ribosomal processes in SK-6 24 h p.i.

Differences in protein levels relevant for the annotated pathways are depicted by proportional circle sizes. P values are visualized by the color of the circles, with lowest P values (= highest significance) colored in red. Gene ontology (GO) enrichment analysis was done in R Studio (package: clusterProfiler). Statistical test: t-test.

Upon closer examination of the top 50 most upregulated proteins in response to rCedV-nTurbo635 infection, important ISGs and antiviral effector molecules, such as MX1, ISG15, ISG20, OAS1, OASL, or IDO1 [266,272] were among the highest induced proteins (**Figure 5.31, Supplementary Figure 10.13**). Members of the OAS family, which were consistently induced in all three cell lines**,** among other less-defined functions, inhibit replication by depleting viral RNA through the activation of RNase L [272]. When focusing on pro- and anti-apoptotic proteins,

such as Bak, Bcl-2, and various caspases, the three cell lines exhibited similar responses (**Supplementary Figure 10.14**). Notably, caspase-1 and -4 specific peptides were only detected in A549.

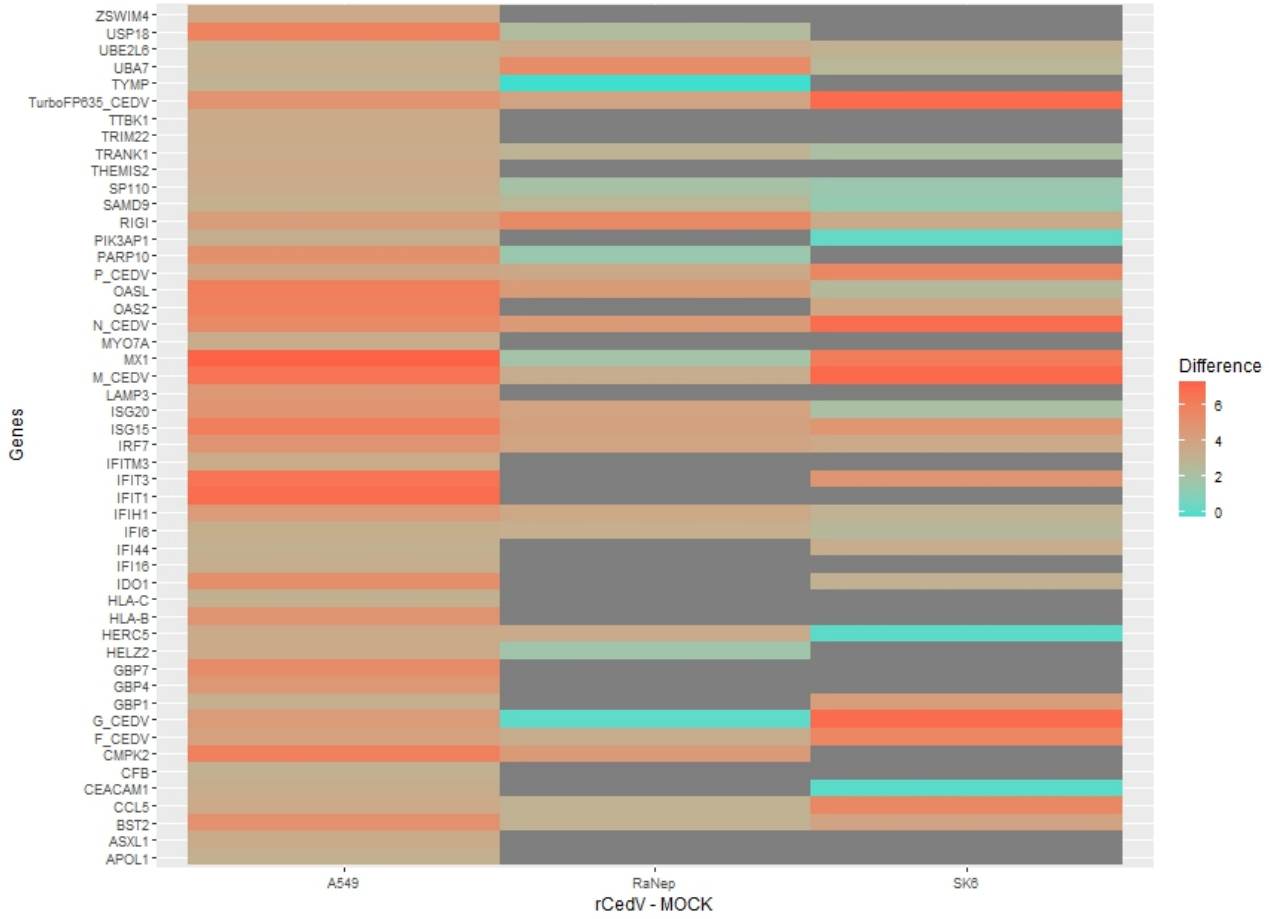

Figure 5.31. Upregulation of proteins related to antiviral response and innate immune activation.
Heatmap of top 50 most upregulated proteins (gene names) after rCedV-nTurbo635 infection in A549 in comparison to RaNep and SK-6. The color scale represents differences in protein expression levels (log_2 fold changes) between MOCK and rCedV-nTurbo635 infected samples. Whenever values are not available tile is colored in grey. Most upregulated proteins are salmon-colored, while least upregulated proteins are displayed in light blue. CedV-nTurbo635 proteins F, G, M, N, P, as well as the Turbo635 fluorescent protein can be detected in all three cell lines. Heatmap was created in R Studio.

When directly comparing A549, RaNep, and SK-6 in terms of differences in protein abundance, even though RaNep also increased ISG expression, the other cell lines exhibited a stronger induction in response to the infection. Due to incomplete genome annotation, some of the 50 most abundant proteins in infected RaNep are still unknown, but could play a role in viral infections or be bat-specific ISGs (**Supplementary Figure 10.13**). Among the most differentially expressed proteins, the antiviral proteins OAS3 and TRIM36 stood out as RaNep-specific. Additionally, A549 reacted to the infection with MX1 induction, whereas RaNep increased MX2 expression, and SK-6 upregulated both.

5.5. Cellular stress in response to rCedV-nTurbo635 infection

Viral infections cause accumulation of un- or misfolded proteins, which can lead to ER stress, and if this is not resolved, to cell death [273]. Additionally, the henipavirus glycoproteins G and F are processed in the ER before being transported to the cell surface, placing even more pressure on the ER machinery [274]. Since CedV is classified as a non-pathogenic henipavirus, one aim of this project was to investigate its effects on ER stress and whether it can cause cell death.

5.5.1. rCedV-nTurbo635 causes cellular stress on a transcriptional level

All three UPR signaling cascades are initiated by the dissociation of BiP from its receptors (PERK, ATF6, IRE1) [275]. Therefore, an increase in soluble BiP is indicative of an activation of the UPR on the protein level. To investigate whether rCedV-nTurbo635 infection can cause ER stress, A549, RaNep, and SK-6 were seeded in 6-well plates and infected at MOI 0.1. Higher MOIs lead to low protein yields due to increased cell death, especially in SK-6. Protein samples were prepared for SDS-PAGE at 8 h, 16 h, 24 h, and 48 h p.i. to analyze BiP abundance and phosphorylation of eukaryotic translation initiation factor (eIF2α), downstream of PERK activation, within the first 48 h of infection (**Figure 5.32**). Tunicamycin stimulation served as a positive control, as it abrogates N-linked glycosylation of newly synthesized proteins in the ER, causing an accumulation of unfolded proteins [276].

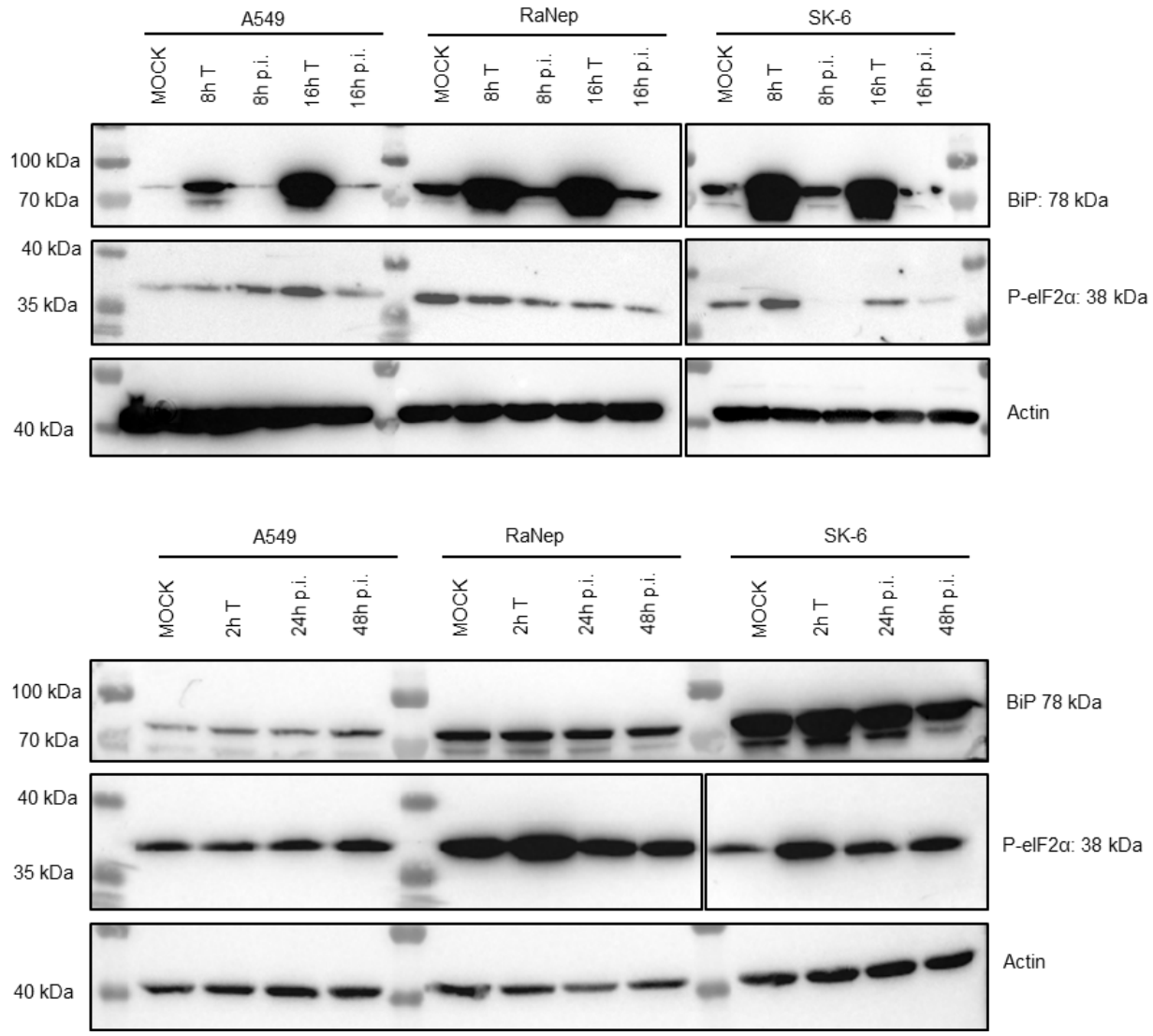

Figure 5.32. Unaltered BiP/P-eIF2α levels in response to rCedV-nTurbo635 infection.
Western blot analysis of A549, RaNep and SK-6 infected with rCedV-nTurbo635 at MOI 0.1, 8 h, 16 h, 24 h, and 48 h p.i. Tunicamycin (T) stimulation for 2 h, 8 h, and 16 h served as positive control for ER stress. An anti-β-Actin antibody was used as the loading control. The anti-P-eIF2α antibody recognizes Ser51 phosphorylation, indicative of protein synthesis inhibition. Images are representative of 3 independent experiments.

BiP abundance increased drastically 8 h after Tunicamycin stimulation; however, significant differences in rCedV-nTurbo635 infected samples could not be measured at any time point (**Figure 5.33**). A549 exhibited a marginal increase in response to infection at all time points, whereas RaNep increased BiP on a small scale at 24 h p.i.

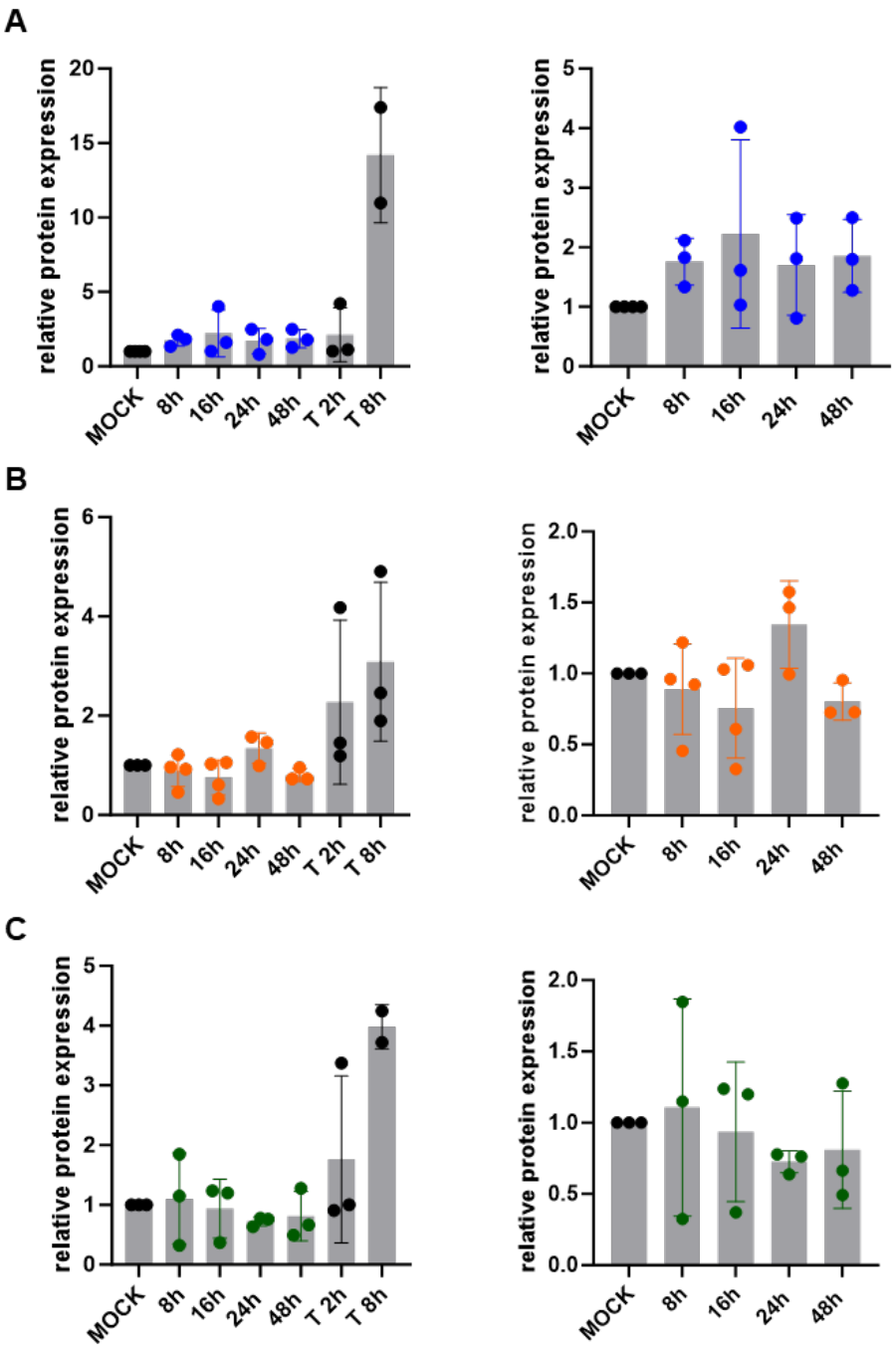

Figure 5.33. Densitometry analysis reveals unaltered BiP levels in response to rCedV-nTurbo635 infection. Quantification of BiP amounts in A549 (A), RaNep (B), and SK-6 (C) relative to β-Actin and normalized to the uninfected control (MOCK). Densitometry measurements and analysis were done using Image lab. Graphs on the right show data without the Tunicamycin-stimulated positive controls. Plotted are mean ± *SD*.

Regarding eIF2α phosphorylation, Tunicamycin stimulation did not present an equally convincing positive control in A549 and RaNep, as it did in SK-6, which could be due to a suboptimal sampling time point. In A549, eIF2α phosphorylation increased slightly at all time points compared to the control. In contrast, phosphorylation of RaNep eIF2α was only slightly

induced at least 24 h p.i., which complements the observed increase in BiP. In SK-6, phosphorylated eIF2α was induced to some extent 16 h p.i. (**Figure 5.34**).

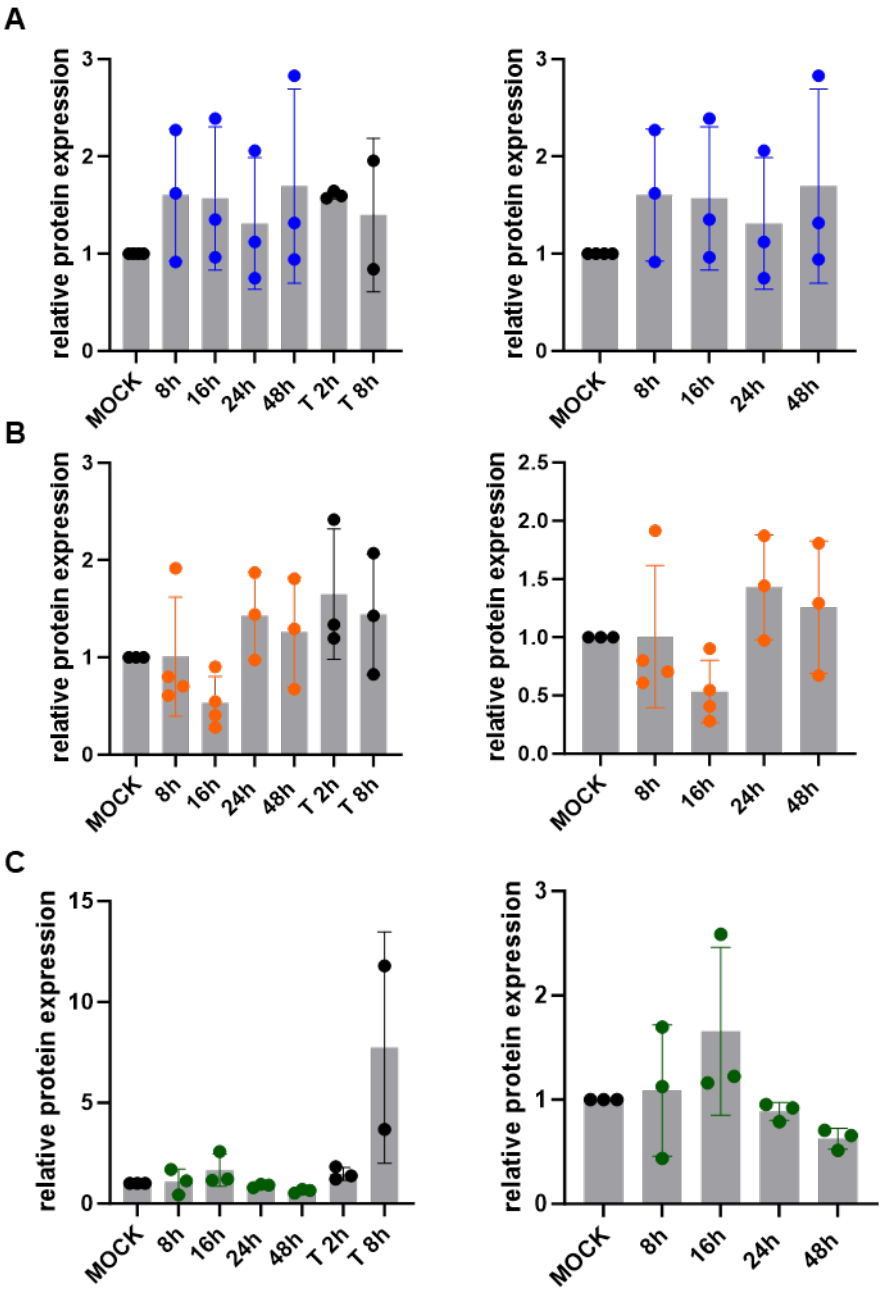

Figure 5.34. Densitometry analysis reveals unaltered phosphorylation of eIF2α in response to rCedV-nTurbo635 infection.

Quantification of phosphorylated eIF2α in A549 (A), RaNep (B), and SK-6 (C) relative to β-Actin and normalized to the uninfected control (MOCK). Densitometry measurements and analysis were done using Image lab. Graphs on the right show data without the positive controls. Plotted are mean ± *SD.*

CedV-nTurbo635, a low-pathogenic henipavirus, did not cause severe ER stress-related changes on the protein level in any of the tested cell lines.

On a transcriptional level, BiP (*HSP5A*), the activating transcription factor 4 (*ATF4*), C/EBP homologous protein (CHOP), also known as DNA damage-inducible gene (*DDIT3*), and heat shock protein 60 (*HSP60*, only in RaNep, **Supplementary Figure 10.9**) were examined. ATF4 acts as a transcription factor downstream of PERK/eIF2α signaling, and phosphorylation of eIF2α additionally induces ATF4 translation [209]. ATF4 expression is regulated through translation, as it is usually transcribed in abundance [114,209]. As expected, ATF4 transcript levels remained unaltered in response to rCedV-nTurbo635 infection in all three epithelial cell lines (**Figure 5.35**).

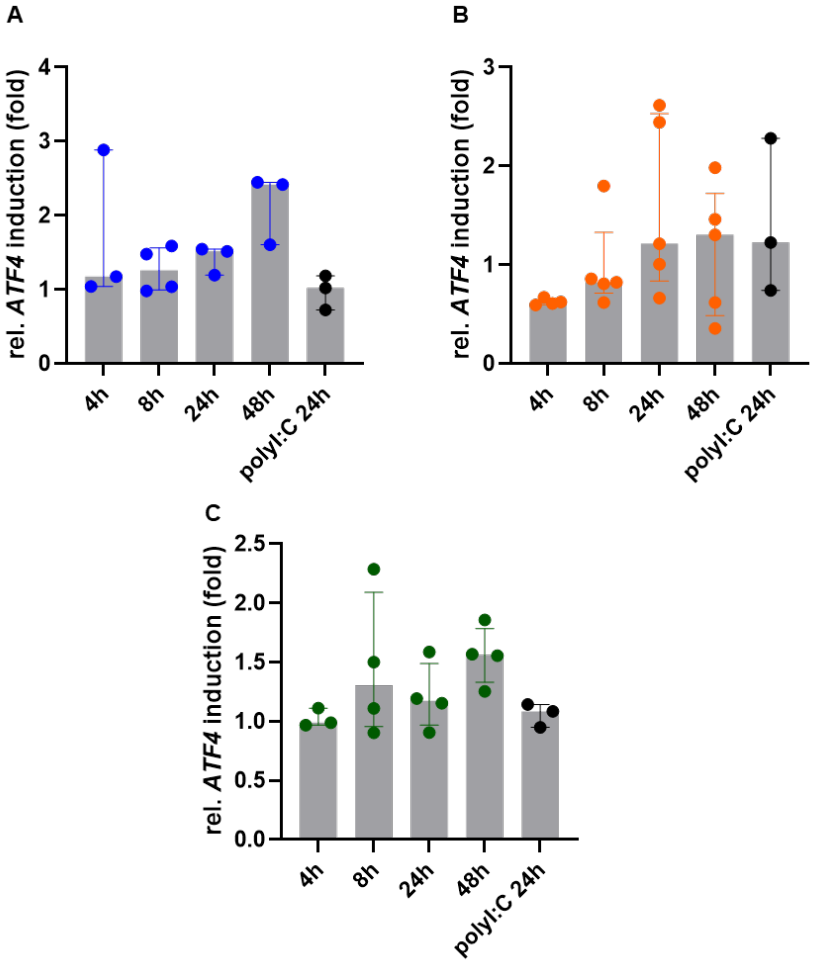

Figure 5.35. *ATF4* levels remain unaltered after rCedV-nTurbo635 infection.
qPCR data of *ATF4* expression in A549 (A), RaNep (B), and SK-6 (C) infected with rCedV-nTurbo635 at MOI 0.1. for 4 h, 8 h, 24 h, and 48 h normalized to the uninfected control. The data show median ± *IQR* of at least 3 independent experiments. Statistical test: Kruskal-Wallis without Dunn's correction. $p < 0.05$ (*), $p < 0.01$(**), $p < 0.001$(***)., $p < 0.0001$(****).

HSP5A transcription increased marginally in A549 and SK-6 at 48 h p.i., whereas it remained steady in RaNep over the 48 h time course of infection (**Figure 5.36**).

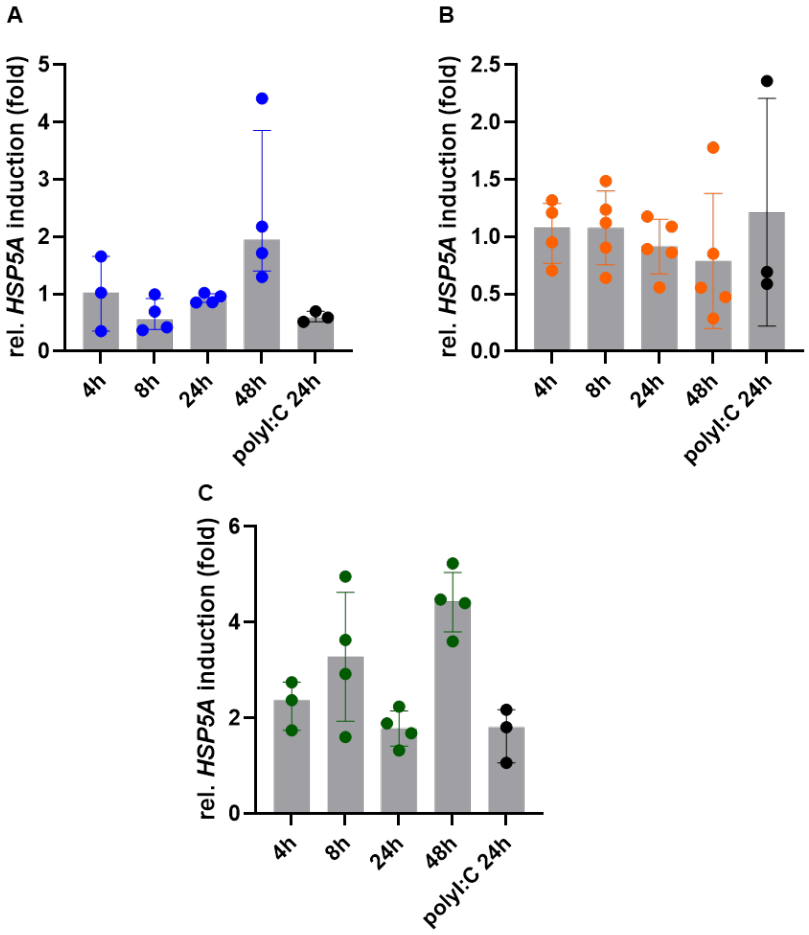

Figure 5.36. *HSP5A* levels remain unaltered in RaNep in response to rCedV-nTurbo635 infection.
qPCR data of *HSP5A* expression in A549 (A), RaNep (B), and SK-6 (C) infected with rCedV-nTurbo635 at MOI 0.1. for 4 h, 8 h, 24 h, and 48 h normalized to the uninfected control. The data show median ± *IQR* of at least 3 independent experiments. Statistical test: Kruskal-Wallis without Dunn's correction. $p < 0.05$ (*), $p < 0.01$(**), $p < 0.001$(***)., $p < 0.0001$(****).

However, *DDIT3* transcripts were significantly induced in all three cell lines, in A549 within the first 24 h p.i and in RaNep and SK-6 at 48 h p.i. (**Figure 5.37**). PolyI:C stimulated samples do not show an increase in any of the measured parameters. Cellular stress is a transient process, therefore 24 h after polyI:C stimulation, the cells could have resolved the ER stress and returned to equilibrium, already.

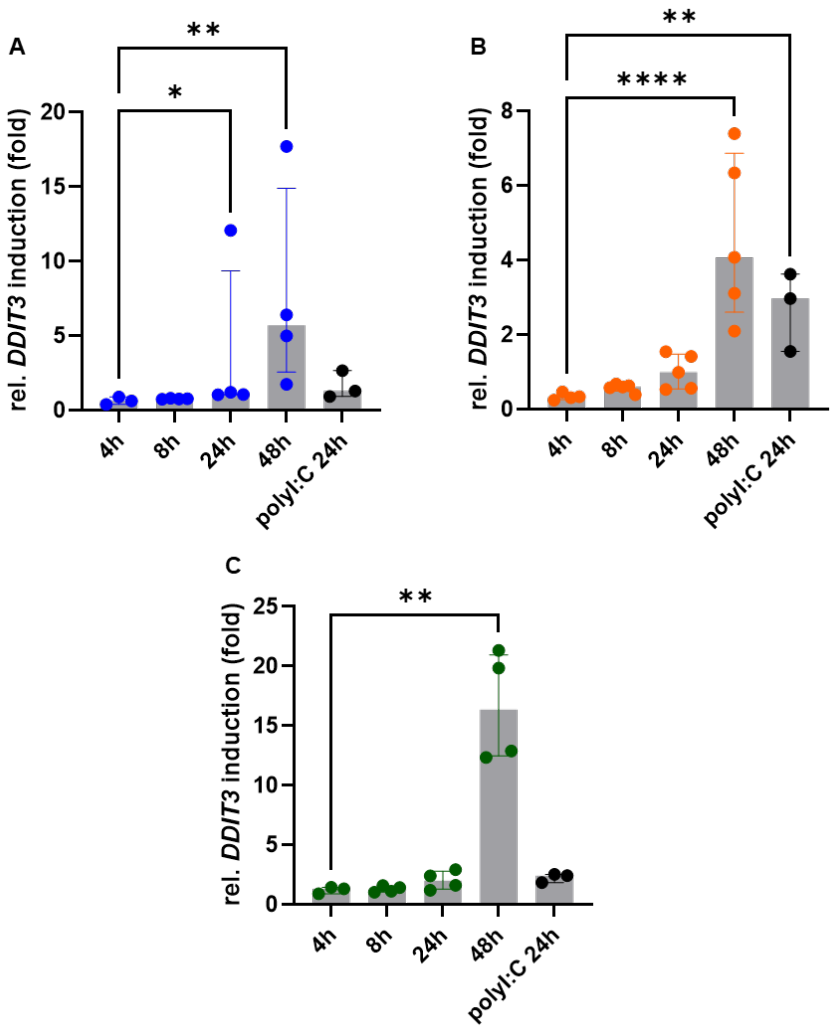

Figure 5.37. *DDIT3* levels increase significantly at 48 h p.i.

qPCR data of *DDIT3* expression in A549 (A), RaNep (B), and SK-6 (C) infected with rCedV-nTurbo635 at MOI 0.1. for 4 h, 8 h, 24 h, and 48 h normalized to the uninfected control. The data show median ± *IQR* of at least 3 independent experiments. Statistical test: Kruskal-Wallis without Dunn's correction. $p < 0.05$ (*), $p < 0.01$(**), $p < 0.001$(***)., $p < 0.0001$(****).

5.5.2. rCedV-nTurbo635 differentially promotes apoptosis

When cell membranes are damaged by cellular stress, toxins, drugs, or viruses, LDH is released into the cell culture supernatant, which can be indirectly quantified in commercially available assays. To assess the cytotoxic potential of rCedV-nTurbo635, A549, RaNep, and SK-6 were seeded in 96-well plates and infected at MOI 1. Cytotoxicity was calculated in relation to a completely lysed positive control and an untreated negative control at 8 h, 24 h, and 48 h p.i. Significant amounts of LDH were only released in RaNep and SK-6 at 48 h p.i., indicating cell death caused by rCedV-nTurbo635 infection (**Figure 5.38**). A549 showed a minor, non-significant increase in LDH release when comparing MOCK and rCedV-nTurbo635-infected samples.

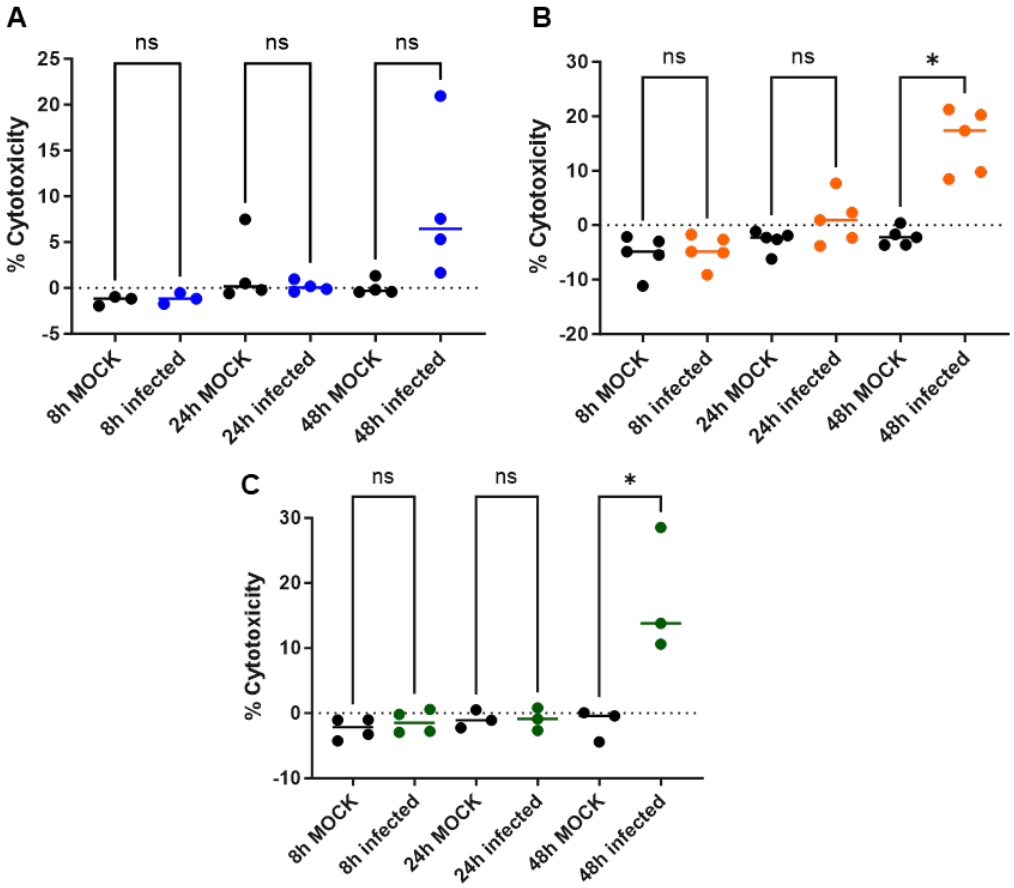

Figure 5.38. rCedV-nTurbo635 infection differentially causes cell death in human, porcine, and bat epithelial cell lines.

LDH release assay of rCedV-nTurbo635 infected A549 (A), RaNep (B), and SK-6 (C) in comparison to MOCK control (black) 8 h, 24 h, and 48 h p.i. Background was subtracted from each measurement, and cytotoxicity was calculated in relation to completely lysed wells (high control). The data show median of at least 3 independent experiments in triplicate. Statistical test: Kruskal-Wallis without Dunn's correction. $p < 0.05$ (*).

Since *DDIT3* induction, as seen before in RT-qPCR, is a hallmark of ER stress induced apoptosis [215,277], we hypothesized that the observed cell death was most likely apoptosis. Both the extrinsic and the intrinsic pathway lead to apoptosis via caspase-3 and -7 cleavage [221,222], which makes it an ideal target to investigate. The three epithelial cell lines were infected with rCedV-nTurbo635 at MOI 0.1, protein samples were prepared from cell lysates at 24 h and 48 h p.i. and Western blot was performed. The lower MOI was chosen, as SK-6 infected at MOI 1 already show substantial cell death at 48 h p.i., which complicates protein sample preparation. Nevertheless, even at MOI 0.1 rCedV-nTurbo635 infection caused caspase-3 cleavage, and thereby activation in SK-6 48 h p.i. (**Figure 5.39**). The resulting amount of the large fragment (17 kDa) was comparable to the positive control (Staurosporine treatment (STSP)), however, in infected samples there was no visible reduction in full-length caspase-3. Cellular poly-(ADP-ribose) polymerase (PARP) is cleaved by active caspase-3 into a large (89 kDa) and a small fragment (not visible in WB) and served here as a second indicator of programmed cell death. SK-6 samples at 48 h p.i. showed a reduction in 116 kDa PARP, which for the other cell lines was merely visible in the STSP treated samples. Cleavage of caspase-3 could not be detected in the A549 samples, but the reduction in full-length caspase-3 in the STSP control was presumably due to cleavage. In RaNep, substantial caspase-3 and PARP cleavage were only induced by STSP treatment, not the infection.

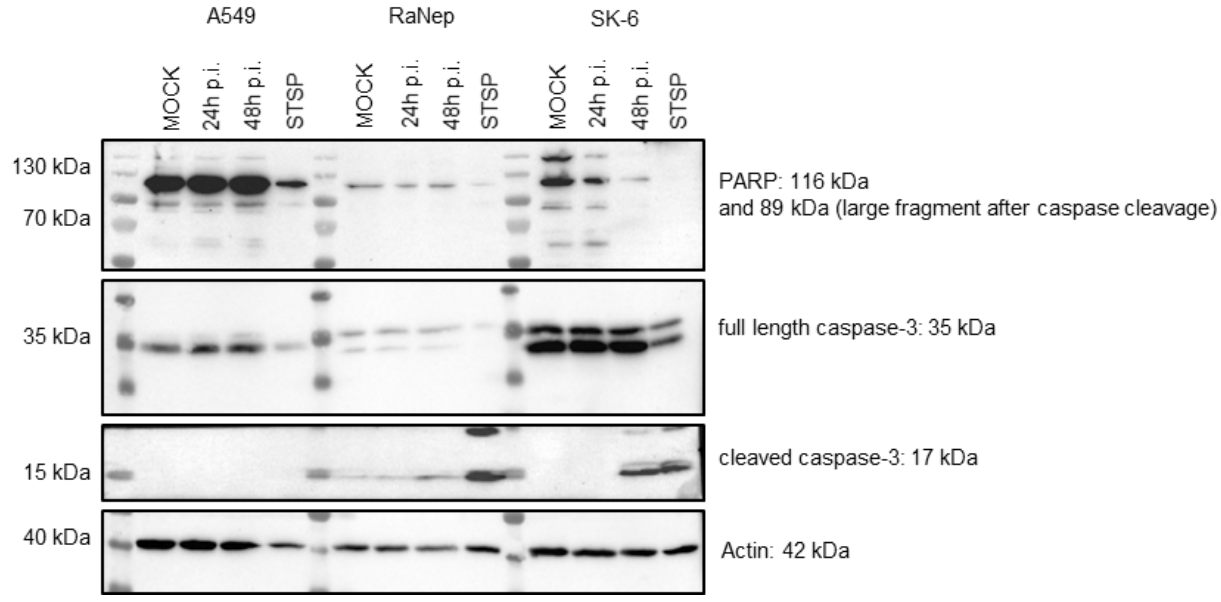

Figure 5.39. rCedV-nTurbo635 infection induces caspase-3 cleavage in SK-6.

Western blot analysis of rCedV-nTurbo635-infected (MOI 0.1) A549, RaNep, and SK-6 at 24 h and 48 h p.i. compared to a MOCK control and 16 h to 24 h Staurosporine (STSP) treatment as a positive control. In addition to caspase-3 cleavage, reduction of full-length caspase-3 and PARP cleavage was measured. B-Actin served as the loading control. Image is representative of 3 independent experiments.

Since the results from this antibody-based approach were not unambiguous, the data were further validated with a probe-based assay, which determines caspase-3/7 activation. To this end, A549, RaNep, and SK-6 were seeded in 96-well plates, infected at MOI 0.1 and after 24 h, respectively, 48 h, they were stained with the green CellEvent™ caspase-3/7 detection reagent. A549 and RaNep were additionally stained with a viability dye, which stains cells with compromised membranes, indicating necrosis. High-content image analysis was performed on fixed cells using the Thermo Scientific CellInsight CX7 (additional information on the protocol can be found in **Supplementary Figure 10.16**). A549 and RaNep exhibited activation of the effector caspases in response to rCedV-nTurbo635 infection to a comparable extent with about 3 % of infected cells stained positive for caspase-3/7 activation 48 h p.i. (**Figure 5.40 A**). In SK-6, on the other hand, 12 % of infected cells showed signs of apoptosis. In comparison, in MOCK-infected cells, caspase-3/-7 staining did not increase with time, as indicated by the total percentage of apoptotic cells (**Figure 5.40 B**). MOCK infected RaNep at 48 h stained positive for caspase-3/7 activation disproportionately often, which might be due to autofluorescence. These false positive results were, however, mitigated by only counting the cells stained for caspase-3/7 activation, which were also infected (**Figure 5.40 A**). Of those A549 and RaNep, which were counted as apoptotic in response to the viral infection, only very few were in late stages of apoptosis 48 h p.i., defined by double positive (caspase-3/7 and Zombie NIR) staining (**Figure 5.40 C, D**). Even though necrosis increased between 24 h and 48 h p.i., only low percentages of infected A549 and RaNep tested positive for necrosis, rendering it a negligible form of cell death in rCedV-nTurbo635 infection.

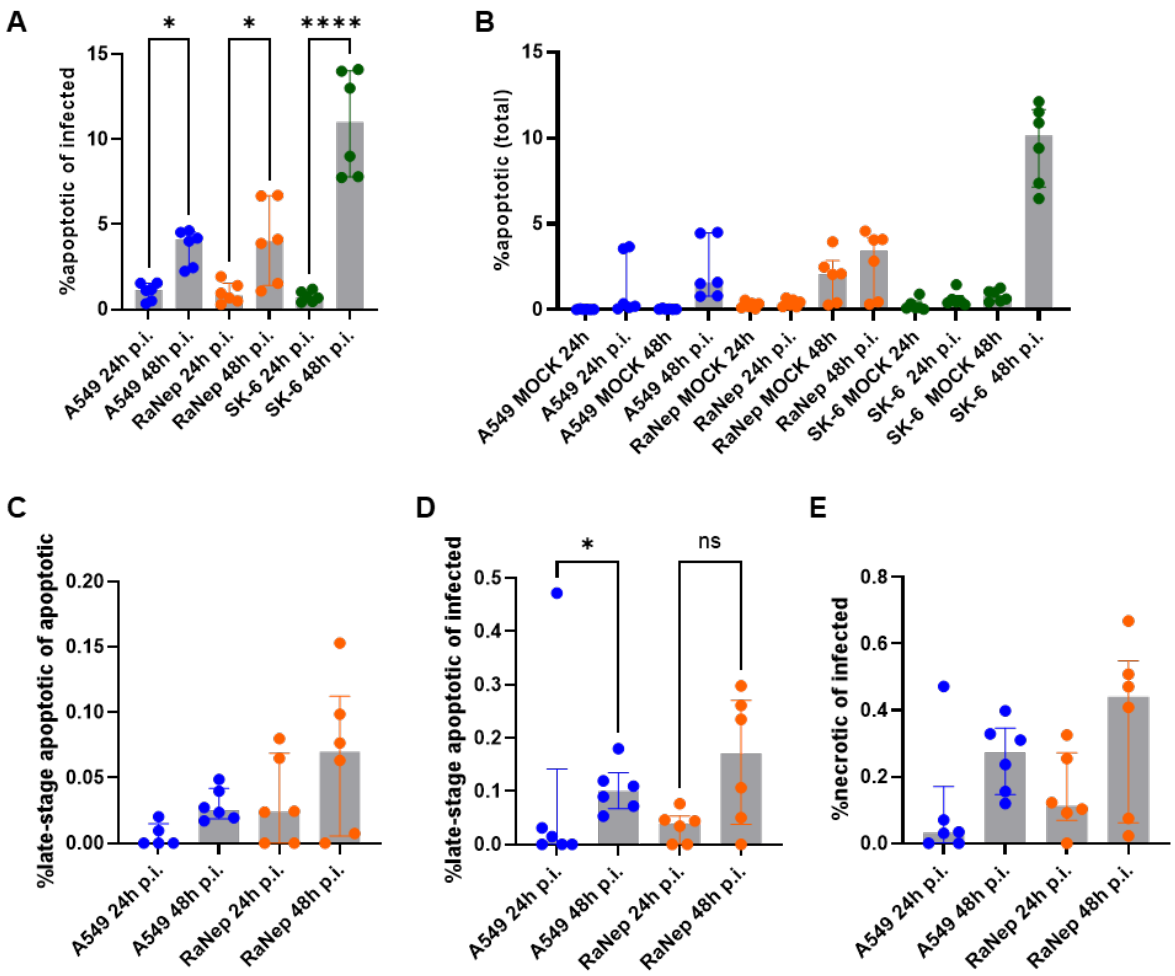

Figure 5.40. rCedV-nTurbo635 infection differentially causes caspase-3/7 activation in epithelial cell lines.
A549, RaNep, and SK-6 were seeded in 96-well plates, infected at MOI 0.1, and stained using a green caspase-3/7 activity-based dye (CellEvent™ Caspase-3/7 detection reagent) 24 h/ 48 h p.i. A549 and RaNep were additionally stained with a viability dye (Zombie NIR) to distinguish late-stage apoptotic and necrotic cells. Then the cells were fixed in 4% PFA. Image acquisition and data analysis was done using the CellInsight CX7 high-content microscopy platform.

(A) Percentage: caspase-3/7 positive (= apoptotic) of infected cells.

(B) Percentage: apoptotic cells of all counted cells.

(C) Percentage: late-stage apoptotic (double positive for caspase-3/7 and Zombie NIR staining) of all infected, apoptotic cells. One outlier value for A549 at 24 h p.i. is not depicted.

(D) Percentage: late-stage apoptotic of all infected cells

(E) Percentage necrotic of all infected cells.

The data show median ± *IQR* of 3 independent experiments in duplicate. Statistical test: Kruskal-Wallis without Dunn's correction. $p < 0.05$ (*), $p < 0.01$(**), $p < 0.001$(***), $p < 0.0001$(****).

SK-6 detached from the cell culture plates in response to the viability dye staining; therefore, no data are available on the significance of necrosis or late-stage apoptosis in those cells. rCedV-nTurbo635 infection caused apoptosis in RaNep and A549, but highest percentages of affected cells were observed in SK-6.

5.6. Generation and characterization of primary ERB lung endothelia-like cells (PELENDO) to assess endothelial barrier damage in response to rCedV-nTurbo635 infection

Since NiV/HeV pathogenicity and disease symptoms are closely linked to their ability to infect endothelial cells in various organs and disrupt the endothelial cell barrier [4,75], one aim of this project was to investigate the effect of CedV infection on ERB-derived endothelial cells. To this end, primary ERB lung endothelia-like cells (PELENDO) were generated from the lung tissue of three healthy adult ERB and cultivated in collagen-coated flasks using endothelial cell medium.

5.6.1. PELENDO display endothelial cell characteristics

Endothelial cell characteristics were assessed by microscopy, (RT-q)PCR, Von Willebrand factor (VWF) expression in immunofluorescence and evidence of Weibel-Palade bodies (WPB) in transmission electron microscopy (TEM). PELENDO grew in a monolayer and exhibited contact-dependent growth inhibition (**Figure 5.41**). Some capillary-like structures could be observed (arrow). PELENDO were cuboid shaped and showed in some cell aggregations the typical endothelial “cobblestone” morphology (arrowhead). As none of the single-cell dilutions were successful, each primary cell preparation most likely contained a mixture of ERB lung derived cells.

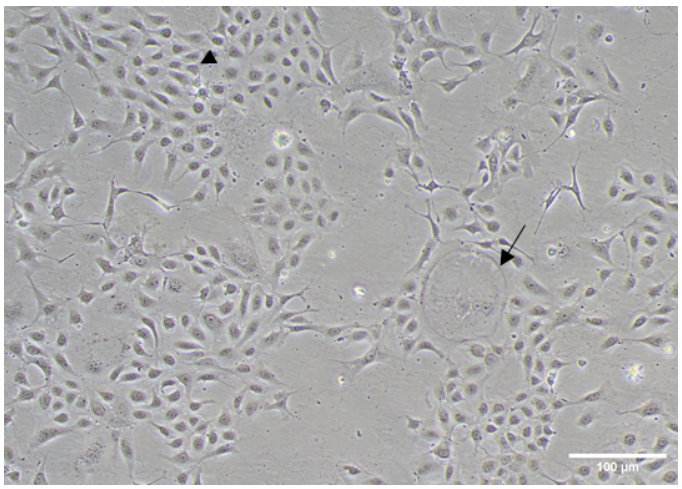

Figure 5.41. PELENDO display typical endothelial cell characteristics in culture.
Primary ERB lung endothelia-like cells (PELENDO) were grown in collagen-coated flasks in endothelial cell medium. PELENDO displayed “cobblestone” morphology (arrowhead) and formation of vascular-like structures (arrow) in culture. Image was taken using the 10X objective on a Nikon Eclipse microscope. Scale bar: 100 µm.

Expression of typical endothelial cell markers, Cadherin 5 (*CDH5*)/VE-Cadherin and vascular endothelial growth factor receptor 2 (*VEGFR2*) [278] , was assessed using RT-qPCR and conventional PCR (**Figure 5.42 A, B**). Additionally, ephrin expression in PELENDO was quantified relative to the housekeeping gene EEF1A1 to assess susceptibility to CedV infection (**Figure 5.42 A**). ERB ephrins B1, B2, and to a lower extent, A5 can mediate CedV entry [237], all of which were expressed in comparably high levels in PELENDO.

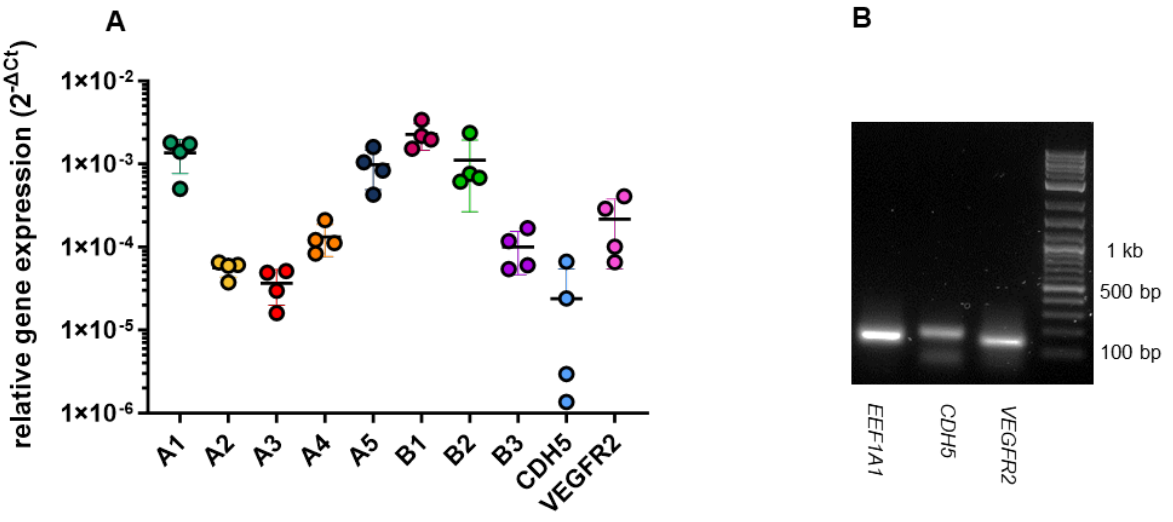

Figure 5.42. PELENDO express CedV entry receptors ephrin B1 and B2 alongside endothelial cell markers.

(A) RT-qPCR data show ephrin expression levels and endothelial cell markers *CDH5* and *VEGFR2* relative to the housekeeping gene *EEF1A1*. Plotted are mean ± *SD.*

(B) Agarose gel showing the expression of *CDH5* and *VEGFR2* next to the housekeeping gene *EEF1A1*.

To further characterize PELENDO, cells were stained with anti-human CD31 (PECAM-1) and CD34 (hematopoietic progenitor cell antigen) antibodies, which unfortunately did not cross-react with ERB target antigens. Low passages of PELENDO expressed Von Willebrand factor (VWF), which is essential for hemostasis and is stored in Weibel-Palade bodies in the intima of blood vessels (**Figure 5.43**) [279–281]. It is worth noting that not all PELENDO preparations tested positive for VWF staining, and those that did lost the expression within a few passages. For comparison, ERB lung epithelial cells (PELEPI) served as a negative control for VWF expression and as a positive control for the epithelial cell marker, cytokeratin [282]. PELENDO, on the other hand, did not express cytokeratin.

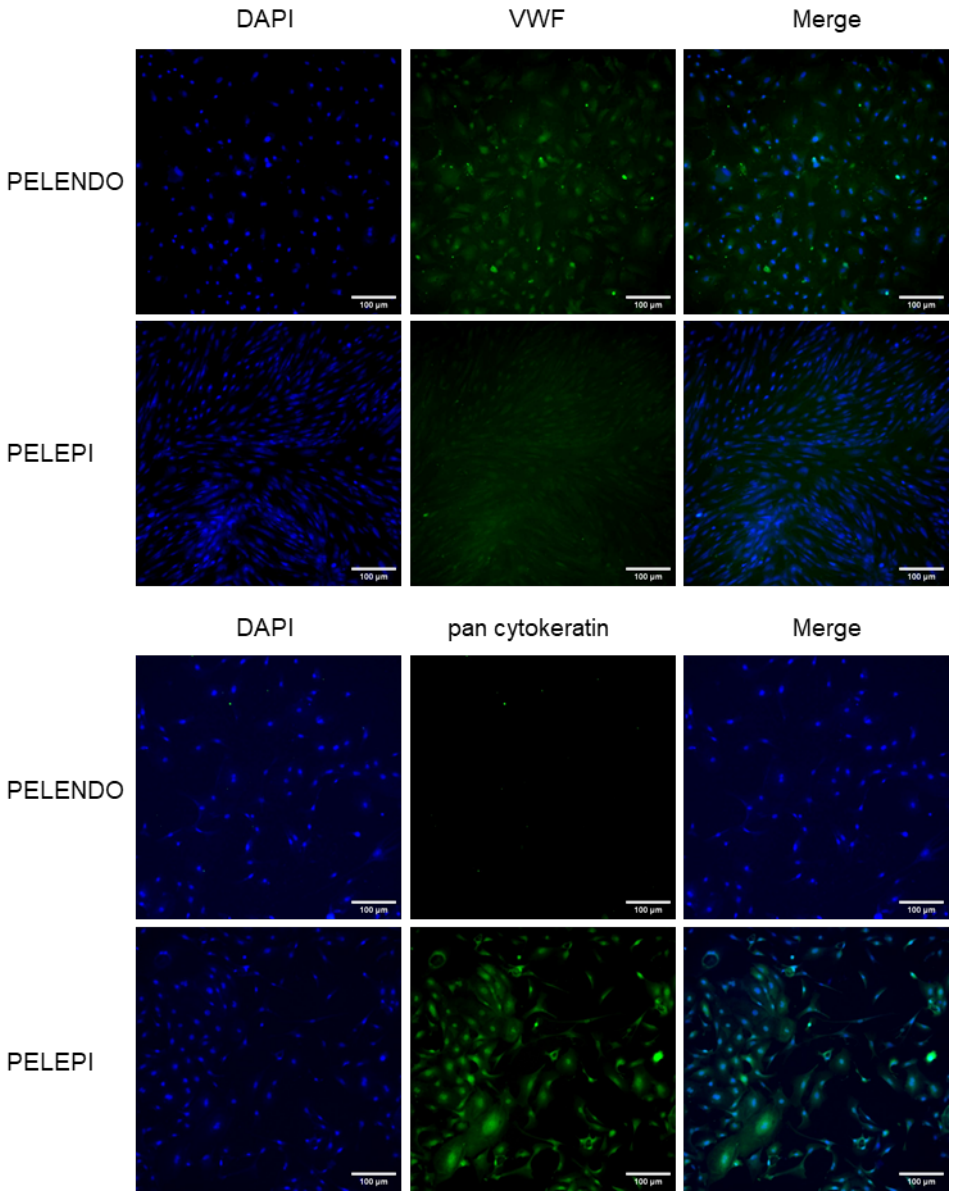

Figure 5.43. PELENDO express low levels of Von Willebrand factor (VWF) and no cytokeratin.
Immunofluorescence images of PELENDO and PELEPI. Cells were fixed in 4% PFA and incubated with the α-Von-Willebrand-factor/α-pan-cytokeratin antibody overnight. The α-pan-cytokeratin antibody is FITC-labelled, and a FITC-conjugated α-rabbit IgG antibody was used for visualizing VWF. Images were captured with the CX7, and brightness/contrast adjustments were performed in ImageJ. Scale bar: 100 µm.

To validate the cross-reactivity of the anti-human-VWF antibody, used for immunofluorescence, immunohistochemistry (IHC) was performed on ERB lung slices, which displayed specific staining for the intima of blood vessels (**Figure 5.44**).

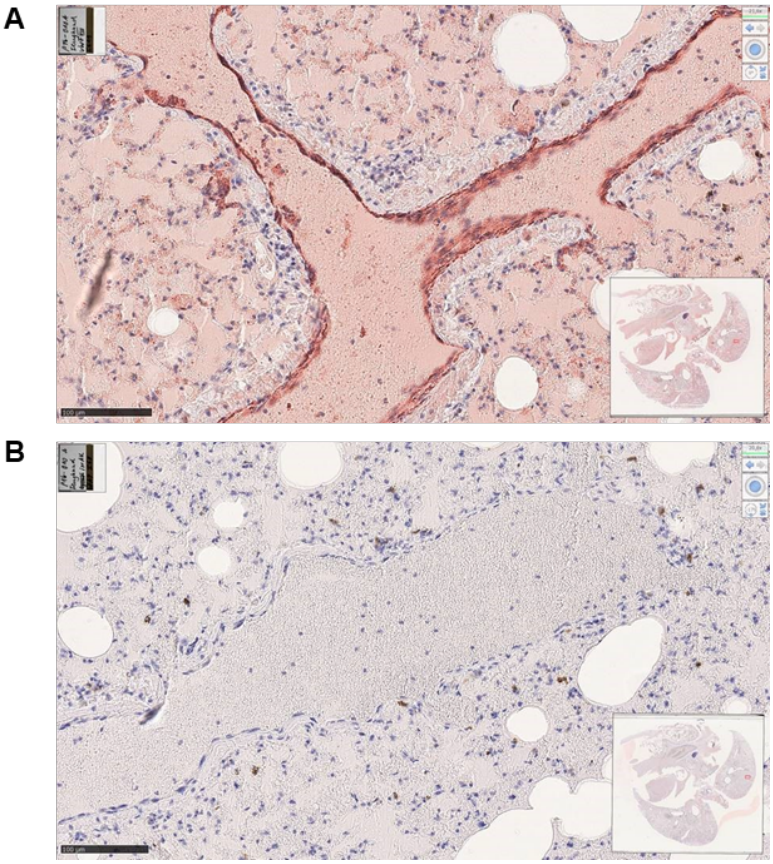

Figure 5.44. Anti-Von-Willebrand-factor antibody specifically binds to ERB lung blood vessel endothelium.

Immunohistochemistry (IHC) of ERB lung tissue. ERB lung tissue was embedded in paraffin and incubated with an anti-von-Willebrand-factor antibody (1:200) overnight (A). The control (B) was only incubated with the secondary α-rabbit antibody. IHC was performed by Silvia Schuparis (ATB).

Given the expression of VWF in PELENDO, WPB formation was to be determined in electron microscopy. WPBs are formed in the Golgi apparatus and store VWF in tubules. These tubules appear as striations when WPBs are viewed in longitudinal sections under transmission electron microscopy, or as dots in cross-sections [279,280,283]. PELENDO displayed WPB-like structures (**Figure 5.45, arrows**), characterized by tightly packed tubules in a less dense matrix, enclosed by a lipid bilayer [280,284].

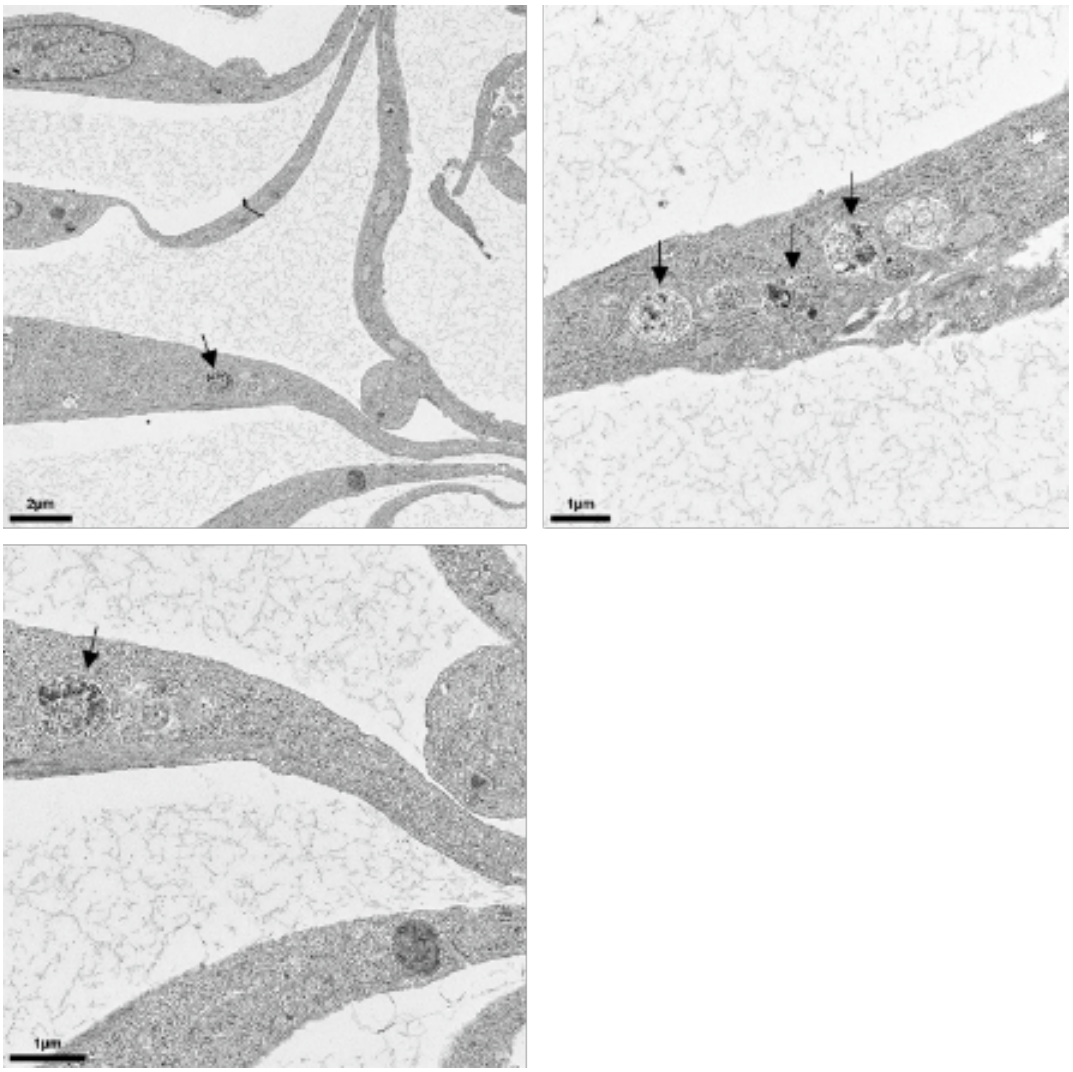

Figure 5.45. PELENDO produce Weibel Palade body-like structures in low passage numbers.
Transmission electron microscopy images were taken of PELENDO (animal 2, passage 3). Multiple Weibel-Palade body-like structures, characterized as tubules, surrounded by a less dense matrix, encapsidated by a membrane, are visible in the cytosol (arrows). Electron microscopy was performed using a Talos F200i (Thermofisher Scientific) and images were taken with a digital camera (Ceta, 16 MP, Software Velox). Scale bar: 2 µm (A), 1 µm (B, C). Sample acquisition and analysis was done by Dr. Kati Franzke.

Notably, the WPBs in PELENDO, measuring approximately 1 µm in diameter, were significantly larger than those found in human and rat endothelial cells, which have been reported to range from 1-5 µm in length and 0.1-0.3 µm in width in previous studies [280,284].

Species identification by cytochrome c oxidase 1 barcoding (*CO1* barcoding) from genomic DNA was performed to exclude contamination with other cell lines, kept in the lab (**Figure 5.46**).

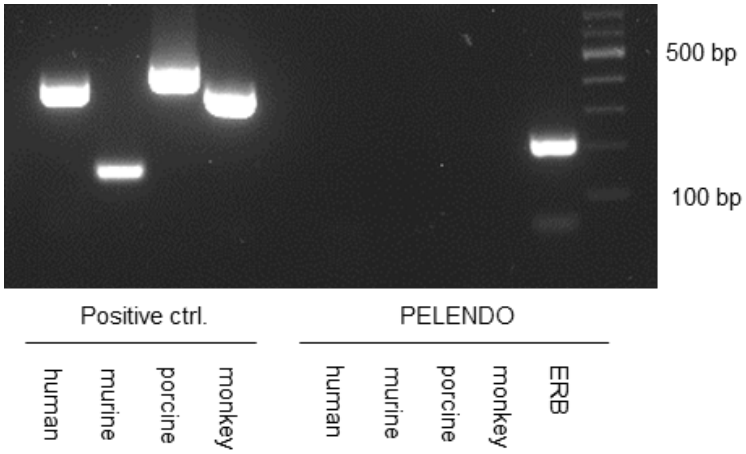

Figure 5.46. PELENDO are of ERB origin.

Agarose gel of *CO1* barcoding PCR for species identification established by Cooper *et al* [241]. Lanes 1-4 show positive controls for species, from which cells were cultivated in the lab at the same time. Lanes 6-10 contain PELENDO genomic DNA samples run with the species-specific primer sets. Amplicon sizes: human: 390 bp, pig: 460 bp, mouse: 150 bp, Tamarin monkey: 400 bp, ERB: 250 bp

In all, PELENDO were demonstrated to originate from ERB tissue and displayed typical endothelia-like characteristics, which made them a suitable model to proceed with rCedV-nTurbo635 infection.

5.6.2. PELENDO are susceptible to infection and undergo apoptosis in response to rCedV-nTurbo635 infection

As PELENDO express the necessary receptors for rCedV infection, ephrin B1 and B2 (**Figure 5.42**), and cells were generally susceptible to rCedV-nTurbo635 infection (**Supplementary Figure 10.17**), further experiments regarding the susceptibility and response to infection were performed. To this end, PELENDO were seeded in 96-well plates and infected at MOI 0.5 (as determined on RaNep). At 24 h and 48 h p.i., plates were stained with the CellEvent reagent, which is activated through cleavage by active caspase-3/7, thereby indicating apoptosis. Infection rates and apoptosis in response to rCedV-nTurbo635 infection were determined for PELENDO preparations derived from two different donor animals using the CellInsight CX7 high-content screening platform. After 24 h, infected PELENDO exhibited significantly more

apoptosis than the MOCK-infected wells (**Figure 5.47 B**) and, within an additional 24 h, apoptosis rates increased to approximately 9% (**Figure 5.47 A**).

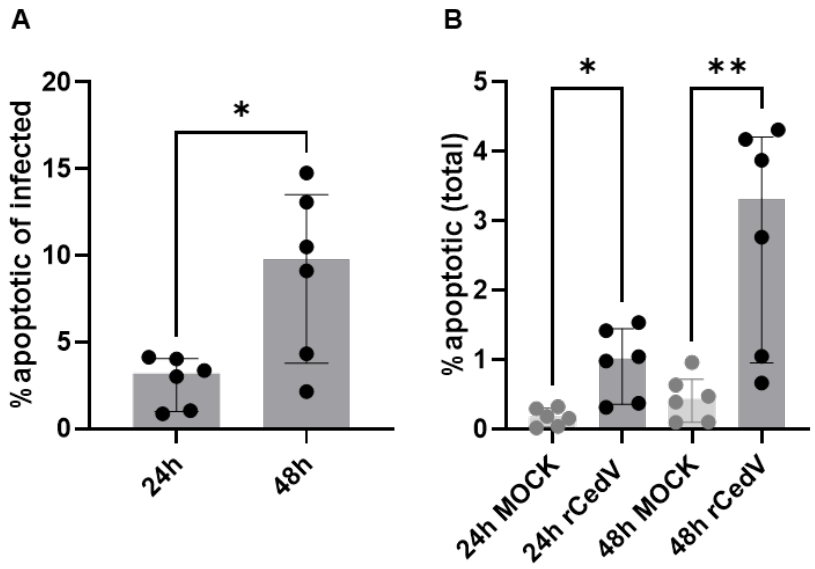

Figure 5.47. Significant caspase-3/7 activation in PELENDO in response to rCedV-nTurbo635 infection.
PELENDO were infected at MOI 0.5 and stained using the green caspase-3/7 activity-based dye (CellEvent™ Caspase-3/7 detection reagent) at 24 h/ 48 h p.i. Cells were fixed in 4% PFA. Image acquisition and data analysis were done using the CellInsight CX7 high-content microscopy platform.
(A) Percentage: caspase-3/7 positive (= apoptotic) of infected cells.
(B) Percentage: apoptotic of all counted cells.
Data stem from 2 independent experiments, each performed in duplicate. Plotted are median ± *IQR*. Statistical test: A: Mann-Whitney, B: Kruskal-Wallis without Dunn's correction. $p < 0.05$ (*), $p < 0.01$(**).

As PELENDO were most likely a mixture of ERB lung-derived primary cells that were differentiated using endothelial cell medium, differences occurred between donor animals and preparations. Apoptosis induction was markedly higher for PELENDO, originating from animal 2 (**Figure 5.48**).

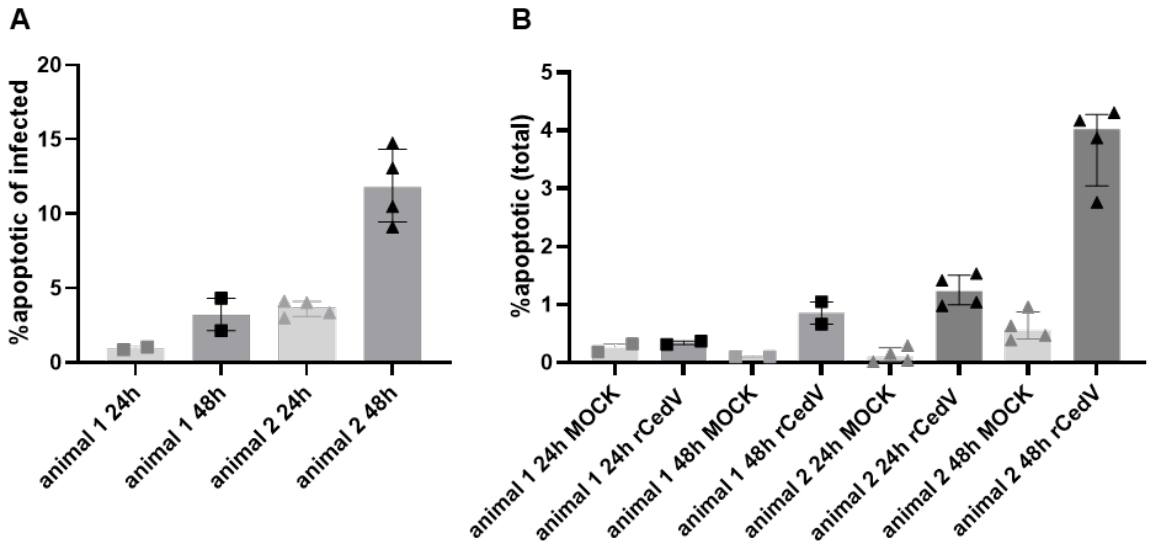

Figure 5.48. Apoptosis rates differ between animal 1 and 2.

PELENDO were seeded in 96-well plates, infected at MOI 0.5 (as titrated on RaNep) and stained using the green caspase-3/7 activity-based dye (CellEvent™ Caspase-3/7 detection reagent) at 24 h/ 48 h p.i. Cells were fixed in 4% PFA, image acquisition and data analysis were done using the CellInsight CX7 high-content microscopy platform. Data stem from 2 independent experiments, performed in duplicate. Individual data points are depicted as squares (animal 1) or triangles (animal 2). Plotted are median ± *IQR*.

(A) Percentage: caspase-3/7 positive (= apoptotic) of infected cells.

(B) Percentage: apoptotic of all counted cells.

Even though visual assessment did not expose substantial differences in infection rates between 24 h and 48 h p.i. (**Figure 5.49 A**), quantitative analysis showed a reduction of infected cells (**Figure 5.49 B**). This decrease in infection rate was accompanied by fewer cells counted in the automated image analysis (**Figure 5.49 C**). While cell numbers in MOCK-infected wells increased substantially, infected wells experienced either attenuated growth or loss of infected cells, which could explain decreasing infection rates.

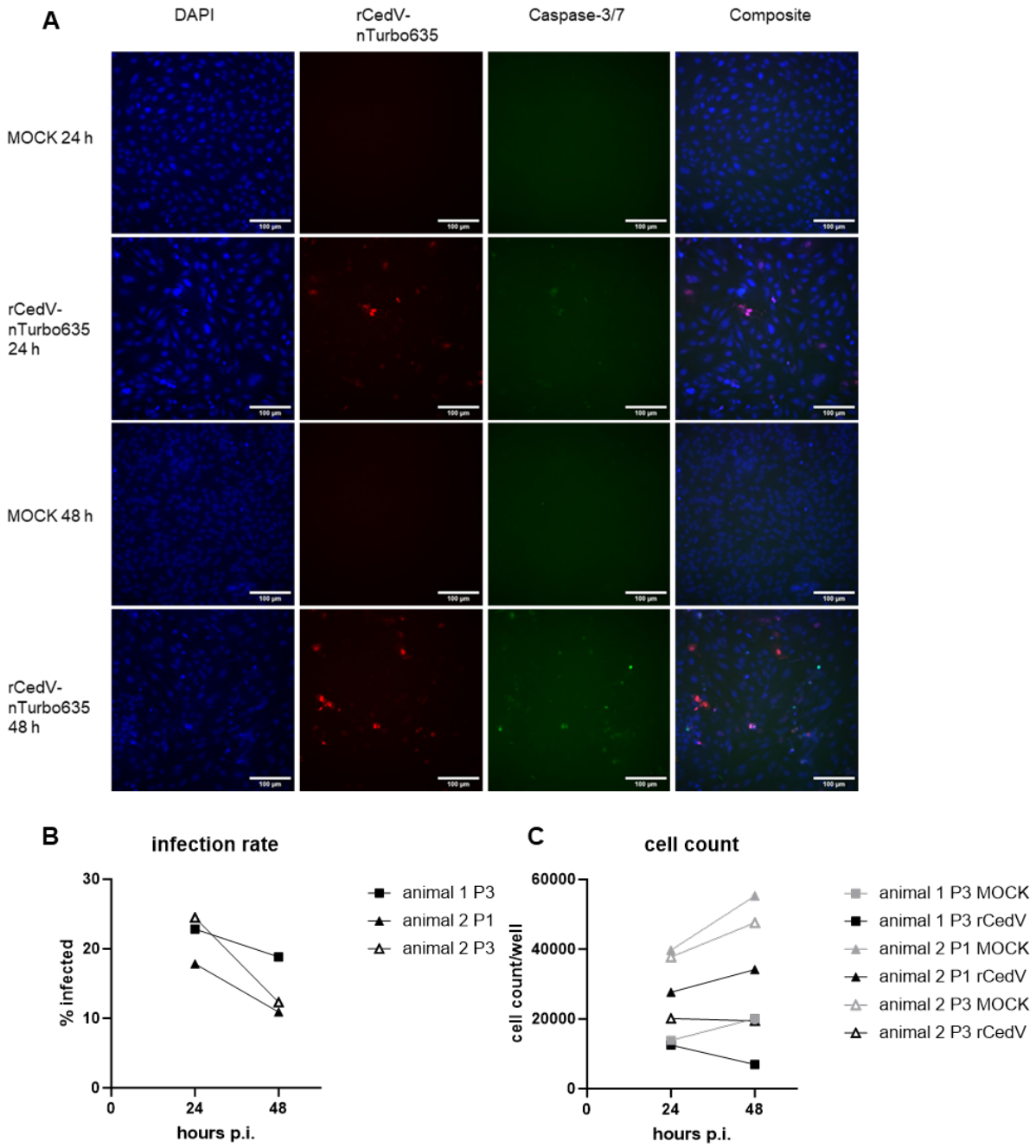

Figure 5.49. Infection rate of PELENDO decreases with time.

PELENDO were seeded in 96-well plates, infected at MOI 0.5, and stained using the green caspase-3/7 activity-based dye at 24 h/ 48 h p.i. Cells were fixed in 4% PFA. Image acquisition and brightness adjustments were done using the CellInsight CX7 high-content microscopy platform and images were colorized using Image J (A). Scale bar: 100 µm.

(B) Infection rate in percent.

(C) Cell count per well.

Individual data points are depicted as squares (animal 1) or triangles (animal 2).

Overall, PELENDO were susceptible to rCedV-nTurbo635 infection, with a small percentage of cells beginning to undergo apoptosis at 24 h p.i. While apoptosis rates increased within 48 h p.i., compared to the MOCK control, infection rates decreased after 24 h.

5.7. Original CedV WT isolate infections *in vitro* and *in vivo*

Since CedV was first isolated from *Pteropus* bats in Australia, the original wildtype isolate (CedV WT) is restricted to the high-containment area (BSL-4) [6]. Accordingly, experiments using the original isolate are elaborate and rare. Here, we have expanded the significance of our previous findings by including data generated at the BSL-4 facilities at the FLI. Infection experiments in the BSL-4 area were conducted by Dr. Sandra Diederich, all subsequent experiments and data analysis was done by the author.

5.7.1. CedV WT replicates to similar titers on A549 and RaNep

RaNep and A549 were infected with CedV WT, respectively Nipah virus Malaysia (NiV-M) for comparison, at MOI 0.1 and viral RNA copy numbers in the supernatants were determined by RT-qPCR. In accordance with previous publications on experimental NiV infections of ERB and ERB derived cell lines [45], RaNep did not support NiV replication, whereas in A549, NiV RNA copies increased by approximately 256-fold within 48 h (**Figure 5.50 A**). CedV WT replication was comparable in A549 and RaNep with a difference of about 8-9 Ct values within the first 48 h (**Figure 5.50 B**), even though CedV WT infection of ERB *in vivo* was not successful, as reported [44]. It is important to keep in mind, that the RT-qPCR measures viral RNA copies, which does not automatically translate to infectious viral particles produced. Nonetheless, CedV WT seemingly replicated on both A549 and RaNep, whereas NiV-M RNA copy numbers only increased in A549.

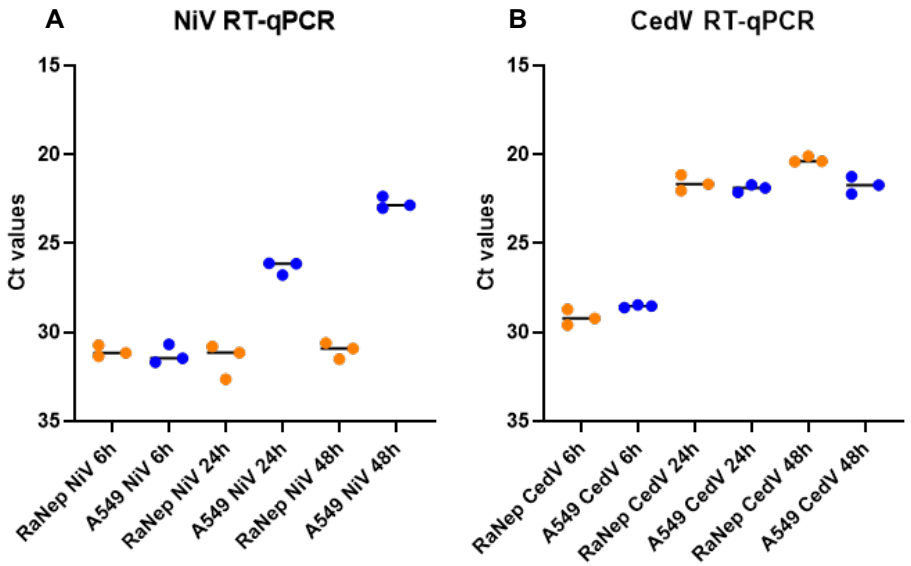

Figure 5.50. NiV-M and CedV WT replication are similar in A549, whereas RaNep only support CedV WT replication.

RT-qPCR results of NiV-M (A) and CedV WT (B) replication in A549 and RaNep. The cells were infected at MOI 0.1 in the BSL-4 lab by Dr. Sandra Diederich and the supernatants (6 h, 24 h, and 48 h p.i.) were transferred to the BSL-2 area for RNA extraction and RT-qPCR (performed by the author). RT-qPCR was run according to the protocols published by Mohl *et al.* [44] and Feldman *et al.* [246]. The data show median of 3 biological replicates. Each sample was tested in duplicate.

As expected, syncytia formed in A549 in response to NiV-M infection (**Figure 5.51 A**), however, no obvious morphological changes occurred in those cells in spite of CedV WT replication. RaNep, on the other hand, reacted to CedV WT infection with substantial cell death (**Figure 5.51 B**), but did not exhibit any syncytia formation in response to NiV-M infection.

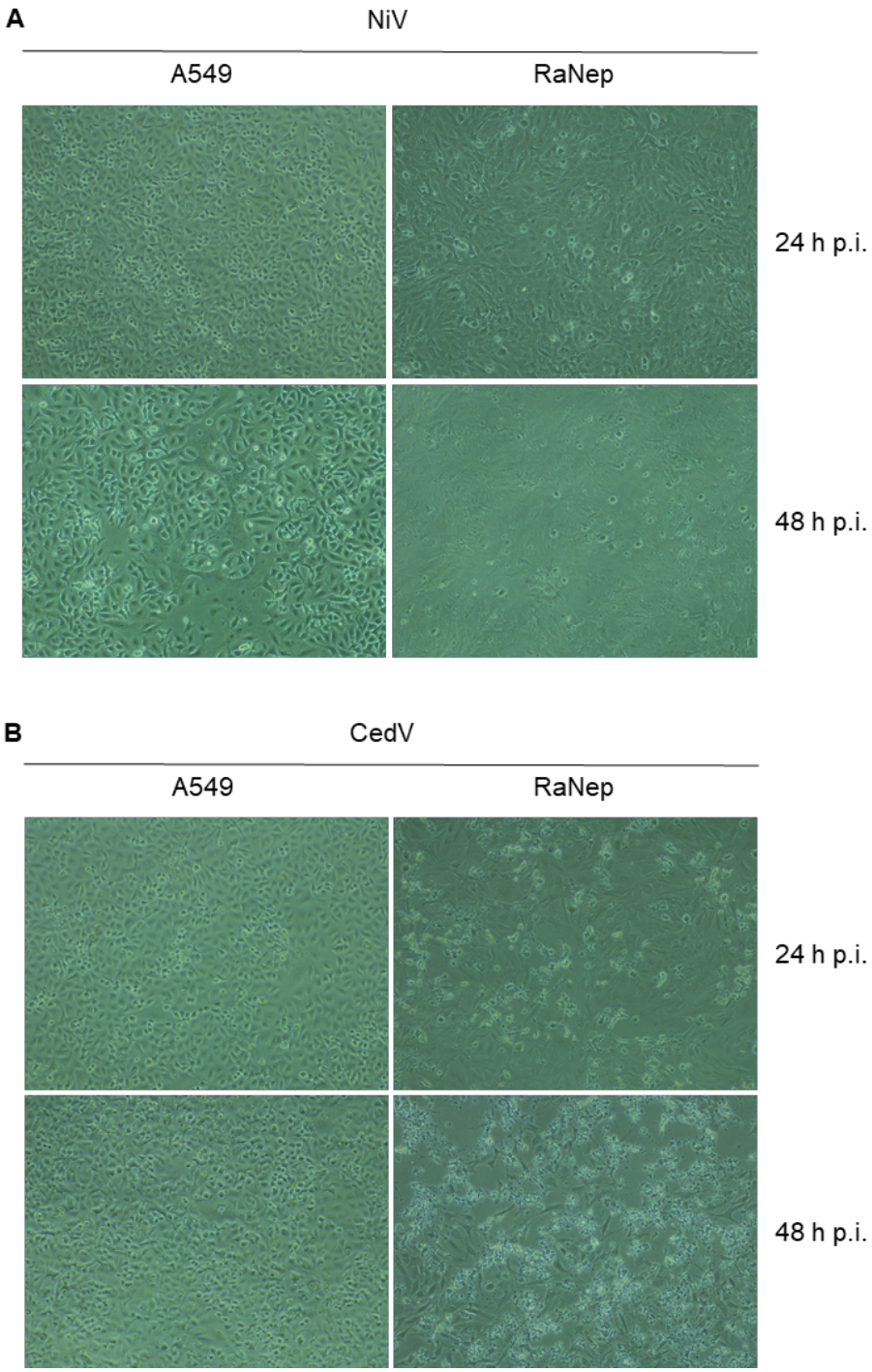

Figure 5.51. CedV WT infection causes cell death in RaNep.

Bright field images of A549 and RaNep infected with NiV-M (A) and CedV WT (B) at MOI 0.1 at 24 h/ 48 h p.i. Images were taken by Dr. Sandra Diederich in the BSL-4 lab on a Nikon Eclipse TS100 (10X objective).

5.7.2. IFN induction in upper respiratory tract of ERB in response to CedV WT infection *in vivo*

Next to the published study, investigating the susceptibility of ERB to CedV WT infection [44], our aim was to asses early IFN responses to CedV WT in different organs of ERB. After intranasal infection at 8 x 10^4 PFU (plaque forming units) per animal, none of the bats showed clinical signs, shed virus or seroconverted [44], indicating that ERB were either refractory to the infection or the mode and route of infection were not optimal. Nonetheless, one animal euthanized on day 6 p.i. showed a trend towards *IFNL* upregulation in the respiratory tract (**Figure 5.52**).

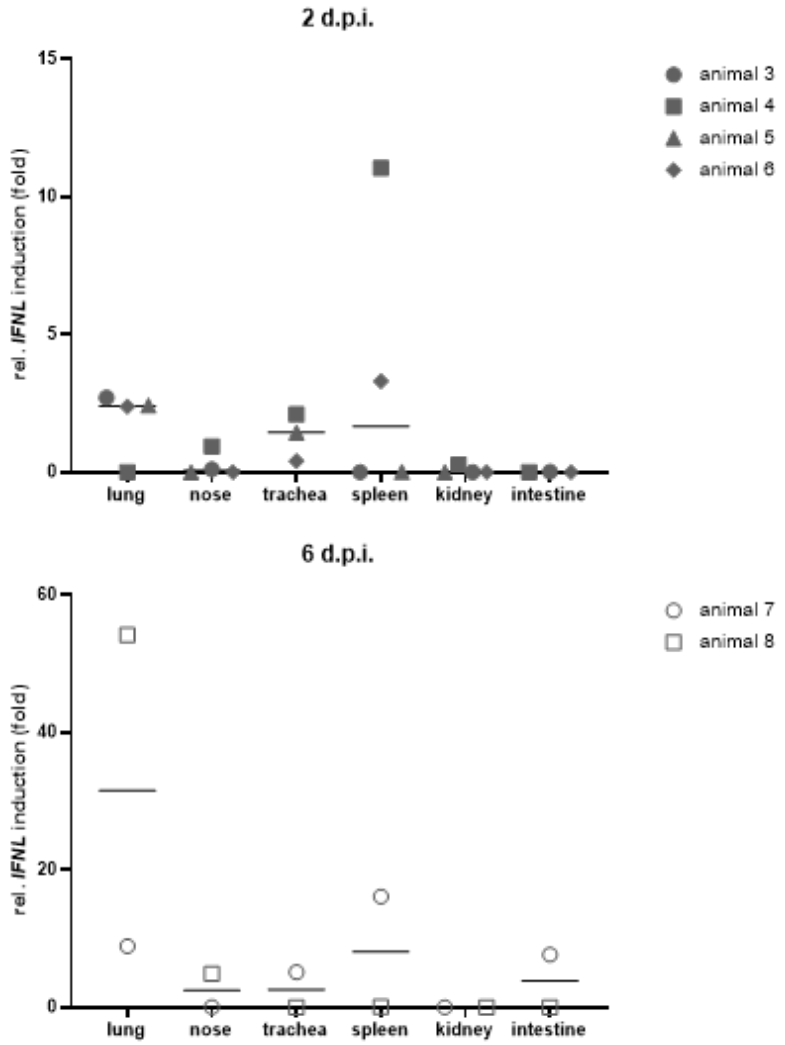

Figure 5.52. Indications of *IFNL* induction in the upper respiratory tract of one ERB in response to CedV WT infection.

RT-qPCR results of *IFNL* induction in ERB organ samples, 2 and 6 days p.i. normalized to the uninfected control. Graphs show median and all available data points. 4 animals were euthanized 2 d.p.i. and 2 animals were euthanized 6 d.p.i.

On the other hand, *IFNB* was induced 2 d.p.i. in nose and trachea, compared to the MOCK-infected bats (**Figure 5.53**). Only one of the infected bats tested positive for viral RNA in the kidneys, which is consistent with low *IFNB* and *IFNL* levels in all but one sample.

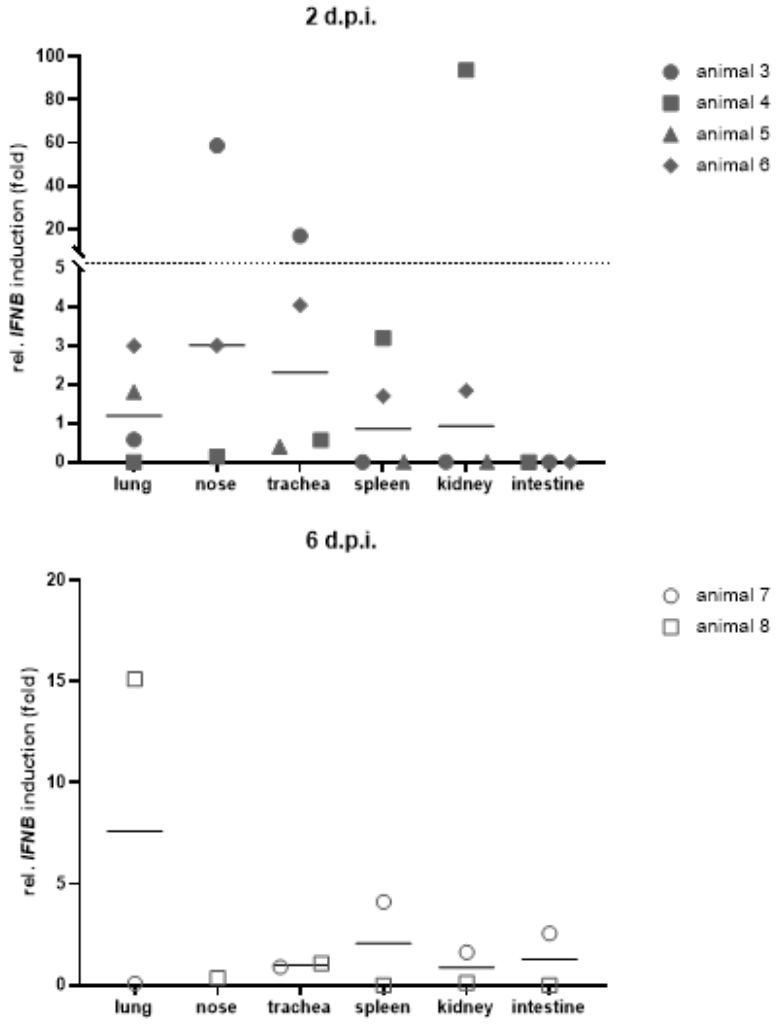

Figure 5.53. Indications of *IFNB* induction in the upper respiratory tract of ERB in response to WT CedV infection.

RT-qPCR results of *IFNB* induction in ERB organ samples, 2 and 6 days p.i. normalized to the uninfected control. Graphs show median and all available data points. 4 animals were euthanized 2 d.p.i. and 2 animals were euthanized 6 d.p.i.

The group sizes were too small to reach significance in any of the measured parameters. Future studies will evaluate, whether alternative routes of infection lead to establishment of a productive infection.

6. Discussion

Most emerging human diseases are zoonoses, and among those, RNA viruses predominate as causative agents, by far [285–289]. As humans encroach on previously undisturbed natural areas and growing overlaps between human and wildlife territories, the risk of spillover events is increasing constantly [287,289–291]. Bats (Chiroptera) and rodents stand out as orders that harbor a disproportionate number of zoonotic viruses, which have either already caused outbreaks and epidemics or have the potential for spillover [286,292]. Bats are reservoir hosts for coronaviruses [293], filoviruses (such as MARV) [88,89], henipaviruses (e.g., HeV/NiV) [26,28], lyssaviruses [294,295] , and many other pathogens [292]. Characterizing viruses that originated from important reservoir species, regarding susceptibility of potential host species, their tissue tropism, and induced immune responses, is an essential task within the scope of emergency preparedness. This project examines host cell entry, elicited innate immune responses, and cell death upon CedV infection, thereby contributing to the field of henipavirus research in general. The knowledge gained here provides deeper insight into host-pathogen interactions during henipavirus infections, laying the foundation for more application-oriented research.

6.1. CedV entry via ERB ephrins: consequences for tissue tropism and reservoir potential

HeV and NiV enter cells via the Eph-receptor ligands, ephrin B2 and B3 [66–68]. In contrast, CedV G protein attaches to ephrin B1 and B2 to enter human cells, and it additionally shows a marginal binding affinity for ephrin A2 and A5 [9,11,296]. Since ephrins are highly conserved among vertebrates, henipaviruses potentially have a very broad host range [81,297]. CedV originates from black flying foxes (*P. alecto*), and henipavirus sequences with the highest similarity to CedV have been found in ERB [6,42]. In this work, ERB cells were shown to be susceptible to rCedV-nTurbo635 infection, and viral entry was mediated by ERB ephrin B1 and B2. Contrary to studies on human ephrins [9], CedV entry was not observed via ERB ephrin A2, and ephrin A5 usage was only detected by flow cytometry experiments with prolonged infection times. This discrepancy in results could be due to differences in the expression levels of the ERB ephrins, which was accounted for by analyzing large cell quantities in flow cytometry and high-content microscopy. However, a more recent study also questions the importance of A ephrins as relevant CedV receptors [296]. The findings from artificially expressed ERB ephrins were additionally validated by knocking down ephrin B2 and B1/B2 expression in an immortalized ERB cell line, which led to a significant decrease in infection rates. Unfortunately, the establishment of RaNep single ephrin B1 knockdown cells was not successful, which limits

the informative value as to which B ephrin can be considered the major CedV receptor. Since the receptor binding domains of *P. alecto* and ERB ephrins proved to be almost identical, entry receptors discussed for ERB, most likely apply to *P. alecto*, the CedV reservoir, as well.

The abundance and tissue distribution of viral receptors significantly influence disease outcome and virus spread. The ability of HeV and NiV to utilize ephrin B3 for cell entry has been linked to disease-determining pathology, such as vasculitis, endothelial barrier damage, and encephalitis [4,75]. However, the difference between severe neurological symptoms seen in NiV/HeV patients and the non-pathogenic CedV cannot be solely attributed to the usage of ephrin B3 vs. ephrin B1, as many ephrins, especially ephrin B2, are also expressed in certain parts of the adult brain [76,298–300]. Along those lines, Dufloo *et al.* report similar and overlapping tissue preferences for NiV and CedV pseudotypes [296]. From ERB nose epithelium-derived RaNep, as well as ERB endothelia-like cells, expressed high levels of ephrin B1 and B2, and both proved to be susceptible to rCedV-nTurbo635 infection. The results regarding replication efficiency differed between the TCID50 titrations using rCedV-nTurbo635 and the PFU/ml calculated from the RT-qPCR of CedV WT-infected cells. This was either a real discrepancy between recombinant and WT virus or due to the fact that different parameters were measured in these assays, which do not necessarily result in identical titers. Using RT-qPCR, the number of genome copies in the supernatant of infected cells is determined by the abundance of the nucleocapsid gene, which does not automatically translate to infectious virus. Titrating the supernatant on permissive cells, on the other hand, is a less sensitive and less accurate method, which only measures infectious viral particles. To dispel any doubts, the supernatants of rCedV-nTurbo635-infected cells should also be analyzed by RT-qPCR. CedV WT was able to replicate efficiently on RaNep; nevertheless, intranasal inoculation of ERB is not followed by productive infection or seroconversion [44]. A subsequent animal trial is necessary to draw more definitive conclusions about the reservoir capacity of ERB for CedV. This study should compare multiple routes of infection and include a broader representation of ERB across different sexes and age groups. It is worth noting how NiV did not replicate in RaNep, even though these cells express the NiV receptors, ephrin B2 and B3. This indicates that CedV tissue distribution and absence of specific lesions may similarly be limited by additional factors, independent of receptor expression and entry.

The ephrin G-H-loop, which mediates binding to Eph-receptors and henipavirus G proteins, only makes up a 12 amino acid-long stretch of the extracellular domain and is highly conserved among the B ephrins [68]. Differences in Eph-receptor or G protein binding affinities are based on small-scale amino acid substitutions, e.g. mutation of the Tyr-Met motif within the ephrin B1 G-H-loop to the Leu-Trp, found in ephrin B2 and B3 at the equivalent position, enables NiV G

protein to use ephrin B1 for entry [68]. Furthermore, HeV and NiV G proteins are able to bind to ephrin B3, because the tyrosine residue within the G protein's first pocket (P1) forms a pi-stack with the tyrosine Y120 of the ephrin B3 G-H-loop, thereby stabilizing the interaction [9]. The CedV G protein's asparagine residue N602 lacks the necessary benzol ring for a stable interaction, therefore ephrin B3 usage is sterically unfavorable [9]. Laing *et al.* suggest in their *in-silico* predictions that single amino acid mutations in the G protein sequence could confer ephrin B3 usage to CedV [9]. Whether this holds true *in vitro*, could be investigated using different pseudovirus systems and recombinant viruses, which would also give more insight into the relevance of receptor preferences for disease pathology.

6.2. Type I IFN signaling: Innate, but indispensable

HeV and NiV P gene products, V and W protein, are major virulence factors that inhibit type I IFN induction and signaling [5,13–16,174,176,177,180,181,189,191,192], thereby enhancing viral replication and disease pathogenesis [40,194,264]. The CedV genome does not encode for a V or W protein, and its P protein cannot efficiently suppress STAT signaling [6,7]. This work investigated whether any of the CedV proteins, in addition to the M protein's influence on IKKε [17], have evolved mechanisms of inhibiting the host's IFN response. Unlike NiV C protein [174,193,195,196], CedV C did not affect *IFNB* induction. In line with previous findings on HeV and NiV [18], CedV N protein reduced *IFNB* induction significantly; however, the exact mechanism remains to be elucidated. IRF3 translocation to the nucleus remained unchanged by expression of CedV N protein, and an unspecific effect on transcription or translation was not observed either. The sensitivity of both the Western blot and the luciferase assays could have been low, as no positive control for inhibition of *IFNB* induction or IRF3 translocation was employed. Results from luciferase assays indicated no influence on STAT signaling, which contradicts published data on HeV/NiV N proteins [18] and remains to be verified in immunofluorescence assays, assessing co-localization and STAT translocation to the nucleus. An influence of CedV N protein on NF-κB signaling, similar to the interaction of NiV W protein with 14-3-3, which reduces p65-dependent transcription [191,192], was not investigated in this work. It could, however, be a possible mechanism of inhibiting *IFNB* induction. As bat genomes show positive selection and gene losses related to NF-κB signaling [156,163], it would be of particular interest to directly compare the effect of CedV N protein expression on NF-κB signaling between human and ERB cells. Unfortunately, the establishment of a comparable luciferase assay in RaNep was unsuccessful, as human RIG-I-CA overexpression did not result in significant *IFNB* promoter activation. Since ERB and human RIG-I are similar in sequence and signaling [301], the human

RIG-I-CA is expected to induce a strong *IFNB* promoter activation in ERB cells. The efforts to optimize this assay and delineate innate signaling pathways in ERB cells need to be continued.

In infected cells, N protein directly interacts with viral genomic RNA and the P protein [56,302,303], which could limit its accessibility and thereby diminish its IFN inhibitory properties during infection. Nevertheless, henipavirus N proteins are produced in excess during infection, as paramyxovirus genomes are transcribed in a decreasing gradient, starting with the N protein [51]. To better understand the intricate processes of a real infection and the role of the N protein, additional experiments need to be performed using co-transfections and live virus.

Even though CedV retained some IFN inhibitory properties, these were not sufficient to significantly impair innate immunity, as demonstrated by the strong induction of *IFNB* and ISGs in infected cell lines at later time points p.i. It is undisputed that IFN is essential for antiviral defense. This was reiterated by the substantial titer increase in human and bat cells, treated with AZD4604, compared to the untreated control. The fact that the replication curve in AZD4604-treated RaNep deviated 24 h later from the untreated control, as compared to A549, reflected the delayed *IFNB* and ISG induction observed in qPCR. An increase in viral titers in response to inhibition of IFN signaling *in vitro* allows speculations about the effects of generalized immunosuppression on viral shedding in naturally infected, free-ranging bats in response to environmental, nutritional, or reproductive stress. Animal trials, including an artificially immunosuppressed group, e.g., by AZD4604 or dexamethasone treatment, could further explore this. The informative value of a similar approach has been demonstrated by MARV infection of immunosuppressed ERB, which has elucidated bat-specific correlates of protection, such as localized foci of controlled inflammation [304].

The data presented here emphasize that functional IFN induction and signaling play a major role in controlling henipavirus replication and pathology. In comparison to its highly pathogenic relatives, CedV is severely limited in virulence by its reduced ability to inhibit the host's innate immune response.

6.3. ISG induction in response to rCedV-nTurbo635 infection

A549, RaNep, and SK-6 are all immortalized epithelial cell lines that originate from different tissues (lung, nose, and kidney). Their innate immune response to rCedV-nTurbo635 infection was similar in terms of *IFNB* and ISG induction; however, differences in the timing and magnitude of fold changes were observed. Whether those were species- or tissue-specific

could not be conclusively determined. To specifically elucidate inter-species differences, improved results could be achieved by using primary cells of comparable tissue origin, which was not feasible due to limited access and the increased expenditure associated with working with primary cells. Nevertheless, the low induction of pro-inflammatory cytokines, such as *TNFA* and *IL6* in RaNep aligns with the reduced pro-inflammatory phenotype published for bats [103,145,156,165] and is most likely translatable to other ERB tissues.

Analysis of the proteome at 24 h p.i. provided a non-biased overview of relevant pathways during the infection and enabled large-scale comparisons between the cell lines. Even though generally similar proteins and pathways were enriched, some differences are worth discussing.

Even though all cell lines enriched NF-κB signaling and its regulation in response to rCedV-nTurbo635 infection, only A549 and SK-6 reacted with substantial *TNFA* and *IL6* expression. Many sites of positive selection in bat genomes, combined with gene losses related to NF-κB signaling, suggest bat-specific modifications within these pathways [102,156,163]. One distinction between human and bat cells in NF-κB signaling is the c-Rel-dependent suppression of *TNFA* transcription observed in bat cells [165]. NF-κB also regulates the NLRP3 inflammasome at the transcriptional level by promoting the transcription of pro-*IL1B*, pro-*IL18,* and *NLRP3* [305]. Altered NF-κB signaling could be another mechanism for dampening inflammasome activation in bats, leading to the low induction of *IL1B* transcription, as measured in RaNep, similar to the dampened *IL1B* expression observed in other bat cells [113,165]. In addition, other mechanisms, possibly influencing other cytokine promoters, must also take effect and need to be investigated further.

In contrast to the other cell lines, RaNep increased the expression of OAS3, in addition to OAS2 and OASL. OAS3 is required for RNase L activation in response to viral RNA sensing in human and ERB cells [160,306], which provides antiviral protection by degrading viral RNA and amplifies IFN responses via additional RIG-I activation [161]. Furthermore, RNAse L cleaves cellular and viral RNA and can contribute to apoptosis [162]. The proteomics data presented in this work indicate OAS3 induced RNase L activation in rCedV-nTurbo635-infected ERB cells, emphasizing its role in viral control. Unlike in *P. alecto* [157], ERB *RNASEL* expression is not inducible by IFN [160]. Consistently, our proteomic analysis only shows significant upregulation of OAS3 expression, but not RNase L.

Potent antiviral effector molecules, such as MX1/MX2, ISG15, or ISG20, were enriched at 24 h p.i. in all three cell lines. Whether induction of homologous proteins leads to the same effect on viral replication remains to be investigated. Recently, Morales *et al.* have demonstrated significant differences between ISG15 from different bats and human ISG15 in their capability

to restrict virus replication [163]. Their data suggest that ISG15 from a species that co-evolved with a pathogen is a more potent inhibitor of that pathogen. Assessing the efficiency of the induced antiviral proteins was not within the scope of this project. It could, however, shed more light on species-specific antiviral responses.

RaNep controlled rCedV-nTurbo635 infection by a strong *IFNB* response, combined with low pro-inflammatory cytokine (*IL6*, *TNFA*, *IL1B*) expression, induction of antiviral proteins (ISG15, ISG20, OAS3, MX2), and controlled apoptosis (Caspase-3/-7 activation). These observations suggest, once more, that bats do not merely tolerate viral infection, but rather mount an effective antiviral response while restricting inflammatory tissue damage.

6.4. Is anti-viral apoptosis the answer?

Even though rCedV-nTurbo635 infection did not induce severe ER stress, it caused apoptosis in all three epithelial cell lines and the primary ERB lung endothelial cells. Apoptosis is a tightly regulated, ATP-dependent process. Unlike lytic forms of cell death, such as pyroptosis, necroptosis, or necrosis, which lead to the release of cytokines/chemokines and DAMPs, apoptosis does not cause additional inflammation [307–309].

PELENDO initiated apoptosis earlier than RaNep, and a higher percentage of cells were affected, even at the low MOI used. PaKi cells react similarly to CedV infection, but in contrast to RaNep, *TNFA* is highly induced, leading to death-receptor-mediated apoptosis [203]. HeV can counteract the IFN and ISG response in PaKi and HeLa (human cervical carcinoma) cells and initiate apoptosis in various bat and human cell lines [202,203]. While apoptosis is induced in cell lines from both species, PaKi cells retain more viability despite HeV infection [202,310]. Apoptosis is not a bat cell-specific reaction to henipavirus infection; nevertheless, it plays a vital role in infections with both highly and non-pathogenic viruses. Since NLRP3 activation and therefore pyroptosis induction are reduced in bats, they may be more prone to non-inflammatory cell death alternatives, such as apoptosis or autophagy [100,101,104,311,312]. A tendency towards non-inflammatory cell death aligns with bats being able to control viral replication while efficiently mitigating hyperinflammation. In line with this assumption, no caspase-1 or -4 specific peptides were detected in RaNep, whereas both were induced in A549 following infection. Caspase-1 functionality and IL-1β cleavage are dampened in many bat species, but it has not been demonstrated for ERB specifically [312].

Whether rCedV-nTurbo635 induced apoptosis via the extrinsic or intrinsic pathway was not

investigated in depth. While *DDIT3*/CHOP [313] induction suggested ER stress-mediated intrinsic apoptosis, increased *TNFA* expression, in addition to marginally increased FAS/DAXX [314] abundance, provided evidence for death receptor-mediated cell death. Future studies will determine the contribution of the two apoptosis pathways.

In conclusion, although CedV is a non-pathogenic virus, it can induce apoptosis in various cell lines and primary cells. In case of henipavirus infections, apoptosis could be beneficial to the host as a means to limit viral spread while maintaining a low inflammatory profile.

6.5. Endothelial cells as a "gateway" to the CNS

Endothelial cells from human veins, brain, and lung, but not the aorta, can be infected by NiV and mount a strong IFN and cytokine/chemokine response, which attracts immune cells [195,315,316]. According to the "gateway theory" localized inflammation or regional stimulation of sympathetic nerves can open gateways to overcome the blood-brain barrier (BBB) without causing gross lesions and massive immune cell infiltration [317,318]. Satterfield *et al*. suggest that NiV replication in endothelial cells may cause these small leakages, thereby leading to the central nervous system (CNS) pathology observed in ferrets and humans [194]. The opening of those gates into the CNS is triggered and amplified by IL17/IL6, which induces chemokine release via NF-κB/STAT3 signaling [317]. The challenge studies in the ferret model, performed by Satterfield *et al.*, show that as soon as NF-κB signaling is no longer dampened by W protein, neurological symptoms increase drastically, which could indicate an NF-κB-mediated mechanism of CNS invasion by NiV [40,194]. This hypothesis also explains why bats do not exhibit neurological symptoms following NiV infection. Their generally dampened NF-κB signaling [156,163,165] could protect the CNS from gateway-mediated viral spread and immune cell infiltration.

Susceptibility of endothelial cells to NiV infection is dependent on ephrin B2 expression [316]. PELENDO expressed high levels of ephrin B2 and were, as expected, permissive to rCedV-nTurbo635 infection. Apoptosis was initiated in response to the infection at a low MOI. PELENDO were a mixture of lung-derived primary cells, which limits the validity of the obtained results. Nevertheless, VWF staining, lack of cytokeratin expression, evidence of WPBs, and expression of endothelial cell markers demonstrated a dominance of endothelial cells in low passages, which were exclusively used for infection experiments. Future studies will focus on establishing primary brain endothelial cells to investigate potential CedV- or NiV-induced breaches of the BBB in ERB. Recent advances in the development of primary cells and

immortalized cell lines from bat tissues, as well as the successful generation of stem cells from *P. alecto,* will facilitate future studies [319–321]. In addition to the published methods for investigating innate immunity in ERB [244,245], this work provides the necessary tools to assess ephrin expression, investigate cellular stress, and quantify apoptosis in ERB cells.

7. Summary

Henipaviruses, like Hendra and Nipah virus (HeV, NiV), cause outbreaks with devastating mortality rates in Australia and Southeast Asia. In recent years, novel henipaviruses have been identified in various countries, elevating the genus to a global public health concern. Fruit bats are reservoir hosts for many highly pathogenic viruses, including henipaviruses like HeV and NiV. Unlike humans or intermediate hosts like pigs, bats can harbor these viruses with minimal to no clinical symptoms, and they do not succumb to the infection. Deciphering why bats are this impervious to these viral diseases and how the bat immune system reacts to pathogens in comparison to other species is an important objective in the field of bat immunology. This work provides novel insights into the susceptibility of Egyptian fruit bat (ERB) cells to henipaviruses, exemplified by the non-pathogenic Cedar virus (CedV) and elucidates similarities and differences in innate immunity by comparing cell lines from potential host species.

Different entry assays using a recombinant, fluorescent CedV (rCedV-nTurbo635), identified ERB ephrins B1 and B2 as the main CedV receptors. Furthermore, low entry efficiency could also be mediated by ephrin A5. To further confirm those findings, stable ERB ephrin B1/B2 knockdown cells were generated using the lentivirus shRNA system. Reduced infection rates, measured in the knockdown cells, highlighted the importance of ephrin B1/B2 as CedV receptors.

To investigate the interactions between CedV and the host cell IFN response, CedV proteins were tested for their potential to inhibit *IFNB* induction, and CedV-nTurbo635 replication was evaluated on IFN signaling-deficient cells. The CedV nucleocapsid protein N suppressed *IFNB* induction by an unknown mechanism, but its influence was not sufficient to substantially impair IFN responses in an infection with replication-competent virus. A sharp increase in rCedV-nTurbo635 replication in IFN signaling-impaired cells impressively demonstrated the importance of intact IFN signaling in restricting CedV replication.

To comprehensively compare innate immune responses of human, pig, and ERB *in vitro*, three epithelial cell lines were chosen and infected at a low MOI. Interferon and ISG transcript induction, in combination with proteome analysis, revealed the enrichment of similar pathways in response to rCedV-nTurbo635 infection. While all cell lines presented a strong *IFNB* response, ERB cells deviated from the others by producing low levels of pro-inflammatory cytokines (*TNFA*, *IL6*, *IL1B*). Antiviral proteins, such as MX1, MX2, OAS-family members, ISG15, or ISG20 were similarly upregulated; however, some of the identified proteins were

induced explicitly in ERB cells. In addition to the unidentified loci, which could be hitherto uncharacterized ISGs, OAS3 was one example of the most prominent upregulated proteins. It develops its antiviral function by activating RNaseL, which degrades cellular and viral RNA and thereby reduces viral burden while simultaneously enhancing IFN induction. In addition to potent antiviral responses, apoptosis was identified as a non-inflammatory mechanism for controlling viral burden in epithelial cell lines, as well as in the primary ERB lung endothelia-like cells.

In conclusion, this project demonstrated the susceptibility of ERB cells to CedV infection *in vitro* and showed that ERB ephrins B1 and B2 mediate viral entry. In line with the relevant literature, bat cells controlled viral burden without inducing excessive inflammation. Importantly, a functional IFN I response limited CedV replication, allowing conclusions to be drawn regarding the importance of IFN competence in infections with highly pathogenic henipaviruses. This work contributes to fundamental research on henipaviruses and bat immunology, paving the way for the prevention of outbreaks and the development of novel therapeutic interventions.

8. Zusammenfassung (Deutsch)

Henipaviren, wie das Hendra und das Nipah Virus (HeV, NiV), verursachen in Australien und Südostasien Ausbrüche mit verheerenden Sterberaten. In den letzten Jahren wurden immer mehr neuartige Henipaviren in verschiedenen Ländern entdeckt, wodurch die Gattung zu einer globalen Bedrohung für die öffentliche Gesundheit wurde. Flughunde sind Reservoirwirte für viele hochpathogene Viren, darunter auch Henipaviren wie HeV und NiV. Im Gegensatz zum Menschen oder zu Zwischenwirten wie Schweinen können Fledermäuse mit diesen Viren infiziert sein und zeigen dabei wenige bis gar keine klinischen Anzeichen und versterben auch nicht an der Erkrankung. Zu entschlüsseln warum Fledermäuse so unempfindlich gegenüber Viruserkrankungen sind und wie das Immunsystem von Fledermäusen im Vergleich zu anderen Arten auf Krankheitserreger reagiert, ist ein wichtiges Ziel auf dem Gebiet der Fledermausimmunologie. Diese Arbeit bietet neue Einblicke in die Infizierbarkeit von Zellen des Ägyptischen Flughundes (ERB) mit Henipaviren am Beispiel des nicht-pathogenen Cedar Virus (CedV) und deckt Gemeinsamkeiten und Unterschiede in der angeborenen Immunität zwischen Zelllinien potenzieller Wirtsspezies auf.

Verschiedene mit einem rekombinanten, fluoreszierenden CedV (rCedV-nTurbo635) durchgeführte Eintrittsassays identifizierten die ERB Ephrine B1 und B2 als die wichtigsten CedV Rezeptoren. Darüber hinaus konnte eine geringe Eintrittseffizienz auch durch Ephrin A5 vermittelt werden. Um diese Ergebnisse weiter zu bestätigen, wurden stabile ERB Ephrin B1/B2-Knockdown-Zellen mit Hilfe des Lentivirus-shRNA-Systems erzeugt. Die in den Knockdown-Zellen gemessenen verringerten Infektionsraten unterstrichen die Bedeutung von ERB Ephrin B1 und B2 als CedV Rezeptoren.

Um die Wechselwirkungen zwischen CedV und der Interferonantwort der Wirtszelle zu untersuchen, wurden CedV Proteine auf ihr Potenzial die *IFNB* Induktion zu hemmen, getestet und die CedV Replikation auf Zellen mit inhibiertem Interferonsignalweg analysiert. Das CedV Nukleokapsidprotein N unterdrückte die *IFNB* Induktion auf unbekannte Weise, aber sein Einfluss reichte nicht aus, um die Interferonantwort im Falle einer Infektion mit replikationsfähigem Virus maßgeblich zu beeinträchtigen. Ein starker Anstieg der rCedV-nTurbo635 Replikation in Zellen mit beeinträchtigtem Interferonsignalweg zeigte eindrucksvoll die Bedeutung von Interferonkompetenz für die Wirtszelle.

Um die angeborene Immunantwort von Menschen, Schweinen und ERB *in vitro* umfassend zu vergleichen, wurden drei Epithelzelllinien ausgewählt und mit einer niedrigen Virusdosis infiziert. Die Interferon- und ISG-Induktion in Kombination mit der Proteomanalyse ergab, dass

ähnliche Signalwege als Reaktion auf eine rCedV-nTurbo635 Infektion ausgelöst wurden. Während alle Zelllinien eine starke *IFNB*-Antwort zeigten, unterschieden sich die ERB-Zellen von den anderen durch eine geringe Produktion proinflammatorischer Zytokine (*TNFA*, *IL6*, *IL1B*). Antivirale Proteine wie MX1, MX2, Mitglieder der OAS-Familie, ISG15 oder ISG20 wurden in ähnlicher Weise hochreguliert, einige der identifizierten Proteine wurden jedoch speziell in ERB-Zellen induziert. Neben den nicht identifizierten Loci, bei denen es sich um bisher nicht charakterisierte ISGs handeln könnte, war OAS3 ein Beispiel für die am stärksten hochregulierten Proteine. Es entfaltet seine antivirale Funktion durch Aktivierung von RNaseL, die zelluläre und virale RNA abbaut und dadurch die virale Belastung reduziert, während gleichzeitig die Interferoninduktion verstärkt wird. Zusätzlich zu den starken antiviralen Reaktionen zeigte sich Apoptose als bedeutsame nicht-entzündliche Methode zur viralen Kontrolle in den Epithelzelllinien sowie in den primären ERB-Lungenendothel-ähnlichen Zellen.

Zusammenfassend lässt sich sagen, dass dieses Projekt die Infizierbarkeit von ERB-Zellen mit CedV zeigen konnte sowie, dass der Eintritt des Virus durch die ERB-Ephrine B1 und B2 vermittelt wird. Im Einklang mit der einschlägigen Literatur konnte festgestellt werden, dass Fledermauszellen die virale Belastung kontrollieren, ohne eine übermäßige Entzündungsreaktion auszulösen. Wichtig ist, dass eine funktionierende Interferonantwort die CedV Replikation einschränkte, was Rückschlüsse auf die Bedeutung von Interferonkompetenz bei Infektionen mit hochpathogenen Henipaviren zulässt. Diese Arbeit trägt zur Grundlagenforschung über Henipaviren und Fledermausimmunologie bei, die den Weg zur Prävention von Ausbrüchen und zur Entwicklung neuer therapeutischer Maßnahmen ebnen wird.

9. References

1. Quarleri, J., Galvan, V. & Delpino, M. V. Henipaviruses: an expanding global public health concern? *GeroScience* **44,** 2447–2459; 10.1007/s11357-022-00670-9 (2022).

2. Mehand, M. S., Al-Shorbaji, F., Millett, P. & Murgue, B. The WHO R&D Blueprint: 2018 review of emerging infectious diseases requiring urgent research and development efforts. *Antiviral research* **159,** 63–67; 10.1016/j.antiviral.2018.09.009 (2018).

3. Wang, L. F., Michalski, W. P., Yu, M., Pritchard, L. I., Crameri, G., Shiell, B. & Eaton, B. T. A novel P/V/C gene in a new member of the Paramyxoviridae family, which causes lethal infection in humans, horses, and other animals. *Journal of virology* **72,** 1482–1490; 10.1128/JVI.72.2.1482-1490.1998 (1998).

4. Wong, K. T., Shieh, W.-J., Kumar, S., Norain, K., Abdullah, W., Guarner, J., Goldsmith, C. S., Chua, K. B., Lam, S. K., Tan, C. T., Goh, K. J., Chong, H. T., Jusoh, R., Rollin, P. E., Ksiazek, T. G. & Zaki, S. R. Nipah virus infection: pathology and pathogenesis of an emerging paramyxoviral zoonosis. *The American journal of pathology* **161,** 2153–2167; 10.1016/S0002-9440(10)64493-8 (2002).

5. Rodriguez, J. J. & Horvath, C. M. Host evasion by emerging paramyxoviruses: Hendra virus and Nipah virus v proteins inhibit interferon signaling. *Viral Immunol* **17,** 210–219; 10.1089/0882824041310568 (2004).

6. Marsh, G. A., Jong, C. de, Barr, J. A., Tachedjian, M., Smith, C., Middleton, D., Yu, M., Todd, S., Foord, A. J., Haring, V., Payne, J., Robinson, R., Broz, I., Crameri, G., Field, H. E. & Wang, L.-F. Cedar virus: a novel Henipavirus isolated from Australian bats. *PLoS pathogens* **8,** e1002836; 10.1371/journal.ppat.1002836 (2012).

7. Lieu, K. G., Marsh, G. A., Wang, L.-F. & Netter, H. J. The non-pathogenic Henipavirus Cedar paramyxovirus phosphoprotein has a compromised ability to target STAT1 and STAT2. *Antiviral research* **124,** 69–76; 10.1016/j.antiviral.2015.09.017 (2015).

8. Schountz, T., Campbell, C., Wagner, K., Rovnak, J., Martellaro, C., DeBuysscher, B. L., Feldmann, H. & Prescott, J. Differential Innate Immune Responses Elicited by Nipah Virus and Cedar Virus Correlate with Disparate In Vivo Pathogenesis in Hamsters. *Viruses* **11**; 10.3390/v11030291 (2019).

9. Laing, E. D., Navaratnarajah, C. K., Da Cheliout Silva, S., Petzing, S. R., Xu, Y., Sterling, S. L., Marsh, G. A., Wang, L. F., Amaya, M., Nikolov, D. B., Cattaneo, R., Broder, C. C. & Xu, K. Structural and functional analyses reveal promiscuous and species specific use of ephrin receptors by Cedar virus. *Proc Natl Acad Sci U S A* **116,** 20707–20715; 10.1073/pnas.1911773116 (2019).

10. Laing, E. D., Amaya, M., Navaratnarajah, C. K., Feng, Y. R., Cattaneo, R., Wang, L. F. & Broder, C. C. Rescue and characterization of recombinant cedar virus, a non-pathogenic Henipavirus species. *Virol J* **15,** 56; 10.1186/s12985-018-0964-0 (2018).

11. Pryce, R., Azarm, K., Rissanen, I., Harlos, K., Bowden, T. A. & Lee, B. A key region of molecular specificity orchestrates unique ephrin-B1 utilization by Cedar virus. *Life Sci Alliance* **3**; 10.26508/lsa.201900578 (2020).

12. Maginnis, M. S. Virus-Receptor Interactions: The Key to Cellular Invasion. *Journal of molecular biology* **430,** 2590–2611; 10.1016/j.jmb.2018.06.024 (2018).

13. Rodriguez, J. J., Parisien, J.-P. & Horvath, C. M. Nipah virus V protein evades alpha and gamma interferons by preventing STAT1 and STAT2 activation and nuclear accumulation. *Journal of virology* **76,** 11476–11483; 10.1128/jvi.76.22.11476-11483.2002 (2002).

14. Rodriguez, J. J., Wang, L.-F. & Horvath, C. M. Hendra virus V protein inhibits interferon signaling by preventing STAT1 and STAT2 nuclear accumulation. *Journal of virology* **77,** 11842–11845; 10.1128/jvi.77.21.11842-11845.2003 (2003).

15. Shaw, M. L., Cardenas, W. B., Zamarin, D., Palese, P. & Basler, C. F. Nuclear localization of the Nipah virus W protein allows for inhibition of both virus- and toll-like receptor 3-triggered signaling pathways. *Journal of virology* **79,** 6078–6088; 10.1128/JVI.79.10.6078-6088.2005 (2005).

16. Shaw, M. L., García-Sastre, A., Palese, P. & Basler, C. F. Nipah virus V and W proteins have a common STAT1-binding domain yet inhibit STAT1 activation from the cytoplasmic and nuclear compartments, respectively. *Journal of virology* **78,** 5633–5641; 10.1128/JVI.78.11.5633-5641.2004 (2004).

17. Bharaj, P., Wang, Y. E., Dawes, B. E., Yun, T. E., Park, A., Yen, B., Basler, C. F., Freiberg, A. N., Lee, B. & Rajsbaum, R. The Matrix Protein of Nipah Virus Targets the E3-Ubiquitin Ligase TRIM6 to Inhibit the IKKε Kinase-Mediated Type-I IFN Antiviral Response. *PLoS pathogens* **12,** e1005880; 10.1371/journal.ppat.1005880 (2016).

18. Sugai, A., Sato, H., Takayama, I., Yoneda, M. & Kai, C. Nipah and Hendra Virus Nucleoproteins Inhibit Nuclear Accumulation of Signal Transducer and Activator of Transcription 1 (STAT1) and STAT2 by Interfering with Their Complex Formation. *Journal of virology* **91**; 10.1128/JVI.01136-17 (2017).

19. O'Sullivan, J. D., Allworth, A. M., Paterson, D. L., Snow, T. M., Boots, R., Gleeson, L. J., Gould, A. R., Hyatt, A. D. & Bradfield, J. Fatal encephalitis due to novel paramyxovirus transmitted from horses. *Lancet (London, England)* **349,** 93–95; 10.1016/s0140-6736(96)06162-4 (1997).

20. Selvey, L. A., Wells, R. M., McCormack, J. G., Ansford, A. J., Murray, K., Rogers, R. J., Lavercombe, P. S., Selleck, P. & Sheridan, J. W. Infection of humans and horses by a newly described morbillivirus. *The Medical journal of Australia* **162,** 642–645; 10.5694/j.1326-5377.1995.tb126050.x (1995).

21. Murray, K., Selleck, P., Hooper, P., Hyatt, A., Gould, A., Gleeson, L., Westbury, H., Hiley, L., Selvey, L. & Rodwell, B. A morbillivirus that caused fatal disease in horses and humans. *Science (New York, N.Y.)* **268,** 94–97; 10.1126/science.7701348 (1995).

22. Chua, K. B., Goh, K. J., Wong, K. T., Kamarulzaman, A., Tan, P. S., Ksiazek, T. G., Zaki, S. R., Paul, G., Lam, S. K. & Tan, C. T. Fatal encephalitis due to Nipah virus among pig-farmers in Malaysia. *Lancet (London, England)* **354,** 1257–1259; 10.1016/S0140-6736(99)04299-3 (1999).

23. Parashar, U. D., Sunn, L. M., Ong, F., Mounts, A. W., Arif, M. T., Ksiazek, T. G., Kamaluddin, M. A., Mustafa, A. N., Kaur, H., Ding, L. M., Othman, G., Radzi, H. M., Kitsutani, P. T., Stockton, P. C., Arokiasamy, J., Gary, H. E. & Anderson, L. J. Case-control study of risk factors for human infection with a new zoonotic paramyxovirus, Nipah virus, during a 1998-1999 outbreak of severe encephalitis in Malaysia. *The Journal of infectious diseases* **181,** 1755–1759; 10.1086/315457 (2000).

24. World Health Organization (WHO). Nipah virus. Available at https://www.who.int/news-room/fact-sheets/detail/nipah-virus (2018).

25. Yadav, P. D., Raut, C. G., Shete, A. M., Mishra, A. C., Towner, J. S., Nichol, S. T. & Mourya, D. T. Detection of Nipah virus RNA in fruit bat (Pteropus giganteus) from India. *The American journal of tropical medicine and hygiene* **87,** 576–578; 10.4269/ajtmh.2012.11-0416 (2012).

26. Halpin, K., Young, P. L., Field, H. E. & Mackenzie, J. S. Isolation of Hendra virus from pteropid bats: a natural reservoir of Hendra virus. *The Journal of general virology* **81,** 1927–1932; 10.1099/0022-1317-81-8-1927 (2000).

27. Luby, S. P., Rahman, M., Hossain, M. J., Blum, L. S., Husain, M. M., Gurley, E., Khan, R., Ahmed, B.-N., Rahman, S., Nahar, N., Kenah, E., Comer, J. A. & Ksiazek, T. G. Foodborne transmission of Nipah virus, Bangladesh. *Emerging Infectious Diseases* **12,** 1888–1894; 10.3201/eid1212.060732 (2006).

28. Halpin, K., Hyatt, A. D., Fogarty, R., Middleton, D., Bingham, J., Epstein, J. H., Rahman, S. A., Hughes, T., Smith, C., Field, H. E. & Daszak, P. Pteropid bats are confirmed as the reservoir hosts of henipaviruses: a comprehensive experimental study of virus transmission. *The American journal of tropical medicine and hygiene* **85,** 946–951; 10.4269/ajtmh.2011.10-0567 (2011).

29. Gurley, E. S., Montgomery, J. M., Hossain, M. J., Bell, M., Azad, A. K., Islam, M. R., Molla, M. A. R., Carroll, D. S., Ksiazek, T. G., Rota, P. A., Lowe, L., Comer, J. A., Rollin, P., Czub, M., Grolla, A., Feldmann, H., Luby, S. P., Woodward, J. L. & Breiman, R. F. Person-to-person transmission of Nipah virus in a Bangladeshi community. *Emerging Infectious Diseases* **13,** 1031–1037; 10.3201/eid1307.061128 (2007).

30. Homaira, N., Rahman, M., Hossain, M. J., Epstein, J. H., Sultana, R., Khan, M. S. U., Podder, G., Nahar, K., Ahmed, B., Gurley, E. S., Daszak, P., Lipkin, W. I., Rollin, P. E., Comer, J. A., Ksiazek, T. G. & Luby, S. P. Nipah virus outbreak with person-to-person transmission in a district of Bangladesh, 2007. *Epidemiol Infect* **138,** 1630–1636; 10.1017/S0950268810000695 (2010).

31. Wang, L. F., Yu, M., Hansson, E., Pritchard, L. I., Shiell, B., Michalski, W. P. & Eaton, B. T. The exceptionally large genome of Hendra virus: support for creation of a new genus

within the family Paramyxoviridae. *Journal of virology* **74,** 9972–9979; 10.1128/jvi.74.21.9972-9979.2000 (2000).

32. Eaton, B. T., Broder, C. C., Middleton, D. & Wang, L.-F. Hendra and Nipah viruses: different and dangerous. *Nature reviews. Microbiology* **4,** 23–35; 10.1038/nrmicro1323 (2006).

33. Drexler, J. F., Corman, V. M., Müller, M. A., Maganga, G. D., Vallo, P., Binger, T., Gloza-Rausch, F., Cottontail, V. M., Rasche, A., Yordanov, S., Seebens, A., Knörnschild, M., Oppong, S., Sarkodie, Y. A., Pongombo, C., Lukashev, A. N., Schmidt-Chanasit, J., Stöcker, A., Carneiro, A. J. B., Erbar, S., Maisner, A., Fronhoffs, F., Buettner, R., Kalko, E. K. V., Kruppa, T., Franke, C. R., Kallies, R., Yandoko, E. R., Herrler, G., Reusken, C., Hassanin, A., Krüger, D. H., Matthee, S., Ulrich, R. G., Leroy, E. M. & Drosten, C. Bats host major mammalian paramyxoviruses. *Nature communications* **3**; 10.1038/ncomms1796 (2012).

34. Lee, S.-H., Kim, K., Kim, J., No, J. S., Park, K., Budhathoki, S., Lee, S. H., Lee, J., Cho, S. H., Cho, S., Lee, G.-Y., Hwang, J., Kim, H.-C., Klein, T. A., Uhm, C.-S., Kim, W.-K. & Song, J.-W. Discovery and Genetic Characterization of Novel Paramyxoviruses Related to the Genus Henipavirus in Crocidura Species in the Republic of Korea. *Viruses* **13**; 10.3390/v13102020 (2021).

35. Madera, S., Kistler, A., Ranaivoson, H. C., Ahyong, V., Andrianiaina, A., Andry, S., Raharinosy, V., Randriambolamanantsoa, T. H., Ravelomanantsoa, N. A. F., Tato, C. M., DeRisi, J. L., Aguilar, H. C., Lacoste, V., Dussart, P., Heraud, J. M. & Brook, C. E. Discovery and Genomic Characterization of a Novel Henipavirus, Angavokely Virus, from Fruit Bats in Madagascar. *J Virol* **96,** e0092122; 10.1128/jvi.00921-22 (2022).

36. Vanmechelen, B., Meurs, S., Horemans, M., Loosen, A., Joly Maes, T., Laenen, L., Vergote, V., Koundouno, F. R., Magassouba, N., Konde, M. K., Condé, I. S., Carroll, M. W. & Maes, P. The characterization of multiple novel paramyxoviruses highlights the diverse nature of the subfamily Orthoparamyxovirinae. *Virus evolution* **8,** veac061; 10.1093/ve/veac061 (2022).

37. Zhang, X.-A., Li, H., Jiang, F.-C., Zhu, F., Zhang, Y.-F., Chen, J.-J., Tan, C.-W., Anderson, D. E., Fan, H., Dong, L.-Y., Li, C., Zhang, P.-H., Li, Y., Ding, H., Fang, L.-Q., Wang, L.-F. & Liu, W. A Zoonotic Henipavirus in Febrile Patients in China. *The New England journal of medicine* **387,** 470–472; 10.1056/NEJMc2202705 (2022).

38. Wu, Z., Yang, L., Yang, F., Ren, X., Jiang, J., Dong, J., Sun, L., Zhu, Y., Zhou, H. & Jin, Q. Novel Henipa-like virus, Mojiang Paramyxovirus, in rats, China, 2012. *Emerging Infectious Diseases* **20,** 1064–1066; 10.3201/eid2006.131022 (2014).

39. Hernández, L. H. A., Da Paz, T. Y. B., Da Silva, S. P., Da Silva, F. S., Barros, B. C. V. de, Nunes, B. T. D., Casseb, L. M. N., Medeiros, D. B. A., Da Vasconcelos, P. F. C. & Cruz, A. C. R. First Genomic Evidence of a Henipa-like Virus in Brazil. *Viruses* **14**; 10.3390/v14102167 (2022).

40. Satterfield, B. A., Cross, R. W., Fenton, K. A., Agans, K. N., Basler, C. F., Geisbert, T. W. & Mire, C. E. The immunomodulating V and W proteins of Nipah virus determine disease course. *Nature communications* **6,** 7483; 10.1038/ncomms8483 (2015).

41. Mortlock, M., Kuzmin, I. V., Weyer, J., Gilbert, A. T., Agwanda, B., Rupprecht, C. E., Nel, L. H., Kearney, T., Malekani, J. M. & Markotter, W. Novel Paramyxoviruses in Bats from Sub-Saharan Africa, 2007-2012. *Emerging Infectious Diseases* **21,** 1840–1843; 10.3201/eid2110.140368 (2015).

42. Mortlock, M., Geldenhuys, M., Dietrich, M., Epstein, J. H., Weyer, J., Pawęska, J. T. & Markotter, W. Seasonal shedding patterns of diverse henipavirus-related paramyxoviruses in Egyptian rousette bats. *Scientific reports* **11,** 24262; 10.1038/s41598-021-03641-w (2021).

43. Juman, M. M., Gibson, L., Suu-Ire, R. D., Languon, S., Quaye, O., Fleischer, G., Asumah, S., Jolma, E. R., Gautam, A., Sterling, S. L., Yan, L., Broder, C. C., Laing, E. D., Wood, J. L. N., Cunningham, A. A. & Restif, O. Ecological and Reproductive Cycles Drive Henipavirus Seroprevalence in the African Straw-Coloured Fruit Bat (Eidolon helvum). *Ecology and evolution* **14,** e70555; 10.1002/ece3.70555 (2024).

44. Mohl, B.-P., Diederich, S., Fischer, K. & Balkema-Buschmann, A. Rousettus aegyptiacus Fruit Bats Do Not Support Productive Replication of Cedar Virus upon Experimental Challenge. *Viruses* **16**; 10.3390/v16091359 (2024).

45. Seifert, S. N., Letko, M. C., Bushmaker, T., Laing, E. D., Saturday, G., Meade-White, K., van Doremalen, N., Broder, C. C. & Munster, V. J. Rousettus aegyptiacus Bats Do Not Support Productive Nipah Virus Replication. *The Journal of infectious diseases* **221,** S407-S413; 10.1093/infdis/jiz429 (2020).

46. Williamson, M. M., Hooper, P. T., Selleck, P. W., Gleeson, L. J., Daniels, P. W., Westbury, H. A. & Murray, P. K. Transmission studies of Hendra virus (equine morbillivirus) in fruit bats, horses and cats. *Australian veterinary journal* **76,** 813–818; 10.1111/j.1751-0813.1998.tb12335.x (1998).

47. Williamson, M. M., Hooper, P. T., Selleck, P. W., Westbury, H. A. & Slocombe, R. F. Experimental hendra virus infectionin pregnant guinea-pigs and fruit Bats (Pteropus poliocephalus). *Journal of Comparative Pathology* **122,** 201–207; 10.1053/jcpa.1999.0364 (2000).

48. Middleton, D. J., Morrissy, C. J., van der Heide, B. M., Russell, G. M., Braun, M. A., Westbury, H. A., Halpin, K. & Daniels, P. W. Experimental Nipah virus infection in pteropid bats (Pteropus poliocephalus). *Journal of Comparative Pathology* **136,** 266–272; 10.1016/j.jcpa.2007.03.002 (2007).

49. Rima, B., Balkema-Buschmann, A., Dundon, W. G., Duprex, P., Easton, A., Fouchier, R., Kurath, G., Lamb, R., Lee, B., Rota, P., Wang, L. & Ictv, R. C. ICTV Virus Taxonomy Profile: Paramyxoviridae. *The Journal of general virology* **100,** 1593–1594; 10.1099/jgv.0.001328 (2019).

50. Parks, G. D. & Alexander-Miller, M. A. Paramyxovirus activation and inhibition of innate immune responses. *Journal of molecular biology* **425,** 4872–4892; 10.1016/j.jmb.2013.09.015 (2013).

51. Bloyet, L.-M. The Nucleocapsid of Paramyxoviruses: Structure and Function of an Encapsidated Template. *Viruses* **13**; 10.3390/v13122465 (2021).

52. Morin, B., Kranzusch, P. J., Rahmeh, A. A. & Whelan, S. P. J. The polymerase of negative-stranded RNA viruses. *Current opinion in virology* **3,** 103–110; 10.1016/j.coviro.2013.03.008 (2013).

53. Ogino, T., Kobayashi, M., Iwama, M. & Mizumoto, K. Sendai virus RNA-dependent RNA polymerase L protein catalyzes cap methylation of virus-specific mRNA. *The Journal of biological chemistry* **280,** 4429–4435; 10.1074/jbc.M411167200 (2005).

54. Jordan, P. C., Liu, C., Raynaud, P., Lo, M. K., Spiropoulou, C. F., Symons, J. A., Beigelman, L. & Deval, J. Initiation, extension, and termination of RNA synthesis by a paramyxovirus polymerase. *PLoS pathogens* **14,** e1006889; 10.1371/journal.ppat.1006889 (2018).

55. Wignall-Fleming, E. B., Hughes, D. J., Vattipally, S., Modha, S., Goodbourn, S., Davison, A. J. & Randall, R. E. Analysis of Paramyxovirus Transcription and Replication by High-Throughput Sequencing. *Journal of virology* **93**; 10.1128/JVI.00571-19 (2019).

56. Ranadheera, C., Proulx, R., Chaiyakul, M., Jones, S., Grolla, A., Leung, A., Rutherford, J., Kobasa, D., Carpenter, M. & Czub, M. The interaction between the Nipah virus nucleocapsid protein and phosphoprotein regulates virus replication. *Scientific reports* **8,** 15994; 10.1038/s41598-018-34484-7 (2018).

57. Kolakofsky, D., Roux, L., Garcin, D. & Ruigrok, R. W. H. Paramyxovirus mRNA editing, the "rule of six" and error catastrophe: a hypothesis. *The Journal of general virology* **86,** 1869–1877; 10.1099/vir.0.80986-0 (2005).

58. El Najjar, F., Schmitt, A. P. & Dutch, R. E. Paramyxovirus glycoprotein incorporation, assembly and budding: a three way dance for infectious particle production. *Viruses* **6,** 3019–3054; 10.3390/v6083019 (2014).

59. Liljeroos, L. & Butcher, S. J. Matrix proteins as centralized organizers of negative-sense RNA virions. *Frontiers in bioscience (Landmark edition)* **18,** 696–715; 10.2741/4132 (2013).

60. Bowden, T. A., Crispin, M., Harvey, D. J., Jones, E. Y. & Stuart, D. I. Dimeric architecture of the Hendra virus attachment glycoprotein: evidence for a conserved mode of assembly. *Journal of virology* **84,** 6208–6217; 10.1128/JVI.00317-10 (2010).

61. Bossart, K. N., Crameri, G., Dimitrov, A. S., Mungall, B. A., Feng, Y.-R., Patch, J. R., Choudhary, A., Wang, L.-F., Eaton, B. T. & Broder, C. C. Receptor binding, fusion inhibition, and induction of cross-reactive neutralizing antibodies by a soluble G

glycoprotein of Hendra virus. *Journal of virology* **79,** 6690–6702; 10.1128/JVI.79.11.6690-6702.2005 (2005).

62. Steffen, D. L., Xu, K., Nikolov, D. B. & Broder, C. C. Henipavirus mediated membrane fusion, virus entry and targeted therapeutics. *Viruses* **4,** 280–308; 10.3390/v4020280 (2012).

63. Pager, C. T. & Dutch, R. E. Cathepsin L is involved in proteolytic processing of the Hendra virus fusion protein. *Journal of virology* **79,** 12714–12720; 10.1128/JVI.79.20.12714-12720.2005 (2005).

64. Meulendyke, K. A., Wurth, M. A., McCann, R. O. & Dutch, R. E. Endocytosis plays a critical role in proteolytic processing of the Hendra virus fusion protein. *Journal of virology* **79,** 12643–12649; 10.1128/JVI.79.20.12643-12649.2005 (2005).

65. Vogt, C., Eickmann, M., Diederich, S., Moll, M. & Maisner, A. Endocytosis of the Nipah virus glycoproteins. *J Virol* **79,** 3865–3872; 10.1128/JVI.79.6.3865-3872.2005 (2005).

66. Bonaparte, M. I., Dimitrov, A. S., Bossart, K. N., Crameri, G., Mungall, B. A., Bishop, K. A., Choudhry, V., Dimitrov, D. S., Wang, L.-F., Eaton, B. T. & Broder, C. C. Ephrin-B2 ligand is a functional receptor for Hendra virus and Nipah virus. *Proceedings of the National Academy of Sciences of the United States of America* **102,** 10652–10657; 10.1073/pnas.0504887102 (2005).

67. Negrete, O. A., Levroney, E. L., Aguilar, H. C., Bertolotti-Ciarlet, A., Nazarian, R., Tajyar, S. & Lee, B. EphrinB2 is the entry receptor for Nipah virus, an emergent deadly paramyxovirus. *Nature* **436,** 401–405; 10.1038/nature03838 (2005).

68. Negrete, O. A., Wolf, M. C., Aguilar, H. C., Enterlein, S., Wang, W., Muhlberger, E., Su, S. V., Bertolotti-Ciarlet, A., Flick, R. & Lee, B. Two key residues in ephrinB3 are critical for its use as an alternative receptor for Nipah virus. *PLoS Pathog* **2,** e7; 10.1371/journal.ppat.0020007 (2006).

69. Lisabeth, E. M., Falivelli, G. & Pasquale, E. B. Eph receptor signaling and ephrins. *Cold Spring Harbor perspectives in biology* **5**; 10.1101/cshperspect.a009159 (2013).

70. Frisén, J., Holmberg, J. & Barbacid, M. Ephrins and their Eph receptors: multitalented directors of embryonic development. *The EMBO journal* **18,** 5159–5165; 10.1093/emboj/18.19.5159 (1999).

71. Wilkinson, D. G. Interplay of Eph-Ephrin Signalling and Cadherin Function in Cell Segregation and Boundary Formation. *Frontiers in cell and developmental biology* **9,** 784039; 10.3389/fcell.2021.784039 (2021).

72. Palmer, A. & Klein, R. Multiple roles of ephrins in morphogenesis, neuronal networking, and brain function. *Genes & development* **17,** 1429–1450; 10.1101/gad.1093703 (2003).

73. Bergemann, A. D., Zhang, L., Chiang, M. K., Brambilla, R., Klein, R. & Flanagan, J. G. Ephrin-B3, a ligand for the receptor EphB3, expressed at the midline of the developing neural tube. *Oncogene* **16,** 471–480; 10.1038/sj.onc.1201557 (1998).

74. Hruska, M. & Dalva, M. B. Ephrin regulation of synapse formation, function and plasticity. *Molecular and cellular neurosciences* **50,** 35–44; 10.1016/j.mcn.2012.03.004 (2012).

75. Hooper, P., Zaki, S., Daniels, P. & Middleton, D. Comparative pathology of the diseases caused by Hendra and Nipah viruses. *Microbes and infection* **3,** 315–322; 10.1016/s1286-4579(01)01385-5 (2001).

76. The Human Protein Atlas Project. EFNB2. Available at https://www.proteinatlas.org/ (2025).

77. Uhlén, M., Fagerberg, L., Hallström, B. M., Lindskog, C., Oksvold, P., Mardinoglu, A., Sivertsson, Å., Kampf, C., Sjöstedt, E., Asplund, A., Olsson, I., Edlund, K., Lundberg, E., Navani, S., Szigyarto, C. A.-K., Odeberg, J., Djureinovic, D., Takanen, J. O., Hober, S., Alm, T., Edqvist, P.-H., Berling, H., Tegel, H., Mulder, J., Rockberg, J., Nilsson, P., Schwenk, J. M., Hamsten, M., Feilitzen, K. von, Forsberg, M., Persson, L., Johansson, F., Zwahlen, M., Heijne, G. von, Nielsen, J. & Pontén, F. Proteomics. Tissue-based map of the human proteome. *Science (New York, N.Y.)* **347,** 1260419; 10.1126/science.1260419 (2015).

78. Toth, J., Cutforth, T., Gelinas, A. D., Bethoney, K. A., Bard, J. & Harrison, C. J. Crystal structure of an ephrin ectodomain. *Developmental cell* **1,** 83–92; 10.1016/S1534-5807(01)00002-8 (2001).

79. Middleton, D. J., Westbury, H. A., Morrissy, C. J., van der Heide, B. M., Russell, G. M., Braun, M. A. & Hyatt, A. D. Experimental Nipah virus infection in pigs and cats. *Journal of Comparative Pathology* **126,** 124–136; 10.1053/jcpa.2001.0532 (2002).

80. Wong, K. T., Grosjean, I., Brisson, C., Blanquier, B., Fevre-Montange, M., Bernard, A., Loth, P., Georges-Courbot, M.-C., Chevallier, M., Akaoka, H., Marianneau, P., Lam, S. K., Wild, T. F. & Deubel, V. A Golden Hamster Model for Human Acute Nipah Virus Infection. *The American journal of pathology* **163,** 2127–2137 (2003).

81. Bossart, K. N., Tachedjian, M., McEachern, J. A., Crameri, G., Zhu, Z., Dimitrov, D. S., Broder, C. C. & Wang, L.-F. Functional studies of host-specific ephrin-B ligands as Henipavirus receptors. *Virology* **372,** 357–371; 10.1016/j.virol.2007.11.011 (2008).

82. Yoneda, M., Guillaume, V., Ikeda, F., Sakuma, Y., Sato, H., Wild, T. F. & Kai, C. Establishment of a Nipah virus rescue system. *Proceedings of the National Academy of Sciences of the United States of America* **103,** 16508–16513; 10.1073/pnas.0606972103 (2006).

83. Burgin, C. J., Colella, J. P., Kahn, P. L. & Upham, N. S. How many species of mammals are there? *Journal of Mammalogy* **99,** 1–14; 10.1093/jmammal/gyx147 (2018).

84. Taylor, M. & Tuttle, M. D. (eds.). *Bats. An illustrated guide to all species* (Smithsonian Books, Washington, DC, 2018).

85. Benda, P., Vallo, P., Hulva, P. & Horáček, I. The Egyptian fruit bat Rousettus aegyptiacus (Chiroptera: Pteropodidae) in the Palaearctic: Geographical variation and taxonomic status. *Biologia* **67,** 1230–1244; 10.2478/s11756-012-0105-y (2012).

86. Rousettus aegyptiacus (E.Geoffroy, 1810) in GBIF Secretariat (2023). GBIF Backbone Taxonomy. Available at https://www.gbif.org/species/2432953 (last accessed 09.09.2025) (2023).

87. Amman, B. R., Jones, M. E. B., Sealy, T. K., Uebelhoer, L. S., Schuh, A. J., Bird, B. H., Coleman-McCray, J. D., Martin, B. E., Nichol, S. T. & Towner, J. S. Oral shedding of Marburg virus in experimentally infected Egyptian fruit bats (Rousettus aegyptiacus). *Journal of wildlife diseases* **51,** 113–124; 10.7589/2014-08-198 (2015).

88. Towner, J. S., Amman, B. R., Sealy, T. K., Carroll, S. A. R., Comer, J. A., Kemp, A., Swanepoel, R., Paddock, C. D., Balinandi, S., Khristova, M. L., Formenty, P. B. H., Albarino, C. G., Miller, D. M., Reed, Z. D., Kayiwa, J. T., Mills, J. N., Cannon, D. L., Greer, P. W., Byaruhanga, E., Farnon, E. C., Atimnedi, P., Okware, S., Katongole-Mbidde, E., Downing, R., Tappero, J. W., Zaki, S. R., Ksiazek, T. G., Nichol, S. T. & Rollin, P. E. Isolation of genetically diverse Marburg viruses from Egyptian fruit bats. *PLoS pathogens* **5,** e1000536; 10.1371/journal.ppat.1000536 (2009).

89. Towner, J. S., Pourrut, X., Albariño, C. G., Nkogue, C. N., Bird, B. H., Grard, G., Ksiazek, T. G., Gonzalez, J.-P., Nichol, S. T. & Leroy, E. M. Marburg virus infection detected in a common African bat. *PLoS One* **2,** e764; 10.1371/journal.pone.0000764 (2007).

90. Geldenhuys, M., Ross, N., Dietrich, M., Vries, J. L. de, Mortlock, M., Epstein, J. H., Weyer, J., Pawęska, J. T. & Markotter, W. Viral maintenance and excretion dynamics of coronaviruses within an Egyptian rousette fruit bat maternal colony: considerations for spillover. *Scientific reports* **13,** 15829; 10.1038/s41598-023-42938-w (2023).

91. Amman, B. R., Albariño, C. G., Bird, B. H., Nyakarahuka, L., Sealy, T. K., Balinandi, S., Schuh, A. J., Campbell, S. M., Ströher, U., Jones, M. E. B., Vodzack, M. E., Reeder, D. M., Kaboyo, W., Nichol, S. T. & Towner, J. S. A Recently Discovered Pathogenic Paramyxovirus, Sosuga Virus, is Present in Rousettus aegyptiacus Fruit Bats at Multiple Locations in Uganda. *Journal of wildlife diseases* **51,** 774–779; 10.7589/2015-02-044 (2015).

92. Amman, B. R., Schuh, A. J., Sealy, T. K., Spengler, J. R., Welch, S. R., Kirejczyk, S. G. M., Albariño, C. G., Nichol, S. T. & Towner, J. S. Experimental infection of Egyptian rousette bats (Rousettus aegyptiacus) with Sosuga virus demonstrates potential transmission routes for a bat-borne human pathogenic paramyxovirus. *PLoS neglected tropical diseases* **14,** e0008092; 10.1371/journal.pntd.0008092 (2020).

93. Mackenzie, J. S., Childs, J. E., Field, H. E., Wang, L.-F. & Breed, A. C. The Role of Bats as Reservoir Hosts of Emerging Neuroviruses. In *Neurotropic viral infections. Volume 2:*

Neurotropic retroviruses, DNA viruses, immunity and transmission, edited by C. S. Reiss (Springer International Publishing, Cham, 2016), pp. 403–454.

94. Chua, K. B., Koh, C. L., Hooi, P. S., Wee, K. F., Khong, J. H., Chua, B. H., Chan, Y. P., Lim, M. E. & Lam, S. K. Isolation of Nipah virus from Malaysian Island flying-foxes. *Microbes and infection* **4,** 145–151; 10.1016/s1286-4579(01)01522-2 (2002).

95. Li, W., Shi, Z., Yu, M., Ren, W., Smith, C., Epstein, J. H., Wang, H., Crameri, G., Hu, Z., Zhang, H., Zhang, J., McEachern, J., Field, H., Daszak, P., Eaton, B. T., Zhang, S. & Wang, L.-F. Bats are natural reservoirs of SARS-like coronaviruses. *Science (New York, N.Y.)* **310,** 676–679; 10.1126/science.1118391 (2005).

96. Pei, G., Balkema-Buschmann, A. & Dorhoi, A. Disease tolerance as immune defense strategy in bats: One size fits all? *PLoS pathogens* **20,** e1012471; 10.1371/journal.ppat.1012471 (2024).

97. O'Shea, T. J., Cryan, P. M., Cunningham, A. A., Fooks, A. R., Hayman, D. T. S., Luis, A. D., Peel, A. J., Plowright, R. K. & Wood, J. L. N. Bat flight and zoonotic viruses. *Emerging Infectious Diseases* **20,** 741–745; 10.3201/eid2005.130539 (2014).

98. Kulzer, E. Temperaturregulation bei Flughunden der Gattung Rousettus Gray. *Z. Vergl. Physiol.* **46,** 595–618; 10.1007/BF00298161 (1963).

99. Zhou, P., Tachedjian, M., Wynne, J. W., Boyd, V., Cui, J., Smith, I., Cowled, C., Ng, J. H. J., Mok, L., Michalski, W. P., Mendenhall, I. H., Tachedjian, G., Wang, L.-F. & Baker, M. L. Contraction of the type I IFN locus and unusual constitutive expression of IFN-α in bats. *Proceedings of the National Academy of Sciences of the United States of America* **113,** 2696–2701; 10.1073/pnas.1518240113 (2016).

100. Ahn, M., Chen, V. C., Rozario, P., Ng, W. L., Kong, P. S., Sia, W. R., Kang, A. E. Z., Su, Q., Nguyen, L. H., Zhu, F., Chan, W. O. Y., Tan, C. W., Cheong, W. S., Hey, Y. Y., Foo, R., Guo, F., Lim, Y. T., Li, X., Chia, W. N., Sobota, R. M., Fu, N. Y., Irving, A. T. & Wang, L. F. Bat ASC2 suppresses inflammasomes and ameliorates inflammatory diseases. *Cell* **186,** 2144-2159 e22; 10.1016/j.cell.2023.03.036 (2023).

101. Ahn, M., Anderson, D. E., Zhang, Q., Tan, C. W., Lim, B. L., Luko, K., Wen, M., Chia, W. N., Mani, S., Wang, L. C., Ng, J. H. J., Sobota, R. M., Dutertre, C.-A., Ginhoux, F., Shi, Z.-L., Irving, A. T. & Wang, L.-F. Dampened NLRP3-mediated inflammation in bats and implications for a special viral reservoir host. *Nature microbiology* **4,** 789–799; 10.1038/s41564-019-0371-3 (2019).

102. Zhang, G., Cowled, C., Shi, Z., Huang, Z., Bishop-Lilly, K. A., Fang, X., Wynne, J. W., Xiong, Z., Baker, M. L., Zhao, W., Tachedjian, M., Zhu, Y., Zhou, P., Jiang, X., Ng, J., Yang, L., Wu, L., Xiao, J., Feng, Y., Chen, Y., Sun, X., Zhang, Y., Marsh, G. A., Crameri, G., Broder, C. C., Frey, K. G., Wang, L.-F. & Wang, J. Comparative analysis of bat genomes provides insight into the evolution of flight and immunity. *Science (New York, N.Y.)* **339,** 456–460; 10.1126/science.1230835 (2013).

103. Moreno Santillán, D. D., Lama, T. M., Gutierrez Guerrero, Y. T., Brown, A. M., Donat, P., Zhao, H., Rossiter, S. J., Yohe, L. R., Potter, J. H., Teeling, E. C., Vernes, S. C., Davies, K. T. J., Myers, E., Hughes, G. M., Huang, Z., Hoffmann, F., Corthals, A. P., Ray, D. A. & Dávalos, L. M. Large-scale genome sampling reveals unique immunity and metabolic adaptations in bats. *Molecular ecology* **30,** 6449–6467; 10.1111/mec.16027 (2021).

104. Ahn, M., Cui, J., Irving, A. T. & Wang, L.-F. Unique Loss of the PYHIN Gene Family in Bats Amongst Mammals: Implications for Inflammasome Sensing. *Scientific reports* **6,** 21722; 10.1038/srep21722 (2016).

105. He, Y., Hara, H. & Núñez, G. Mechanism and Regulation of NLRP3 Inflammasome Activation. *Trends in biochemical sciences* **41,** 1012–1021; 10.1016/j.tibs.2016.09.002 (2016).

106. Hornung, V., Ablasser, A., Charrel-Dennis, M., Bauernfeind, F., Horvath, G., Caffrey, D. R., Latz, E. & Fitzgerald, K. A. AIM2 recognizes cytosolic dsDNA and forms a caspase-1-activating inflammasome with ASC. *Nature* **458,** 514–518; 10.1038/nature07725 (2009).

107. Bürckstümmer, T., Baumann, C., Blüml, S., Dixit, E., Dürnberger, G., Jahn, H., Planyavsky, M., Bilban, M., Colinge, J., Bennett, K. L. & Superti-Furga, G. An orthogonal proteomic-genomic screen identifies AIM2 as a cytoplasmic DNA sensor for the inflammasome. *Nature Immunology* **10,** 266–272; 10.1038/ni.1702 (2009).

108. Unterholzner, L., Keating, S. E., Baran, M., Horan, K. A., Jensen, S. B., Sharma, S., Sirois, C. M., Jin, T., Latz, E., Xiao, T. S., Fitzgerald, K. A., Paludan, S. R. & Bowie, A. G. IFI16 is an innate immune sensor for intracellular DNA. *Nature Immunology* **11,** 997–1004; 10.1038/ni.1932 (2010).

109. Ding, Y., Wang, L., Su, L.-K., Frey, J. A., Shao, R., Hunt, K. K. & Yan, D.-H. Antitumor activity of IFIX, a novel interferon-inducible HIN-200 gene, in breast cancer. *Oncogene* **23,** 4556–4566; 10.1038/sj.onc.1207592 (2004).

110. Guito, J. C., Prescott, J. B., Arnold, C. E., Amman, B. R., Schuh, A. J., Spengler, J. R., Sealy, T. K., Harmon, J. R., Coleman-McCray, J. D., Kulcsar, K. A., Nagle, E. R., Kumar, R., Palacios, G. F., Sanchez-Lockhart, M. & Towner, J. S. Asymptomatic Infection of Marburg Virus Reservoir Bats Is Explained by a Strategy of Immunoprotective Disease Tolerance. *Current biology : CB* **31,** 257-270.e5; 10.1016/j.cub.2020.10.015 (2021).

111. Prescott, J., Guito, J. C., Spengler, J. R., Arnold, C. E., Schuh, A. J., Amman, B. R., Sealy, T. K., Guerrero, L. W., Palacios, G. F., Sanchez-Lockhart, M., Albariño, C. G. & Towner, J. S. Rousette Bat Dendritic Cells Overcome Marburg Virus-Mediated Antiviral Responses by Upregulation of Interferon-Related Genes While Downregulating Proinflammatory Disease Mediators. *mSphere* **4**; 10.1128/mSphere.00728-19 (2019).

112. Irving, A. T., Ahn, M., Goh, G., Anderson, D. E. & Wang, L.-F. Lessons from the host defences of bats, a unique viral reservoir. *Nature* **589,** 363–370; 10.1038/s41586-020-03128-0 (2021).

113. Banerjee, A., Baker, M. L., Kulcsar, K., Misra, V., Plowright, R. & Mossman, K. Novel Insights Into Immune Systems of Bats. *Frontiers in immunology* **11,** 26; 10.3389/fimmu.2020.00026 (2020).

114. Begeman, L., Suu-Ire, R., Banyard, A. C., Drosten, C., Eggerbauer, E., Freuling, C. M., Gibson, L., Goharriz, H., Horton, D. L., Jennings, D., Marston, D. A., Ntiamoa-Baidu, Y., Riesle Sbarbaro, S., Selden, D., Wise, E. L., Kuiken, T., Fooks, A. R., Müller, T., Wood, J. L. N. & Cunningham, A. A. Experimental Lagos bat virus infection in straw-colored fruit bats: A suitable model for bat rabies in a natural reservoir species. *PLoS neglected tropical diseases* **14,** e0008898; 10.1371/journal.pntd.0008898 (2020).

115. Suu-Ire, R., Begeman, L., Banyard, A. C., Breed, A. C., Drosten, C., Eggerbauer, E., Freuling, C. M., Gibson, L., Goharriz, H., Horton, D. L., Jennings, D., Kuzmin, I. V., Marston, D., Ntiamoa-Baidu, Y., Riesle Sbarbaro, S., Selden, D., Wise, E. L., Kuiken, T., Fooks, A. R., Müller, T., Wood, J. L. N. & Cunningham, A. A. Pathogenesis of bat rabies in a natural reservoir: Comparative susceptibility of the straw-colored fruit bat (Eidolon helvum) to three strains of Lagos bat virus. *PLoS neglected tropical diseases* **12,** e0006311; 10.1371/journal.pntd.0006311 (2018).

116. Jackson, F. R., Turmelle, A. S., Farino, D. M., Franka, R., McCracken, G. F. & Rupprecht, C. E. Experimental rabies virus infection of big brown bats (Eptesicus fuscus). *Journal of wildlife diseases* **44,** 612–621; 10.7589/0090-3558-44.3.612 (2008).

117. Turner GG, Reeder DAM, Coleman JTH. *A five-year assessment of mortality and geographic spread of white-nose syndrome in North American bats and a look to the future* (2011).

118. Frick, W. F., Pollock, J. F., Hicks, A. C., Langwig, K. E., Reynolds, D. S., Turner, G. G., Butchkoski, C. M. & Kunz, T. H. An emerging disease causes regional population collapse of a common North American bat species. *Science (New York, N.Y.)* **329,** 679–682; 10.1126/science.1188594 (2010).

119. Lindenmann, J., Burke, D. C. & Isaacs, A. Studies on the Production, Mode of Action and Properties of Interferon. *British Journal of Experimental Pathology* **38,** 551–562 (1957).

120. Isaacs, A. & Lindenmann, J. Virus interference. I. The interferon. *Proceedings of the Royal Society of London. Series B, Biological sciences* **147,** 258–267; 10.1098/rspb.1957.0048 (1957).

121. Isaacs, A., Lindenmann, J. & VALENTINE, R. C. Virus interference. II. Some properties of interferon. *Proceedings of the Royal Society of London. Series B, Biological sciences* **147,** 268–273; 10.1098/rspb.1957.0049 (1957).

122. Platanias, L. C. Mechanisms of type-I- and type-II-interferon-mediated signalling. *Nat Rev Immunol* **5,** 375–386; 10.1038/nri1604 (2005).

123. Taylor, M. W. Interferons. *Viruses and Man: A History of Interactions,* 101–119; 10.1007/978-3-319-07758-1_7 (2014).

124. Nagano, Y., Kojima, Y. & Sawai, Y. Immunité et interférence dans la vaccine; inhibition de l'infection dermique par le virus inactivé. *Comptes rendus des seances de la Societe de biologie et de ses filiales* **148,** 750–752 (1954).

125. Tang, D., Kang, R., Coyne, C. B., Zeh, H. J. & Lotze, M. T. PAMPs and DAMPs: signal 0s that spur autophagy and immunity. *Immunological Reviews* **249,** 158–175; 10.1111/j.1600-065X.2012.01146.x (2012).

126. Clayton, E. & Munir, M. Fundamental Characteristics of Bat Interferon Systems. *Frontiers in Cellular and Infection Microbiology* **10**; 10.3389/fcimb.2020.527921 (2020).

127. Thompson, M. R., Kaminski, J. J., Kurt-Jones, E. A. & Fitzgerald, K. A. Pattern Recognition Receptors and the Innate Immune Response to Viral Infection. *Viruses* **3,** 920–940; 10.3390/v3060920 (2011).

128. Rehwinkel, J. & Gack, M. U. RIG-I-like receptors: their regulation and roles in RNA sensing. *Nature reviews. Immunology* **20,** 537–551; 10.1038/s41577-020-0288-3 (2020).

129. Ullah, M. O., Sweet, M. J., Mansell, A., Kellie, S. & Kobe, B. TRIF-dependent TLR signaling, its functions in host defense and inflammation, and its potential as a therapeutic target. *Journal of leukocyte biology* **100,** 27–45; 10.1189/jlb.2RI1115-531R (2016).

130. Wheelock, E. F. Interferon-Like Virus-Inhibitor Induced in Human Leukocytes by Phytohemagglutinin. *Science (New York, N.Y.)* **149,** 310–311; 10.1126/science.149.3681.310 (1965).

131. Johnson, H. M., Stanton, G. J. & Baron, S. Relative Ability of Mitogens to Stimulate Production of Interferon by Lymphoid Cells and to Induce Suppression of the in Vitro Immune Response. *Experimental Biology and Medicine* **154,** 138–141; 10.3181/00379727-154-39622 (1977).

132. Bhat, P., Leggatt, G., Waterhouse, N. & Frazer, I. H. Interferon-γ derived from cytotoxic lymphocytes directly enhances their motility and cytotoxicity. *Cell Death Dis* **8,** e2836; 10.1038/cddis.2017.67 (2017).

133. Kotenko, S. V., Gallagher, G., Baurin, V. V., Lewis-Antes, A., Shen, M., Shah, N. K., Langer, J. A., Sheikh, F., Dickensheets, H. & Donnelly, R. P. IFN-lambdas mediate antiviral protection through a distinct class II cytokine receptor complex. *Nature Immunology* **4,** 69–77; 10.1038/ni875 (2003).

134. Goel, R. R., Kotenko, S. V. & Kaplan, M. J. Interferon lambda in inflammation and autoimmune rheumatic diseases. *Nature reviews. Rheumatology* **17,** 349–362; 10.1038/s41584-021-00606-1 (2021).

135. Yang, L., Luo, Y., Wei, J. & He, S. Integrative genomic analyses on IL28RA, the common receptor of interferon-lambda1, -lambda2 and -lambda3. *International journal of molecular medicine* **25,** 807–812 (2010).

136. Sheppard, P., Kindsvogel, W., Xu, W., Henderson, K., Schlutsmeyer, S., Whitmore, T. E., Kuestner, R., Garrigues, U., Birks, C., Roraback, J., Ostrander, C., Dong, D., Shin, J., Presnell, S., Fox, B., Haldeman, B., Cooper, E., Taft, D., Gilbert, T., Grant, F. J., Tackett, M., Krivan, W., McKnight, G., Clegg, C., Foster, D. & Klucher, K. M. IL-28, IL-29 and their class II cytokine receptor IL-28R. *Nature Immunology* **4,** 63–68; 10.1038/ni873 (2003).

137. Weerd, N. A. de & Nguyen, T. The interferons and their receptors--distribution and regulation. *Immunology and cell biology* **90,** 483–491; 10.1038/icb.2012.9 (2012).

138. Sommereyns, C., Paul, S., Staeheli, P. & Michiels, T. IFN-lambda (IFN-lambda) is expressed in a tissue-dependent fashion and primarily acts on epithelial cells in vivo. *PLoS pathogens* **4,** e1000017; 10.1371/journal.ppat.1000017 (2008).

139. Lee, A. K., Kulcsar, K. A., Elliott, O., Khiabanian, H., Nagle, E. R., Jones, M. E. B., Amman, B. R., Sanchez-Lockhart, M., Towner, J. S., Palacios, G. & Rabadan, R. De novo transcriptome reconstruction and annotation of the Egyptian rousette bat. *BMC genomics* **16,** 1033; 10.1186/s12864-015-2124-x (2015).

140. Kelley, J., Bono, B. de & Trowsdale, J. IRIS: a database surveying known human immune system genes. *Genomics* **85,** 503–511; 10.1016/j.ygeno.2005.01.009 (2005).

141. Cowled, C., Baker, M., Tachedjian, M., Zhou, P., Bulach, D. & Wang, L.-F. Molecular characterisation of Toll-like receptors in the black flying fox Pteropus alecto. *Dev Comp Immunol* **35,** 7–18; 10.1016/j.dci.2010.07.006 (2011).

142. Papenfuss, A. T., Baker, M. L., Feng, Z.-P., Tachedjian, M., Crameri, G., Cowled, C., Ng, J., Janardhana, V., Field, H. E. & Wang, L.-F. The immune gene repertoire of an important viral reservoir, the Australian black flying fox. *BMC genomics* **13,** 261; 10.1186/1471-2164-13-261 (2012).

143. Cowled, C., Baker, M. L., Zhou, P., Tachedjian, M. & Wang, L.-F. Molecular characterisation of RIG-I-like helicases in the black flying fox, Pteropus alecto. *Dev Comp Immunol* **36,** 657–664; 10.1016/j.dci.2011.11.008 (2012).

144. Feng, H., Sander, A.-L., Moreira-Soto, A., Yamane, D., Drexler, J. F. & Lemon, S. M. Hepatovirus 3ABC proteases and evolution of mitochondrial antiviral signaling protein (MAVS). *Journal of hepatology* **71,** 25–34; 10.1016/j.jhep.2019.02.020 (2019).

145. Fu, F., Shao, Q., Wang, J., Zhang, J., Wang, Z., Ma, J., Yan, Y., Sun, J. & Cheng, Y. Bat MAVS involved in antiviral innate immunity via regulating IFN-beta production. *Dev Comp Immunol,* 104724; 10.1016/j.dci.2023.104724 (2023).

146. Zhou, P., Cowled, C., Wang, L.-F. & Baker, M. L. Bat Mx1 and Oas1, but not Pkr are highly induced by bat interferon and viral infection. *Dev Comp Immunol* **40,** 240–247; 10.1016/j.dci.2013.03.006 (2013).

147. Zhou, P., Cowled, C., Mansell, A., Monaghan, P., Green, D., Wu, L., Shi, Z., Wang, L.-F. & Baker, M. L. IRF7 in the Australian black flying fox, Pteropus alecto: evidence for a

unique expression pattern and functional conservation. *PLoS One* **9,** e103875; 10.1371/journal.pone.0103875 (2014).

148. Banerjee, A., Zhang, X., Yip, A., Schulz, K. S., Irving, A. T., Bowdish, D., Golding, B., Wang, L.-F. & Mossman, K. Positive Selection of a Serine Residue in Bat IRF3 Confers Enhanced Antiviral Protection. *iScience* **23,** 100958; 10.1016/j.isci.2020.100958 (2020).

149. Pavlovich, S. S., Lovett, S. P., Koroleva, G., Guito, J. C., Arnold, C. E., Nagle, E. R., Kulcsar, K., Lee, A., Thibaud-Nissen, F., Hume, A. J., Mühlberger, E., Uebelhoer, L. S., Towner, J. S., Rabadan, R., Sanchez-Lockhart, M., Kepler, T. B. & Palacios, G. The Egyptian Rousette Genome Reveals Unexpected Features of Bat Antiviral Immunity. *Cell* **173,** 1098-1110.e18; 10.1016/j.cell.2018.03.070 (2018).

150. Omatsu, T., Bak, E.-J., Ishii, Y., Kyuwa, S., Tohya, Y., Akashi, H. & Yoshikawa, Y. Induction and sequencing of Rousette bat interferon alpha and beta genes. *Veterinary immunology and immunopathology* **124,** 169–176; 10.1016/j.vetimm.2008.03.004 (2008).

151. Zhang, Q., Zeng, L.-P., Zhou, P., Irving, A. T., Li, S., Shi, Z.-L. & Wang, L.-F. IFNAR2-dependent gene expression profile induced by IFN-α in Pteropus alecto bat cells and impact of IFNAR2 knockout on virus infection. *PLoS One* **12,** e0182866; 10.1371/journal.pone.0182866 (2017).

152. Zhou, P., Cowled, C., Todd, S., Crameri, G., Virtue, E. R., Marsh, G. A., Klein, R., Shi, Z., Wang, L.-F. & Baker, M. L. Type III IFNs in pteropid bats: differential expression patterns provide evidence for distinct roles in antiviral immunity. *Journal of immunology (Baltimore, Md. : 1950)* **186,** 3138–3147; 10.4049/jimmunol.1003115 (2011).

153. Zhou, P., Cowled, C., Marsh, G. A., Shi, Z., Wang, L.-F. & Baker, M. L. Type III IFN receptor expression and functional characterisation in the pteropid bat, Pteropus alecto. *PLoS One* **6,** e25385; 10.1371/journal.pone.0025385 (2011).

154. Fujii, H., Watanabe, S., Yamane, D., Ueda, N., Iha, K., Taniguchi, S., Kato, K., Tohya, Y., Kyuwa, S., Yoshikawa, Y. & Akashi, H. Functional analysis of Rousettus aegyptiacus "signal transducer and activator of transcription 1" (STAT1). *Dev Comp Immunol* **34,** 598–602; 10.1016/j.dci.2010.01.004 (2010).

155. Glennon, N. B., Jabado, O., Lo, M. K. & Shaw, M. L. Transcriptome Profiling of the Virus-Induced Innate Immune Response in Pteropus vampyrus and Its Attenuation by Nipah Virus Interferon Antagonist Functions. *Journal of virology* **89,** 7550–7566; 10.1128/JVI.00302-15 (2015).

156. Jebb, D., Huang, Z., Pippel, M., Hughes, G. M., Lavrichenko, K., Devanna, P., Winkler, S., Jermiin, L. S., Skirmuntt, E. C., Katzourakis, A., Burkitt-Gray, L., Ray, D. A., Sullivan, K. A. M., Roscito, J. G., Kirilenko, B. M., Dávalos, L. M., Corthals, A. P., Power, M. L., Jones, G., Ransome, R. D., Dechmann, D. K. N., Locatelli, A. G., Puechmaille, S. J., Fedrigo, O., Jarvis, E. D., Hiller, M., Vernes, S. C., Myers, E. W. & Teeling, E. C. Six reference-quality genomes reveal evolution of bat adaptations. *Nature* **583,** 578–584; 10.1038/s41586-020-2486-3 (2020).

157. La Cruz-Rivera, P. C. de, Kanchwala, M., Liang, H., Kumar, A., Wang, L.-F., Xing, C. & Schoggins, J. W. The IFN Response in Bats Displays Distinctive IFN-Stimulated Gene Expression Kinetics with Atypical RNASEL Induction. *Journal of immunology (Baltimore, Md. : 1950)* **200,** 209–217; 10.4049/jimmunol.1701214 (2018).

158. Fuchs, J., Hölzer, M., Schilling, M., Patzina, C., Schoen, A., Hoenen, T., Zimmer, G., Marz, M., Weber, F., Müller, M. A. & Kochs, G. Evolution and Antiviral Specificities of Interferon-Induced Mx Proteins of Bats against Ebola, Influenza, and Other RNA Viruses. *Journal of virology* **91**; 10.1128/JVI.00361-17 (2017).

159. Zhou, A., Hassel, B. A. & Silverman, R. H. Expression cloning of 2-5A-dependent RNAase: a uniquely regulated mediator of interferon action. *Cell* **72,** 753–765; 10.1016/0092-8674(93)90403-d (1993).

160. Li, Y., Dong, B., Wei, Z., Silverman, R. H. & Weiss, S. R. Activation of RNase L in Egyptian Rousette Bat-Derived RoNi/7 Cells Is Dependent Primarily on OAS3 and Independent of MAVS Signaling. *mBio* **10**; 10.1128/mbio.02414-19 (2019).

161. Malathi, K., Dong, B., Gale, M. & Silverman, R. H. Small self-RNA generated by RNase L amplifies antiviral innate immunity. *Nature* **448,** 816–819; 10.1038/nature06042 (2007).

162. Li, G., Xiang, Y., Sabapathy, K. & Silverman, R. H. An apoptotic signaling pathway in the interferon antiviral response mediated by RNase L and c-Jun NH2-terminal kinase. *The Journal of biological chemistry* **279,** 1123–1131; 10.1074/jbc.M305893200 (2004).

163. Morales, A. E., Dong, Y., Brown, T., Baid, K., Kontopoulos, D.-G., Gonzalez, V., Huang, Z., Ahmed, A.-W., Bhuinya, A., Hilgers, L., Winkler, S., Hughes, G., Li, X., Lu, P., Yang, Y., Kirilenko, B. M., Devanna, P., Lama, T. M., Nissan, Y., Pippel, M., Dávalos, L. M., Vernes, S. C., Puechmaille, S. J., Rossiter, S. J., Yovel, Y., Prescott, J. B., Kurth, A., Ray, D. A., Lim, B. K., Myers, E., Teeling, E. C., Banerjee, A., Irving, A. T. & Hiller, M. Bat genomes illuminate adaptations to viral tolerance and disease resistance. *Nature* **638,** 449–458; 10.1038/s41586-024-08471-0 (2025).

164. van Tol, S., Hage, A., Rajsbaum, R. & Freiberg, A. N. Pteropus vampyrus TRIM40 Is an Interferon-Stimulated Gene That Antagonizes RIG-I-like Receptors. *Viruses* **15**; 10.3390/v15112147 (2023).

165. Banerjee, A., Rapin, N., Bollinger, T. & Misra, V. Lack of inflammatory gene expression in bats: a unique role for a transcription repressor. *Scientific reports* **7,** 2232; 10.1038/s41598-017-01513-w (2017).

166. Jacquet, S., Culbertson, M., Zhang, C., El Filali, A., La Myre Mory, C. de, Pons, J. B., Filippi-Codaccioni, O., Lauterbur, M. E., Ngoubangoye, B., Duhayer, J., Verez, C., Park, C., Dahoui, C., Carey, C. M., Brennan, G., Enard, D., Cimarelli, A., Rothenburg, S., Elde, N. C., Pontier, D. & Etienne, L. Adaptive duplication and genetic diversification of protein kinase R contribute to the specificity of bat-virus interactions. *Sci Adv* **8,** eadd7540; 10.1126/sciadv.add7540 (2022).

167. Sudhakar, A., Ramachandran, A., Ghosh, S., Hasnain, S. E., Kaufman, R. J. & Ramaiah, K. V. Phosphorylation of serine 51 in initiation factor 2 alpha (eIF2 alpha) promotes complex formation between eIF2 alpha(P) and eIF2B and causes inhibition in the guanine nucleotide exchange activity of eIF2B. *Biochemistry* **39,** 12929–12938; 10.1021/bi0008682 (2000).

168. Gilfoy, F. D. & Mason, P. W. West Nile virus-induced interferon production is mediated by the double-stranded RNA-dependent protein kinase PKR. *Journal of virology* **81,** 11148–11158; 10.1128/JVI.00446-07 (2007).

169. Zhang, S., Sun, Y., Chen, H., Dai, Y., Zhan, Y., Yu, S., Qiu, X., Tan, L., Song, C. & Ding, C. Activation of the PKR/eIF2α signaling cascade inhibits replication of Newcastle disease virus. *Virol J* **11,** 62; 10.1186/1743-422X-11-62 (2014).

170. Hayward, J. A., Tachedjian, M., Cui, J., Cheng, A. Z., Johnson, A., Baker, M. L., Harris, R. S., Wang, L.-F. & Tachedjian, G. Differential Evolution of Antiretroviral Restriction Factors in Pteropid Bats as Revealed by APOBEC3 Gene Complexity. *Molecular biology and evolution* **35,** 1626–1637; 10.1093/molbev/msy048 (2018).

171. Kato, A., Cortese-Grogan, C., Moyer, S. A., Sugahara, F., Sakaguchi, T., Kubota, T., Otsuki, N., Kohase, M., Tashiro, M. & Nagai, Y. Characterization of the amino acid residues of sendai virus C protein that are critically involved in its interferon antagonism and RNA synthesis down-regulation. *Journal of virology* **78,** 7443–7454; 10.1128/JVI.78.14.7443-7454.2004 (2004).

172. Kubota, T., Yokosawa, N., Yokota, S.-I., Fujii, N., Tashiro, M. & Kato, A. Mumps virus V protein antagonizes interferon without the complete degradation of STAT1. *Journal of virology* **79,** 4451–4459; 10.1128/JVI.79.7.4451-4459.2005 (2005).

173. Parisien, J. P., Lau, J. F., Rodriguez, J. J., Sullivan, B. M., Moscona, A., Parks, G. D., Lamb, R. A. & Horvath, C. M. The V protein of human parainfluenza virus 2 antagonizes type I interferon responses by destabilizing signal transducer and activator of transcription 2. *Virology* **283,** 230–239; 10.1006/viro.2001.0856 (2001).

174. Park, M.-S., Shaw, M. L., Muñoz-Jordan, J., Cros, J. F., Nakaya, T., Bouvier, N., Palese, P., García-Sastre, A. & Basler, C. F. Newcastle disease virus (NDV)-based assay demonstrates interferon-antagonist activity for the NDV V protein and the Nipah virus V, W, and C proteins. *Journal of virology* **77,** 1501–1511; 10.1128/jvi.77.2.1501-1511.2003 (2003).

175. Hartenian, E., Nandakumar, D., Lari, A., Ly, M., Tucker, J. M. & Glaunsinger, B. A. The molecular virology of coronaviruses. *The Journal of biological chemistry* **295,** 12910–12934; 10.1074/jbc.REV120.013930 (2020).

176. Rodriguez, J. J., Cruz, C. D. & Horvath, C. M. Identification of the nuclear export signal and STAT-binding domains of the Nipah virus V protein reveals mechanisms underlying interferon evasion. *Journal of virology* **78,** 5358–5367; 10.1128/jvi.78.10.5358-5367.2004 (2004).

177. Ciancanelli, M. J., Volchkova, V. A., Shaw, M. L., Volchkov, V. E. & Basler, C. F. Nipah virus sequesters inactive STAT1 in the nucleus via a P gene-encoded mechanism. *Journal of virology* **83,** 7828–7841; 10.1128/JVI.02610-08 (2009).

178. Andrejeva, J., Young, D. F., Goodbourn, S. & Randall, R. E. Degradation of STAT1 and STAT2 by the V proteins of simian virus 5 and human parainfluenza virus type 2, respectively: consequences for virus replication in the presence of alpha/beta and gamma interferons. *Journal of virology* **76,** 2159–2167; 10.1128/jvi.76.5.2159-2167.2002 (2002).

179. Virtue, E. R., Marsh, G. A. & Wang, L.-F. Interferon signaling remains functional during henipavirus infection of human cell lines. *Journal of virology* **85,** 4031–4034; 10.1128/JVI.02412-10 (2011).

180. Andrejeva, J., Childs, K. S., Young, D. F., Carlos, T. S., Stock, N., Goodbourn, S. & Randall, R. E. The V proteins of paramyxoviruses bind the IFN-inducible RNA helicase, mda-5, and inhibit its activation of the IFN-beta promoter. *Proc Natl Acad Sci U S A* **101,** 17264–17269; 10.1073/pnas.0407639101 (2004).

181. Childs, K., Stock, N., Ross, C., Andrejeva, J., Hilton, L., Skinner, M., Randall, R. & Goodbourn, S. mda-5, but not RIG-I, is a common target for paramyxovirus V proteins. *Virology* **359,** 190–200; 10.1016/j.virol.2006.09.023 (2007).

182. Davis, M. E., Wang, M. K., Rennick, L. J., Full, F., Gableske, S., Mesman, A. W., Gringhuis, S. I., Geijtenbeek, T. B. H., Duprex, W. P. & Gack, M. U. Antagonism of the phosphatase PP1 by the measles virus V protein is required for innate immune escape of MDA5. *Cell host & microbe* **16,** 19–30; 10.1016/j.chom.2014.06.007 (2014).

183. Wies, E., Wang, M. K., Maharaj, N. P., Chen, K., Zhou, S., Finberg, R. W. & Gack, M. U. Dephosphorylation of the RNA sensors RIG-I and MDA5 by the phosphatase PP1 is essential for innate immune signaling. *Immunity* **38,** 437–449; 10.1016/j.immuni.2012.11.018 (2013).

184. Kato, H., Takeuchi, O., Sato, S., Yoneyama, M., Yamamoto, M., Matsui, K., Uematsu, S., Jung, A., Kawai, T., Ishii, K. J., Yamaguchi, O., Otsu, K., Tsujimura, T., Koh, C.-S., Reis e Sousa, C., Matsuura, Y., Fujita, T. & Akira, S. Differential roles of MDA5 and RIG-I helicases in the recognition of RNA viruses. *Nature* **441,** 101–105; 10.1038/nature04734 (2006).

185. Kawai, T., Takahashi, K., Sato, S., Coban, C., Kumar, H., Kato, H., Ishii, K. J., Takeuchi, O. & Akira, S. IPS-1, an adaptor triggering RIG-I- and Mda5-mediated type I interferon induction. *Nature Immunology* **6,** 981–988; 10.1038/ni1243 (2005).

186. Yoneyama, M. & Fujita, T. Structural mechanism of RNA recognition by the RIG-I-like receptors. *Immunity* **29,** 178–181; 10.1016/j.immuni.2008.07.009 (2008).

187. Satoh, T., Kato, H., Kumagai, Y., Yoneyama, M., Sato, S., Matsushita, K., Tsujimura, T., Fujita, T., Akira, S. & Takeuchi, O. LGP2 is a positive regulator of RIG-I- and MDA5-

mediated antiviral responses. *Proceedings of the National Academy of Sciences of the United States of America* **107,** 1512–1517; 10.1073/pnas.0912986107 (2010).

188. Venkataraman, T., Valdes, M., Elsby, R., Kakuta, S., Caceres, G., Saijo, S., Iwakura, Y. & Barber, G. N. Loss of DExD/H box RNA helicase LGP2 manifests disparate antiviral responses. *Journal of immunology (Baltimore, Md. : 1950)* **178,** 6444–6455; 10.4049/jimmunol.178.10.6444 (2007).

189. Childs, K., Randall, R. & Goodbourn, S. Paramyxovirus V proteins interact with the RNA Helicase LGP2 to inhibit RIG-I-dependent interferon induction. *Journal of virology* **86,** 3411–3421; 10.1128/JVI.06405-11 (2012).

190. Parisien, J.-P., Bamming, D., Komuro, A., Ramachandran, A., Rodriguez, J. J., Barber, G., Wojahn, R. D. & Horvath, C. M. A shared interface mediates paramyxovirus interference with antiviral RNA helicases MDA5 and LGP2. *Journal of virology* **83,** 7252–7260; 10.1128/JVI.00153-09 (2009).

191. Enchéry, F., Dumont, C., Iampietro, M., Pelissier, R., Aurine, N., Bloyet, L.-M., Carbonnelle, C., Mathieu, C., Journo, C., Gerlier, D. & Horvat, B. Nipah virus W protein harnesses nuclear 14-3-3 to inhibit NF-κB-induced proinflammatory response. *Communications biology* **4,** 1292; 10.1038/s42003-021-02797-5 (2021).

192. Edwards, M. R., Hoad, M., Tsimbalyuk, S., Menicucci, A. R., Messaoudi, I., Forwood, J. K. & Basler, C. F. Henipavirus W Proteins Interact with 14-3-3 To Modulate Host Gene Expression. *Journal of virology* **94**; 10.1128/JVI.00373-20 (2020).

193. Yoneda, M., Guillaume, V., Sato, H., Fujita, K., Georges-Courbot, M.-C., Ikeda, F., Omi, M., Muto-Terao, Y., Wild, T. F. & Kai, C. The nonstructural proteins of Nipah virus play a key role in pathogenicity in experimentally infected animals. *PLoS One* **5,** e12709; 10.1371/journal.pone.0012709 (2010).

194. Satterfield, B. A., Cross, R. W., Fenton, K. A., Borisevich, V., Agans, K. N., Deer, D. J., Graber, J., Basler, C. F., Geisbert, T. W. & Mire, C. E. Nipah Virus C and W Proteins Contribute to Respiratory Disease in Ferrets. *Journal of virology* **90,** 6326–6343; 10.1128/JVI.00215-16 (2016).

195. Mathieu, C., Guillaume, V., Volchkova, V. A., Pohl, C., Jacquot, F., Looi, R. Y., Wong, K. T., Legras-Lachuer, C., Volchkov, V. E., Lachuer, J. & Horvat, B. Nonstructural Nipah virus C protein regulates both the early host proinflammatory response and viral virulence. *Journal of virology* **86,** 10766–10775; 10.1128/jvi.01203-12 (2012).

196. Lo, M. K., Peeples, M. E., Bellini, W. J., Nichol, S. T., Rota, P. A. & Spiropoulou, C. F. Distinct and overlapping roles of Nipah virus P gene products in modulating the human endothelial cell antiviral response. *PLoS One* **7,** e47790; 10.1371/journal.pone.0047790 (2012).

197. Sleeman, K., Bankamp, B., Hummel, K. B., Lo, M. K., Bellini, W. J. & Rota, P. A. The C, V and W proteins of Nipah virus inhibit minigenome replication. *The Journal of general virology* **89,** 1300–1308; 10.1099/vir.0.83582-0 (2008).

198. Pfaller, C. K., Radeke, M. J., Cattaneo, R. & Samuel, C. E. Measles Virus C Protein Impairs Production of Defective Copyback Double-Stranded Viral RNA and Activation of Protein Kinase R. *J Virol* **88,** 456–468; 10.1128/JVI.02572-13 (2014).

199. Yamaguchi, M., Kitagawa, Y., Zhou, M., Itoh, M. & Gotoh, B. An anti-interferon activity shared by paramyxovirus C proteins: inhibition of Toll-like receptor 7/9-dependent alpha interferon induction. *FEBS letters* **588,** 28–34; 10.1016/j.febslet.2013.11.015 (2014).

200. Hagmaier, K., Stock, N., Goodbourn, S., Wang, L.-F. & Randall, R. A single amino acid substitution in the V protein of Nipah virus alters its ability to block interferon signalling in cells from different species. *The Journal of general virology* **87,** 3649–3653; 10.1099/vir.0.82261-0 (2006).

201. Virtue, E. R., Marsh, G. A., Baker, M. L. & Wang, L.-F. Interferon production and signaling pathways are antagonized during henipavirus infection of fruit bat cell lines. *PLoS One* **6,** e22488; 10.1371/journal.pone.0022488 (2011).

202. Wynne, J. W., Shiell, B. J., Marsh, G. A., Boyd, V., Harper, J. A., Heesom, K., Monaghan, P., Zhou, P., Payne, J., Klein, R., Todd, S., Mok, L., Green, D., Bingham, J., Tachedjian, M., Baker, M. L., Matthews, D. & Wang, L.-F. Proteomics informed by transcriptomics reveals Hendra virus sensitizes bat cells to TRAIL-mediated apoptosis. *Genome biology* **15,** 532; 10.1186/PREACCEPT-1718798964145132 (2014).

203. Chen, M., Tachedjian, M., Marsh, G. A., Cui, J. & Wang, L.-F. Distinct Cell Transcriptomic Landscapes Upon Henipavirus Infections. *Frontiers in microbiology* **11,** 986; 10.3389/fmicb.2020.00986 (2020).

204. Jheng, J.-R., Ho, J.-Y. & Horng, J.-T. ER stress, autophagy, and RNA viruses. *Frontiers in microbiology* **5,** 388; 10.3389/fmicb.2014.00388 (2014).

205. Halperin, L., Jung, J. & Michalak, M. The many functions of the endoplasmic reticulum chaperones and folding enzymes. *IUBMB life* **66,** 318–326; 10.1002/iub.1272 (2014).

206. Fribley, A., Zhang, K. & Kaufman, R. J. Regulation of apoptosis by the unfolded protein response. *Methods in molecular biology (Clifton, N.J.)* **559,** 191–204; 10.1007/978-1-60327-017-5_14 (2009).

207. Harding, H. P., Zhang, Y., Bertolotti, A., Zeng, H. & Ron, D. Perk is essential for translational regulation and cell survival during the unfolded protein response. *Molecular cell* **5,** 897–904; 10.1016/s1097-2765(00)80330-5 (2000).

208. Li, A., Song, N.-J., Riesenberg, B. P. & Li, Z. The Emerging Roles of Endoplasmic Reticulum Stress in Balancing Immunity and Tolerance in Health and Diseases: Mechanisms and Opportunities. *Frontiers in immunology* **10,** 3154; 10.3389/fimmu.2019.03154 (2019).

209. Harding, H. P., Novoa, I., Zhang, Y., Zeng, H., Wek, R., Schapira, M. & Ron, D. Regulated translation initiation controls stress-induced gene expression in mammalian cells. *Molecular cell* **6,** 1099–1108; 10.1016/S1097-2765(00)00108-8 (2000).

210. Harding, H. P., Zhang, Y., Zeng, H., Novoa, I., Lu, P. D., Calfon, M., Sadri, N., Yun, C., Popko, B., Paules, R., Stojdl, D. F., Bell, J. C., Hettmann, T., Leiden, J. M. & Ron, D. An integrated stress response regulates amino acid metabolism and resistance to oxidative stress. *Molecular cell* **11,** 619–633; 10.1016/s1097-2765(03)00105-9 (2003).

211. Novoa, I., Zeng, H., Harding, H. P. & Ron, D. Feedback inhibition of the unfolded protein response by GADD34-mediated dephosphorylation of eIF2alpha. *The Journal of cell biology* **153,** 1011–1022; 10.1083/jcb.153.5.1011 (2001).

212. Connor, J. H., Weiser, D. C., Li, S., Hallenbeck, J. M. & Shenolikar, S. Growth arrest and DNA damage-inducible protein GADD34 assembles a novel signaling complex containing protein phosphatase 1 and inhibitor 1. *Molecular and Cellular Biology* **21,** 6841–6850; 10.1128/MCB.21.20.6841-6850.2001 (2001).

213. Yamaguchi, H. & Wang, H.-G. CHOP is involved in endoplasmic reticulum stress-induced apoptosis by enhancing DR5 expression in human carcinoma cells. *The Journal of biological chemistry* **279,** 45495–45502; 10.1074/jbc.M406933200 (2004).

214. Marciniak, S. J., Yun, C. Y., Oyadomari, S., Novoa, I., Zhang, Y., Jungreis, R., Nagata, K., Harding, H. P. & Ron, D. CHOP induces death by promoting protein synthesis and oxidation in the stressed endoplasmic reticulum. *Genes & development* **18,** 3066–3077; 10.1101/gad.1250704 (2004).

215. McCullough, K. D., Martindale, J. L., Klotz, L. O., Aw, T. Y. & Holbrook, N. J. Gadd153 sensitizes cells to endoplasmic reticulum stress by down-regulating Bcl2 and perturbing the cellular redox state. *Molecular and Cellular Biology* **21,** 1249–1259; 10.1128/MCB.21.4.1249-1259.2001 (2001).

216. Zong, W.-X., Li, C., Hatzivassiliou, G., Lindsten, T., Yu, Q.-C., Yuan, J. & Thompson, C. B. Bax and Bak can localize to the endoplasmic reticulum to initiate apoptosis. *The Journal of cell biology* **162,** 59–69; 10.1083/jcb.200302084 (2003).

217. Crompton, M. The mitochondrial permeability transition pore and its role in cell death. *Biochemical Journal* **341 (Pt 2),** 233–249 (1999).

218. Nakagawa, T. & Yuan, J. Cross-talk between two cysteine protease families. Activation of caspase-12 by calpain in apoptosis. *The Journal of cell biology* **150,** 887–894; 10.1083/jcb.150.4.887 (2000).

219. Rao, R. V., Hermel, E., Castro-Obregon, S., del Rio, G., Ellerby, L. M., Ellerby, H. M. & Bredesen, D. E. Coupling endoplasmic reticulum stress to the cell death program. Mechanism of caspase activation. *The Journal of biological chemistry* **276,** 33869–33874; 10.1074/jbc.M102225200 (2001).

220. Tan, Y., Dourdin, N., Wu, C., Veyra, T. de, Elce, J. S. & Greer, P. A. Ubiquitous calpains promote caspase-12 and JNK activation during endoplasmic reticulum stress-induced apoptosis. *The Journal of biological chemistry* **281,** 16016–16024; 10.1074/jbc.M601299200 (2006).

221. Hengartner, M. O. The biochemistry of apoptosis. *Nature* **407,** 770–776; 10.1038/35037710 (2000).

222. Shi, Y. Mechanisms of Caspase Activation and Inhibition during Apoptosis. *Molecular cell* **9,** 459–470; 10.1016/S1097-2765(02)00482-3 (2002).

223. Kerr, J. F. R., Wyllie, A. H. & Currie, A. R. Apoptosis: A Basic Biological Phenomenon with Wideranging Implications in Tissue Kinetics. *Br J Cancer* **26,** 239–257; 10.1038/bjc.1972.33 (1972).

224. LeBlanc, H. N. & Ashkenazi, A. Apo2L/TRAIL and its death and decoy receptors. *Cell Death Differ* **10,** 66–75; 10.1038/sj.cdd.4401187 (2003).

225. Walczak, H. & Krammer, P. H. The CD95 (APO-1/Fas) and the TRAIL (APO-2L) Apoptosis Systems. *Experimental cell research* **256,** 58–66; 10.1006/excr.2000.4840 (2000).

226. Rathore, A. P. S., Ng, M.-L. & Vasudevan, S. G. Differential unfolded protein response during Chikungunya and Sindbis virus infection: CHIKV nsP4 suppresses eIF2α phosphorylation. *Virology journal* **10,** 36; 10.1186/1743-422X-10-36 (2013).

227. Tu, Y.-C., Yu, C.-Y., Liang, J.-J., Lin, E., Liao, C.-L. & Lin, Y.-L. Blocking double-stranded RNA-activated protein kinase PKR by Japanese encephalitis virus nonstructural protein 2A. *Journal of virology* **86,** 10347–10358; 10.1128/JVI.00525-12 (2012).

228. Liao, Y., Fung, T. S., Huang, M., Fang, S. G., Zhong, Y. & Liu, D. X. Upregulation of CHOP/GADD153 during coronavirus infectious bronchitis virus infection modulates apoptosis by restricting activation of the extracellular signal-regulated kinase pathway. *Journal of virology* **87,** 8124–8134; 10.1128/JVI.00626-13 (2013).

229. Peluso, R. W., Lamb, R. A. & Choppin, P. W. Infection with paramyxoviruses stimulates synthesis of cellular polypeptides that are also stimulated in cells transformed by Rous sarcoma virus or deprived of glucose. *Proceedings of the National Academy of Sciences of the United States of America* **75,** 6120–6124; 10.1073/pnas.75.12.6120 (1978).

230. Watowich, S. S., Morimoto, R. I. & Lamb, R. A. Flux of the paramyxovirus hemagglutinin-neuraminidase glycoprotein through the endoplasmic reticulum activates transcription of the GRP78-BiP gene. *Journal of virology* **65,** 3590–3597; 10.1128/JVI.65.7.3590-3597.1991 (1991).

231. Han, Y., Wang, C., Bai, C., Diao, E., Yuan, B., Lu, K., Dong, X., Zhang, R., Han, B., Liu, H., Wang, J., Wang, X., Xiao, S. & Yang, Z. Bovine parainfluenza virus type 3 infections induce ER stress-mediated autophagy to facilitate virus replication. *Veterinary microbiology* **292,** 110051; 10.1016/j.vetmic.2024.110051 (2024).

232. Munir, M. & Berg, M. The multiple faces of proteinkinase R in antiviral defense. *Virulence* **4,** 85–89; 10.4161/viru.23134 (2013).

233. Metz, D. H. & Esteban, M. Interferon inhibits viral protein synthesis in L cells infected with vaccinia virus. *Nature* **238,** 385–388; 10.1038/238385a0 (1972).

234. González Aparicio, L. J., Yang, Y., Hackbart, M. & López, C. B. Copy-back viral genomes induce a cellular stress response that interferes with viral protein expression without affecting antiviral immunity. *PLoS biology* **21,** e3002381; 10.1371/journal.pbio.3002381 (2023).

235. Hassan, I., Gaines, K. S., Hottel, W. J., Wishy, R. M., Miller, S. E., Powers, L. S., Rutkowski, D. T. & Monick, M. M. Inositol-requiring enzyme 1 inhibits respiratory syncytial virus replication. *The Journal of biological chemistry* **289,** 7537–7546; 10.1074/jbc.M113.510594 (2014).

236. Qiao, D., Skibba, M., Xu, X., Garofalo, R. P., Zhao, Y. & Brasier, A. R. Paramyxovirus replication induces the hexosamine biosynthetic pathway and mesenchymal transition via the IRE1α-XBP1s arm of the unfolded protein response. *American journal of physiology. Lung cellular and molecular physiology* **321,** L576-L594; 10.1152/ajplung.00127.2021 (2021).

237. Lenhard, L., Müller, M., Diederich, S., Loerzer, L., Friedrichs, V., Köllner, B., Finke, S., Dorhoi, A. & Pei, G. Ephrin B1 and B2 Mediate Cedar Virus Entry into Egyptian Fruit Bat Cells. *Viruses* **17**; 10.3390/v17040573 (2025).

238. Robert, X. & Gouet, P. Deciphering key features in protein structures with the new ENDscript server. *Nucleic acids research* **42,** W320-4; 10.1093/nar/gku316 (2014).

239. Fischer, K., Groschup, M. H. & Diederich, S. Importance of Endocytosis for the Biological Activity of Cedar Virus Fusion Protein. *Cells* **9**; 10.3390/cells9092054 (2020).

240. Tom, R., Bisson, L. & Durocher, Y. Transfection of HEK293-EBNA1 Cells in Suspension with Linear PEI for Production of Recombinant Proteins. *CSH protocols* **2008,** pdb.prot4977; 10.1101/pdb.prot4977 (2008).

241. Senichkin, V. V., Prokhorova, E. A., Zhivotovsky, B. & Kopeina, G. S. Simple and Efficient Protocol for Subcellular Fractionation of Normal and Apoptotic Cells. *Cells* **10**; 10.3390/cells10040852 (2021).

242. Cooper, J. K., Sykes, G., King, S., Cottrill, K., Ivanova, N. V., Hanner, R. & Ikonomi, P. Species identification in cell culture: a two-pronged molecular approach. *In Vitro Cell Dev Biol Anim* **43,** 344–351; 10.1007/s11626-007-9060-2 (2007).

243. Chomczynski, P. & Sacchi, N. Single-step method of RNA isolation by acid guanidinium thiocyanate-phenol-chloroform extraction. *Analytical biochemistry* **162,** 156–159; 10.1006/abio.1987.9999 (1987).

244. Friedrichs, V., Balkema-Buschmann, A., Dorhoi, A. & Pei, G. Selection and stability validation of reference gene candidates for transcriptional analysis in Rousettus aegyptiacus. *Scientific reports* **11,** 21662; 10.1038/s41598-021-01260-z (2021).

245. Virginia Friedrichs. *Immune responses of the Egyptian Rousette Bat - Deciphering the unique immunity of an important reservoir host for zoonotic viruses* (2022).

246. Feldman, K. S., Foord, A., Heine, H. G., Smith, I. L., Boyd, V., Marsh, G. A., Wood, J. L. N., Cunningham, A. A. & Wang, L.-F. Design and evaluation of consensus PCR assays for henipaviruses. *Journal of virological methods* **161,** 52–57; 10.1016/j.jviromet.2009.05.014 (2009).

247. Schrell, L., Fuchs, H. L., Dickmanns, A., Scheibner, D., Olejnik, J., Hume, A. J., Reineking, W., Störk, T., Müller, M., Graaf-Rau, A., Diederich, S., Finke, S., Baumgärtner, W., Mühlberger, E., Balkema-Buschmann, A. & Dobbelstein, M. *Inhibitors of dihydroorotate dehydrogenase synergize with the broad antiviral activity of 4'-fluorouridine* (2024).

248. Shcherbo, D., Merzlyak, E. M., Chepurnykh, T. V., Fradkov, A. F., Ermakova, G. V., Solovieva, E. A., Lukyanov, K. A., Bogdanova, E. A., Zaraisky, A. G., Lukyanov, S. & Chudakov, D. M. Bright far-red fluorescent protein for whole-body imaging. *Nat Methods* **4,** 741–746; 10.1038/nmeth1083 (2007).

249. Guangchuang Yu , Li-Gen Wang , GiovanniDall'Olio. *clusterProfiler. https://bioconductor.org/packages/release/bioc/html/clusterProfiler.html (last accessed 09.09.2025)* (Bioconductor, 2017).

250. Guangchuang Yu. *enrichplot. https://bioconductor.org/packages/release/bioc/html/enrichplot.html (last accessed 09.09.2025)* (Bioconductor, 2018).

251. Xu, S. *CRAN: Contributed Packages. ggstar: Multiple Geometric Shape Point Layer for 'ggplot2', https://cran.r-project.org/web/packages/ggstar/index.html (last accessed 09.09.2025)* (2020).

252. Campitelli, E. *CRAN: Contributed Packages. ggnewscale: Multiple Fill and Colour Scales in 'ggplot2', https://eliocamp.github.io/ggnewscale/ (last accessed 09.09.2025)* (2019).

253. Yu, G., Wang, L.-G., Yan, G.-R. & He, Q.-Y. DOSE: an R/Bioconductor package for disease ontology semantic and enrichment analysis. *Bioinformatics (Oxford, England)* **31,** 608–609; 10.1093/bioinformatics/btu684 (2015).

254. Marc Carlson. *org.Hs.eg.db. https://bioconductor.org/packages/release/data/annotation/html/org.Hs.eg.db.html (last accessed 09.09.2025)* (Bioconductor, 2017).

255. Wickham, H., François, R., Henry, L., Müller, K. & Vaughan, D. *CRAN: Contributed Packages. dplyr: A Grammar of Data Manipulation, https://cran.r-project.org/web/packages/dplyr/index.html (last accessed 09.09.2025)* (2014).

256. Wickham, H., Averick, M., Bryan, J., Chang, W., McGowan, L., François, R., Grolemund, G., Hayes, A., Henry, L., Hester, J., Kuhn, M., Pedersen, T., Miller, E., Bache, S., Müller,

K., Ooms, J., Robinson, D., Seidel, D., Spinu, V., Takahashi, K., Vaughan, D., Wilke, C., Woo, K. & Yutani, H. Welcome to the Tidyverse. *JOSS* **4,** 1686; 10.21105/joss.01686 (2019).

257. Neuwirth, E. *CRAN: Contributed Packages. ColorBrewer Palettes, https://cran.r-project.org/web/packages/RColorBrewer/refman/RColorBrewer.html (last accessed 09.09.2025)* (2002).

258. Huynh-Do, U., Vindis, C., Liu, H., Cerretti, D. P., McGrew, J. T., Enriquez, M., Chen, J. & Daniel, T. O. Ephrin-B1 transduces signals to activate integrin-mediated migration, attachment and angiogenesis. *Journal of cell science* **115,** 3073–3081; 10.1242/jcs.115.15.3073 (2002).

259. Kowalinski, E., Lunardi, T., McCarthy, A. A., Louber, J., Brunel, J., Grigorov, B., Gerlier, D. & Cusack, S. Structural basis for the activation of innate immune pattern-recognition receptor RIG-I by viral RNA. *Cell* **147,** 423–435; 10.1016/j.cell.2011.09.039 (2011).

260. Lin, R., Heylbroeck, C., Pitha, P. M. & Hiscott, J. Virus-dependent phosphorylation of the IRF-3 transcription factor regulates nuclear translocation, transactivation potential, and proteasome-mediated degradation. *Molecular and Cellular Biology* **18,** 2986–2996; 10.1128/MCB.18.5.2986 (1998).

261. Wulan, W. N., Heydet, D., Walker, E. J., Gahan, M. E. & Ghildyal, R. Nucleocytoplasmic transport of nucleocapsid proteins of enveloped RNA viruses. *Frontiers in microbiology* **6,** 553; 10.3389/fmicb.2015.00553 (2015).

262. Dastoor, Z. & Dreyer, J. L. Potential role of nuclear translocation of glyceraldehyde-3-phosphate dehydrogenase in apoptosis and oxidative stress. *Journal of cell science* **114,** 1643–1653; 10.1242/jcs.114.9.1643 (2001).

263. Hara, M. R., Agrawal, N., Kim, S. F., Cascio, M. B., Fujimuro, M., Ozeki, Y., Takahashi, M., Cheah, J. H., Tankou, S. K., Hester, L. D., Ferris, C. D., Hayward, S. D., Snyder, S. H. & Sawa, A. S-nitrosylated GAPDH initiates apoptotic cell death by nuclear translocation following Siah1 binding. *Nature cell biology* **7,** 665–674; 10.1038/ncb1268 (2005).

264. Satterfield, B. A., Borisevich, V., Foster, S. L., Rodriguez, S. E., Cross, R. W., Fenton, K. A., Agans, K. N., Basler, C. F., Geisbert, T. W. & Mire, C. E. Antagonism of STAT1 by Nipah virus P gene products modulates disease course but not lethal outcome in the ferret model. *Scientific reports* **9,** 16710; 10.1038/s41598-019-53037-0 (2019).

265. Fan, J., Li, Q., Liang, J., Chen, Z., Chen, L., Lai, J. & Chen, Q. Regulation of IFNβ expression: focusing on the role of its promoter and transcription regulators. *Frontiers in microbiology* **14,** 1158777; 10.3389/fmicb.2023.1158777 (2023).

266. Schoggins, J. W., Wilson, S. J., Panis, M., Murphy, M. Y., Jones, C. T., Bieniasz, P. & Rice, C. M. A diverse range of gene products are effectors of the type I interferon antiviral response. *Nature* **472,** 481–485; 10.1038/nature09907 (2011).

267. Otsuki, K., Maeda, J., Yamamoto, H. & Tsubokura, M. Studies on avian infectious bronchitis virus (IBV). III. Interferon induction by and sensitivity to interferon of IBV. *Archives of Virology* **60,** 249–255; 10.1007/BF01317496 (1979).

268. Habjan, M., Penski, N., Spiegel, M. & Weber, F. T7 RNA polymerase-dependent and -independent systems for cDNA-based rescue of Rift Valley fever virus. *The Journal of general virology* **89,** 2157–2166; 10.1099/vir.0.2008/002097-0 (2008).

269. Chikhoune, L., Poggi, C., Moreau, J., Dubucquoi, S., Hachulla, E., Collet, A. & Launay, D. JAK inhibitors (JAKi): Mechanisms of action and perspectives in systemic and autoimmune diseases. *La Revue de medecine interne* **46,** 89–106; 10.1016/j.revmed.2024.10.452 (2025).

270. Reid, E. & Charleston, B. Type I and III interferon production in response to RNA viruses. *Journal of interferon & cytokine research : the official journal of the International Society for Interferon and Cytokine Research* **34,** 649–658; 10.1089/jir.2014.0066 (2014).

271. Ye, L., Schnepf, D. & Staeheli, P. Interferon-λ orchestrates innate and adaptive mucosal immune responses. *Nature reviews. Immunology* **19,** 614–625; 10.1038/s41577-019-0182-z (2019).

272. Choi, U. Y., Kang, J.-S., Hwang, Y. S. & Kim, Y.-J. Oligoadenylate synthase-like (OASL) proteins: dual functions and associations with diseases. *Experimental & molecular medicine* **47,** e144; 10.1038/emm.2014.110 (2015).

273. Zhang, L. & Wang, A. Virus-induced ER stress and the unfolded protein response. *Frontiers in plant science* **3,** 293; 10.3389/fpls.2012.00293 (2012).

274. Fischer, K., Topallar, S., Kraatz, F., Groschup, M. H. & Diederich, S. The role of N-linked glycosylation in proteolytic processing and cell surface transport of the Cedar virus fusion protein. *Virol J* **19,** 136; 10.1186/s12985-022-01864-5 (2022).

275. Kopp, M. C., Larburu, N., Durairaj, V., Adams, C. J. & Ali, M. M. U. UPR proteins IRE1 and PERK switch BiP from chaperone to ER stress sensor. *Nature structural & molecular biology* **26,** 1053–1062; 10.1038/s41594-019-0324-9 (2019).

276. Heifetz, A., Keenan, R. W. & Elbein, A. D. Mechanism of action of tunicamycin on the UDP-GlcNAc:dolichyl-phosphate Glc-NAc-1-phosphate transferase. *Biochemistry* **18,** 2186–2192; 10.1021/bi00578a008 (1979).

277. Zinszner, H., Kuroda, M., Wang, X., Batchvarova, N., Lightfoot, R. T., Remotti, H., Stevens, J. L. & Ron, D. CHOP is implicated in programmed cell death in response to impaired function of the endoplasmic reticulum. *Genes & development* **12,** 982–995; 10.1101/gad.12.7.982 (1998).

278. Ordóñez, N. G. Immunohistochemical endothelial markers: a review. *Advances in anatomic pathology* **19,** 281–295; 10.1097/PAP.0b013e3182691c2a (2012).

279. Wagner, D. D., Olmsted, J. B. & Marder, V. J. Immunolocalization of von Willebrand protein in Weibel-Palade bodies of human endothelial cells. *The Journal of cell biology* **95,** 355–360; 10.1083/jcb.95.1.355 (1982).

280. Weibel, E. R. & Palade, G. E. New cytoplasmic components in arterial endothelia. *The Journal of cell biology* **23,** 101–112; 10.1083/jcb.23.1.101 (1964).

281. Sakariassen, K. S., Bolhuis, P. A. & Sixma, J. J. Human blood platelet adhesion to artery subendothelium is mediated by factor VIII-Von Willebrand factor bound to the subendothelium. *Nature* **279,** 636–638; 10.1038/279636a0 (1979).

282. Franke, W. W., Schiller, D. L., Moll, R., Winter, S., Schmid, E., Engelbrecht, I., Denk, H., Krepler, R. & Platzer, B. Diversity of cytokeratins. Differentiation specific expression of cytokeratin polypeptides in epithelial cells and tissues. *Journal of molecular biology* **153,** 933–959; 10.1016/0022-2836(81)90460-5 (1981).

283. Mourik, M. J., Faas, F. G. A., Zimmermann, H., Eikenboom, J. & Koster, A. J. Towards the imaging of Weibel-Palade body biogenesis by serial block face-scanning electron microscopy. *Journal of Microscopy* **259,** 97–104; 10.1111/jmi.12222 (2015).

284. Valentijn, K. M., Sadler, J. E., Valentijn, J. A., Voorberg, J. & Eikenboom, J. Functional architecture of Weibel-Palade bodies. *Blood* **117,** 5033–5043; 10.1182/blood-2010-09-267492 (2011).

285. Woolhouse, M. E. J., Haydon, D. T. & Antia, R. Emerging pathogens: the epidemiology and evolution of species jumps. *Trends in ecology & evolution* **20,** 238–244; 10.1016/j.tree.2005.02.009 (2005).

286. Olival, K. J., Hosseini, P. R., Zambrana-Torrelio, C., Ross, N., Bogich, T. L. & Daszak, P. Host and viral traits predict zoonotic spillover from mammals. *Nature* **546,** 646–650; 10.1038/nature22975 (2017).

287. Parrish, C. R., Holmes, E. C., Morens, D. M., Park, E.-C., Burke, D. S., Calisher, C. H., Laughlin, C. A., Saif, L. J. & Daszak, P. Cross-species virus transmission and the emergence of new epidemic diseases. *Microbiology and molecular biology reviews : MMBR* **72,** 457–470; 10.1128/MMBR.00004-08 (2008).

288. Geoghegan, J. L., Duchêne, S. & Holmes, E. C. Comparative analysis estimates the relative frequencies of co-divergence and cross-species transmission within viral families. *PLoS Pathog* **13**; 10.1371/journal.ppat.1006215 (2017).

289. Jones, K. E., Patel, N. G., Levy, M. A., Storeygard, A., Balk, D., Gittleman, J. L. & Daszak, P. Global trends in emerging infectious diseases. *Nature* **451,** 990–993; 10.1038/nature06536 (2008).

290. Patz, J. A., Daszak, P., Tabor, G. M., Aguirre, A. A., Pearl, M., Epstein, J., Wolfe, N. D., Kilpatrick, A. M., Foufopoulos, J., Molyneux, D. & Bradley, D. J. Unhealthy Landscapes: Policy Recommendations on Land Use Change and Infectious Disease Emergence. *Environmental Health Perspectives* **112,** 1092–1098; 10.1289/ehp.6877 (2004).

291. Eby, P., Peel, A. J., Hoegh, A., Madden, W., Giles, J. R., Hudson, P. J. & Plowright, R. K. Pathogen spillover driven by rapid changes in bat ecology. *Nature* **613,** 340–344; 10.1038/s41586-022-05506-2 (2023).

292. Luis, A. D., Hayman, D. T. S., O'Shea, T. J., Cryan, P. M., Gilbert, A. T., Pulliam, J. R. C., Mills, J. N., Timonin, M. E., Willis, C. K. R., Cunningham, A. A., Fooks, A. R., Rupprecht, C. E., Wood, J. L. N. & Webb, C. T. A comparison of bats and rodents as reservoirs of zoonotic viruses: are bats special? *Proceedings of the Royal Society B: Biological Sciences* **280,** 20122753; 10.1098/rspb.2012.2753 (2013).

293. Ruiz-Aravena, M., McKee, C., Gamble, A., Lunn, T., Morris, A., Snedden, C. E., Yinda, C. K., Port, J. R., Buchholz, D. W., Yeo, Y. Y., Faust, C., Jax, E., Dee, L., Jones, D. N., Kessler, M. K., Falvo, C., Crowley, D., Bharti, N., Brook, C. E., Aguilar, H. C., Peel, A. J., Restif, O., Schountz, T., Parrish, C. R., Gurley, E. S., Lloyd-Smith, J. O., Hudson, P. J., Munster, V. J. & Plowright, R. K. Ecology, evolution and spillover of coronaviruses from bats. *Nature reviews. Microbiology* **20,** 299–314; 10.1038/s41579-021-00652-2 (2022).

294. Streicker, D. G., Turmelle, A. S., Vonhof, M. J., Kuzmin, I. V., McCracken, G. F. & Rupprecht, C. E. Host phylogeny constrains cross-species emergence and establishment of rabies virus in bats. *Science (New York, N.Y.)* **329,** 676–679; 10.1126/science.1188836 (2010).

295. Davis, P. L., Holmes, E. C., Larrous, F., van der Poel, W. H. M., Tjørnehøj, K., Alonso, W. J. & Bourhy, H. Phylogeography, population dynamics, and molecular evolution of European bat lyssaviruses. *Journal of virology* **79,** 10487–10497; 10.1128/jvi.79.16.10487-10497.2005 (2005).

296. Dufloo, J., Andreu-Moreno, I., Moreno-García, J., Valero-Rello, A. & Sanjuán, R. Receptor-binding proteins from animal viruses are broadly compatible with human cell entry factors. *Nature microbiology* **10,** 405–419; 10.1038/s41564-024-01879-4 (2025).

297. Drescher, U. Eph family functions from an evolutionary perspective. *Current opinion in genetics & development* **12,** 397–402; 10.1016/s0959-437x(02)00316-7 (2002).

298. Liebl, D. J., Morris, C. J., Henkemeyer, M. & Parada, L. F. mRNA expression of ephrins and Eph receptor tyrosine kinases in the neonatal and adult mouse central nervous system. *Journal of neuroscience research* **71,** 7–22; 10.1002/jnr.10457 (2003).

299. Zarbalis, K. & Wurst, W. Expression domains of murine ephrin-A5 in the pituitary and hypothalamus. *Mechanisms of development* **93,** 165–168; 10.1016/s0925-4773(00)00252-5 (2000).

300. Sjöstedt, E., Zhong, W., Fagerberg, L., Karlsson, M., Mitsios, N., Adori, C., Oksvold, P., Edfors, F., Limiszewska, A., Hikmet, F., Huang, J., Du, Y., Lin, L., Dong, Z., Yang, L., Liu, X., Jiang, H., Xu, X., Wang, J., Yang, H., Bolund, L., Mardinoglu, A., Zhang, C., Feilitzen, K. von, Lindskog, C., Pontén, F., Luo, Y., Hökfelt, T., Uhlén, M. & Mulder, J. An atlas of the protein-coding genes in the human, pig, and mouse brain. *Science (New York, N.Y.)* **367**; 10.1126/science.aay5947 (2020).

301. Schoen, A., Hölzer, M., Müller, M. A., Wallerang, K. B., Drosten, C., Marz, M., Lamp, B. & Weber, F. Functional comparisons of the virus sensor RIG-I from humans, the microbat Myotis daubentonii, and the megabat Rousettus aegyptiacus, and their response to SARS-CoV-2 infection. *Journal of virology* **97,** e0020523; 10.1128/jvi.00205-23 (2023).

302. Chan, Y. P., Koh, C. L., Lam, S. K. & Wang, L.-F. Mapping of domains responsible for nucleocapsid protein-phosphoprotein interaction of Henipaviruses. *The Journal of general virology* **85,** 1675–1684; 10.1099/vir.0.19752-0 (2004).

303. Omi-Furutani, M., Yoneda, M., Fujita, K., Ikeda, F. & Kai, C. Novel phosphoprotein-interacting region in Nipah virus nucleocapsid protein and its involvement in viral replication. *Journal of virology* **84,** 9793–9799; 10.1128/JVI.00339-10 (2010).

304. Guito, J. C., Kirejczyk, S. G. M., Schuh, A. J., Amman, B. R., Sealy, T. K., Graziano, J., Spengler, J. R., Harmon, J. R., Wozniak, D. M., Prescott, J. B. & Towner, J. S. Coordinated inflammatory responses dictate Marburg virus control by reservoir bats. *Nature communications* **15,** 1826; 10.1038/s41467-024-46226-7 (2024).

305. Liu, T., Zhang, L., Joo, D. & Sun, S.-C. NF-κB signaling in inflammation. *Signal Transduction and Targeted Therapy* **2,** 17023; 10.1038/sigtrans.2017.23 (2017).

306. Li, Y., Banerjee, S., Wang, Y., Goldstein, S. A., Dong, B., Gaughan, C., Silverman, R. H. & Weiss, S. R. Activation of RNase L is dependent on OAS3 expression during infection with diverse human viruses. *Proceedings of the National Academy of Sciences of the United States of America* **113,** 2241–2246; 10.1073/pnas.1519657113 (2016).

307. Voll, R. E., Herrmann, M., Roth, E. A., Stach, C., Kalden, J. R. & Girkontaite, I. Immunosuppressive effects of apoptotic cells. *Nature* **390,** 350–351; 10.1038/37022 (1997).

308. Fadok, V. A., Bratton, D. L., Konowal, A., Freed, P. W., Westcott, J. Y. & Henson, P. M. Macrophages that have ingested apoptotic cells in vitro inhibit proinflammatory cytokine production through autocrine/paracrine mechanisms involving TGF-beta, PGE2, and PAF. *The Journal of clinical investigation* **101,** 890–898; 10.1172/JCI1112 (1998).

309. Martin, S. J., Henry, C. M. & Cullen, S. P. A perspective on mammalian caspases as positive and negative regulators of inflammation. *Molecular cell* **46,** 387–397; 10.1016/j.molcel.2012.04.026 (2012).

310. Gupta, M., Lo, M. K. & Spiropoulou, C. F. Activation and cell death in human dendritic cells infected with Nipah virus. *Virology* **441,** 49–56; 10.1016/j.virol.2013.03.004 (2013).

311. Laing, E. D., Sterling, S. L., Weir, D. L., Beauregard, C. R., Smith, I. L., Larsen, S. E., Wang, L.-F., Snow, A. L., Schaefer, B. C. & Broder, C. C. Enhanced Autophagy Contributes to Reduced Viral Infection in Black Flying Fox Cells. *Viruses* **11**; 10.3390/v11030260 (2019).

312. Goh, G., Ahn, M., Zhu, F., Lee, L. B., Luo, D., Irving, A. T. & Wang, L.-F. Complementary regulation of caspase-1 and IL-1β reveals additional mechanisms of dampened inflammation in bats. *Proceedings of the National Academy of Sciences of the United States of America* **117,** 28939–28949; 10.1073/pnas.2003352117 (2020).

313. Hu, H., Tian, M., Ding, C. & Yu, S. The C/EBP Homologous Protein (CHOP) Transcription Factor Functions in Endoplasmic Reticulum Stress-Induced Apoptosis and Microbial Infection. *Frontiers in immunology* **9,** 3083; 10.3389/fimmu.2018.03083 (2018).

314. Yang, X., Khosravi-Far, R., Chang, H. Y. & Baltimore, D. Daxx, a Novel Fas-Binding Protein That Activates JNK and Apoptosis. *Cell* **89,** 1067–1076 (1997).

315. Lo, M. K., Miller, D., Aljofan, M., Mungall, B. A., Rollin, P. E., Bellini, W. J. & Rota, P. A. Characterization of the antiviral and inflammatory responses against Nipah virus in endothelial cells and neurons. *Virology* **404,** 78–88; 10.1016/j.virol.2010.05.005 (2010).

316. Erbar, S., Diederich, S. & Maisner, A. Selective receptor expression restricts Nipah virus infection of endothelial cells. *Virology journal* **5,** 142; 10.1186/1743-422X-5-142 (2008).

317. Kamimura, D., Yamada, M., Harada, M., Sabharwal, L., Meng, J., Bando, H., Ogura, H., Atsumi, T., Arima, Y. & Murakami, M. The gateway theory: bridging neural and immune interactions in the CNS. *Frontiers in neuroscience* **7,** 204; 10.3389/fnins.2013.00204 (2013).

318. Barkhordarian, A., Thames, A. D., Du, A. M., Jan, A. L., Nahcivan, M., Nguyen, M. T., Sama, N. & Chiappelli, F. Viral immune surveillance: Toward a TH17/TH9 gate to the central nervous system. *Bioinformation* **11,** 47–54; 10.6026/97320630011047 (2015).

319. Aurine, N., Baquerre, C., Gaudino, M., Jean, C., Dumont, C., Rival-Gervier, S., Kress, C., Horvat, B. & Pain, B. Reprogrammed Pteropus Bat Stem Cells as A Model to Study Host-Pathogen Interaction during Henipavirus Infection. *Microorganisms* **9**; 10.3390/microorganisms9122567 (2021).

320. Alcock, D., Power, S., Hogg, B., Sacchi, C., Kacprzyk, J., McLoughlin, S., Bertelsen, M. F., Fletcher, N. F., O'Riain, A. & Teeling, E. C. Generating bat primary and immortalised cell-lines from wing biopsies. *Scientific reports* **14,** 27633; 10.1038/s41598-024-76790-3 (2024).

321. Deng, F., Morales-Sosa, P., Bernal-Rivera, A., Wang, Y., Tsuchiya, D., Javier, J. E., Rohner, N., Zhao, C. & Camacho, J. Establishing Primary and Stable Cell Lines from Frozen Wing Biopsies for Cellular, Physiological, and Genetic Studies in Bats. *bioRxiv : the preprint server for biology*; 10.1101/2024.03.22.586286 (2024).

10. Supplements

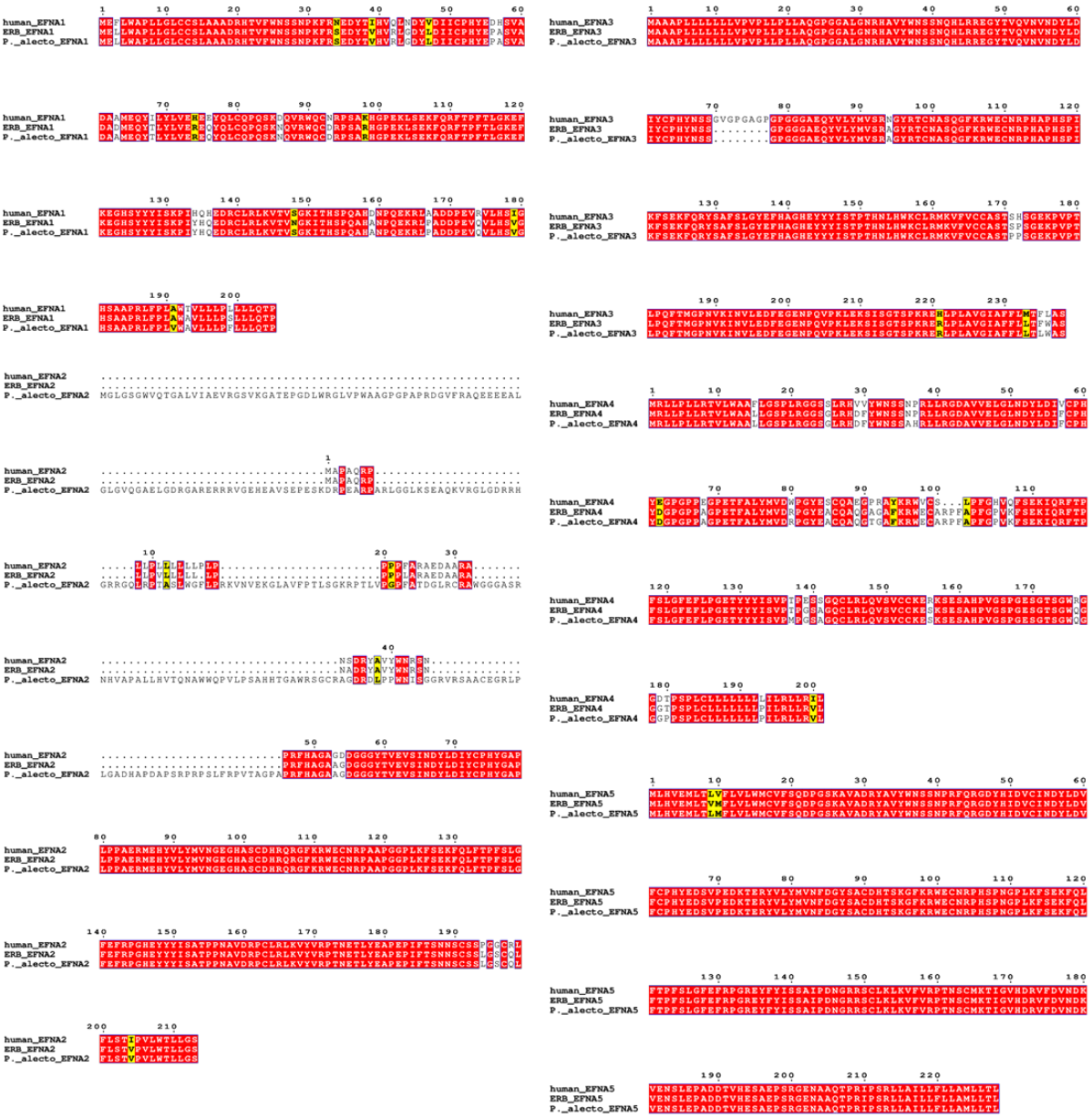

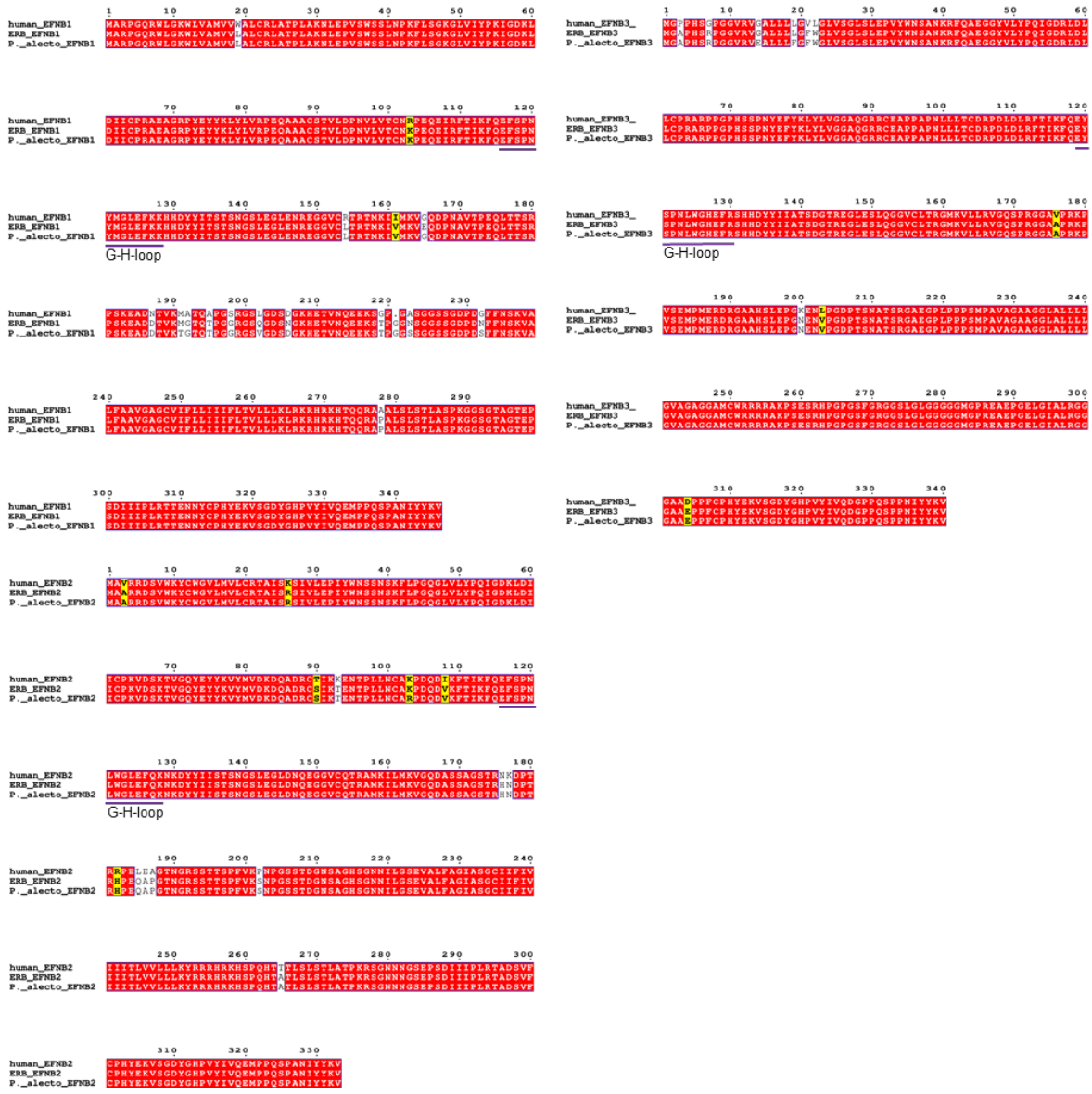

Supplementary Figure 10.1. Protein alignment of human, ERB, and *P. alecto* ephrins reveals little differences.

The G-H-loop of B ephrins is identical in all three species and marked in purple. Alignment of the amino acid sequences from NCBI Genbank (Reference genomes: *P. alecto*: GCF_000325575.1, ERB: GCF_001466805.2, human: GCF_000001405.40) was done with Geneious Prime (2021.0.1) and graphic was generated using ESPript 3.0. This figure was modified from the one published by Lenhard *et al.* [236].

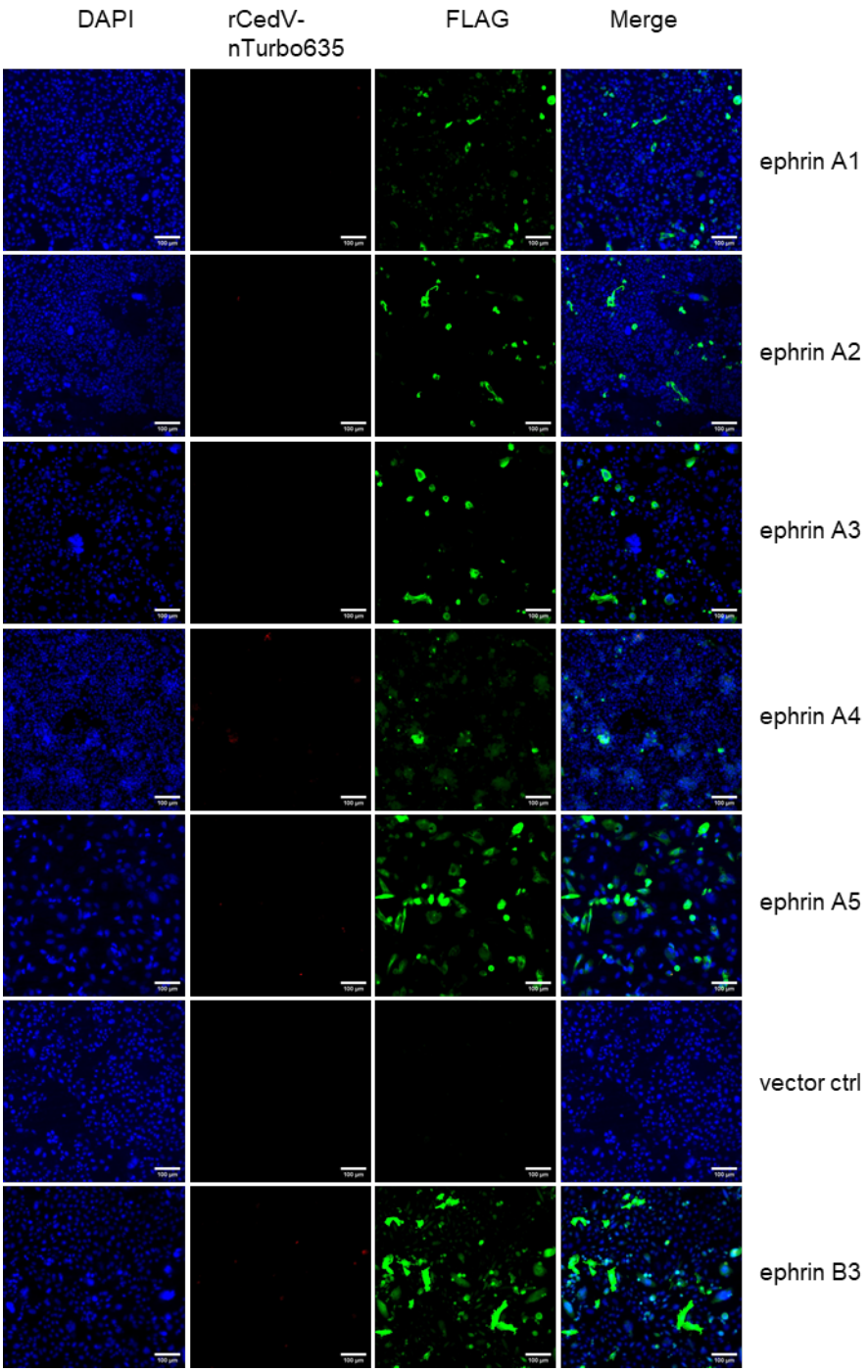

Supplementary Figure 10.2. No rCedV-nTurbo635 entry via ERB ephrins A1-5 and B3.
Immunofluorescence images of CHO-K1 stably expressing ERB ephrins or the empty vector infected with rCedV-nTurbo635 at MOI 2. FLAG-tagged ephrins were stained with an Alexa488 fluorophore and Turbo635 was visualized in the Cy3 channel. The cells were fixed 24 h p.i. and visualized using a Nikon Eclipse Ti microscope. Images are representative of 3 independent experiments. Image processing in the FITC channel was done separately for EFNB1/B2 and the rest of the ephrins. Brightness and contrast adjustments in the Cy3 channel were standardized for all images. Scale bar: 100 µm. This figure was modified from the one published by Lenhard *et al.* [236].

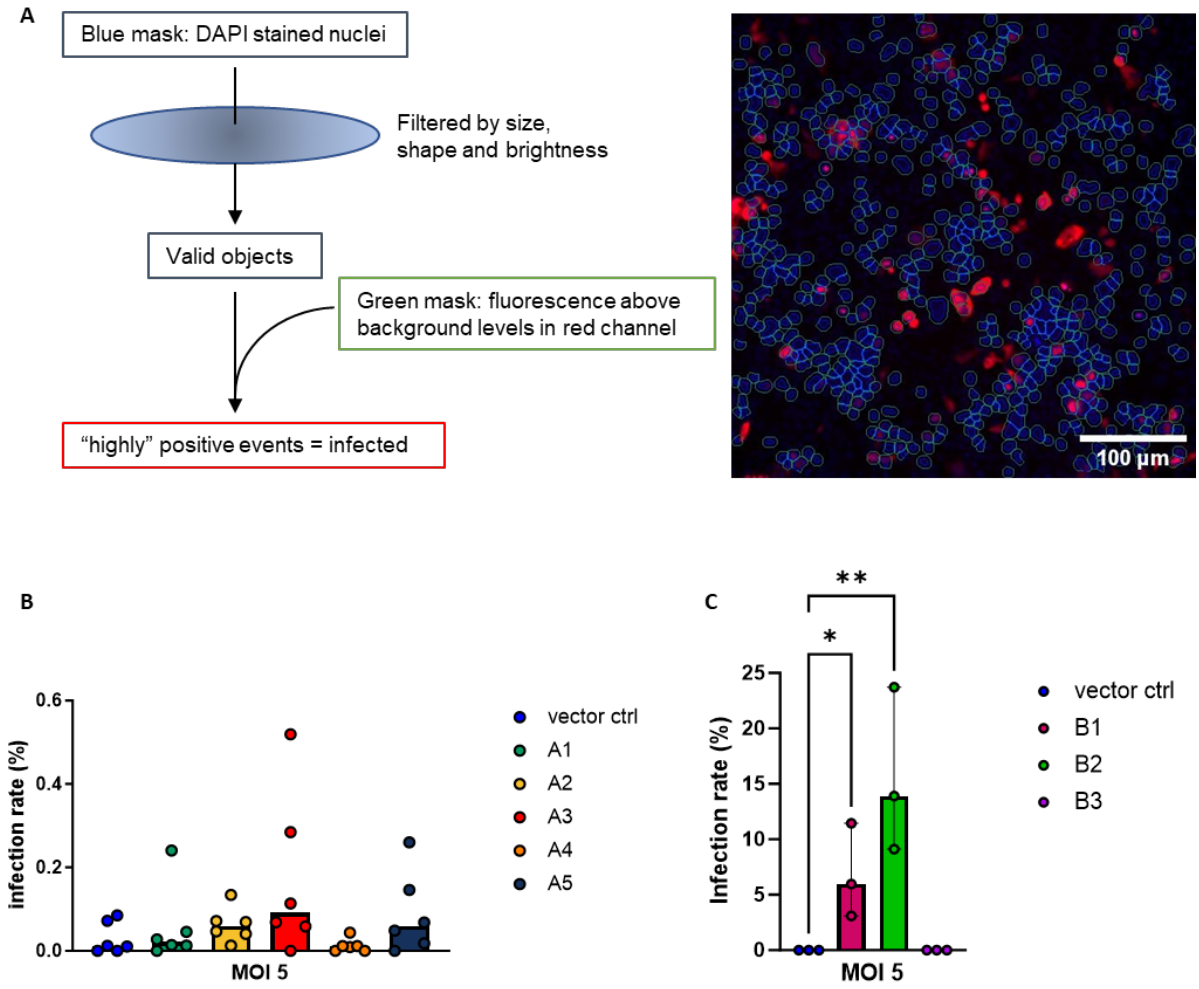

Supplementary Figure 10.3. High content imaging microscopy using the CellInsight CX7.

(A) Details on the algorithm used to quantify infected cells. First, cells are recognized by their DAPI stained nuclei and then filtered by size and shape. The resulting "valid objects" are counted as positive events, if fluorescence above background levels is detected in the red channel (ex. 561 nm) and in close vicinity to a nucleus. In analysis only "highly positive events were counted as infected. Thresholds were set according to values determined by infected BHK-21, as positive control, and rCedV-nTurbo635 inoculated CHO-K1 as negative control. Image shows example of infected CHO-B2 with nuclei surrounded by a blue mask and red fluorescence recognized in a green mask. Scale bar: 100 µm.

(B, C) Infection rate at MOI 5, as determined by high content microscopy.

CHO-K1 stably expressing ERB ephrins were re-transfected (A ephrins) or directly infected with rCedV-nTurbo635 at MOI 5 and infection rate was determined 24 h later. Graphs show median and range of 3 independent experiments in duplicate. $p < 0.05$ (*), $p < 0.01$(**). Statistical test: Kruskal-Wallis without Dunn's correction. This figure was modified from the one published by Lenhard *et al.* [236].

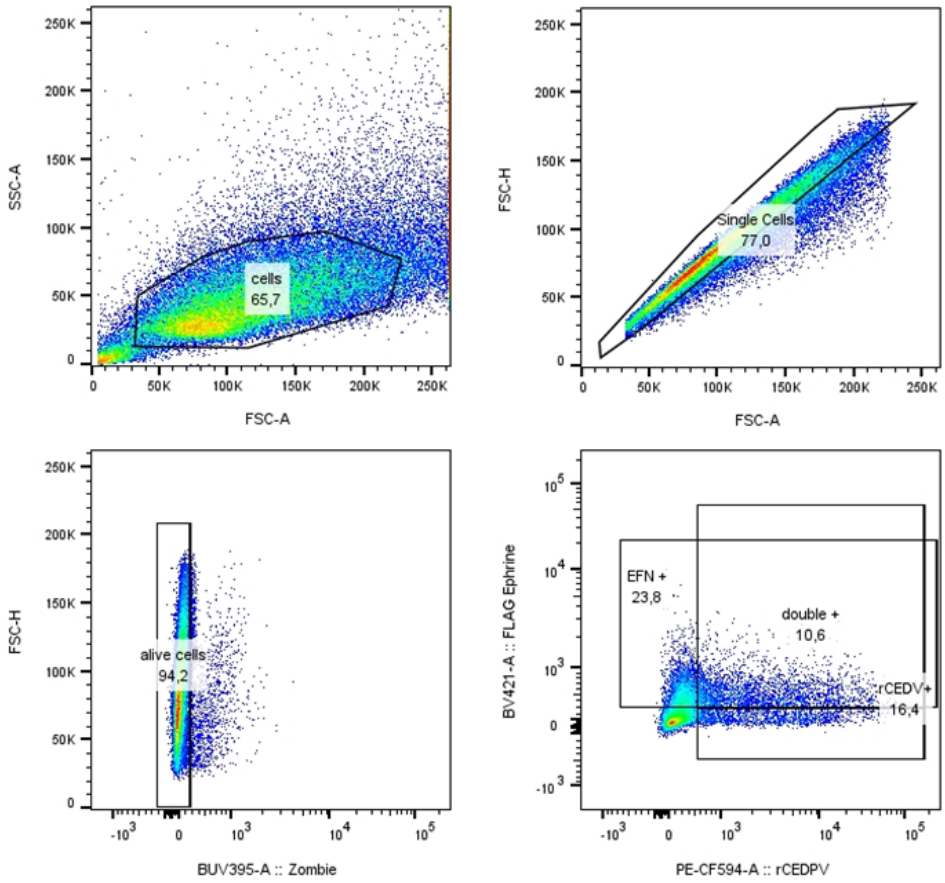

Supplementary Figure 10.4. Gating strategy for analysis of infection rate in flow cytometry.

Cell population of interest was determined by area and granularity. Doublets and dead cells were excluded before placing one gate on FLAG-expressing (BV421 positive) and one gate on rCedV-nTurbo635 infected (CF594 positive) populations. To determine infection rate of ephrin knockdown cells, similar gates were applied except for the ephrin staining. Measurements were performed on a BD FACSymphony™ A3 and analysis was done in FlowJo_v10.9.0. This figure was modified from the one published by Lenhard *et al.* [236].

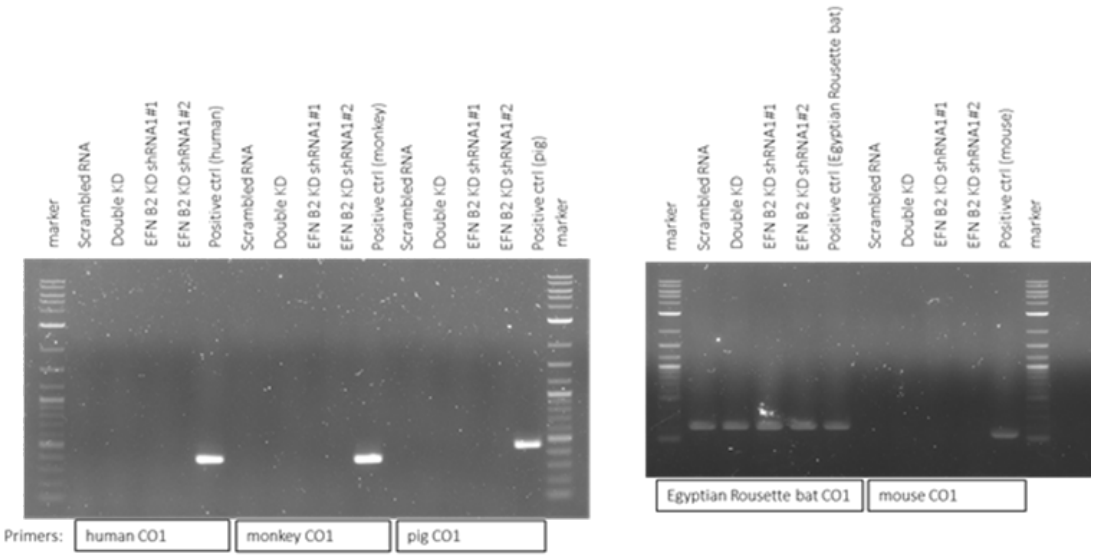

Supplementary Figure 10.5. Species identification of RaNep EFN KD cells by *CO1* barcoding.

ERB origin of RaNep ephrin knockdown cells was confirmed by cytochrome c oxidase 1 (*CO1*) barcoding PCR. Amplicon sizes of controls: human: 390 bp, pig: 460 bp, mouse: 150 bp, Egyptian Rousette bat: 250 bp, Tamarin monkey: 400 bp. This figure was modified from the one published by Lenhard *et al.* [236].

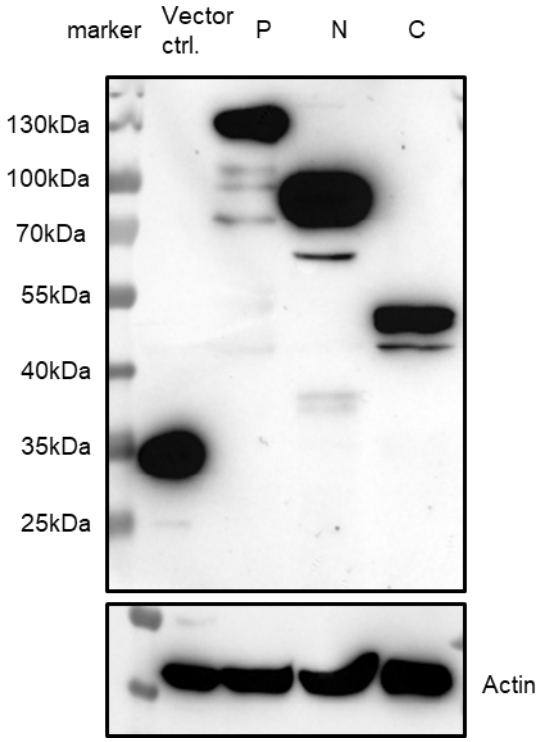

Supplementary Figure 10.6. Western blot analysis of HEK-293T expressing CedV proteins P, N, and C.
HEK-293T cells were seeded in a 12-well plate and transfected with plasmids encoding for the CedV proteins phosphoprotein P (84 kDa), nucleocapsid protein N (57 kDa), and the P gene-derived C protein (20 kDa). GFP-tagged proteins were visualized using a mouse anti-GFP antibody (Invitrogen) and transfection of the empty pEGFP-C1 vector served as a control. Loading control: β-Actin.

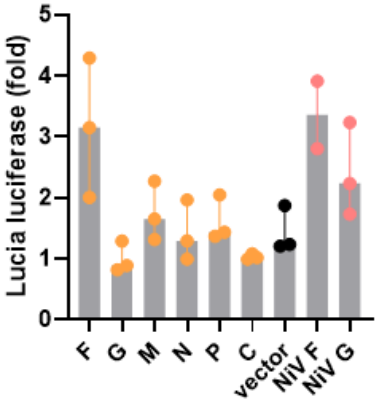

Supplementary Figure 10.7. Lucia luciferase assay of RaNep cells transfected with human RIG-I-CA does not show sufficient luciferase induction in the positive control.
RaNep cells were transfected with human RIG-I-CA, a plasmid expressing Lucia luciferase under the ERB *IFNB* promoter, and plasmids encoding for the different CedV proteins, Nipah G and F (Dr. Sandra Diederich), or the empty vector. The negative control consisted of just the luciferase plasmid and the empty vector, adjusted to the same total amount of transfected DNA. The data show median ± *IQR* of 3 independent experiments in duplicate normalized to the negative control.

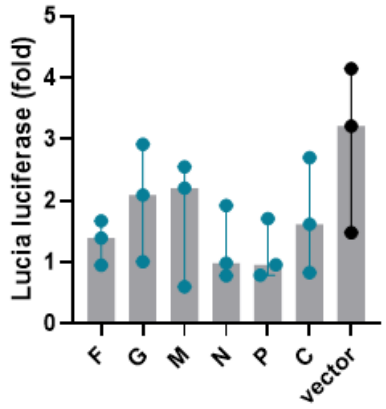

Supplementary Figure 10.8. Lucia luciferase assay of HEK-293T cells transfected with MDA5 does not show sufficient luciferase induction in the positive control.

HEK-293T cells were transfected with MDA5, a plasmid expressing Lucia luciferase under the murine *IFNB* promoter and plasmids encoding for the different CedV proteins, or the empty vector. The negative control consisted of just the luciferase plasmid and the empty vector, adjusted to the same total amount of transfected DNA. The data show median ± *IQR* of 3 independent experiments in duplicate normalized to the negative control.

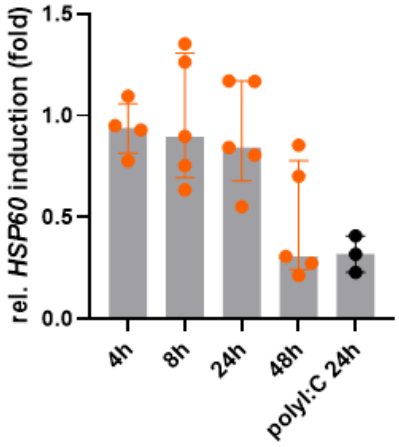

Supplementary Figure 10.9. *HSP60* levels remain unaltered in RaNep in response to rCedV-nTurbo635 infection.

qPCR data of *HSP60* expression in RaNep infected with rCedV-nTurbo635 at MOI 0.1. for 4 h, 8 h, 24 h, and 48 h and after polyI:C stimulation for 24 h normalized to the uninfected control. The data show median ± *IQR* of at least 3 independent experiments.

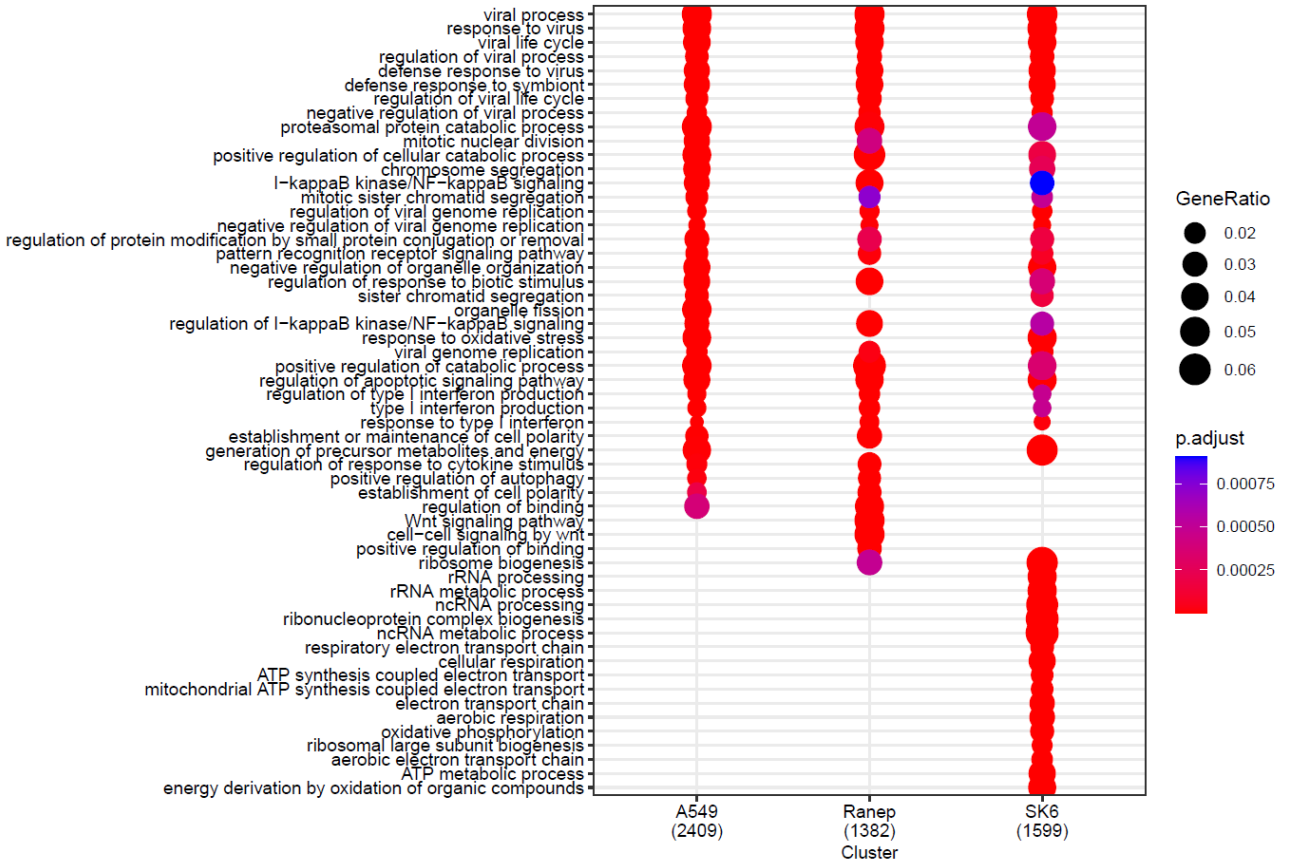

Supplementary Figure 10.10. Biological process (BP) pathway enrichment analysis reveals differences in energy metabolism in SK-6 24 h p.i.

Differences in protein levels relevant for the annotated pathways are depicted by proportional circle sizes. P values are visualized by the color of the circles, with lowest P values (= highest significance) colored in red. Gene Ontology enrichment analysis was done in R Studio (package: clusterProfiler). Statistical test: t-test.

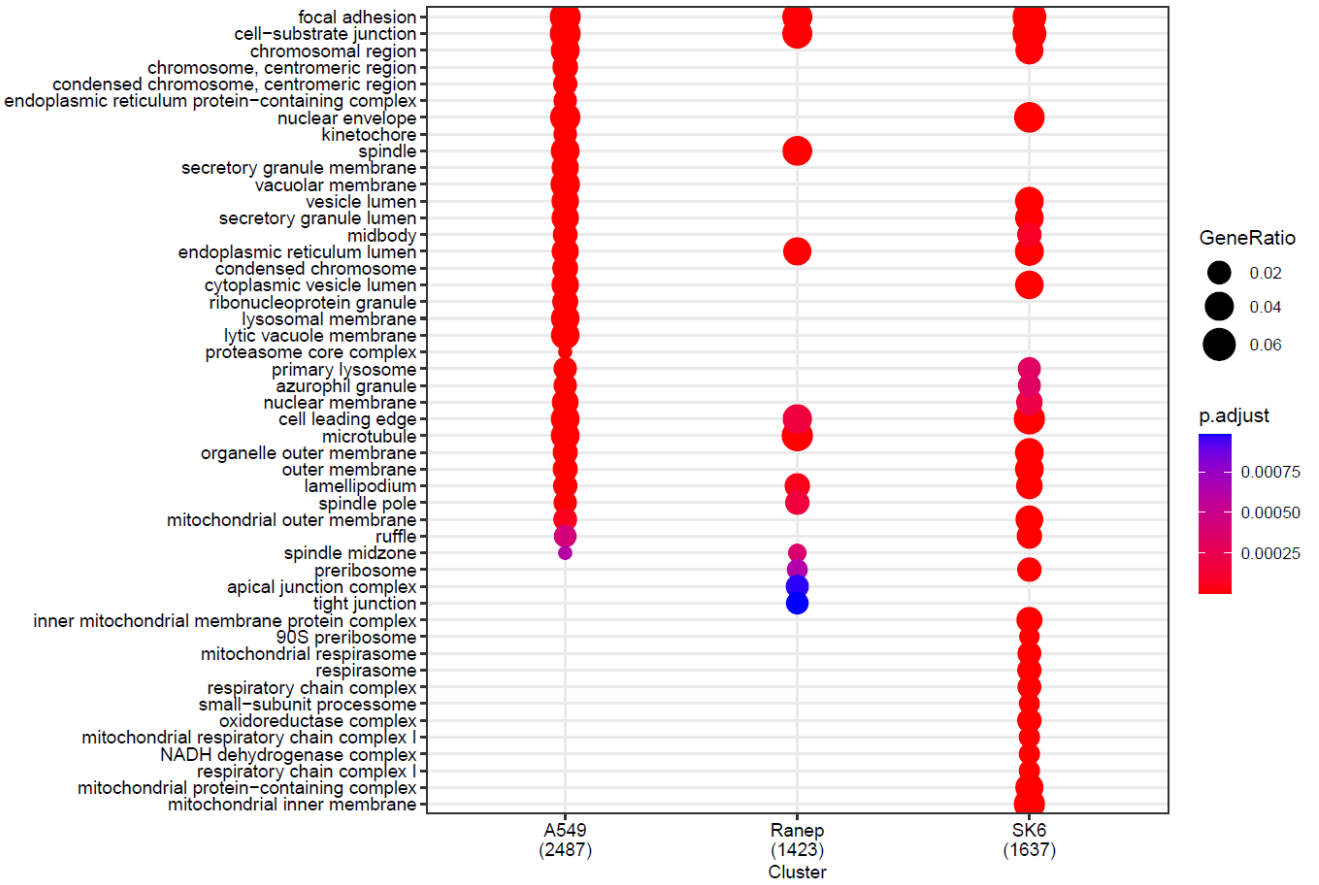

Supplementary Figure 10.11. Cellular component (CC) pathway enrichment analysis reveals differences in mitochondrial function in SK-6 24 h p.i.

Differences in protein levels relevant for the annotated pathways are depicted by proportional circle sizes. P values are visualized by the color of the circles, with lowest P values (= highest significance) colored in red. Gene Ontology enrichment analysis was done in R Studio (package: clusterProfiler). Statistical test: t-test.

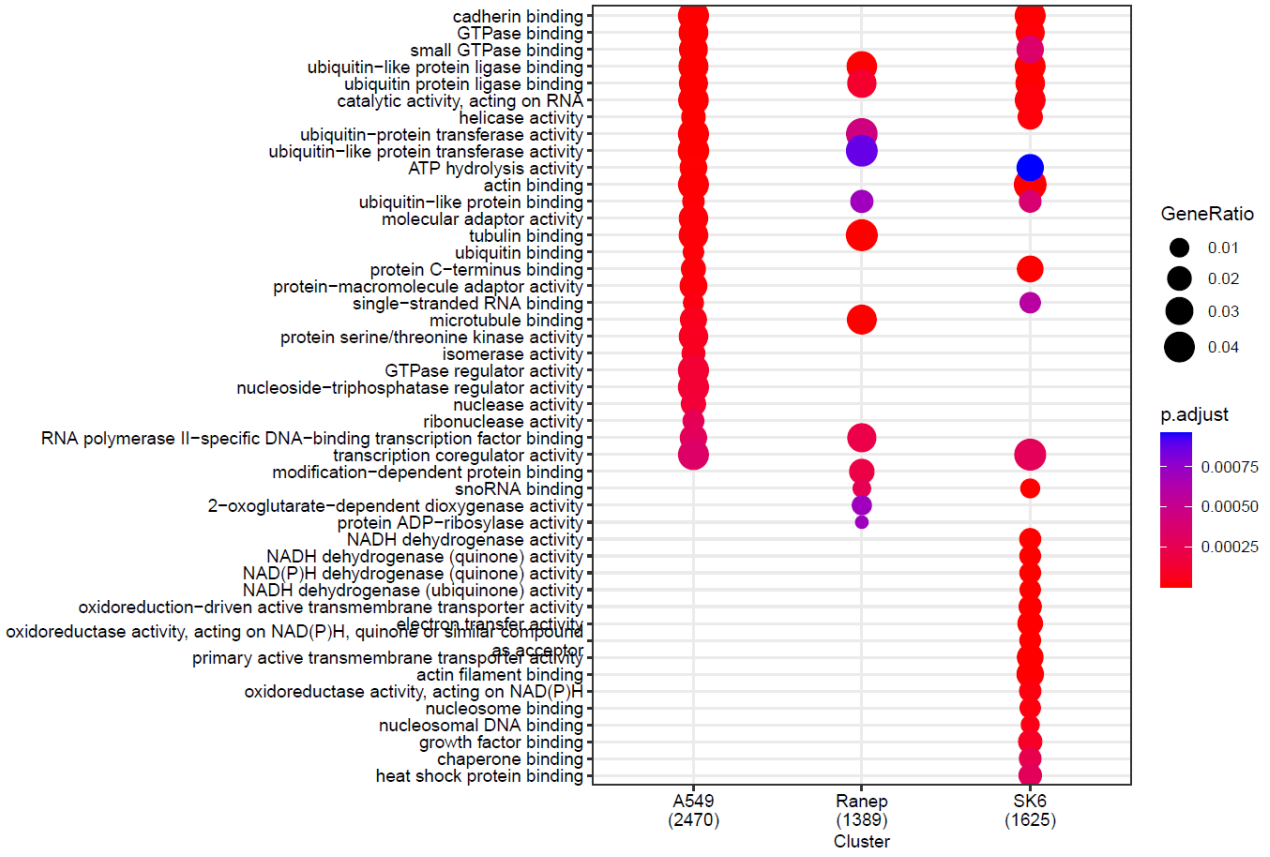

Supplementary Figure 10.12. Molecular function (MF) pathway enrichment analysis.

Differences in protein levels relevant for the annotated pathways are depicted by proportional circle sizes. P values are visualized by the color of the circles, with lowest P values (= highest significance) colored in red. Gene Ontology enrichment analysis was done in R Studio (package: clusterProfiler). Statistical test: t-test.

Supplementary Figure 10.13. Upregulation of proteins related to antiviral response and innate immune activation.

Heatmap of top 50 most upregulated proteins (gene names) after rCedV-nTurbo635 infection in RaNep in comparison to A549 and SK-6. The color scale represents differences in protein expression levels (log_2 fold changes) between MOCK and rCedV-nTurbo635 infected samples. Whenever values were not available tile is colored in grey. Most upregulated proteins are salmon-colored, while least upregulated proteins are displayed in light blue. CedV proteins F, G, M, N, P, as well as the Turbo635 fluorescent protein can be detected in all 3 cell lines. The heatmap was created in R Studio.

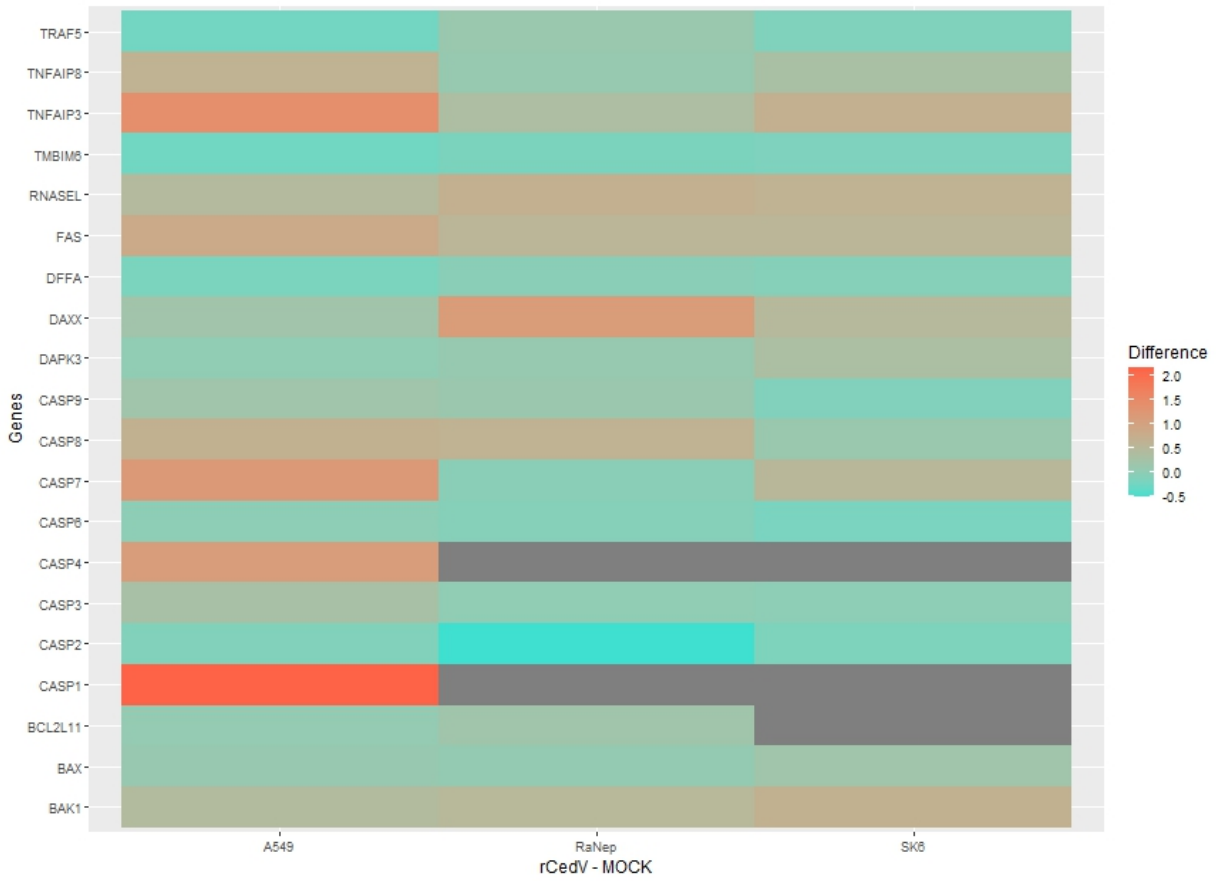

Supplementary Figure 10.14 Differentially regulated pro- and anti-apoptotic proteins.

Heatmap of selected proteins, involved in apoptosis. The color scale represents differences in protein expression levels (log_2 fold changes) between MOCK and rCedV-nTurbo635 infected samples. Whenever values were not available tile is colored in grey. Most upregulated proteins are salmon-colored, while least upregulated or downregulated proteins are displayed in light blue. The heatmap was created in R Studio.

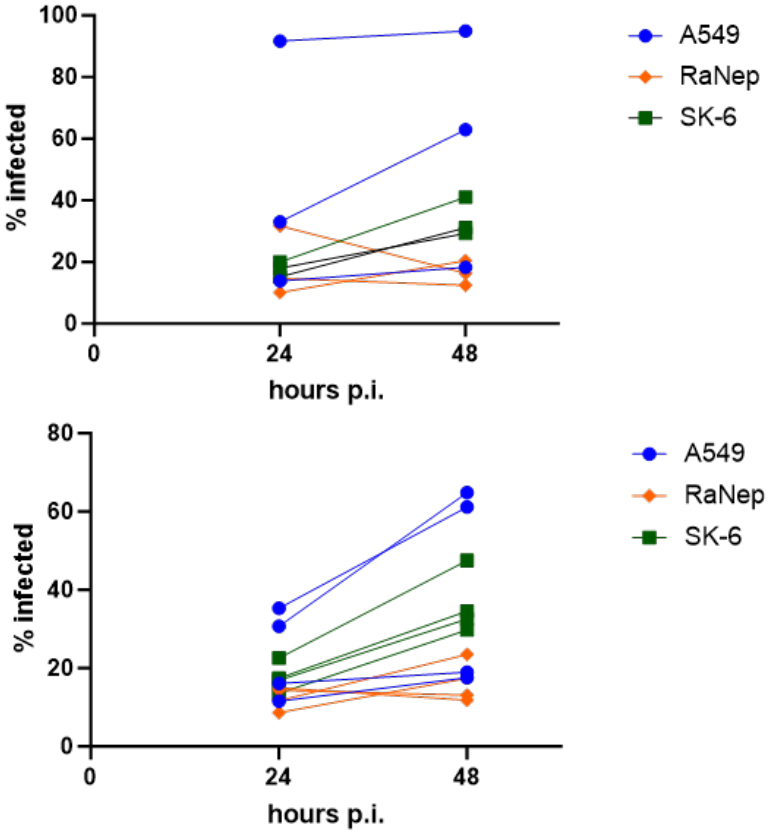

Supplementary Figure 10.15. High content image analysis of infection rate.

A549, RaNep and SK-6 were seeded in 96-well plates and infected with rCedV-nTurbo635 at MOI 0.1. Infection rate was quantified by SpotCount in channel 2 (ex. 561 nm) at 24 h/48 h p.i.

(A) Mean infection rate of duplicate on each plate that was run for cell death assay.

(B) Infection rate of duplicate with outlier removed, showing replication on A549 and SK-6 within 24 h.

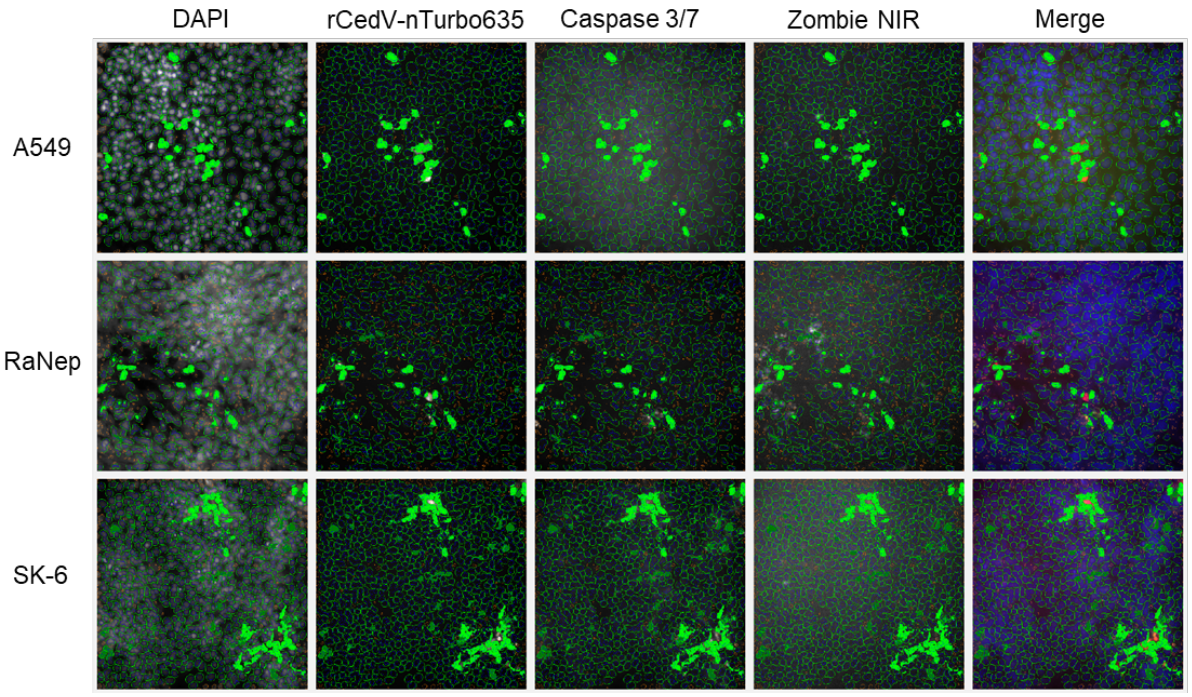

Supplementary Figure 10.16. High content image analysis of caspase-3/7 activation in response to rCedV-nTurbo635 infection.

A549, RaNep, and SK-6 were seeded in 96-well plates and infected with rCedV-nTurbo635 at MOI 0.1. 24 h/48 h p.i. plates were stained with the green CellEvent™ Caspase-3/7 detection reagent and fixed in 4% PFA. A549 and RaNep were additionally stained with the Zombie NIR viability dye to quantify late-stage apoptosis and necrosis. Excitation wave lengths: rCedV-nTurbo635: 561 nm; caspase-3/7: 485 nm; Zombie NIR: 650 nm;

PELENDO cell death assay protocol was adjusted to primary cell shapes and sizes and no Zombie NIR staining was performed.

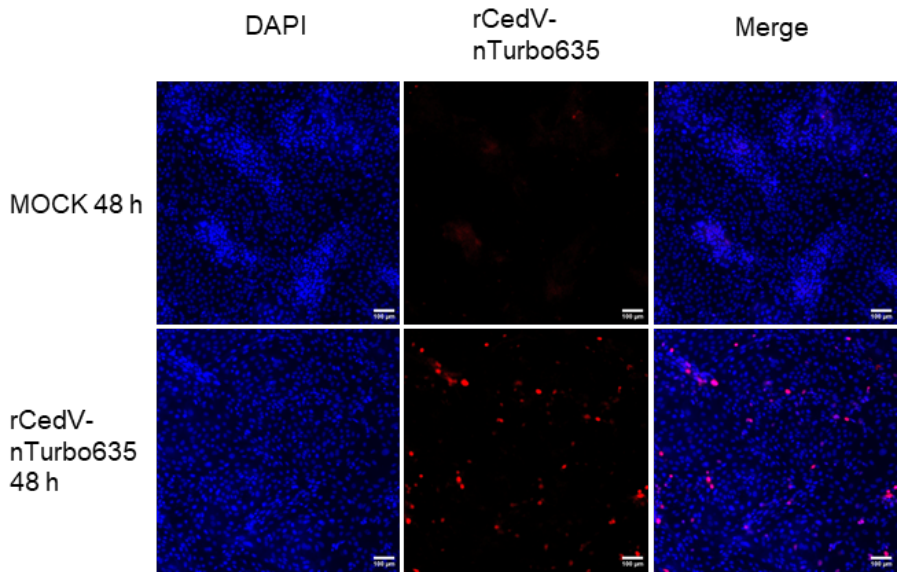

Supplementary Figure 10.17. PELENDO are susceptible to rCedV-nTurbo635 infection.
PELENDO were seeded in 96-well plates, infected at MOI 0.5, and fixed in 4% PFA at 48 h p.i. Pictures were taken using the Nikon Eclipse Ti microscope and brightness/contrast adjustments were done in ImageJ. Scale bar: 100 µm.

11. Abbreviations

Abbreviation	Meaning
ATF 4	Activating transcription factor 4
ATF 6	Activating transcription factor 6
AIM2	Absent in melanoma 2
Asp, D	Aspartic acid
Bak	Bcl-2-associated K protein
Bax	Bcl-2-associated X protein
BBB	Blood brain barrier
BiP/GRP78	Binding immunoglobulin protein/ 78 kDa glucose-regulated protein
BSL	Biosafety level
CARD	Caspase recruitment domain
CedV	Cedar virus
CedV WT	Cedar virus wildtype isolate
rCedV-nTurbo635	Recombinant Cedar virus with a Turbo635 fluorescent signal localized to the nucleus of infected cells
CHOP/*GADD153*	C/EBP homologous protein/ growth arrest- and DNA damage-inducible gene 153
CNS	Central nervous system
DAMP	Damage associated molecular patterns
DAPI	4′,6-diamidino-2-phenylindole

DDIT3	DNA damage inducible transcript 3 (CHOP gene)
DR5	Death receptor 5
dsRNA	Double strand RNA
ECGS	Endothelial cell growth supplement
EFN	ephrin
EGF	Epithelial growth factor
ELMI	Electron microscopy
ER	Endoplasmic reticulum
ERAD	ER-associated protein degradation
ERO1α	ER oxidoreductase 1 alpha
ERB	Egyptian Rousette bat, *Rousettus aegyptiacus*
eIF2α	Eukaryotic translation initiation factor 2 α
GADD34	Growth Arrest and DNA Damage-Inducible Protein 34
GAS	Gamma interferon activation site
GPI	Glycosylphosphatidylinositol
HeV	Hendra virus
HSPA5	Heat Shock Protein Family A (Hsp70) Member 5 (BiP gene)
IF	Immunofluorescence
IFI	Interferon inducible gene
IFN	Interferon

IFNGR	Interferon gamma receptor
IFNLR	Interferon lambda receptor
IKKε	I-kappa-B kinase ε
IL	Interleukin
IQR	Interquartile range
IRE1	Inositol-requiring enzyme 1
IRF	Interferon regulatory factor
ISG	Interferon stimulated gene
ISRE	Interferon stimulated response elements
JAK	Janus kinase
KD	Knockdown
LGP2	Laboratory of genetics and physiology 2
MARV	Marburg virus
MAVS	Mitochondrial antiviral signaling protein
MDA5	melanoma differentiation-associated gene 5
Met	Methionine
MOI	Multiplicity of infection
MX1	Myxoma resistance 1
MYD88	myeloid differentiation primary response-88
NF-κB	Nuclear factor κ-light-chain-enhancer of activated B cells
NiV	Nipah virus

NLRP3	NOD-, LRR- and pyrin domain-containing protein 3
OAS	2',5'-oligoadenylate synthetase
OASL	2',5'-oligoadenylate synthetase 1-like protein
ORF	Open reading frame
PaKi	*P. alecto* kidney cells
PAMP	Pathogen associated molecular patterns
PARP	Poly(ADP-ribose)-Polymerase
PBS	Phosphate-buffered saline
PCR	Polymerase chain reaction
PELENDO	Primary ERB lung endothelia-like cells
PELEPI	Primary ERB lung epithelial cells
PERK	PKR-like ER kinase
PFU	Plaque forming units
PIV	Parainfluenza virus
PKR	Protein kinase R
polyI:C	Polyinosinic-polycytidylic acid
PP1	Phosphatase 1
PRR	Pattern recognition receptor
PYHIN	PYRIN and HIN domain
RaNep	*Rousettus aegyptiacus* nose epithelial cells
RBP	Receptor binding protein

RdRp	RNA-dependent RNA polymerase
RIG-I	Retinoic acid inducible gene I
RIPA	Radioimmunoprecipitation assay
RLR	RIG-I-like receptors
ROS	Reactive oxygen species
RSV	Respiratory syncytial virus
SD	Standard deviation
SDS-PAGE	Sodium dodecyl-sulfate polyacrylamide gel electrophoresis
Ser, S	Serine
SeV	Sendai virus
STAT	Signal transducer and activator of transcription 1
STSP	Staurosporine
TCID50	Tissue culture infection dose 50
TBK1	TANK-binding kinase 1
Thr, T	Threonine
TRAF6	Tumor necrosis factor receptor associated factor 6
TRIF	Toll/IL-1R domain-containing adaptor-inducing IFNβ
TRIM	Tripartite motif
TLR	Toll-like receptor
TNFA	tumor necrosis factor α

TYK2	Tyrosine kinase 2
Tyr, Y	Tyrosine
UPR	Unfolded protein response
US	United States
VSV	Vesicular stomatitis virus
VWF	Von Willebrand factor
WB	Western blot
XBP1	X-box binding protein 1

12. Tables

13. Figures

14. Acknowledgements

I would like to express my appreciation to Prof. Dr. Anca Dorhoi and Dr. Gang Pei for providing me with the opportunity to conduct my research at the Institute of Immunology at the Friedrich-Loeffler-Institut and for the Institute's intramural funding, which financially supported the work presented here. I am grateful for the support and mentorship I received. Thanks should also go to Prof. Dr. Stefan Finke for sharing his recombinant Cedar virus, without which this project would not have been possible.

This endeavor would not have been possible without the professional support and encouragement from Prof. Dr. Jens Teifke, who was ready to lend an ear or share his knowledge whenever necessary. I would also like to acknowledge Dr. Christine Luttermann, Dr. Birke Tews, and their labs for the regular paper discussions and insights into the world of molecular virology. I am also extremely grateful to Lisa Loerzer for the technical support, the helpful discussions, and many fun moments in the lab. Additionally, I would like to mention my extended lab mates Sandra and Franzi, who kindly shared their knowledge and equipment whenever needed.

I owe a lot of gratitude to my parents, who have always supported my education and career. Special thanks to my friends, who tirelessly listened to my complaints, distracted me from disappointments, and made me laugh throughout this journey. And last, but not least, I would like to acknowledge the fluffiest cat in the world and the most magical horse. I would have never gotten this far if it weren't for you.

15. Declaration (Erklärung)

Hiermit erkläre ich, dass ich die vorgelegte Dissertation selbständig und ohne unerlaubte fremde Hilfe und nur mit den Hilfen angefertigt habe, die ich in der Dissertation angegeben habe. Alle Textstellen, die wörtlich oder sinngemäß aus veröffentlichten oder nicht veröffentlichten Schriften entnommen sind, und alle Angaben, die auf mündlichen Auskünften beruhen, sind als solche kenntlich gemacht. Bei den von mir durchgeführten und in der Dissertation erwähnten Untersuchungen habe ich die Grundsätze guter wissenschaftlicher Praxis, wie sie in der "Satzung der Justus-Liebig-Universität Gießen zur Sicherung guter wissenschaftlicher Praxis" niedergelegt sind, eingehalten.

Ort, Datum

Lea Lenhard